

A scanning electron micrograph (SEM) showing a porous, interconnected network of fibers or cells. Numerous small, rod-like structures (nanorods) are distributed throughout the porous structure, some inside the pores and some on the surface. The background is a light gray, and the nanorods are darker, creating a high-contrast image.

INORGANIC BIOMATERIALS

EDITED BY : Wolfram Höland and Aldo R. Boccaccini

**PUBLISHED IN: Frontiers in Bioengineering and Biotechnology and
Frontiers in Materials**



frontiers

Frontiers Copyright Statement

© Copyright 2007-2016 Frontiers Media SA. All rights reserved.

All content included on this site, such as text, graphics, logos, button icons, images, video/audio clips, downloads, data compilations and software, is the property of or is licensed to Frontiers Media SA ("Frontiers") or its licensees and/or subcontractors. The copyright in the text of individual articles is the property of their respective authors, subject to a license granted to Frontiers.

The compilation of articles constituting this e-book, wherever published, as well as the compilation of all other content on this site, is the exclusive property of Frontiers. For the conditions for downloading and copying of e-books from Frontiers' website, please see the Terms for Website Use. If purchasing Frontiers e-books from other websites or sources, the conditions of the website concerned apply.

Images and graphics not forming part of user-contributed materials may not be downloaded or copied without permission.

Individual articles may be downloaded and reproduced in accordance with the principles of the CC-BY licence subject to any copyright or other notices. They may not be re-sold as an e-book.

As author or other contributor you grant a CC-BY licence to others to reproduce your articles, including any graphics and third-party materials supplied by you, in accordance with the Conditions for Website Use and subject to any copyright notices which you include in connection with your articles and materials.

All copyright, and all rights therein, are protected by national and international copyright laws.

The above represents a summary only. For the full conditions see the Conditions for Authors and the Conditions for Website Use.

ISSN 1664-8714

ISBN 978-2-88919-801-6

DOI 10.3389/978-2-88919-801-6

About Frontiers

Frontiers is more than just an open-access publisher of scholarly articles: it is a pioneering approach to the world of academia, radically improving the way scholarly research is managed. The grand vision of Frontiers is a world where all people have an equal opportunity to seek, share and generate knowledge. Frontiers provides immediate and permanent online open access to all its publications, but this alone is not enough to realize our grand goals.

Frontiers Journal Series

The Frontiers Journal Series is a multi-tier and interdisciplinary set of open-access, online journals, promising a paradigm shift from the current review, selection and dissemination processes in academic publishing. All Frontiers journals are driven by researchers for researchers; therefore, they constitute a service to the scholarly community. At the same time, the Frontiers Journal Series operates on a revolutionary invention, the tiered publishing system, initially addressing specific communities of scholars, and gradually climbing up to broader public understanding, thus serving the interests of the lay society, too.

Dedication to quality

Each Frontiers article is a landmark of the highest quality, thanks to genuinely collaborative interactions between authors and review editors, who include some of the world's best academicians. Research must be certified by peers before entering a stream of knowledge that may eventually reach the public - and shape society; therefore, Frontiers only applies the most rigorous and unbiased reviews.

Frontiers revolutionizes research publishing by freely delivering the most outstanding research, evaluated with no bias from both the academic and social point of view.

By applying the most advanced information technologies, Frontiers is catapulting scholarly publishing into a new generation.

What are Frontiers Research Topics?

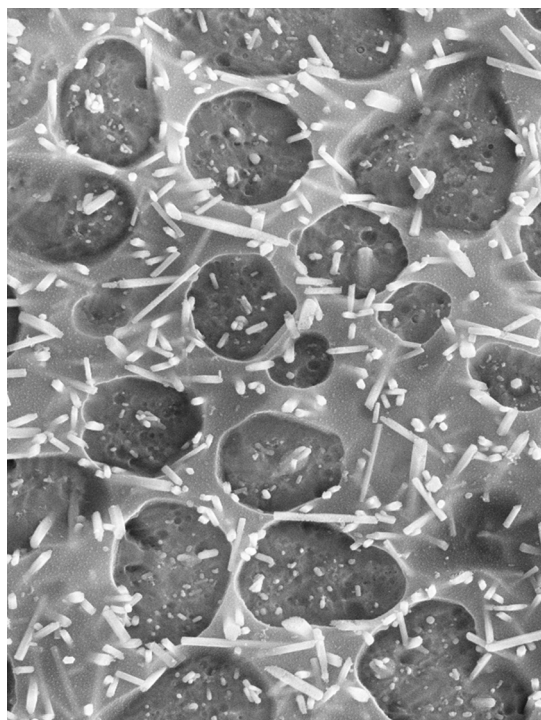
Frontiers Research Topics are very popular trademarks of the Frontiers Journals Series: they are collections of at least ten articles, all centered on a particular subject. With their unique mix of varied contributions from Original Research to Review Articles, Frontiers Research Topics unify the most influential researchers, the latest key findings and historical advances in a hot research area! Find out more on how to host your own Frontiers Research Topic or contribute to one as an author by contacting the Frontiers Editorial Office: researchtopics@frontiersin.org

INORGANIC BIOMATERIALS

Topic Editors:

Wolfram Höland, Ivoclar Vivadent AG, Liechtenstein

Aldo R. Boccaccini, University of Erlangen-Nuremberg, Germany



Radiopaque dental glass-ceramics with crystal phases of $\text{Sr}_5(\text{PO}_4)_3\text{F}$, $\text{RbAlSi}_2\text{O}_6$ and NaSrPO_4 . ESM, etches sample.

The intention of the editors A. R. Boccaccini and W. Höland has been to target this e-book to a broad readership and at the same time to present scientific contributions sufficiently detailed which discuss various specific fundamental aspects of inorganic biomaterials and their biomedical and dental applications. In this context, two large categories of biomaterials need to be mentioned, namely bioactive biomaterials for the replacement and regeneration of hard tissue and biocompatible, non-bioactive biomaterials for restorative dentistry. Both categories include products based on glasses or glass-ceramics as well as organic-inorganic composite materials. Among the bioactive products, BIOGLASS®, developed in the late 1960s by Prof. Dr. L. L. Hench, occupies a prominent position, being BIOGLASS® the first man-made material shown to form strong and functional bonding to living tissue. Sadly, Prof. Hench passed away in December 2015, at the time this e-book was being completed, it is therefore a great honor for the editors

to dedicate this e-book to his memory. Indeed the book contains a comprehensive review written by Prof. Hench, in collaboration with Prof. J. R. Jones (UK), which provides a timely overview of the development and applications of bioactive glasses, including a discussion on the remaining challenges in the field.

Further bioactive materials have been developed over the years by leading scientists such as Prof. Kokubo (Japan). These materials have also found their way into this book. The other

contributions in this book, written by worldwide recognized experts in the field, present the latest advances in relevant areas such as scaffolds for bone tissue engineering, metallic ion releasing systems, cements, bioactive glass–polymer coatings, composites for bone regeneration, and effect of porosity on cellular response to bioceramics.

In addition to bioactive materials, inorganic systems for restorative dentistry are also discussed in this e-book. Biomaterials for dental restorations consist of glassy or crystalline phases. Glass-ceramics represent a special group of inorganic biomaterials for dental restorations. Glass-ceramics are composed of at least one inorganic glassy phase and at least one crystalline phase. These products demonstrate a combination of properties, which include excellent aesthetics and the ability to mimic the optical properties of natural teeth, as well as high strength and toughness. They can be processed using special processing procedures, e.g. machining, moulding and sintering, to fabricate high quality products.

The editors would like to extend their gratitude to the Frontiers team in Lausanne, Switzerland, for their outstanding dedication to make possible the publication of this e-book in a timely manner. It is our wish that the book will contribute to expand the field of inorganic biomaterials, both in terms of fundamental knowledge and applications, and that the book will be useful not only to established researchers but also to the increasing number of young scientists starting their careers in the field of inorganic biomaterials.

Citation: Höland, W., Boccaccini, A. R., eds. (2016). Inorganic Biomaterials. Lausanne: Frontiers Media. doi: 10.3389/978-2-88919-801-6

Table of Contents

- 05 Editorial: Inorganic Biomaterials**
Aldo R. Boccaccini and Wolfram Höland
- 07 Bioactive Glasses: Frontiers and Challenges**
Larry L. Hench and Julian R. Jones
- 19 Growth of novel ceramic layers on metals via chemical and heat treatments for inducing various biological functions**
Tadashi Kokubo and Seiji Yamaguchi
- 32 Electrophoretic deposition of chitosan/45S5 bioactive glass composite coatings doped with Zn and Sr**
Marta Miola, Enrica Verné, Francesca Elisa Ciraldo, Luis Cordero-Arias and Aldo R. Boccaccini
- 45 Uniform surface modification of 3D Bioglass®-based scaffolds with mesoporous silica particles (MCM-41) for enhancing drug delivery capability**
Elena Boccardi, Anahí Philippart, Judith A. Juhasz-Bortuzzo, Ana M. Beltrán, Giorgia Novajra, Chiara Vitale-Brovarone, Erdmann Spiecker and Aldo R. Boccaccini
- 57 Effect of ceramic scaffold architectural parameters on biological response**
Maria Isabella Gariboldi and Serena M. Best
- 68 Therapeutic ion-releasing bioactive glass ionomer cements with improved mechanical strength and radiopacity**
Maximilian Fuchs, Eileen Gentleman, Saroash Shahid, Robert G. Hill and Delia S. Brauer
- 79 Development of Magnesium and Siloxane-Containing Vaterite and Its Composite Materials for Bone Regeneration**
Shinya Yamada, Akiko Obata, Hirotaka Maeda, Yoshio Ota and Toshihiro Kasuga
- 88 Effect of porosity of alumina and zirconia ceramics toward pre-osteoblast response**
Chrystalleni Hadjicharalambous, Oleg Prymak, Kateryna Loza, Ales Buyakov, Sergei Kulkov and Maria Chatzinikolaïdou
- 98 Properties and crystallization phenomena in $\text{Li}_2\text{Si}_2\text{O}_5\text{-Ca}_5(\text{PO}_4)_3\text{F}$ and $\text{Li}_2\text{Si}_2\text{O}_5\text{-Sr}_5(\text{PO}_4)_3\text{F}$ glass-ceramics via twofold internal crystallization**
Markus Rampf, Marc Dittmer, Christian Ritzberger, Marcel Schweiger and Wolfram Höland
- 107 Radiopaque strontium fluoroapatite glass-ceramics**
Wolfram Höland, Marcel Schweiger, Marc Dittmer and Christian Ritzberger



Editorial: Inorganic Biomaterials

Aldo R. Boccaccini^{1*} and Wolfram Höland^{2*}

¹ University of Erlangen-Nuremberg, Erlangen, Germany, ² Ivoclar Vivadent AG, Schaan, Liechtenstein

Keywords: editorial, biomaterials, bone engineering, bioactive glasses, bioceramics, dental restoration, scaffolds, coatings

The Editorial on the Research Topic

Inorganic Biomaterials

The objective of this research topic “Inorganic Biomaterials” within the scope of the article series “Bioengineering and Biotechnology” featured by the open access journal “Frontiers” was to present a comprehensive introduction to the field of inorganic bioactive biomaterials being considered for the replacement of hard tissues, in particular, bone tissue and related topics in bone tissue engineering and dental restoration.

Two important basic articles included in this research topic are written in the form of reviews. One of these articles, a review written by the inventor of Bioglass® and pioneer of the field of inorganic biomaterials, Prof. Larry Hench (USA), in collaboration with Prof. J. R. Jones (UK), provides a comprehensive overview of the development and applications of the biomaterial Bioglass®, including a discussion on the remaining challenges for further research in the field in order to tackle current clinical needs. The second review paper included in this volume is written by one of the pioneers of the field of inorganic bioactive materials, Prof. T. Kokubo (Japan), and it covers scientific approaches to converting metal surfaces into bioactive surfaces through the formation of novel ceramic surface layers.

The subsequent publications have been coauthored by young researchers from the world’s leading research groups headed by renowned scientists in the field, including Prof. T. Kasuga (Japan), Prof. S. Best (UK), Prof. E. Verné (Italy), Prof. D. Brauer (Germany), Prof. R. Hill (UK), and Prof. A. R. Boccaccini (Germany). The aforementioned authors have focused on publishing the latest research results, and their papers cover a series of relevant topics, which include

- three-dimensional preparation and characterization of scaffolds for bone tissue engineering,
- additives to biomaterials, such as metallic ions, which have not yet been investigated fully and might significantly improve the functionality of biomaterials, e.g., cements,
- bioactive glass–polymer composite coatings,
- controlled ion release as a special type of drug delivery,
- special processes for the fabrication of composites for bone regeneration, and
- effect of porosity on bioceramic properties.

In addition to bioactive materials, inorganic biomaterials for restorative dentistry are presented. A special focus has been placed on demonstrating how several crystal phases can be precipitated in a glass–ceramic in a controlled manner. This process is called “twofold nucleation and crystallization in glasses to develop biomaterials” and the resultant biomaterials can be imparted with radiopaque characteristics, which is highly relevant when they are used for dental applications.

The editors would like to extend their gratitude to the Frontiers team in Lausanne, Switzerland, for their outstanding commitment and dedication. It has been a pleasure to create this special edition, even though it entailed intensive and concentrated work. We also thank the International Commission on Glass (ICG) which has contributed financially, via a grant to the Technical Committee 04 (Bioglasses, head: Prof. J. R. Jones), to support this publication. It is our wish that this volume will contribute to

OPEN ACCESS

Edited and Reviewed by:

Hasan Uludag,
University of Alberta, Canada

*Correspondence:

Aldo R. Boccaccini
aldo.boccaccini@www.uni-erlangen.de;
Wolfram Höland
wolfram.hoeland@
ivoclarvivadent.com

Specialty section:

This article was submitted to
Biomaterials,
a section of the journal
Frontiers in Bioengineering and
Biotechnology

Received: 23 December 2015

Accepted: 06 January 2016

Published: 21 January 2016

Citation:

Boccaccini AR and Höland W (2016)
Editorial: Inorganic Biomaterials.
Front. Bioeng. Biotechnol. 4:2.
doi: 10.3389/fbioe.2016.00002

expand the knowledge in the field of inorganic biomaterials, and it will be useful not only to established researchers based both in industry and academia but also to the increasing number of young researchers starting their careers in the field.

At the very moment of writing this editorial, the sad news of the death of the inventor of Bioglass® and pioneer of biomaterials research, Prof. Larry Hench, reached us, giving thus a very special timeliness character to this Frontiers topic. Both editors knew Larry personally and collaborated with him in numerous capacities during many years. Wolfram Höland would like to highlight the many scientific discussions with Prof. Hench, and numerous joint activities involving writing chapters in basic scientific books and creating a joint publication in the field of biomaterials. Aldo R. Boccaccini was a colleague of Prof. Hench for several years at Imperial College London. Through inspiring discussions and scientific exchanges, Prof. Hench became a decisive influence in Aldo R. Boccaccini's academic

career. Since his retirement from Imperial College London, Prof. Hench continued working tirelessly giving lectures, publishing research papers and books, attending conferences, and receiving a number of prizes honoring his achievements. Larry Hench was not only a brilliant materials scientist but also a wonderful and enthusiastic person with a winning personality who has inspired generations of young researchers to follow in his footsteps. His ardor to propose Bioglass® for various applications in hard and soft tissue engineering will influence biomaterials research for years to come.

We dedicate this Frontiers research topic to the memory of Prof. Larry Hench.

AUTHOR CONTRIBUTIONS

The editorial was written jointly by the two editors of the topic.

Conflict of Interest Statement: The authors declare that the research was conducted in the absence of any commercial or financial relationships that could be construed as a potential conflict of interest.

Copyright © 2016 Boccaccini and Höland. This is an open-access article distributed under the terms of the Creative Commons Attribution License (CC BY). The use,

distribution or reproduction in other forums is permitted, provided the original author(s) or licensor are credited and that the original publication in this journal is cited, in accordance with accepted academic practice. No use, distribution or reproduction is permitted which does not comply with these terms.



Bioactive Glasses: Frontiers and Challenges

Larry L. Hench¹ and Julian R. Jones^{2*}

¹ Department of Biomedical Engineering, Florida Institute of Technology, Melbourne, FL, USA, ² Department of Materials, Imperial College London, London, UK

OPEN ACCESS

Edited by:

Wolfram Höland,
Ivoclar Vivadent AG, Liechtenstein

Reviewed by:

Alastair N. Cormack,
Alfred University, USA
Ahmed El-Fiqi,
Dankook University, South Korea

*Correspondence:

Julian R. Jones
julian.r.jones@imperial.ac.uk

Specialty section:

This article was submitted to
Biomaterials,
a section of the journal
Frontiers in Bioengineering and
Biotechnology

Received: 02 August 2015

Accepted: 11 November 2015

Published: 30 November 2015

Citation:

Hench LL and Jones JR (2015)
Bioactive Glasses: Frontiers and
Challenges.
Front. Bioeng. Biotechnol. 3:194.
doi: 10.3389/fbioe.2015.00194

Bioactive glasses were discovered in 1969 and provided for the first time an alternative to nearly inert implant materials. Bioglass formed a rapid, strong, and stable bond with host tissues. This article examines the frontiers of research crossed to achieve clinical use of bioactive glasses and glass-ceramics. In the 1980s, it was discovered that bioactive glasses could be used in particulate form to stimulate osteogenesis, which thereby led to the concept of regeneration of tissues. Later, it was discovered that the dissolution ions from the glasses behaved like growth factors, providing signals to the cells. This article summarizes the frontiers of knowledge crossed during four eras of development of bioactive glasses that have led from concept of bioactivity to widespread clinical and commercial use, with emphasis on the first composition, 45S5 Bioglass®. The four eras are (a) discovery, (b) clinical application, (c) tissue regeneration, and (d) innovation. Questions still to be answered for the fourth era are included to stimulate innovation in the field and exploration of new frontiers that can be the basis for a general theory of bioactive stimulation of regeneration of tissues and application to numerous clinical needs.

Keywords: Bioglass, bioactive glass, inorganic/organic hybrids, sol-gel, scaffold, regenerative medicine, tissue engineering, synthetic bone grafts

INTRODUCTION

It is an honor to present this opening paper in this special journal issue devoted to frontiers of inorganic biomaterials. Our contribution focuses on the frontiers and unmet challenges of bioactive glasses. It is now nearly 50 years since the discovery of bioactive glasses bonding to living bone (Beckham et al., 1971; Hench et al., 1971; Hench and Paschall, 1973; Wilson et al., 1981). Many advances have been made in understanding mechanisms of bonding of this special compositional range of glasses to both bone and soft connective tissues. Numerous published reviews and books have documented these advances (Hench, 1991, 1998, 2015; Hench and Polak, 2002; Hench et al., 2004; Rahaman et al., 2011; Jones, 2013). In the last decade, the primary clinical applications of bioactive glasses have involved turning on the body to repair its own bone, a process called *osteostimulation*, a term approved by the United States Food and Drug Administration (FDA). *Osteostimulation* refers to the activation of progenitor cells in the body, by a material or its dissolution products, producing more bone. The claim is based on *in vivo* data (Oonishi et al., 2000) that showed that Bioglass stimulates more rapid bone repair than other bioactive ceramics and the *in vitro* studies that revealed why this occurred, which was due to the dissolution products stimulating seven families of genes in primary human osteoblasts (Xynos et al., 2000a,b, 2001).

A recently published review summarizes the questions answered in four eras of development of bioactive glasses from the discovery in 1969 to the present, 2015 (Hench, 2015). The eras of development of bioactive glasses are

- (A) Era of Discovery (1969–1979);
- (B) Era of Clinical Application (1980–1995, C);
- (C) Era of Tissue Regeneration (1995–2005);
- (D) Era of Innovation (2005–2025).

Several important unanswered questions for the fourth era were suggested in the review (Hench, 2015). Each of these unanswered questions is at the frontier of understanding and controlling the interaction of bioactive glasses in the living body. The objective of this introductory paper is to discuss these questions further, suggest potential research directions that can answer them to move the frontiers of the field forward to achieve even more clinical applications for an aging population.

WHAT ARE FRONTIERS?

First, it is important to discuss the concept of frontiers of knowledge in general and the frontiers of biomedical materials specifically. We can divide human knowledge into three overlapping and intersecting realms of knowledge: *Nature*, *Self*, and *Social* (Figure 1).

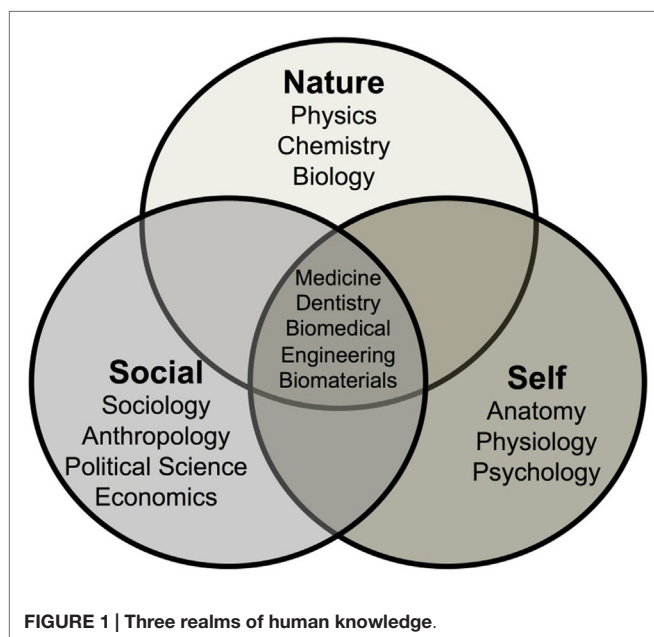
The first field of knowledge, called *Nature*, evolved over millennia as humans strived to understand the natural forces that influenced their lives. The subject was first titled natural history. At one time, it was suggested that natural historians such as Sir Francis Bacon possessed within his own mind most of what was known about the natural world at that time. Now in the twenty-first century, it is impossible for any one individual to know or understand even a very small fraction of the knowledge of nature.

The field has been divided into the major scientific disciplines of physics, chemistry, and biology then subsequently subdivided into an ever-increasing number of subdisciplines, such as astronomy, astrophysics, cosmology, quantum mechanics, solid-state physics, inorganic chemistry, organic chemistry, biochemistry, molecular biology, etc. Although enormous depth of understanding of these topics has been achieved, there are still many frontiers in the knowledge of nature. These frontiers are at the boundary between certainty and uncertainty. Those boundaries exist at the extremes of scale of distance and time limits of our universe. Distances of very small, sub nanometer size, and very large, light years in dimension, comprise the bounds of uncertainties. There are discoveries every year that push back the age of the universe and the complexity and beauty of the subatomic particles that were created during the “Big Bang” beginning of the universe that comprise the atomic and molecular-based world that we live in today.

The knowledge of *Self* also emerged during the last few millennia as a set of disciplines, such as anatomy, physiology, and psychiatry. Intersections between the knowledge of *Self* and *Nature* have become ever more blurred in today’s scientific community with the application of many of the techniques used to explore the natural universe also applied to understanding the human body, the brain, and the mind. The frontiers of knowledge of *Self* are still largely unexplored and the origins of thought, memory, and emotions are active subfields of investigation. Advances in the understanding of *Nature* and *Self* have made it possible to control the life and the death of billions of humans.

The third sphere of knowledge, evolved over the last few hundred years, can be considered *Social* knowledge. Subdisciplines, such as sociology, anthropology, economics, and political science, have been developed to attempt to explain the complex interrelationships between individuals. Social knowledge includes small group interactions, such as couples, to large-scale interdependence of communities involving millions of individuals. Levels of uncertainty in the field of social knowledge are extremely high. This is because of the difficulty of predicting the behavior of large number of individuals interacting together. To become a science, it is necessary to achieve repeatable observation, verification, and quantification, followed by predictability. Such criteria are met in the natural sciences and the ever-increasing knowledge of *Self*.

However, there are high levels of unpredictability in the area of social knowledge. Thus, world conflicts continue to occur with enormous toll on human suffering and life without a means to predict or prevent such calamities. Unpredictable political changes, such as the breakup of the Soviet Republic were seldom, if at all, predicted by social scientists. Even breakups of interpersonal relationships of couples are, for the most part, unpredictable. Likewise, it is very difficult to predict the impact of a new medical therapy on the behavior of a large population. Self-delusion and susceptibility to persuasion can easily warp the attitude of large numbers of individuals and replace logical reasoning in decision making. As an example, many surgeons find it difficult to accept that a bioactive synthetic bone graft can be equal or superior to autogenous bone (bone transplanted from another part of the patient), even though clinical studies have shown that to be the case for some applications, even though the autograft leads to donor site morbidity.



Of particular concern in this introductory paper is a discussion of the area where the three realms of knowledge overlap and intersect, as illustrated in **Figure 1**. Medicine, Dentistry, Biomedical Engineering, and Biomaterials lie at the intersection of the three realms of knowledge. This region could also be broadly named Healthcare. Here, the uncertainties of each realm of *Nature*, *Self*, and *Social*, are additive and perhaps even multiplicative. Thus, it becomes nearly impossible to predict the effects on long-term survivability (20–40 years) of a change in a biomaterial or device in a single individual. This is because the healthcare predictions, derived from overlapping regions of the three realms of knowledge, are based upon statistical results of the survivability of a large number of patients. The uniqueness of an individual is not reflected in statistical data, only within the distribution of results.

This fact is extremely important to recognize, as the field of repair and regeneration of the human body increases to deal with an aging population numbering in the hundreds of millions. It is important for the entire healthcare community, and the general public, to recognize that there are no such things as miracle materials or miracle cures. There is always the possibility of failure. Failure is not necessarily the fault of any individual, surgeon, company, or hospital. Failures of materials, devices, and biotechnology are a natural consequence of the large-scale complexity of the human body and its intricate interactions in a social environment where outside influences affect uncertainty of the quality of life of the individual as well as the length of life.

Let us discuss one example of an unmet challenge to illustrate the impact of the uncertainties of these overlapping regions of knowledge on inorganic biomaterials device development. During the last 40 years, numerous research efforts have been made to develop a long-term stable (not biodegradable) load-bearing replacements for diseased, damaged, or missing bone. The closest bioceramic to achieve this objective was the apatite–wollastonite (A/W) bioactive glass–ceramic, Cerabone, developed in Japan, at the University at Kyoto, by professors Yamamuro, Kokubo, Nakamura, and colleagues (Kokubo et al., 1990). Tens of thousands of successful Cerabone implants were made and implanted for a variety of orthopedic applications in Japan, especially in spinal repair. Excellent clinical success was achieved for all of the devices. However, a very high stiffness (elastic modulus) led to concern about long-term stress shielding in high load-bearing applications. Stress shielding occurs when load is transmitted through the implant, and it is not transmitted to the surrounding bone. When bone is not loaded, it loses volume as the body removes it through osteoclast cell activity. A high production cost also limited commercial interest. The product was not introduced internationally and is no longer on the market. Thus, the goal of replacing load-bearing cortical bone is still an unmet challenge.

Our issues of concern are the uncertainties associated with the intersections of the three worlds of knowledge. The laws of nature make it possible to perform accurate mechanical testing of a new biomaterial, such as a potential load-bearing bioactive ceramic. Mechanical testing can be extended to a sufficiently large number of test devices to establish the distribution of results and strain rate dependencies of strength can lead to lifetime prediction diagrams of the mechanical behavior under particular levels

of load. The science behind the knowledge of *Self* now makes it possible to obtain quantitative computed tomography (CT) data (Midha et al., 2013), and by use of rapid prototyping replicate precisely, the anatomical shape needed for a device made of a new load-bearing bioactive ceramic (Brie et al., 2013). The science of ceramic, glass, and glass–ceramic processing is sufficiently advanced to make individual components by rapid prototyping or computer-guided machining at reasonable cost. Developments, such as 3-D printing, make it possible to manufacture anisotropic microstructures that mimic the structure of cortical bone as well as trabecular bone (Fu et al., 2011a,b).

Uncertainties, however, have great impact on the economics of the overlap between *Nature*, *Self*, and *Society*. Limitations on new medical product development come in several forms. Achieving governmental regulatory approval of a new device that must last for many years requires a highly rigorous set of simulation testing and large monetary investment. The keyword here is simulation. Simulated body solutions are a standard use in the bioceramics testing field and have been adopted as international and regulatory standards (Macon et al., 2015). However, the non-cellular simulated body fluids do not lead to an ability to predict in long term the effect of a physiological body environment on a material or device that is exposed to a complex mixture of mechanical loads (Bohner and Lemaître, 2009). It is well known that bone cells respond to mechanical cues and the architecture and the quality of bone that forms is dependent on those cues. Multiaxial fatigue data can be generated under simulated physiological conditions, but such environments do not embrace the uncertainty of the effect of the living bone – bioactive ceramic contact area and its changes with time and physiology of the patient.

Especially important is the fact that there is no way to predict the effect of age and load distribution on the mechanical properties of the loaded bone bonded to the bioactive ceramic. Consequently, in order to have a sufficiently acceptable set of preclinical data, it is necessary to establish reasonably equivalent animal data for the regulatory authorities. Approval for clinical application of an innovative bioactive load-bearing bioceramic will require large animal data. This is where the overlap of *Nature*, *Self*, and *Social* is especially important because the cost of producing large animal data for a statistically significant number of implants is very high.

The costs escalate after successful animal data has been generated because most regulatory agencies will require clinical trials. The number is large because there is no predicate load-bearing cortical bone implant to establish equivalence under the FDA 510K provisions. It is very difficult to predict the cost of clinical trials because the survivability for approval must surely be established for a minimum of three, and more than likely 5 years. Thus, the cumulative cost of bringing a new product, such as a new bioactive ceramic material, into the market is in the millions of dollars. Although there are tens of thousands such devices potentially needed annually, it is very hard to calculate the potential cost/profit or risk/reward ratios. These limitations and barriers to achieving frontiers of clinical use are independent of the successful development of the biomaterial that satisfies the ideal combination of properties needed for cortical bone; i.e., strength, toughness, fatigue resistance, bioactivity, and elastic modulus that do not shield the bone from stress following bonding to bone.

The above example illustrates our opinion that emphasis on “improved” bioactive ceramics, where the primary function of the material is to replace the diseased, damaged, or missing tissue is unlikely to have many successes that are economically viable. These considerations lead to the conclusion that the most significant long-term frontier is expansion of efforts in the field toward the frontiers of regenerative medicine. This era of innovation will be discussed briefly next. The critical unmet challenges and frontiers will be discussed later. However, let us first look at what can be considered a frontier in this field of inorganic biomaterials.

The word *frontier* implies exploring the unknown hoping to find within the unknown something new and useful. In directed research, such as biomaterials, new and important developments are driven by clinical need and limited by economics and long-term survivability. Deciding which frontiers to explore is a difficult and demanding step for a research group or company. The history of the field has shown that there are indeed very few frontiers that have been crossed, although there have been thousands of efforts to achieve long-term improvement of biomaterials in general.

An example from the field of bioactive glasses and glass-ceramics can be useful in establishing what is and what is not a frontier of research in the field. The very first material that was found to form a bond with bone was the original bioactive glass composition, 45S5 Bioglass (45 wt% SiO₂, 24.5 wt% CaO, 24.5 wt% Na₂O, and 6 wt% P₂O₅) (Hench et al., 1971). Much of the time in the era of discovery was devoted to understanding the mechanisms of bonding and the nature of the bonds between the glass and bone and soft tissue (Hench and Polak, 2002). This can be considered a major frontier because up until the time of this discovery, it was assumed that all foreign materials would be isolated from the living tissue by a thin acellular fibrous capsule. The discovery showed that encapsulation was not a fundamental restriction of the response of the body to foreign material. When rapid reactions occur at the surface of a bioactive glass or glass-ceramic, the biologically active hydroxyapatite (HA) layer quickly masks the material from immune cells. The cellular recognition mechanisms respond to it as if it were a layer of newly mineralizing bone: the cells attach and extracellular matrix (ECM) is produced, mineralization proceeds to completion and newly formed bone is strongly anchored to the surface of the material with an interfacial bond strength equal to or greater than the natural bone (Hench et al., 1971). Another frontier was discovery of the bonding of the most bioactive of the Bioglasses to soft connective tissues as well as bone through an equivalent mechanism of surface reactions to form a hydroxyl-carbonate apatite layer but with a thicker bonding interface (Wilson and Noletti, 1990).

The compositional boundary between bonding to bone and non-bonding was found to be in the range of 60 wt% silica (Hench, 1998). Effects of additional oxide compositions on the details of the compositional boundaries have been looked at extensively in the decades since (Hoppe et al., 2011). Some investigators proclaim that addition of other oxides to the bioactive glass to enhance the bone bonding is searching the new frontier. This objective is open to question because the measure of frontier advances is delivery of clinical products. Small incremental advances showing a few percent more bone growth in a 30-day period of time is questionable as frontier research, as

the small increase will not warrant the investment required to get the new material to market. However, the realization that the dissolution ions caused osteostimulation was the crossing of an important frontier: cell stimulation by a synthetic material without organic growth factors. If additional therapeutic benefits of other cations can be proven, there is great potential to use bioactive glass as a reservoir for sustained delivery of active ions that can be specific to different medical conditions. An example is strontium oxide, where controlled release of strontium ions, from the glass, is thought to be beneficial for osteoporosis as it can slow osteoclast activity (Lao et al., 2008; Gentleman et al., 2010; Autefage et al., 2015).

What is frontier research in bioactive materials? Returning back to the discussion of long-term survivability of load-bearing long bone implants, research done up to now has not delivered such a material. Consequently, the concept of tissue regeneration to enhance bone formation that is capable of long-term load-bearing is now at the highest level of frontier investigations. This is because the concept of tissue regeneration is to use the material not to replace the diseased, damaged, or missing part of the body, but instead activates the body's own repair mechanism so that the tissue that is grown is replicating both biochemically and biomechanically the original load-bearing tissue. This eliminates the problems of stress shielding and particularly the problem of remodeling of the material or interface when the load distribution changes or health deteriorates. Thus, an active frontier area includes developing an ideal bioactive scaffold for bone that is capable of providing short-term strength with high reliability that is transformed into load-bearing bone and then resorbed. This is one of the most significant levels of frontiers and the progress to achieve it is a highlight of the decade of innovation.

Designing hybrid biomaterials that are bioactive and have controlled rates of resorption and can be molecularly tuned to produce particular combinations of mechanical properties is a major goal of the era of innovation, as discussed in a recent review (Jones, 2013). Success in achieving an ideal scaffold for bone as a frontier would have a large impact on the field. It would open exploration to achieve an ideal scaffold for cartilage regeneration that could provide a long-term solution to the extensive revisions now required for replacement of total hip and knee prostheses due to the biomechanical limitations discussed above. The frontier of designing bioactivity to activate the genetic repair mechanisms for specific lineages of connective tissues is at the highest level of frontier research and will be emphasized in the list of unmet challenges to follow. Of course, to cross the frontiers, the new devices must be translated to clinical products.

ERA OF DISCOVERY (1969–1979) FRONTIERS

The most significant frontier was the discovery in 1969 by Hench, Splinter, Allen, and Greenlee that certain compositions of Na₂O–CaO–P₂O₅–SiO₂ glasses formed a strong, adherent bond to bone (Hench et al., 1971). These biomaterials have become known as “bioactive,” reacting in the physiological environment to form a bond between an artificial material and living

tissue. Studies showed stable and strong bonding between bone and soft tissues in a wide range of mammals: mice, rats, guinea pigs, rabbits, dogs, sheep, pigs, monkeys, and baboons. A stable bone-bonded implant in the anterior region of the mandible of a baboon after 4 years of functional use was reported, one of the longest *in vivo* studies of biomaterials in primates ever published (Stanley et al., 1981).

The second frontier was development of *in vitro* and *in vivo* tests that established the mechanisms and limits of bonding of bioactive glasses and glass–ceramics to bone. The *in vitro* tests showed that the 45S5 Bioglass composition (see **Table 1**) developed a HA layer in test solutions. This HA phase developed on the surface of the implants *in vitro* was equivalent to the interfacial HA crystals observed *in vivo* by Dr. Greenlee's transmission electron micrographs of the bonded interface. The HA crystals *in vivo* were bonded to layers of collagen fibrils produced at the interface by osteoblasts. The chemical bonding of the HA layer to collagen created the strongly bonded interface (Beckham et al., 1971; Hench et al., 1971; Hench and Paschall, 1973).

During the era of discovery, a series of questions was addressed (Hench, 2015). Some of the key questions are summarized here. Question: What is the nature of the bioactive bond? Answer: hydroxycarbonate apatite (HCA) crystals bonded to collagen fibers (Beckham et al., 1971; Hench et al., 1971; Hench and Paschall, 1973). Question: What mechanisms are involved in HCA formation? Answer: five surface reactions at the glass surface occur (cation exchange, Si–OH group formation, on which amorphous calcium phosphate phase deposits, crystallizing to HCA, which binds to collagen). Question: How strong is the bond? Answer: stronger than the host bone (Piotrowski et al., 1975). Question: What compositions of glass can form the bond? 45S5 Bioglass is composed of SiO₂–CaO–Na₂O–P₂O₅ (**Table 1**). In this system, bonding to both bone and soft tissue is possible at 52 wt% SiO₂ (Wilson et al., 1981) and between 52 and 60% SiO₂ bonding is only to bone (Hench, 1998).

Two important aspects of the frontiers were explored in the Era of Discovery. First, the methodology for investigating the reactive glass surface and bonded interfaces of bioactive implants with living tissues had to be developed. There was no precedent for such analyses. Examples are instrumental techniques such as infrared reflection spectroscopy, developed by Sanders and Hench (1973), and applied to bioactive glasses and cryogenic Auger electron spectroscopy (AES), developed by Ohuchi, Pantano, Ogino, and Hench (Clark et al., 1976;

Ogino and Hench, 1980; Ogino et al., 1980). At this stage, tests were conducted primarily on bulk samples or as bioactive coatings on metal, e.g., Co–Cr alloys, or ceramic (e.g., alumina) implants. It was assumed that the eventual applications of bioactive bonding would be to replace a diseased or damaged bone. The second Era of Clinical Applications was based upon this knowledge.

ERA OF CLINICAL APPLICATION FRONTIERS (1980–1995)

An important frontier to cross was clinical translation. The discovery by Wilson et al. (Wilson et al., 1981; Wilson and Noletti, 1990) that Bioglass could bond to soft tissue paved the way for development of the first bioactive glass clinical applications that required both stable bone and soft tissue interfaces: the MEP (middle ear replacement prostheses) (Merwin et al., 1982) and ERMI, endosseous ridge maintenance implants (Stanley et al., 1997). These devices had the objective of replacing diseased, damaged, or missing body parts that require stable bonding to both soft tissues and bone. At the time, most other types of middle ear prostheses were lost by extrusion after a few years. In contrast, Bioglass middle ear devices formed a stable bond to both bone, such as the stapes footplate and the soft tissues of the tympanic membrane and thus remained stable for more than 10 years as reported in follow-up studies at both the University of Florida and Guy's Hospital in London (Rust et al., 1996). Equivalent long term, >10 years, success of the Bioglass ERMIs were reported by Stanley et al. Alternative Class B bioactive implants made of synthetic HA were lost by extrusion or exfoliation from the jaw after only a few years post implantation. In contrast, 45S5 Bioglass implants maintained stable bonding in alveolar bone and a stable gingival interface for long term and maintained thickness of the bone without resorption generally experienced by denture wearers (Wilson et al., 1993; Stanley et al., 1997).

A second frontier crossed by Wilson et al. (1981) was the collation of results of sixteen *in vitro* and *in vivo* tests that established the safety of use of particulate forms of Bioglass in addition to the bulk implants (Wilson et al., 1981). These data provided the basis for ethical committee's approval of the use of Bioglass in clinical trials at the University of Florida and Guy's Hospital in London, as well as application for regulatory approval of commercial sales of these devices by the FDA and a CE mark from the EU. This led to the use of Bioglass in bone regeneration (Hench et al., 2004).

ERA OF TISSUE REGENERATION FRONTIERS (1985–2005)

The discovery of osteoproduction (osteostimulation) and the concept of using Bioglass particulate for regeneration of bone was the key frontier crossed that led to the Era of Tissue Regeneration. Wilson et al. described the effect of various sizes of Bioglass particulate on regeneration of bone in periodontal defects created in a monkey model (Wilson and Low, 1992). The seminal finding was the stimulation of new bone throughout the defect. Bone growth was initiated at the surface of the bioactive

TABLE 1 | Composition and properties of bioactive glasses and glass–ceramics used clinically for medical and dental applications.

Composition (wt%)	45S5 Bioglass (NovaBone, Perioglas, NovaMin, Biogran)	S53P4 (AbminDent1, BonAlive)	A–W glass–ceramic (Cerabone)
Na ₂ O	24.5	23	0
CaO	24.5	20	44.7
CaF ₂	0	0	0.5
MgO	0	0	4.6
P ₂ O ₅	6	4	16.2
SiO ₂	45	53	34

glass particles and rapidly formed connections between the particles regenerating a trabecular bone network that mimicked the original trabecular bone of the jaw prior to creating the defect. The study showed that there was an optimal rate of bone repair when a range of particle sizes of Bioglass was used. The results also showed that bone regeneration was sufficiently rapid that it prevented encapsulation of the site by epithelial tissues. The data provided the foundation for a clinical trial in patients at the University of Florida that led to FDA regulatory approval of the use of bioactive glass particulate for periodontal repair (Perioglas, NovaBone Products LLC, Alachua, FL, USA; **Figure 2**).

NovaBone was compared to autograft in posterior spinal fusion operations for treatment of adolescent idiopathic scoliosis (curvature of the spine) in 88 patients (Ilharreborde et al., 2008). NovaBone performed as well as autograft over 4 years but with fewer infections (2 versus 5%) and fewer mechanical failures (2 versus 7.5%).

The first non-45S5 composition to reach the market was S53P4 (**Table 1**), now known as BonAlive® (BonAlive Biomaterials, Turku, Finland), which received European approval for orthopedic use as bone graft substitute in 2006. It has higher silica content; so bioactivity is expected to be lower than 45S5. Several clinical trials have been published from the work in Finland, importantly using the gold standard autograft as comparison, which is needed to convince surgeons. A mixture of granules with autologous bone allowed the implantation of titanium implants in previously damaged jaw bone and showed more rapid bone repair compared to autograft alone (Turunen et al., 2004). Clinical trials for severe spondylolisthesis (displacement of vertebrae) used granules of 1–2 mm. After 11 years, the fusion rate for the glass was 88% compared to 100% for autograft (Frantzen et al., 2011). Similar results were seen for treatment of osteomyelitis, where bone quality of the vertebrae is reduced due to bacterial infection (Lindfors et al., 2010a). BonAlive was also compared to autograft in the same patients in spondylodesis procedures for treatment of spine burst fractures. At 10-year follow-up, five out of 10 implants had full fusion compared to all 10 autografts (Rantakokko et al., 2012).

In tibial fractures, in which surgery was required to restore joint alignment, BonAlive particles (0.83–3.15 mm) were placed inside the subchondral bone defects with metallic fixation (Perna et al., 2011). Full weight bearing was allowed when radiographs indicated healing had occurred, so the implants were loaded, and 11-year follow-up showed similar bone regeneration compared to autograft. Some particles were still present at 11 years post operation (Heikkilä et al., 2011). The lack of resorption of S53P4 may be due to glass composition, which has higher silica content than 45S5. Improvement over autograft was seen when BonAlive granules (1–4 mm) were used in post-tumor removal bone defects, with cortical bone thickness twice as thick as it was when autograft was used after 14 years (Lindfors et al., 2010b). Remodeling of the bone is slower than it was for autograft (e.g., after 12 months) (Lindfors et al., 2008).

A frontier that provided a scientific foundation for use of bioactive glass in bone regeneration was introduction of an appropriate *in vivo* model that allowed the quantification and comparison of bone regeneration for different bioactive materials. Use of the same model, and the fact that the model is appropriate, will accelerate translation of new medical devices. Quantification and comparison of the effect of bioactive glass on regeneration of bone was based upon a series of important studies conducted by Oonishi et al. in Osaka, Japan (Oonishi et al., 1997, 1999, 2000). The Oonishi investigations used a critical size defect in a rabbit femoral condyle model to compare rates of bone formation in the presence of different types of bioceramic particles of the same particle size. The studies showed there are more bones formed in just 1 week in the presence of 45S5 bioactive glass particulate than are formed when synthetic HA or other calcium phosphate ceramic particulates are placed in the same type of defect for several weeks. After several weeks of bone regeneration, there was almost twice as much new bones present in the defect-containing bioactive glass. By 12 weeks, the amount of bone regenerated by Bioglass particles matched that originally present in the site. Wheeler et al. demonstrated that the mechanical properties of the defect site were restored (Wheeler et al., 2000). Bioactive

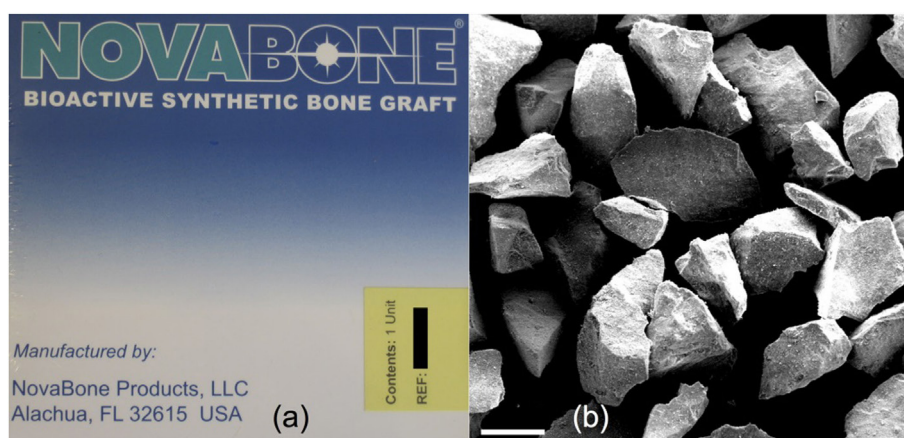


FIGURE 2 | (A) Packaging of NovaBone (45S5 Bioglass) powder for orthopedic applications and **(B)** scanning electron micrograph of NovaBone particles. Modified with permission from Jones (2013).

glasses and ceramics can, therefore, stimulate different rates of bone regeneration inside a bone defect, depending on the type of material (glass, ceramic, or glass–ceramic) and the composition and morphology of the device.

The next frontier was identifying what was really stimulating bone regeneration. While the *in vivo* data showed differences between implants, they were not answering the question why there were differences. Initially, the dissolution of the 45S5 Bioglass particles were thought to cause more bone formation by the HCA layer forming more rapidly and by the glass degrading, making more space for bone ingrowth. This was not the complete story though. Dissolution is important, but mainly because the dissolution ions act as signals to the cells. This was revealed through *in vitro* experiments that showed critical concentrations of Si and Ca ions released from the glasses stimulated cells at the genetic level. Seven families of genes were upregulated when primary human osteoblasts are exposed to the ionic dissolution products of bioactive glasses (Xynos et al., 2000a,b, 2001). The gene expression occurs within 48 h, and includes enhanced expression of more than twofold of seven families of genes. The dissolution products can direct the cycle of a mixed population of cells. Cells that are not capable of differentiation into a mature osteoblast phenotype are switched into apoptosis by the ionic stimuli, eliminating them from the culture environment within the first days of exposure to the bioactive stimuli. Upregulated genes encode nuclear transcription factors and cell cycle regulators (Xynos et al., 2001). Potent growth factors, especially insulin-like growth factor II (IGF-II), were increased by 3.2-fold along with IGF binding proteins and proteases that cleave IGF-II from their binding proteins.

Similar bioactive induction of the transcription of at least five ECM components (2- to 3.7-fold) and their secretion and self-organization into a mineralized matrix are responsible for the rapid formation and growth of bone nodules and differentiation of the mature osteocyte phenotype. Shifts in osteoblast cell cycles were observed as early as 6 h for most experiments, with elimination (by apoptosis) of cells incapable of differentiation. The remaining cells exhibited enhanced synthesis and mitosis. The cells quickly committed to generation of ECM proteins and mineralization of the matrix (Xynos et al., 2000a,b, 2001).

Similar results were seen for fetal osteoblasts, where critical concentrations of Bioglass dissolution products stimulated differentiation into mature phenotypes (Tsigkou et al., 2009). The roles of individual ions are partly understood: extracellular calcium ions increase IGF-II upregulation (Maeno et al., 2005; Marie, 2010) and glutamate production by osteoblasts (Valerio et al., 2009). Silica is released from Bioglass as silicic acid $[\text{Si}(\text{OH})_4]$, which has been shown to stimulate collagen I production by osteoblasts (Reffitt et al., 2003). More detail on cellular response to individual ions is given in Hoppe et al. (2011).

ERA OF INNOVATION (2005–2025) FRONTIERS AND UNMET CHALLENGES

There are many challenges still ahead for the clinical use of bioactive glasses that require advances in a fourth era, an era of innovation. Significant scientific and technological issues remain unanswered.

Frontier: Guidance of Stem Cells by Materials

Tissue regeneration through gene activation by controlled release of inorganic ions is a clinical reality that leads to enhanced osteogenesis. However, the role of the dissolution products on bone marrow-derived adult stem cells [mesenchymal stem cells (MSCs)] is more controversial, sometimes inducing osteogenic differentiation into osteoblast-like cells (Karpov et al., 2008; Brauer et al., 2010) and other times not (Reilly et al., 2007). Human adipose stem cells differentiated into osteogenic cells when cultured with bioactive glasses in the presence of osteogenic supplements (Haimi et al., 2009; Ojansivu et al., 2015). However, neither adipose nor bone marrow MSCs differentiated in the presence of submicron bioactive glass spheres (Labbaf et al., 2011; Tsigkou et al., 2014). The exact type and status of cell cycle of MSCs may be the reason for these differences.

An unmet challenge is to understand the fundamental mechanisms involved in ionic stimulation at the nucleus in the cell, of the many different cell types, that leads to upregulation or activation of genes. Another issue is that not all the articles explain exactly how the bioactive glass particles/dissolution products were applied or what supplements were used in the media. The fundamental mechanisms of stimulation of stem cell differentiation toward specific phenotypes must be understood to avoid potential tumorigenesis. A consolidation of data is needed for the frontier of stem cell guidance by bioactive glasses is still to be crossed.

Unmet Need: Bioactive Glass Scaffolds as Clinical Products

Particles and putties containing a variety of bioactive glass particulates are in widespread clinical use, but surgeons sometimes require large interconnected macroporous scaffolds for regeneration of large bone defects. The porous architecture can guide bone regeneration, acting as temporary templates for tissue growth while allowing space for vascularization. At present, there are no large-scale porous bioactive glasses on the market. The reason is that it took until 2002 for the first porous bioactive glass scaffold with suitable pores to be developed (Sepulveda et al., 2002). This is because the original Bioglass 45S5 crystallizes as the particles are sintered together (Chen et al., 2006). Initially, this was overcome by avoiding sintering through the bottom-up sol–gel process, where gelation of nanoparticles in a sol (polycondensation) forms a glass network (Li et al., 1991). The room temperature gelation process allowed the introduction of a foaming step, with the aim of a surfactant, to produce interconnected pores with compression strength equivalent to porous bone (Jones et al., 2006). An X-ray microtomography image of a bioactive glass sol–gel foam scaffold is shown in Figure 3A.

More recently, melt-quenched glass scaffolds were produced through control of the sintering processing window by tailoring of the glass composition, which was achieved while maintaining bioactivity with new compositions, such as 13–93 (53 wt% SiO_2 , 6 wt% Na_2O , 12 wt% K_2O , 5 wt% MgO , 20 wt% CaO , and 4 wt% P_2O_5) (Brink, 1997; Fu et al., 2010) and ICIE16 (49.46 mol% SiO_2 , 1.07 mol% P_2O_5 , 36.27 mol% CaO , 6.60 mol% Na_2O , and 6.60 mol% K_2O) (Elgayar et al., 2005; Wu et al., 2011). An ICIE16

scaffold is shown in **Figure 3B**. Now sol-gel and melt-derived scaffolds exist but none are being put forward for use by medical device companies, even though comparative *in vivo* studies show benefit over current commercial porous bioactive ceramics (Minaberry and Jobbagy, 2011). This is because the improvements in performance do not warrant the significant investment required to obtain FDA approval and upscale the manufacturing routes to commercial scale, as discussed above.

Frontier: Tissue Engineered Constructs for Clinical Bone Regeneration

Tissue engineered constructs for replacement of large bone defects have been investigated for many years but are still not available as routine clinical products. Is it possible to achieve a stable vasculature *in situ* in tissue engineering constructs that can be maintained in culture before implantation or be generated *in vivo* following implantation? Tsigkou et al. demonstrated that it is possible in mice models (Tsigkou et al., 2010), but can it be translated to the clinic? Does the scaffold affect *in vitro* vascularization? Is the vascularization affected by mechanical load and changes of load with time? Numerous studies demonstrate bioactive stimulation of angiogenesis *in vitro*; however, many studies are on one cell type, often fibroblasts. Most of the studies look for expression of VEGF from the cells, e.g., from fibroblasts (Day et al., 2004; Day, 2005), which was dependent on the dose of Bioglass dissolution ions (Keshaw et al., 2005). Mitogenic stimulation of endothelial cells also occurred when they were cultured in the presence of Bioglass dissolution ions (Leach et al., 2006). Collagen/Bioglass 45S5 composites in rat calvaria also stimulated more neovascularization in 2 weeks than collagen alone (Leu et al., 2009), although similar results are not always seen in other studies. Extracellular calcium ions could be responsible for this effect (Aguirre et al., 2010). *In vitro* enhancement of angiogenesis has also been achieved by incorporating active ions, such as cobalt ions, in the glass network, which can trick the body into recognizing the implant site as hypoxic (low oxygen pressure). This triggers a cascade of processes to produce new blood vessels (Peters et al., 2005; Semenza, 2007; Azevedo et al., 2010, 2015). A

question that needs answering is how long should there be presence of cobalt and a simulation of hypoxia in a bone defect for ideal bone regeneration? Medical device companies will also have to consider whether the benefits of cobalt ion release is worth the investment to claim the “drug-like” effects.

Frontier: Regenerative Scaffolds That Are Truly Load Bearing

Load-bearing devices that can be used in orthopedics over the long term that can also regenerate living bone are still not available clinically. This would be a frontier crossed that would certainly warrant the investment of medical device companies. Is it feasible to produce and test bioactive implants that have predictable 20-year lifetime survivability under simulated load-bearing physiological conditions?

3-D printing has delivered bioactive glass scaffolds with interconnected pores similar in diameter to the porous foam scaffolds developed previously (**Figure 4**), but with compressive strengths at least an order of magnitude higher, increasing from 2.4 MPa for

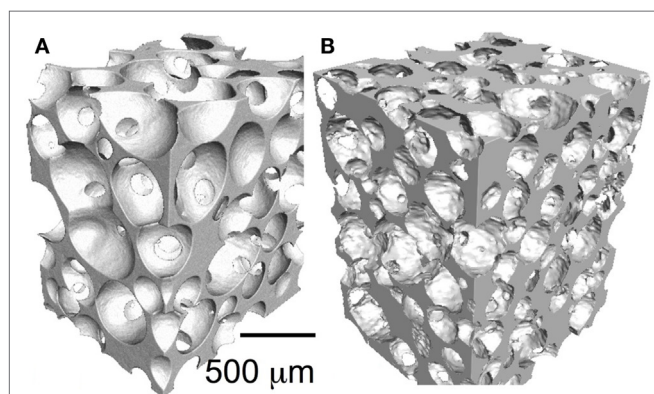


FIGURE 3 | X-ray microtomography images of bioactive glass scaffolds (A) sol-gel foam and (B) melt-derived gel-cast foam. Modified with permission from Jones (2013).

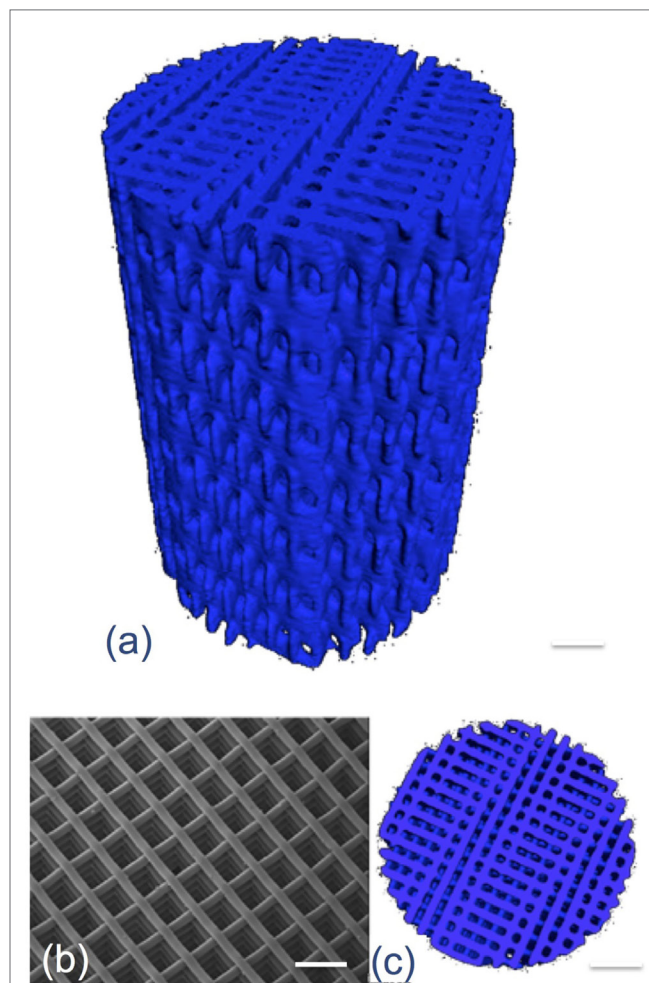


FIGURE 4 | X-ray microtomography image of 3-D printed bioactive glass scaffolds. Modified with permission from Jones (2013).

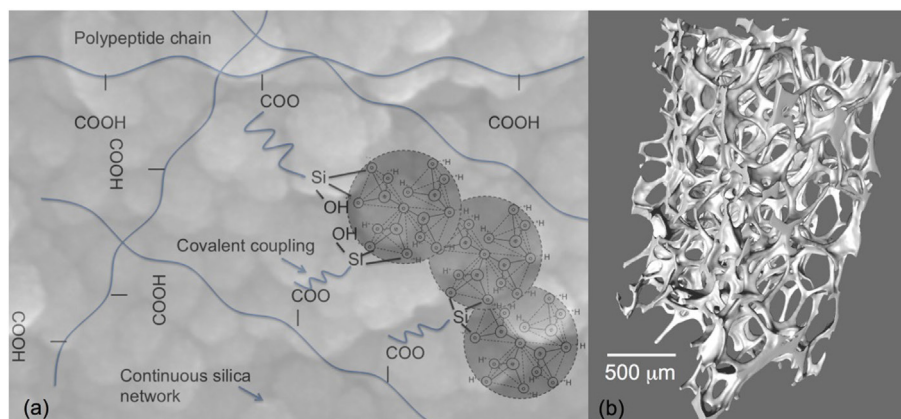


FIGURE 5 | Sol-gel hybrids: (A) schematic of the concept of inorganic/organic hybrids with bonding between components and (B) X-ray microtomography image of sol-gel foam hybrid scaffolds. Modified with permission from Jones (2013).

the foams of 80% porosity (Jones et al., 2006) to >140 MPa for the 3-D printed scaffolds (Fu et al., 2011b). The reason for this is that the layer by layer printing process can deposit thick aligned struts (>50 μm), leaving wide channels in excess of 500 μm, with percentage porosities of 60% (Doiphode et al., 2011; Huang et al., 2011; Kolan et al., 2011).

However, bioactive glass scaffolds are still brittle and therefore not suitable for all grafting applications, such as sites that are under cyclic loads. Tougher scaffolds are required that still have all the bioactive properties of Bioglass. One solution is to use composite materials (Rezwan et al., 2006); however, conventional composites of bioactive glass particles can be masked by the polymer matrix and it is difficult to match degradation rates between the polymer and the bioactive glass. An alternative is inorganic/organic hybrids made by the sol-gel process (Sanchez and In, 1992; Novak, 1993; Jones, 2013). As the gelation process occurs at room temperature, polymers can be incorporated into the sol so that the polymer chains are dispersed between the assembling nanoparticles prior to gelation. This provides molecular scale interactions between the components (Figure 5A), which gives the unique potential for control of mechanical properties and degradation rate while providing a homogeneous surface (at the micron scale) for cell attachment (Arcos and Vallet-Regi, 2010; Jones, 2013). In order for congruent degradation to occur, some covalent bonds are needed between the organic and inorganic components (Figure 5A). Examples are silica/natural polymers: e.g., silica/gelatin (Ren et al., 2002; Mahony et al., 2010, 2014), silica/poly(gamma-glutamic acid) (Poologasundarampillai et al., 2010, 2012, 2014; Valliant et al., 2013), silica/chitosan (Shirosaki et al., 2005, 2010; Connell et al., 2014), silica/polyester (Rhee et al., 2002, 2004; Pandis et al., 2015), and silica/PEG (Liu et al., 2012; Russo et al., 2013; Catauro et al., 2015; Li et al., 2015). The foaming method (Figure 5B) can be introduced to the sol-gel hybrid process (Mahony et al., 2010, 2014) or the sol to gel transition can be used to 3-D print the hybrids (Gao et al., 2013). One of the biggest challenges here is to be able to introduce calcium into the silicate network at these low processing temperatures. In sol-gel glass synthesis, using calcium salts, temperatures of

450°C must be surpassed to allow calcium to enter the silicate network, which is too high for organic components. Therefore, alternative methods for calcium incorporation are needed to impart bioactivity (Valliant et al., 2013; Poologasundarampillai et al., 2014).

The frontier that must be crossed is of tuning the mechanical properties and degradation rates of these exciting new materials so that load can be shared with the host tissue and osteogenic cells experience a transfer of load, and mechanical transduction, so that high quality bone regenerates as the scaffold is remodeled by the host tissue.

Frontier: Use of Inorganic Materials Deliver Ions for Therapeutic Non-Bone Applications

Numerous soft tissue engineering applications have been investigated at an exploratory level but still require development into clinical products (Miguez-Pacheco et al., 2015). Is it possible to obtain regulatory approval for clinical trials of soft tissue applications based upon limited *in vitro* and *in vivo* data and lack of understanding of basic biological mechanisms of soft tissue response to bioactive materials?

CONCLUSION

Important frontiers have been crossed where synthetic materials can bond with host bone, preventing fibrous encapsulation and creating a stable implant. Osteogenic cells are stimulated by inorganic bioactive glasses and their dissolution products. Frontiers still to be crossed in orthopedics are advanced bioactive biomaterials that can share load with host bone, transmit the load to the cells, and then degrade as the bone repairs. The concept of controlled delivery of active cations from a bioactive glass works for bone (osteostimulation). Other cations have been shown to stimulate other cells *in vitro*. A frontier to cross is the availability of bespoke bioactive devices for soft tissue therapy. Frontiers are only truly crossed when patients receive the benefits.

REFERENCES

- Aguirre, A., Gonzalez, A., Planell, J. A., and Engel, E. (2010). Extracellular calcium modulates in vitro bone marrow-derived Flk-1(+) CD34(+) progenitor cell chemotaxis and differentiation through a calcium-sensing receptor. *Biochem. Biophys. Res. Commun.* 393, 156–161. doi:10.1016/j.bbrc.2010.01.109
- Arcos, D., and Vallet-Regi, M. (2010). Sol-gel silica-based biomaterials and bone tissue regeneration. *Acta Biomater.* 6, 2874–2888. doi:10.1016/j.actbio.2010.02.012
- Autefage, H., Gentleman, E., Littmann, E., Hedegaard, M. A. B., Von Erlach, T., O'Donnell, M., et al. (2015). Sparse feature selection methods identify unexpected global cellular response to strontium-containing materials. *Proc. Natl. Acad. Sci. U.S.A.* 112, 4280–4285. doi:10.1073/pnas.1419799112
- Azevedo, M. M., Jell, G., O'Donnell, M. D., Law, R. V., Hill, R. G., and Stevens, M. M. (2010). Synthesis and characterization of hypoxia-mimicking bioactive glasses for skeletal regeneration. *J. Mater. Chem.* 20, 8854–8864. doi:10.1039/c0jm01111h
- Azevedo, M. M., Tsigkou, O., Nair, R., Jones, J. R., Jell, G., and Stevens, M. M. (2015). Hypoxia inducible factor-stabilizing bioactive glasses for directing mesenchymal stem cell behavior. *Tissue Eng. Part A* 21, 382–389. doi:10.1089/ten.tea.2014.0083
- Beckham, C. A., Greenlee, T. K., and Crebo, A. R. (1971). Bone formation at a ceramic implant interface. *Calcif. Tissue Res.* 8, 165–171. doi:10.1007/bf02010133
- Bohner, M., and Lemaire, J. (2009). Can bioactivity be tested in vitro with SBF solution? *Biomaterials* 30, 2175–2179. doi:10.1016/j.biomaterials.2009.01.008
- Brauer, D. S., Karpulthina, N., O'Donnell, M. D., Law, R. V., and Hill, R. G. (2010). Fluoride-containing bioactive glasses: effect of glass design and structure on degradation, pH and apatite formation in simulated body fluid. *Acta Biomater.* 6, 3275–3282. doi:10.1016/j.actbio.2010.01.043
- Brie, J., Chartier, T., Chaput, C., Delage, C., Pradeau, B., Caire, F., et al. (2013). A new custom made bioceramic implant for the repair of large and complex craniofacial bone defects. *J. Craniomaxillofac. Surg.* 41, 403–407. doi:10.1016/j.jcms.2012.11.005
- Brink, M. (1997). The influence of alkali and alkaline earths on the working range for bioactive glasses. *J. Biomed. Mater. Res.* 36, 109–117. doi:10.1002/(SICI)1097-4636(199707)36:1<109::AID-JBM13>3.3.CO;2-Q
- Catauro, M., Bollino, F., Papale, F., Gallicchio, M., and Pacifico, S. (2015). Influence of the polymer amount on bioactivity and biocompatibility of SiO₂/PEG hybrid materials synthesized by sol-gel technique. *Mater. Sci. Eng. C Mater. Biol. Appl.* 48, 548–555. doi:10.1016/j.msec.2014.12.035
- Chen, Q. Z. Z., Thompson, I. D., and Boccaccini, A. R. (2006). 45S5 Bioglass-derived glass-ceramic scaffolds for bone tissue engineering. *Biomaterials* 27, 2414–2425. doi:10.1016/j.biomaterials.2005.11.025
- Clark, A. E., Pantano, C. G., and Hench, L. L. (1976). Auger spectroscopic analysis of Bioglass corrosion films. *J. Am. Ceram. Soc.* 59, 37–39. doi:10.1111/j.1151-2916.1976.tb09382.x
- Connell, L. S., Romer, F., Suarez, M., Valliant, E. M., Zhang, Z. Y., Lee, P. D., et al. (2014). Chemical characterisation and fabrication of chitosan-silica hybrid scaffolds with 3-glycidoxypentyl trimethoxysilane. *J. Mater. Chem. B* 2, 668–680. doi:10.1039/c3tb21507e
- Day, R. M. (2005). Bioactive glass stimulates the secretion of angiogenic growth factors and angiogenesis in vitro. *Tissue Eng.* 11, 768–777. doi:10.1089/ten.2005.11.768
- Day, R. M., Boccaccini, A. R., Shurey, S., Roether, J. A., Forbes, A., Hench, L. L., et al. (2004). Assessment of polyglycolic acid mesh and bioactive glass for soft-tissue engineering scaffolds. *Biomaterials* 25, 5857–5866. doi:10.1016/j.biomaterials.2004.01.043
- Doiphode, N. D., Huang, T., Leu, M. C., Rahaman, M. N., and Day, D. E. (2011). Freeze extrusion fabrication of 13-93 bioactive glass scaffolds for bone repair. *J. Mater. Sci. Mater. Med.* 22, 515–523. doi:10.1007/s10856-011-4236-4
- Elgayar, I., Aliev, A. E., Boccaccini, A. R., and Hill, R. G. (2005). Structural analysis of bioactive glasses. *J. Non Cryst. Solids* 351, 173–183. doi:10.1016/j.jnoncrysol.2004.07.067
- Frantzen, J., Rantakokko, J., Aro, H. T., Heinanen, J., Kajander, S., Gullichsen, E., et al. (2011). Instrumented spondylodesis in degenerative spondylolisthesis with bioactive glass and autologous bone a prospective 11-year follow-up. *J. Spinal Disord. Tech.* 24, 455–461. doi:10.1097/BSD.0b013e31822a20c6
- Fu, Q., Rahaman, M. N., Bal, B. S., Kuroki, K., and Brown, R. F. (2010). In vivo evaluation of 13-93 bioactive glass scaffolds with trabecular and oriented microstructures in a subcutaneous rat implantation model. *J. Biomed. Mater. Res. A* 95A, 235–244. doi:10.1002/jbm.a.32827
- Fu, Q., Saiz, E., and Tomsia, A. P. (2011a). Bioinspired strong and highly porous glass scaffolds. *Adv. Funct. Mater.* 21, 1058–1063. doi:10.1002/adfm.201002030
- Fu, Q., Saiz, E., and Tomsia, A. P. (2011b). Direct ink writing of highly porous and strong glass scaffolds for load-bearing bone defects repair and regeneration. *Acta Biomater.* 7, 3547–3554. doi:10.1016/j.actbio.2011.06.030
- Gao, C., Rahaman, M. N., Gao, Q., Teramoto, A., and Abe, K. (2013). Robotic deposition and in vitro characterization of 3D gelatinbioactive glass hybrid scaffolds for biomedical applications. *J. Biomed. Mater. Res. A* 101, 2027–2037. doi:10.1002/jbm.a.34496
- Gentleman, E., Fredholm, Y. C., Jell, G., Lotfibakhshahi, N., O'Donnell, M. D., Hill, R. G., et al. (2010). The effects of strontium-substituted bioactive glasses on osteoblasts and osteoclasts in vitro. *Biomaterials* 31, 3949–3956. doi:10.1016/j.biomaterials.2010.01.121
- Haimi, S., Moimas, L., Pirhonen, E., Lindroos, B., Huhtala, H., Raty, S., et al. (2009). Calcium phosphate surface treatment of bioactive glass causes a delay in early osteogenic differentiation of adipose stem cells. *J. Biomed. Mater. Res. A* 91A, 540–547. doi:10.1002/jbm.a.32233
- Heikkilä, J. T., Kukkonen, J., Aho, A. J., Moisander, S., Kyyronen, T., and Mattila, K. (2011). Bioactive glass granules: a suitable bone substitute material in the operative treatment of depressed lateral tibial plateau fractures: a prospective, randomized 1 year follow-up study. *J. Mater. Sci. Mater. Med.* 22, 1073–1080. doi:10.1007/s10856-011-4272-0
- Hench, L. L. (1991). Bioceramics – from concept to clinic. *J. Am. Ceram. Soc.* 74, 1487–1510. doi:10.1111/j.1151-2916.1991.tb07132.x
- Hench, L. L. (1998). Bioceramics. *J. Am. Ceram. Soc.* 81, 1705–1728. doi:10.1111/j.1151-2916.1998.tb02540.x
- Hench, L. L. (2015). Opening paper 2015 – some comments on Bioglass: four eras of discovery and development. *Biomed. Glasses* 1, 1–11. doi:10.1515/bglass-2015-0001
- Hench, L. L., and Paschall, H. A. (1973). Direct chemical bonding of bioactive glass-ceramic materials and bone. *J. Biomed. Mater. Res. Symp.* 4, 25–42. doi:10.1002/jbm.820070304
- Hench, L. L., and Polak, J. M. (2002). Third-generation biomedical materials. *Science* 295, 1014–1017. doi:10.1126/science.1067404
- Hench, L. L., Splinter, R. J., Allen, W. C., and Greenlee, T. K. (1971). Bonding mechanisms at the interface of ceramic prosthetic materials. *J. Biomed. Mater. Res. Symp.* 2, 117–141. doi:10.1002/jbm.820050611
- Hench, L. L., Wilson, J., and Greenspan, D. (2004). Bioglass: a short history and bibliography. *J. Aust. Ceram. Soc.* 40, 1–42.
- Hoppe, A., Gueldal, N. S., and Boccaccini, A. R. (2011). A review of the biological response to ionic dissolution products from bioactive glasses and glass-ceramics. *Biomaterials* 32, 2757–2774. doi:10.1016/j.biomaterials.2011.01.004
- Huang, T. S., Rahaman, M. N., Doiphode, N. D., Leu, M. C., Bal, B. S., Day, D. E., et al. (2011). Porous and strong bioactive glass (13-93) scaffolds fabricated by freeze extrusion technique. *Mater. Sci. Eng. C Mater. Biol. Appl.* 31, 1482–1489. doi:10.1016/j.msec.2011.06.004
- Ilharreborde, B., Morel, E., Fitoussi, F., Presedo, A., Souchet, P., Pennecot, G.-F., et al. (2008). Bioactive glass as a bone substitute for spinal fusion in adolescent idiopathic scoliosis a comparative study with iliac crest autograft. *J. Pediatr. Orthop.* 28, 347–351. doi:10.1097/BPO.0b013e318168d1d4
- Jones, J. R. (2013). Review of bioactive glass: from Hench to hybrids. *Acta Biomater.* 9, 4457–4486. doi:10.1016/j.actbio.2012.08.023
- Jones, J. R., Ehrenfried, L. M., and Hench, L. L. (2006). Optimising bioactive glass scaffolds for bone tissue engineering. *Biomaterials* 27, 964–973. doi:10.1016/j.biomaterials.2005.07.017
- Karpov, M., Laczká, M., Leboy, P. S., and Osyczka, A. M. (2008). Sol-gel bioactive glasses support both osteoblast and osteoclast formation from human bone marrow cells. *J. Biomed. Mater. Res. A* 84A, 718–726. doi:10.1002/jbm.a.31386
- Keshaw, H., Forbes, A., and Day, R. M. (2005). Release of angiogenic growth factors from cells encapsulated in alginate beads with bioactive glass. *Biomaterials* 26, 4171–4179. doi:10.1016/j.biomaterials.2004.10.021
- Kokubo, T., Ito, S., Huang, Z. T., Hayashi, T., Sakka, S., Kitsugi, T., et al. (1990). Ca-P-rich layer formed on high-strength bioactive glass-ceramic A-W. *J. Biomed. Mater. Res.* 24, 331–343. doi:10.1002/jbm.820240306

- Kolan, K. C. R., Leu, M. C., Hilmas, G. E., Brown, R. F., and Velez, M. (2011). Fabrication of 13-93 bioactive glass scaffolds for bone tissue engineering using indirect selective laser sintering. *Biofabrication* 3, 025004. doi:10.1088/1758-5082/3/2/025004
- Labbaf, S., Tsigkou, O., Mueller, K. H., Stevens, M. M., Porter, A. E., and Jones, J. R. (2011). Spherical bioactive glass particles and their interaction with human mesenchymal stem cells in vitro. *Biomaterials* 32, 1010–1018. doi:10.1016/j.biomaterials.2010.08.082
- Lao, J., Jallot, E., and Nedelec, J.-M. (2008). Strontium-delivering glasses with enhanced bioactivity: a new biomaterial for antiosteoporotic applications? *Chem. Mater.* 20, 4969–4973. doi:10.1021/cm800993s
- Leach, J. K., Kaigler, D., Wang, Z., Krebsbach, P. H., and Mooney, D. J. (2006). Coating of VEGF-releasing scaffolds with bioactive glass for angiogenesis and bone regeneration. *Biomaterials* 27, 3249–3255. doi:10.1016/j.biomaterials.2006.01.033
- Leu, A., Stieger, S. M., Dayton, P., Ferrara, K. W., and Leach, J. K. (2009). Angiogenic response to bioactive glass promotes bone healing in an irradiated calvarial defect. *Tissue Eng. Part A* 15, 877–885. doi:10.1089/ten.tea.2008.0018
- Li, A., Shen, H., Ren, H., Wang, C., Wu, D., Martin, R. A., et al. (2015). Bioactive organic/inorganic hybrids with improved mechanical performance. *J. Mater. Chem. B* 3, 1379–1390. doi:10.1039/c4tb01776e
- Li, R., Clark, A. E., and Hench, L. L. (1991). An investigation of bioactive glass powders by sol-gel processing. *J. Appl. Biomater.* 2, 231–239. doi:10.1002/jab.770020403
- Lindfors, N. C., Heikkilä, J. T., and Aho, A. J. (2008). Long-term evaluation of blood silicon and osteocalcin in operatively treated patients with benign bone tumors using bioactive glass and autogenous bone. *J. Biomed. Mater. Res. B Appl. Biomater.* 87B, 73–76. doi:10.1002/jbm.b.31070
- Lindfors, N. C., Hyvonen, P., Nyyssonen, M., Kirjavainen, M., Kankare, J., Gullichsen, E., et al. (2010a). Bioactive glass S53P4 as bone graft substitute in treatment of osteomyelitis. *Bone* 47, 212–218. doi:10.1016/j.bone.2010.05.030
- Lindfors, N. C., Koski, I., Heikkilä, J. T., Mattila, K., and Aho, A. J. (2010b). A prospective randomized 14-year follow-up study of bioactive glass and autogenous bone as bone graft substitutes in benign bone tumors. *J. Biomed. Mater. Res. B Appl. Biomater.* 94B, 157–164. doi:10.1002/jbm.b.31636
- Liu, W., Wu, X., Zhan, H., and Yan, F. (2012). Synthesis of bioactive poly(ethylene glycol)/SiO₂-CaO-P₂O₅ hybrids for bone regeneration. *Mater. Sci. Eng. C Mater. Biol. Appl.* 32, 707–711. doi:10.1016/j.msec.2012.01.012
- Macon, A. L. B., Kim, T. B., Valliant, E. M., Goetschius, K., Brow, R. K., Day, D. E., et al. (2015). A unified in vitro evaluation for apatite-forming ability of bioactive glasses and their variants. *J. Mater. Sci. Mater. Med.* 26, 115. doi:10.1007/s10856-015-5403-9
- Maeno, S., Niki, Y., Matsumoto, H., Morioka, H., Yatabe, T., Funayama, A., et al. (2005). The effect of calcium ion concentration on osteoblast viability, proliferation and differentiation in monolayer and 3D culture. *Biomaterials* 26, 4847–4855. doi:10.1016/j.biomaterials.2005.01.006
- Mahony, O., Tsigkou, O., Ionescu, C., Minelli, C., Ling, L., Hanly, R., et al. (2010). Silica-gelatin hybrids with tailorable degradation and mechanical properties for tissue regeneration. *Adv. Funct. Mater.* 20, 3835–3845. doi:10.1002/adfm.201000838
- Mahony, O., Yue, S., Turdean-Ionescu, C., Hanna, J. V., Smith, M. E., Lee, P. D., et al. (2014). Silica-gelatin hybrids for tissue regeneration: inter-relationships between the process variables. *J. Solgel Sci. Technol.* 69, 288–298. doi:10.1007/s10971-013-3214-3
- Marie, P. J. (2010). The calcium-sensing receptor in bone cells: a potential therapeutic target in osteoporosis. *Bone* 46, 571–576. doi:10.1016/j.bone.2009.07.082
- Merwin, G. E., Atkins, J. S., Wilson, J., and Hench, L. L. (1982). Comparison of ossicular replacement materials in a mouse ear model. *Otolaryngol. Head Neck Surg.* 90, 461–469.
- Midha, S., Kim, T. B., Van Den Bergh, W., Lee, P. D., Jones, J. R., and Mitchell, C. A. (2013). Preconditioned 70S30C bioactive glass foams promote osteogenesis in vivo. *Acta Biomater.* 9, 9169–9182. doi:10.1016/j.actbio.2013.07.014
- Miguez-Pacheco, V., Hench, L. L., and Boccaccini, A. R. (2015). Bioactive glasses beyond bone and teeth: emerging applications in contact with soft tissues. *Acta Biomater.* 13, 1–15. doi:10.1016/j.actbio.2014.11.004
- Minaberry, Y., and Jobbagy, M. (2011). Macroporous Bioglass scaffolds prepared by coupling sol-gel with freeze drying. *Chem. Mater.* 23, 2327–2332. doi:10.1021/cm103362c
- Novak, B. M. (1993). Hybrid nanocomposite materials – between inorganic glasses and organic polymers. *Adv. Mater. Weinheim* 5, 422–433. doi:10.1002/adma.19930050603
- Ogino, M., and Hench, L. L. (1980). Formation of calcium-phosphate films on silicate-glasses. *J. Non Cryst. Solids* 3, 673–678. doi:10.1016/0022-3093(80)90514-1
- Ogino, M., Ohuchi, F., and Hench, L. L. (1980). Compositional dependence of the formation of calcium-phosphate films on Bioglass. *J. Biomed. Mater. Res.* 14, 55–64. doi:10.1002/jbm.820140107
- Ojansivu, M., Vanhatupa, S., Björkvik, L., Hakkanen, H., Kellomäki, M., Autio, R., et al. (2015). Bioactive glass ions as strong enhancers of osteogenic differentiation in human adipose stem cells. *Acta Biomater.* 21, 190–203. doi:10.1016/j.actbio.2015.04.017
- Oonishi, H., Hench, L. L., Wilson, J., Sugihara, F., Tsuji, E., Kushitani, S., et al. (1999). Comparative bone growth behavior in granules of bioceramic materials of various sizes. *J. Biomed. Mater. Res.* 44, 31–43. doi:10.1002/(SICI)1097-4636(199901)44:1<31::AID-JBM4>3.3.CO;2-O
- Oonishi, H., Hench, L. L., Wilson, J., Sugihara, F., Tsuji, E., Matsuura, M., et al. (2000). Quantitative comparison of bone growth behavior in granules of Bioglass (R), A-W glass-ceramic, and hydroxyapatite. *J. Biomed. Mater. Res.* 51, 37–46. doi:10.1002/(SICI)1097-4636(200007)51:1<37::AID-JBM6>3.0.CO;2-T
- Oonishi, H., Kushitani, S., Yasukawa, E., Iwaki, H., Hench, L. L., Wilson, J., et al. (1997). Particulate Bioglass compared with hydroxyapatite as a bone graft substitute. *Clin. Orthop. Relat. Res.* 334, 316–325. doi:10.1097/00003086-199701000-00041
- Pandis, C., Trujillo, S., Matos, J., Madeira, S., Rodenas-Rochina, J., Kriptomou, S., et al. (2015). Porous polylactic acid-silica hybrids: preparation, characterization, and study of mesenchymal stem cell osteogenic differentiation. *Macromol. Biosci.* 15, 262–274. doi:10.1002/mabi.201400339
- Pernaa, K., Koski, I., Mattila, K., Gullichsen, E., Heikkilä, J., Aho, A., et al. (2011). Bioactive glass S53P4 and autograft bone in treatment of depressed tibial plateau fractures – a prospective randomized 11-year follow-up. *J. Long Term Eff. Med. Implants* 21, 139–148. doi:10.1615/JLongTermEffMedImplants.v21.i2.40
- Peters, K., Schmidt, H., Unger, R. E., Kamp, G., Prols, F., Berger, B. J., et al. (2005). Paradoxical effects of hypoxia-mimicking divalent cobalt ions in human endothelial cells in vitro. *Mol. Cell. Biochem.* 270, 157–166. doi:10.1007/s11010-005-4504-z
- Piotrowski, G., Hench, L. L., Allen, W. C., and Miller, G. J. (1975). Mechanical studies of bone Bioglass interfacial bond. *J. Biomed. Mater. Res.* 9, 47–61. doi:10.1002/jbm.820090408
- Poolagasundarampillai, G., Ionescu, C., Tsigkou, O., Murugesan, M., Hill, R. G., Stevens, M. M., et al. (2010). Synthesis of bioactive class II poly(gamma-glutamic acid)/silica hybrids for bone regeneration. *J. Mater. Chem.* 20, 8952–8961. doi:10.1039/c0jm00930j
- Poolagasundarampillai, G., Yu, B., Tsigkou, O., Valliant, E. M., Yue, S., Lee, P. D., et al. (2012). Bioactive silica-poly(g-glutamic acid) hybrids for bone regeneration: effect of covalent coupling on dissolution and mechanical properties and fabrication of porous scaffolds. *Soft Matter* 8, 4822–4832. doi:10.1039/c2sm00033d
- Poolagasundarampillai, G., Yu, B., Tsigkou, O., Wang, D., Romer, F., Bhakhri, V., et al. (2014). Poly(gamma-glutamic acid)/silica hybrids with calcium incorporated in the silica network by use of a calcium alkoxide precursor. *Chemistry* 20, 8149–8160. doi:10.1002/chem.201304013
- Rahaman, M. N., Day, D. E., Bal, B. S., Fu, Q., Jung, S. B., Bonewald, L. F., et al. (2011). Bioactive glass in tissue engineering. *Acta Biomater.* 7, 2355–2373. doi:10.1016/j.actbio.2011.03.016
- Rantakokko, J., Frantzen, J. P., Heinanen, J., Kajander, S., Kotilainen, E., Gullichsen, E., et al. (2012). Posterolateral spondylodesis using bioactive glass S53P4 and autogenous bone in instrumented unstable lumbar spine burst fractures. *Scand. J. Surg.* 101, 66–71. doi:10.1177/145749691210100113
- Reffitt, D. M., Ogston, N., Jugdaohsingh, R., Cheung, H. F. J., Evans, B. A. J., Thompson, R. P. H., et al. (2003). Orthosilicic acid stimulates collagen type I synthesis and osteoblastic differentiation in human osteoblast-like cells in vitro. *Bone* 32, 127–135. doi:10.1016/S8756-3282(02)00950-X
- Reilly, G. C., Radin, S., Chen, A. T., and Ducheyne, P. (2007). Differential alkaline phosphatase responses of rat and human bone marrow derived mesenchymal stem cells to 45S5 bioactive glass. *Biomaterials* 28, 4091–4097. doi:10.1016/j.biomaterials.2007.05.038

- Ren, L., Tsuru, K., Hayakawa, S., and Osaka, A. (2002). Novel approach to fabricate porous gelatin-siloxane hybrids for bone tissue engineering. *Biomaterials* 23, 4765–4773. doi:10.1016/S0142-9612(02)00226-0
- Rezwan, K., Chen, Q. Z., Blaker, J. J., and Boccacini, A. R. (2006). Biodegradable and bioactive porous polymer/inorganic composite scaffolds for bone tissue engineering. *Biomaterials* 27, 3413–3431. doi:10.1016/j.biomaterials.2006.01.039
- Rhee, S. H., Choi, J. Y., and Kim, H. M. (2002). Preparation of a bioactive and degradable poly(epsilon-caprolactone)/silica hybrid through a sol-gel method. *Biomaterials* 23, 4915–4921. doi:10.1016/S0142-9612(02)00251-x
- Rhee, S. H., Lee, Y. K., and Lim, B. S. (2004). Evaluation of a novel poly(epsilon-caprolactone)-organosiloxane hybrid material for the potential application as a bioactive and degradable bone substitute. *Biomacromolecules* 5, 1575–1579. doi:10.1021/bm049885n
- Russo, L., Gabrielli, L., Valliant, E. M., Nicotra, F., Jimenez-Barbero, J., Cipolla, L., et al. (2013). Novel silica/bis(3-aminopropyl) polyethylene glycol inorganic/organic hybrids by sol-gel chemistry. *Mater. Chem. Phys.* 140, 168–175. doi:10.1016/j.matchemphys.2013.03.016
- Rust, K. R., Singleton, G. T., Wilson, J., and Antonelli, P. J. (1996). Bioglass middle ear prosthesis: long-term results. *Am. J. Otol.* 17, 371–374.
- Sanchez, C., and In, M. (1992). Molecular design of alkoxide precursors for the synthesis of hybrid organic inorganic gels. *J. Non Cryst. Solids* 147, 1–12. doi:10.1016/S0022-3093(05)80584-8
- Sanders, D. M., and Hench, L. L. (1973). Mechanisms of glass corrosion. *J. Am. Ceram. Soc.* 56, 373–377. doi:10.1111/j.1151-2916.1973.tb12689.x
- Semenza, G. L. (2007). Life with oxygen. *Science* 318, 62–64. doi:10.1126/science.1147949
- Sepulveda, P., Jones, J. R., and Hench, L. L. (2002). Bioactive sol-gel foams for tissue repair. *J. Biomed. Mater. Res.* 59, 340–348. doi:10.1002/jbm.1250
- Shirosaki, Y., Tsuru, K., Hayakawa, S., Osaka, A., Lopes, M. A., Santos, J. D., et al. (2005). In vitro cytocompatibility of MG63 cells on chitosan-organosiloxane hybrid membranes. *Biomaterials* 26, 485–493. doi:10.1016/j.biomaterials.2004.02.056
- Shirosaki, Y., Tsuru, K., Moribayashi, H., Hayakawa, S., Nakamura, Y., Gibson, I. R., et al. (2010). Preparation of osteocompatible Si(IV)-enriched chitosan-silicate hybrids. *J. Ceram. Soc. Jpn.* 118, 989–992. doi:10.2109/jcersj2.118.989
- Stanley, H. R., Hall, M. B., Clark, A. E., King, C. J., Hench, L. L., and Berte, J. J. (1997). Using 45S5 Bioglass cones as endosseous ridge maintenance implants to prevent alveolar ridge resorption: a 5-year evaluation. *Int. J. Oral Maxillofac. Implants* 12, 95–105.
- Stanley, H. R., Hench, L. L., Bennett, C. G. Jr., Chellemi, S. J., King, C. J. III, Going, R. E., et al. (1981). The implantation of natural tooth form Bioglass in baboons – long term results. *Implantologist* 2, 26–36.
- Tsigkou, O., Jones, J. R., Polak, J. M., and Stevens, M. M. (2009). Differentiation of fetal osteoblasts and formation of mineralized bone nodules by 45S5 Bioglass (R) conditioned medium in the absence of osteogenic supplements. *Biomaterials* 30, 3542–3550. doi:10.1016/j.biomaterials.2009.03.019
- Tsigkou, O., Labbaf, S., Stevens, M. M., Porter, A. E., and Jones, J. R. (2014). Monodispersed bioactive glass submicron particles and their effect on bone marrow and adipose tissue-derived stem cells. *Adv. Healthc. Mater.* 3, 115–125. doi:10.1002/adhm.201300126
- Tsigkou, O., Pomerantseva, I., Spencer, J. A., Redondo, P. A., Hart, A. R., O'Doherty, E., et al. (2010). Engineered vascularized bone grafts. *Proc. Natl. Acad. Sci. U.S.A.* 107, 3311–3316. doi:10.1073/pnas.0905445107
- Turunen, T., Peltola, J., Yli-Urpo, A., and Happonen, R. P. (2004). Bioactive glass granules as a bone adjunctive material in maxillary sinus floor augmentation. *Clin. Oral Implants Res.* 15, 135–141. doi:10.1111/j.1600-0501.2004.00989.x
- Valerio, P., Pereira, M. M., Goes, A. M., and Leite, M. F. (2009). Effects of extracellular calcium concentration on the glutamate release by bioactive glass (BG60S) preincubated osteoblasts. *Biomed. Mater.* 4, 045011. doi:10.1088/1748-6041/4/4/045011
- Valliant, E. M., Romer, F., Wang, D., Mcphail, D. S., Smith, M. E., Hanna, J. V., et al. (2013). Bioactivity in silica/poly(gamma-glutamic acid) sol-gel hybrids through calcium chelation. *Acta Biomater.* 9, 7662–7671. doi:10.1016/j.actbio.2013.04.037
- Wheeler, D. L., Eschbach, E. J., Hoellrich, R. G., Montfort, M. J., and Chamberland, D. L. (2000). Assessment of resorbable bioactive material for grafting of critical-size cancellous defects. *J. Orthop. Res.* 18, 140–148. doi:10.1002/jor.1100180120
- Wilson, J., Clark, A. E., Hall, M., and Hench, L. L. (1993). Tissue response to Bioglass endosseous ridge maintenance implants. *J. Oral Implantol.* 19, 295–302.
- Wilson, J., and Low, S. B. (1992). Bioactive ceramics for periodontal treatment – comparative studies in the Patas monkey. *J. Appl. Biomater.* 3, 123–129. doi:10.1002/jab.770030208
- Wilson, J., and Noletti, D. (1990). “Bonding of soft tissues to Bioglass®” in *Handbook of Bioactive Ceramics*, eds Yamamuro T., Hench L. L., and Wilson J. (Boca Raton, FL: CRC Press), 283–302.
- Wilson, J., Pigott, G. H., Schoen, F. J., and Hench, L. L. (1981). Toxicology and biocompatibility of Bioglasses. *J. Biomed. Mater. Res.* 15, 805–817. doi:10.1002/jbm.820150605
- Wu, Z. Y., Hill, R. G., Yue, S., Nightingale, D., Lee, P. D., and Jones, J. R. (2011). Melt-derived bioactive glass scaffolds produced by a gel-cast foaming technique. *Acta Biomater.* 7, 1807–1816. doi:10.1016/j.actbio.2010.11.041
- Xynos, I. D., Edgar, A. J., Buttery, L. D. K., Hench, L. L., and Polak, J. M. (2000a). Ionic products of bioactive glass dissolution increase proliferation of human osteoblasts and induce insulin-like growth factor II mRNA expression and protein synthesis. *Biochem. Biophys. Res. Commun.* 276, 461–465. doi:10.1006/bbrc.2000.3503
- Xynos, I. D., Hukkanen, M. V. J., Batten, J. J., Buttery, L. D., Hench, L. L., and Polak, J. M. (2000b). Bioglass 45S5 stimulates osteoblast turnover and enhances bone formation in vitro: implications and applications for bone tissue engineering. *Calcif. Tissue Int.* 67, 321–329. doi:10.1007/s002230001134
- Xynos, I. D., Edgar, A. J., Buttery, L. D. K., Hench, L. L., and Polak, J. M. (2001). Gene-expression profiling of human osteoblasts following treatment with the ionic products of Bioglass (R) 45S5 dissolution. *J. Biomed. Mater. Res.* 55, 151–157. doi:10.1002/1097-4636(200105)55:2<151::AID-JBM1001>3.0.CO;2-D

Conflict of Interest Statement: The authors declare that the research was conducted in the absence of any commercial or financial relationships that could be construed as a potential conflict of interest. The Associate Editor Wolfram Höland declared a past coauthorship with the author Julian R. Jones and states that the process, nevertheless, met the standards of a fair and objective review.

Copyright © 2015 Hench and Jones. This is an open-access article distributed under the terms of the Creative Commons Attribution License (CC BY). The use, distribution or reproduction in other forums is permitted, provided the original author(s) or licensor are credited and that the original publication in this journal is cited, in accordance with accepted academic practice. No use, distribution or reproduction is permitted which does not comply with these terms.



Growth of novel ceramic layers on metals via chemical and heat treatments for inducing various biological functions

Tadashi Kokubo* and Seiji Yamaguchi

Department of Biomedical Sciences, College of Life and Health Sciences, Chubu University, Kasugai, Japan

OPEN ACCESS

Edited by:

Aldo R. Boccaccini,
University of Erlangen-Nuremberg,
Germany

Reviewed by:

Ilaria Cacciotti,
University of Rome Niccolò
Cusano, Italy
Oscar Castano,
Institute for Bioengineering of
Catalonia, Spain

*Correspondence:

Tadashi Kokubo
kokubo@isc.chubu.ac.jp

Specialty section:

This article was submitted to
Biomaterials, a section of the
journal *Frontiers in Bioengineering
and Biotechnology*

Received: 20 July 2015

Accepted: 13 October 2015

Published: 27 October 2015

Citation:

Kokubo T and Yamaguchi S (2015)
Growth of novel ceramic layers on
metals via chemical and heat
treatments for inducing various
biological functions.
Front. Bioeng. Biotechnol. 3:176.
doi: 10.3389/fbioe.2015.00176

The present authors' systematic studies on growth of novel ceramic layers on Ti metal and its alloys by chemical and heat treatments for inducing bone-bonding bioactivity and some other biological functions are reviewed. Ti metal formed an apatite on its surface in a simulated body fluid, when heat-treated after exposure to strong acid solutions to form rutile surface layer, or to strong alkali solutions to form sodium titanate surface layer. Both types of Ti metal tightly bonded to the living bone. The alkali and heat treatment was applied to the surface Ti metal of an artificial hip joint and successfully used in the clinic since 2007. The acid and heat treatments were applied to porous Ti metal to induce osteoconductivity as well as osteoinductivity. The resulting product was successfully used in clinical trials for spinal fusion devices. For the Ti-based alloys, the alkali and heat treatment was little modified to form calcium titanate surface layer. Bone-growth promoting Mg, Sr, and Zn ions as well as the antibacterial Ag ion were successfully incorporated into the calcium titanate layer.

Keywords: bioactivity, osteoconduction, osteoinduction, Ti metal, Ti-based alloys, apatite, alkali and heat treatment, acid and heat treatment

INTRODUCTION

A considerable amount of material is needed to repair bone defects in both orthopedics and dentistry. Autogenous bone is the best bone substitute material in terms of compatibility with the surrounding tissue. However, only a small amount of bone can be harvested from the healthy part. Allogenic bone is the second choice, commonly results in side effects such as foreign body reaction and/or infection. Therefore, synthetic materials free of antigens or toxic impurities are obviously required.

Various kinds of synthetic materials have been used as bone substitutes, including organic polymers, ceramics, metals, and composites. However, most of them are encapsulated in a collagenous fibrous tissue so as to be isolated from living bone (Park and Lakes, 1992). This is a normal foreign body reaction that protects living tissue. However, because of this reaction, synthetic materials do not become stably fixed to the surrounding bone for a long period of time.

In contrast, certain kinds of ceramics such as Bioglass® in Na₂O–CaO–SiO₂–P₂O₅, glass-ceramic A-W-containing crystalline apatite and Wollastonite in MgO–CaO–SiO₂–P₂O₅, sintered hydroxyapatite of the composition Ca₁₀(PO₄)₆(OH)₂, sintered β-tricalcium phosphate of the composition 3CaO·P₂O₅, and biphasic calcium phosphates composed of hydroxyapatite and β-tricalcium phosphate have all been found to bond to living bone without forming fibrous tissue around them.

They are called “bioactive ceramics” and are already in clinical uses as important bone substitutes (Kokubo, 2008). However, their mechanical strength and fracture toughness are not as high as those of human cortical bone, so they cannot be used under load-bearing conditions.

Under load-bearing conditions, metallic materials such as stainless steel, Co–Cr–Mo alloys, titanium (Ti) metal, and its alloys are mainly used, because of their high mechanical strengths and superior corrosion resistances (Park and Lakes, 1992). However, even Ti metal and Ti-based alloys, which exhibit best biocompatibility among them, are also encapsulated by fibrous tissue and do not bond to living bone (Hacking et al., 2002). Their fixation also does not become stable for long period of time.

In order to confer bone-bonding bioactivity to the metallic materials, some bioactive ceramics such as hydroxyapatite have been coated on them using various techniques, such as plasma spraying, flame spraying, sputtering, sol–gel deposition, biomimetic method (Leeuwenburgh et al., 2008), and alternating soaking (Taguchi et al., 2001). However, the coated layer is not stable in the living body, because of its vulnerability to cracking, transformation, and degradation (Leeuwenburgh et al., 2008).

The present authors recently reported that certain metallic materials such as Ti metal and its alloys exhibit bone-bonding bioactivity when a certain kind of thin ceramic layer is grown on their surface via simple chemical and heat treatments. In the present paper, the recent results of our research on this subject are reviewed.

BASIC CONCEPT FOR CONFERRING BONE-BONDING BIOACTIVITY TO METALS

It was found by the present authors that Bioglass®, glass-ceramic A-W and sintered hydroxyapatite bond to living bone through an apatite layer that forms on their surfaces in the living body. In contrast, glass-ceramic A-W(Al) containing crystalline apatite and wollastonite similar to glass-ceramic A-W, but added with a small amount of Al₂O₃, neither formed the apatite on its surface in the living body nor bonded to living bone. Consequently, it was concluded that a material able to form the apatite on its surface in the living body is able to bond to living bone through the apatite layer, but a material unable to form the surface apatite does not bond to living bone (Kokubo and Takadama, 2006). Therefore, it is expected that even metallic materials will bond to living bone when their surfaces are modified such that they form the apatite on their surface *in vivo*.

Is it necessary that every metal subjected to different surface modifications should be implanted into animal bone defects to check for the apatite formation on their surfaces? This would require not only considerable cost and time but also the sacrifice of a great many animals.

We demonstrated that the apatite formation on the surfaces of Bioglass®, glass-ceramic A-W and sintered hydroxyapatite *in vivo* can be reproduced, even in an acellular simulated body fluid (SBF) having ion concentrations almost equal to those of the human blood plasma. In contrast, glass-ceramic A-W(Al) did

not form apatite on its surface in SBF nor bonded in the living body. This means that the apatite formation on a material in the living body can be evaluated in SBF without the need of animal experiments (Kokubo and Takadama, 2006).

The next problem was to determine the kind of material that effectively induces apatite formation in SBF. We found that certain simple metal oxide gels, such as TiO₂, ZrO₂, Nb₂O₅, and Ta₂O₅ form the apatite on their surfaces in SBF within a week (Li et al., 1994). Metallic materials are generally covered with a thin oxide layer. In view of this fact, it is expected that metallic materials based on Ti, Zr, Nb, and Ta form the apatite on their surfaces in SBF, as well as in the living body, so as to be able to bond to living bone when their surfaces are appropriately modified.

SURFACE MODIFICATION OF METALS

Ti metal and its alloys are the most widely used type of material as implants in the orthopedic and dental fields among the metallic materials described above because of their better compatibility with living tissue. Therefore, various surface modifications were applied to Ti metal and its alloys for inducing bone-bonding bioactivity using various methods, including ion implantation (Armitage et al., 2007; Nayab et al., 2007; Rautray et al., 2010), electrochemical reaction (Suh, 2003; Bjursten et al., 2010; Shibata et al., 2010; Whiteside et al., 2010; Zhao et al., 2010; Diefenback et al., 2011; Xie et al., 2011; Minagar et al., 2013; Zhang et al., 2013; Zhou et al., 2014), and hydrothermal treatments (Dong et al., 2007; Park et al., 2007, 2010; Chen et al., 2009; Ueda et al., 2009; Zhang et al., 2010). However, these techniques require special equipment and are not readily applicable to large-scale medical devices of complicated or porous structure. In contrast with these techniques, chemical and heat treatments do not have such limitations.

Various kinds of chemical and heat treatments also have been applied to Ti metal and its alloys to induce apatite formation on their surfaces in SBF (Wang et al., 2002; Wu et al., 2004; Takeuchi et al., 2005; Zhao et al., 2005, 2008; Cooper et al., 2006; Lee et al., 2007; Liu et al., 2007; Zhou et al., 2007; Sugino et al., 2009; Karthega and Rajendran, 2010; Li et al., 2010; Turkan and Guden, 2010; Ferraris et al., 2011). However, few results in these studies have been considered in terms of the mechanism of the apatite formation and correlated with the *in vivo* bone-bonding bioactivity.

The following are systematic studies we conducted on chemical and heat treatments of Ti metal and its alloys for inducing apatite formation on their surfaces in SBF along with their correlation with *in vivo* bone-bonding bioactivity.

SIMPLE CHEMICAL AND HEAT TREATMENTS OF Ti METAL

When a rectangular plate of Ti metal was soaked in an aqueous solution in which the pH was systematically changed from almost 0 to 14 by HCl or NaOH at 60°C for 24 h, it formed micrometer-scale roughness, precipitating titanium hydride (TiH_x) on its surface for the strong acid solutions <1.1 in pH,

and nanometer-scale roughness precipitating sodium hydrogen titanate ($\text{Na}_x\text{H}_{2-x}\text{Ti}_3\text{O}_7$, $0 < x < 2$) on its surface (Yamaguchi et al., 2009) for the strong alkali solutions higher than 13.6 in pH, as shown in **Figure 1**.

Only the Ti metal soaked in the strong alkali solutions higher than 13.6 in pH formed the apatite on its surface in SBF within 3 days, as shown in **Figure 1** (Pattanayak et al., 2012).

When the Ti metal was heat-treated at 600°C for 1 h after exposure to the solutions described above, no surface morphological change was observed on its surface as the result of the heat treatment. However, the titanium hydride was transformed into rutile (TiO_2), while the sodium hydrogen titanate was transformed into sodium titanate ($\text{Na}_2\text{Ti}_6\text{O}_{13}$) and rutile by the heat treatment. The Ti metals exposed to the solutions with intermediate pH values also precipitated the rutile on their surfaces by the heat treatment, as shown in **Figure 2**.

Among them, only the Ti metals heat-treated after exposure to the strong acid solutions <1.1 in pH or strong alkali solutions higher than 13.6 in pH formed the apatite on their surfaces in SBF within 3 days, as shown in **Figure 2** (Pattanayak et al., 2012).

It is clear from these results that the apatite formation on Ti metal depends upon neither the specific surface roughness nor crystalline phase. When the zeta potential of the Ti metal heat-treated after exposure to the solutions is measured, it can be seen from **Figure 3** that the apatite formation on the Ti metal is induced by the positive or negative surface charge (Pattanayak et al., 2012).

A positively charged surface might preferentially adsorb negatively charged phosphate ions in SBF. As the phosphate ions accumulate, its surface becomes negatively charged so as to combine with the positively charged calcium ions, forming an amorphous calcium phosphate. This calcium phosphate is metastable and eventually transforms into stable crystalline apatite, as shown in **Figure 4** (Pattanayak et al., 2012).

In contrast, a negatively charged surface would be expected to first preferentially adsorb positively charged calcium ions. As the calcium ions accumulate, its surface becomes positively charged so as to combine with the negatively charged phosphate ions, forming an amorphous calcium phosphate and then the crystalline apatite (Kim et al., 2003).

This sequential adsorption of the phosphate and calcium ions was confirmed by X-ray photoelectron spectroscopy (XPS) (Takadama et al., 2001a) and transmission electron microscopic observation combined with energy dispersive X-ray analysis (Takadama et al., 2001b) of the surface of the Ti metal soaked in SBF for different periods of time, as well as for the Ti metal heat-treated after exposure to the strong acid or alkali solution (Pattanayak et al., 2012).

The positive surface charge of the Ti metal heat-treated after exposure to the strong acid solution might be explained as follows. The Ti metal becomes adsorbed with Cl^- ions during the acid treatment. The Cl^- ions remain even after the heat treatment, and are dissociated in SBF so as to produce a local acidic environment on the Ti metal. It has been reported that titanium oxide is positively charged in an acidic environment (Gold et al., 1989). Consequently, the surface of the Ti metal heat-treated after exposure to strong acid solution is positively charged.

The negative surface charge of the Ti metal heat-treated after exposure to the strong alkali solutions might be explained as follows. The sodium titanate on the surface of the Ti metal releases Na^+ ions via exchange with the H_3O^+ ions in SBF so as to produce a local alkaline environment on the Ti metal. It has been reported that titanium oxide is negatively charged in an alkaline environment (Gold et al., 1989). Consequently, the surface of the Ti metal heat-treated after exposure to the alkali solution is negatively charged.

When the Ti metal is heat-treated after exposure to a neutral solution, it is not charged, since no charge is produced on

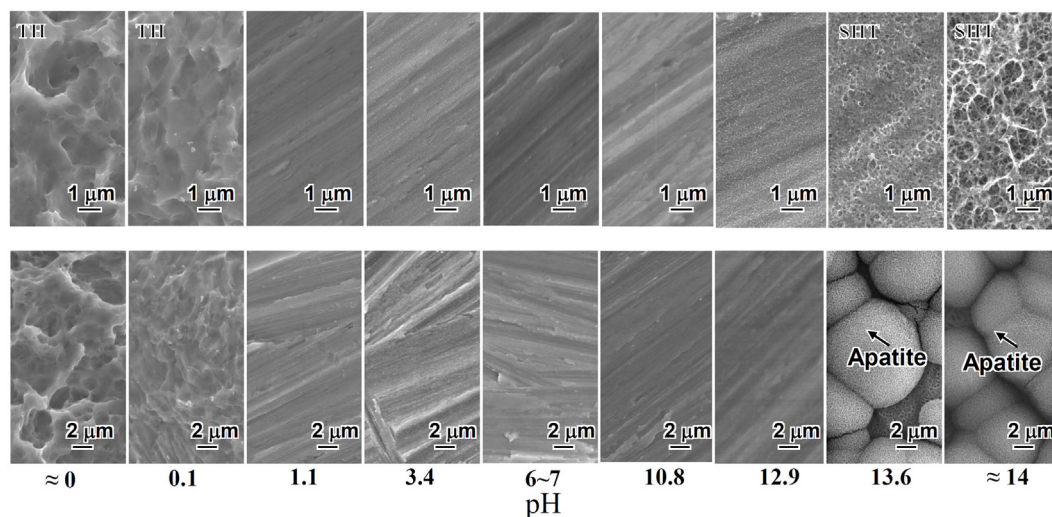


FIGURE 1 | SEM photographs of surfaces of Ti metal exposed to solutions with different pHs (top) and those of the same surfaces after soaking in SBF for 3 days (bottom). TH, titanium hydride; SHT, sodium hydrogen titanate. Reproduced from Pattanayak et al. (2012) with permission The Royal Society.

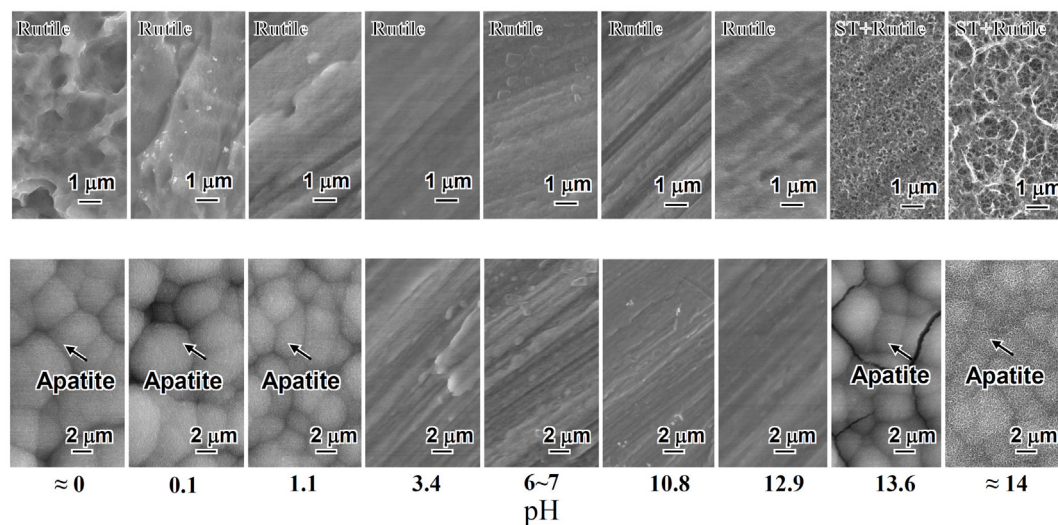


FIGURE 2 | SEM photographs of surfaces of Ti metal heat-treated after exposure to solutions with different pHs (top) and those of the same surfaces after soaking in SBF (bottom). ST, sodium titanate. Reproduced from Pattanayak et al. (2012) with permission The Royal Society.

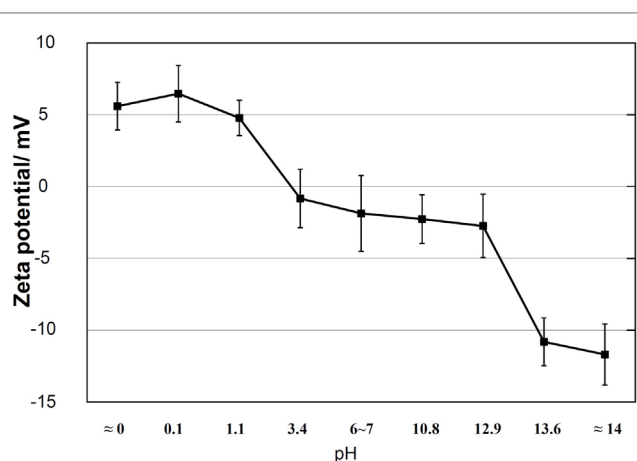


FIGURE 3 | Zeta potentials of Ti metal heat-treated after exposure to solutions with different pH values. Reproduced from Pattanayak et al. (2012) with permission The Royal Society.

its surface. When it is not heat-treated after exposure to the solution, it is not charged except after exposure to the strong alkali solutions, since an electrically insulating oxide layer is not produced on its surface except in the last case. As result, the apatite is not formed on the Ti metal surface in SBF in these cases except the last, as may be seen in **Figures 1 and 2** (Pattanayak et al., 2012).

This dependence of the apatite formation on the Ti metal upon the pH of the exposed solution is valid for different kinds of acid and alkali solutions. For example, the Ti metal also forms the apatite on its surface in SBF when heat-treated at 600°C for 1 h after exposure to strong 66.3% H_2SO_4 /10.6% HCl acid solution at 70°C for 24 h (Kokubo et al., 2010).

When the Ti metal subjected to the H_2SO_4 / HCl acid and heat treatments was implanted into a rabbit tibia, it came into direct contact with the surrounding bone within 4 weeks, without any intervening fibrous tissue at the interface, as shown in **Figure 5D**. The metal became so tightly bonded to the bone that fracture did not occur at their interface but rather in the bone itself when tensile stress was applied to the interface. In contrast, Ti metals subjected to no treatment, only to the H_2SO_4 / HCl acid treatment or only to the heat treatment at 600°C, were encapsulated by fibrous tissue, as shown in **Figures 5A–C** (Kawai et al., 2012).

When the Ti metal plate heat-treated at 600°C after exposure to 5M NaOH solution at 60°C for 24 h was implanted into a rabbit tibia, within 8 weeks it became bonded to the surrounding bone through an apatite layer that formed on the Ti metal surface, as shown in **Figure 6** (Yan et al., 1997). When a rod of the same metal was implanted into the medullary canal of the rabbit femur, it became so tightly bonded to the surrounding bone within 12 weeks that it was not able to be extracted without accompanying bone fragments, as shown in **Figure 7** (Nishiguchi et al., 2003).

These *in vivo* bone-bonding bioactivity findings of the Ti metals are consistent with the *in vitro* apatite formation in SBF of the Ti metals. This consistency could be interpreted in terms of cell response as follows. The Ti metal able to form the apatite on its surface in SBF forms the apatite on its surface soon after implanted into living body. Once the apatite is formed, osteogenic cells actively differentiate on its surface, as observed in culture experiments of rat bone marrow cells (Nishio et al., 2000) and of mouse calvaria osteoblast (Isaac et al., 2010) on a NaOH- and heat-treated Ti metal. Once the bone matrix is formed by the osteogenic cells, it can be tightly bonded to the apatite on the surface of the Ti metal, as observed for bone nodules, which was produced by cells migrated from the calvaria explant of rat, on a NaOH- and heat-treated Ti metal (Isaac et al., 2009). Recently,

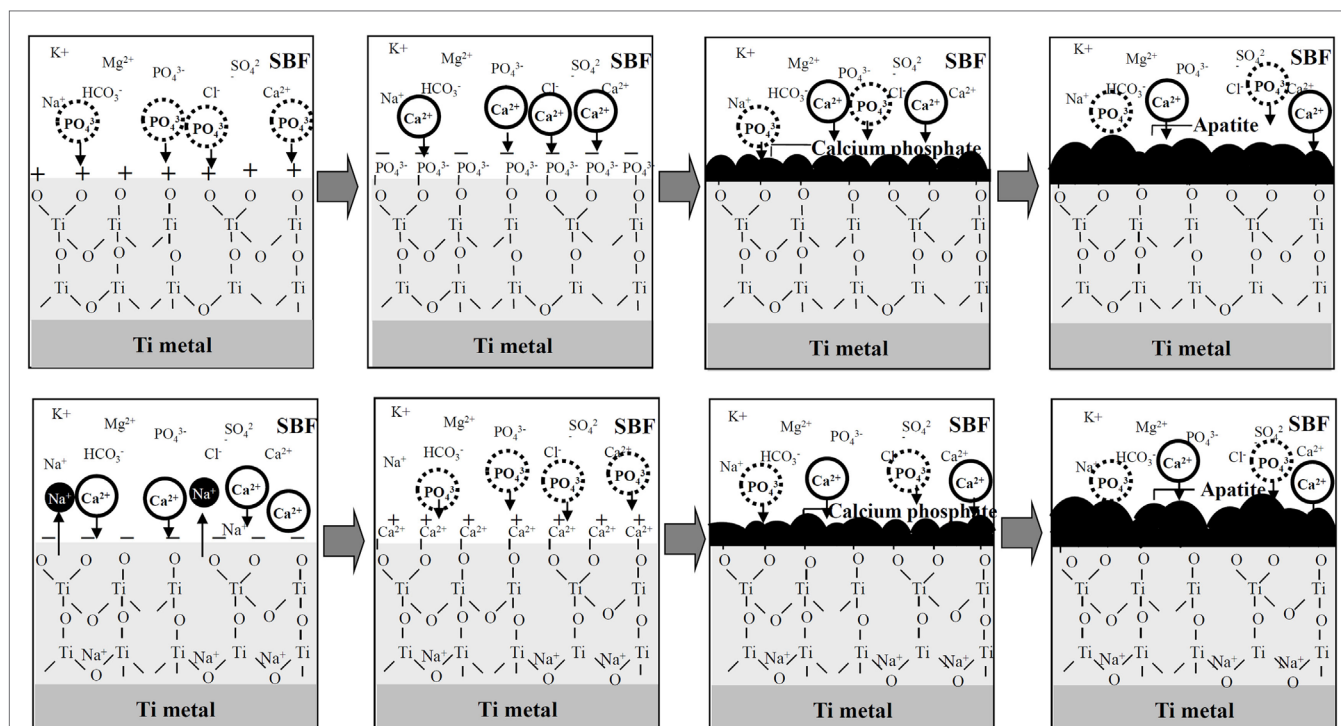


FIGURE 4 | Process of apatite formation on Ti metals heat-treated after exposure to strong acid solutions (top), and to strong alkali solutions (bottom). Reproduced from Pattanayak et al. (2012) with permission The Royal Society.

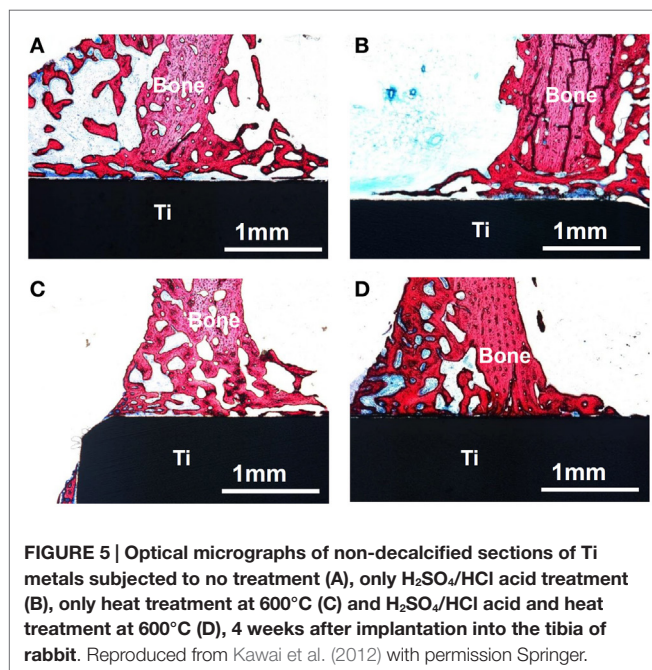


FIGURE 5 | Optical micrographs of non-decalcified sections of Ti metals subjected to no treatment (A), only H₂SO₄/HCl acid treatment (B), only heat treatment at 600°C (C) and H₂SO₄/HCl acid and heat treatment at 600°C (D), 4 weeks after implantation into the tibia of rabbit. Reproduced from Kawai et al. (2012) with permission Springer.

active proliferation and differentiation of osteoblast and multifocal nodule formation on the NaOH- and heat-treated Ti metal were observed for the Ti metal implanted into mouse by using fluorescent osteoblast *in vivo* (Tsukanaga et al., 2013).

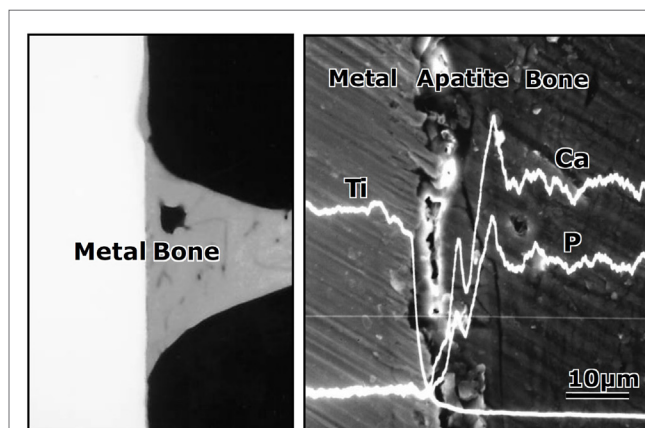


FIGURE 6 | Contact radiomicrograph (left hand) and SEM photograph (right hand) of Ti metal heat-treated after exposure to NaOH solution at its interface with the bone, 8 weeks after implantation into the tibia of rabbits. Reproduced from Yan et al. (1997) with permission John Wiley and Sons.

It is apparent from these results that the natural Ti metal is unable to bond to living bone. When it is subjected to only the acid treatment or only the heat treatment, it also cannot bond to living bone (Kawai et al., 2012). However, it does bond to living bone, when it is heat-treated after exposure to strong acid or alkali solution so that a certain kind of thin ceramic layer is grown on its surface.

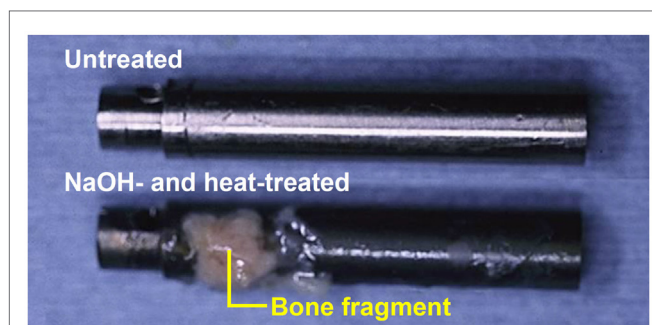


FIGURE 7 | Titanium metal rod untreated (top) and heat-treated after exposure to NaOH solution (bottom), both of which were pulled out after implanted into medullary canal of a rabbit for 12 weeks, after Nishiguchi et al. (2003).

CLINICAL APPLICATIONS OF THE BONE-BONDING BIOACTIVE Ti MEAL PREPARED BY SIMPLE CHEMICAL AND HEAT TREATMENTS

It is well known that commercial dental implants may be subjected to $\text{H}_2\text{SO}_4/\text{HCl}$ acid solution treatment in order to produce micrometer-scale roughness on their surface (Coelho et al., 2009). This treatment can promote mechanical interlocking of the dental implants with the surrounding bone. However, this treatment cannot make direct bonding of the dental implants to the surrounding bone.

The present result indicates that such implants can be induced to bond to bone when subjected to heat treatment after acid treatment, since a rutile layer capable of forming apatite in the living body is formed on its surface by the heat treatment. Such dental implants are expected to remain stably fixed over a long period of time after implantation.

It is expected that once a porous Ti metal layer has been produced on the surface of a Ti-based alloy, for example by a plasma spray method, and then subjected to the NaOH and heat treatments, such a medical device will be stably fixed to the surrounding bone, since the surrounding bone comes into direct contact with the porous Ti metal and grows into the pores (Kim et al., 2000c; Nishiguchi et al., 2001). Such a bone-bonding bioactive porous Ti metal layer was produced on the surface of acetabular shell and femoral stem of a total artificial hip joint made of Ti-6Al-2Nb-Ta alloy, as shown in **Figure 8**. This hip joint has been clinically used in more than 15,000 patients in Japan since 2007 (Kawanae et al., 2009). The result was confirmed by two implants retrieved 2 weeks and 8 years after implantation, respectively, due to femoral fracture and infection that the implant surface had become intimately integrated with newly grown bone as early as 2 weeks after implantation and had maintained this integrity for a minimum of 8 years (So et al., 2013).

Currently, hydroxyapatite is commonly coated on commercial artificial hip joints. For example, hydroxyapatite is coated by a flame-spray method on the rough Ti metal layer produced by the

arc-spray method on the surface of the Ti-15Mo-5Zr-3Al alloy in one such case. Recently, Kawai et al. tried to apply the NaOH and heat treatments on the surface of the rough Ti metal layer produced on the Ti-5Mo-15Zr-3Al alloy by the arc-spray method for comparison. The rectangular plates subjected to the NaOH and heat treatments and hydroxyapatite coating, as well as that untreated were implanted into the tibia of a rabbit. Consequently, it was found that the bonding strength of the implants to the bone was not increased by the hydroxyapatite coating, but it was considerably increased by the NaOH and heat treatments as early as 4 weeks after implantation, and this increase was maintained even after 16 weeks. The lack of a positive effect of the hydroxyapatite coating was attributed to deterioration of the hydroxyapatite layer in the body (Kawai et al., 2015).

It is expected that this kind of simple chemical and heat treatment will also be useful for inducing bone-bonding bioactivity in different kinds of Ti metal implants in the orthopedic and dental fields. However, it will be ineffective for many kinds of Ti-based alloys. This treatment must be modified for such Ti-based alloys.

MODIFICATION OF THE ALKALI AND HEAT TREATMENT

Ti-based alloys such as Ti-6Al-4V, Ti-6Al-2Nb-Ta, and Ti-15Mo-5Zr-3Al exhibit much great mechanical strength and fracture toughness, and hence they are also widely used as implants in orthopedics and dentistry.

The simple heat treatment after exposure to the NaOH solution described above is also effective for these conventional Ti-based alloys in inducing bone-bonding bioactivity (Kim et al., 1996; Ueno et al., 2011). In these cases, alloying elements such as Al, V, and Mo are easily and selectively released during the NaOH treatment, and only the sodium titanate and rutile are precipitated on the surfaces of the alloys after the heat treatment, similar to the pure Ti metal (Kim et al., 1999; Kim et al., 2000a,b). Consequently, they come to exhibit the bone-bonding bioactivity as the result of this simple chemical and heat treatment (Nishiguchi et al., 1999).

On the other hand, Ti-based alloys in the system Ti-Zr-Nb-Ta, which are free of elements suspected of cytotoxicity such as Al and V, were recently developed. Some of these alloys exhibit not only high mechanical strength, but also low elastic modulus close to that of human bone. They are thus expected to be more useful as implants in orthopedics and dentistry. However, the simple alkali and heat treatment is not effective for these alloys in inducing their bone-bonding bioactivity. The alloying elements such as Zr, Nb, and Ta are not as easily released as Al and V during the NaOH treatment, and considerable amounts of them remain even after the subsequent heat treatment, suppressing Na^+ ion release from the alloys and inhibiting apatite formation in SBF as well as in the body environment (Yamaguchi et al., 2011).

It is well known that Ca^{2+} ion release is more effective for apatite formation than Na^+ ion release. Therefore, it is expected that even these alloys could form the apatite on their surfaces in SBF as well as in the body environment if the sodium titanate on their surfaces were replaced with calcium titanate. However, calcium titanate cannot be formed by the simple chemical and heat

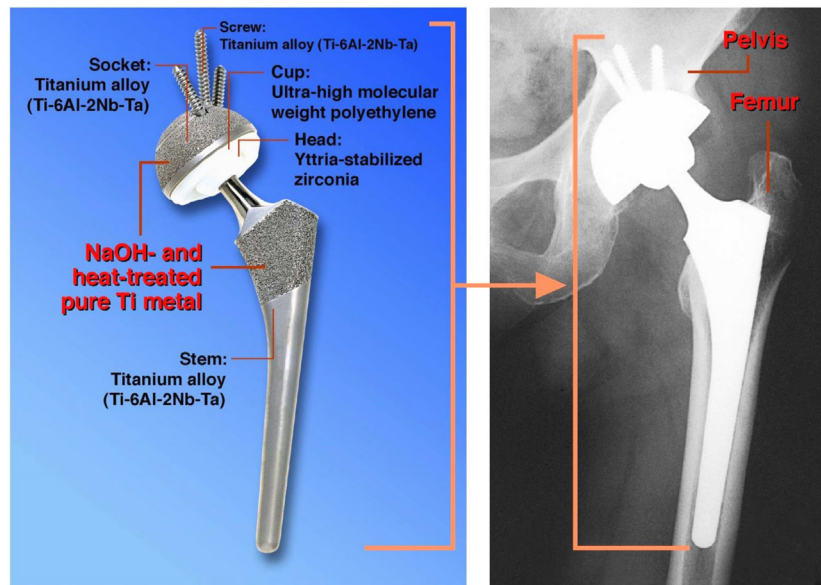


FIGURE 8 | Artificial hip joint, porous Ti metal layer of which was heat-treated after exposure to NaOH solution, after Kawanae et al. (2009).

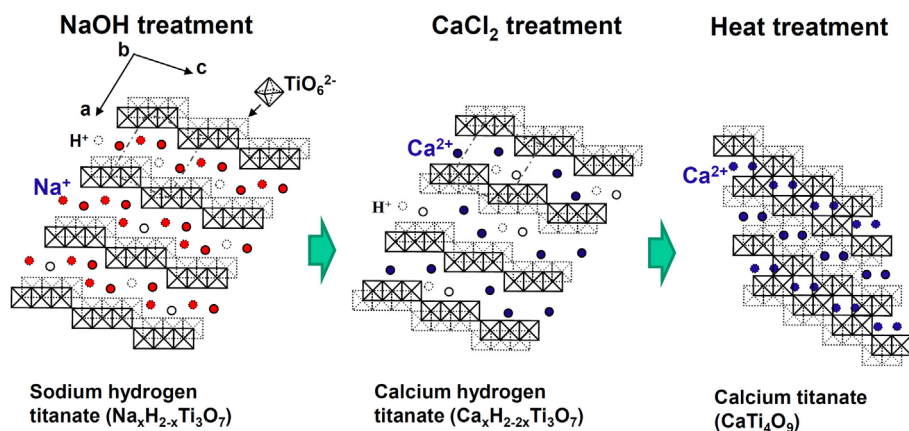


FIGURE 9 | Structures of sodium hydrogen titanate, calcium hydrogen titanate, and calcium titanate projected on a plane perpendicular to the crystallographic *b* axis. Reproduced from Kokubo and Yamaguchi (2015) with permission Elsevier.

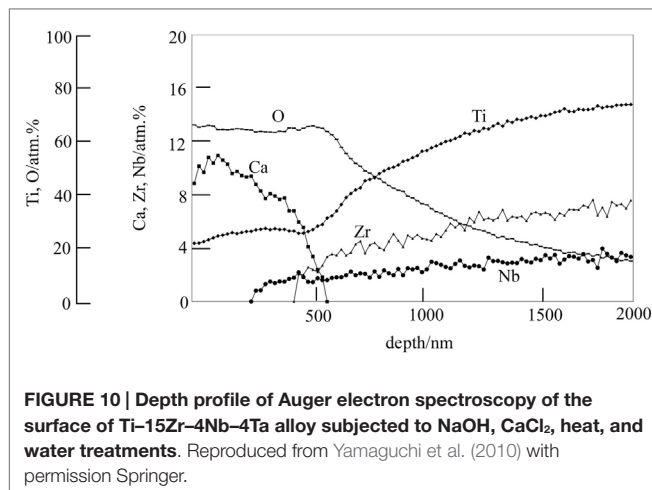
treatment in which the NaOH solution is replaced by $\text{Ca}(\text{OH})_2$ solution, since the solubility of $\text{Ca}(\text{OH})_2$ in water is very low.

Fortunately, the sodium hydrogen titanate that forms on the Ti metal and its alloys by NaOH treatment has a well-developed layered structure, as shown in Figure 9 (Kokubo and Yamaguchi, 2015). It is expected that the Na^+ ions in the layered structure may be completely replaced with the Ca^{2+} ions in the CaCl_2 solution to form a calcium hydrogen titanate. This phase might be transformed into calcium titanate by the subsequent heat treatment. When the Ti metal and its alloys were heat-treated after exposure to the NaOH and subsequent exposure to 100 mM CaCl_2 solution at 40°C for 24 h, they formed the calcium titanate on their surfaces, as expected. However, the resulting products

did not exhibit apatite formation on their surfaces in SBF. This was attributed to the extremely low release rate of the Ca^{2+} ions from the calcium titanate because of its dense structure (Kizuki et al., 2010).

Therefore, they were finally soaked in a hot water, in order to increase the release rate of the Ca^{2+} ions by partly replacing the Ca^{2+} ions at the surface of the calcium titanate with H_3O^+ ions in the water, as shown in Figure 10 (Yamaguchi et al., 2010). As a result, the Ti-based alloys in the system Ti-Zr-Nb-Ta, as well as the pure Ti metal, formed the apatite on their surfaces in SBF (Kizuki et al., 2010; Yamaguchi et al., 2010, 2012).

When the Ti-based alloys as well as the pure Ti metal that had been subjected to this modified alkali and heat treatment



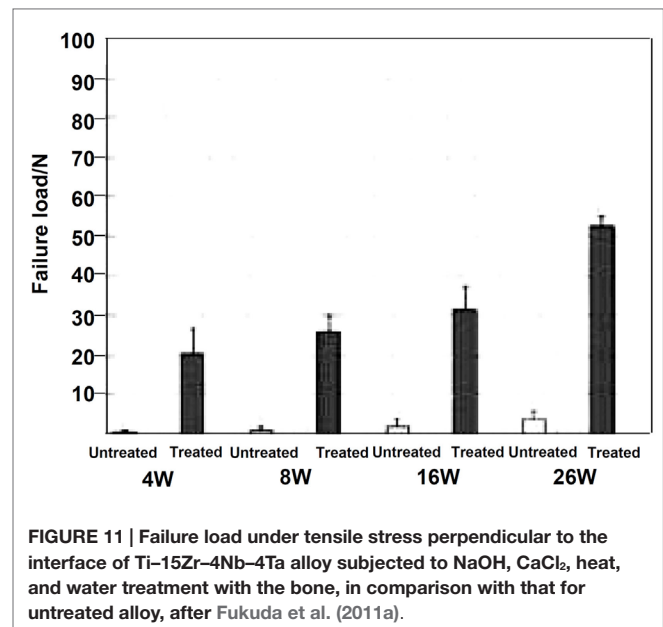
for forming the Ca-deficient calcium titanate on their surfaces were implanted into the tibia of a rabbit, they came into direct contact with the surrounding bone without any intervention of fibrous tissue at their interface within 16 weeks (Fukuda et al., 2011a; Tanaka et al., 2014). When a tensile stress was applied to the interface of the Ti-15Zr-4Nb-4Ta alloy with the bone, the load required for producing the fracture was much higher for the alloy subjected to the modified alkali and heat treatment than the untreated alloy, as shown in **Figure 11**, and this difference increased with an increasing period of time after implantation (Fukuda et al., 2011a).

It should be noted here that this modified alkali and heat treatment that forms Ca-deficient calcium titanate has some advantages over the simple alkali and heat treatment not only for the alloys but also for pure Ti metal, in terms of insensitivity to contamination of a NaOH reagent, and humidity in an environment. In general, even so-called high purity NaOH reagent contains small amount of the calcium ions as an impurity. The calcium ions are concentrated on the Ti metal surface during the course of NaOH solution treatment, to give calcium-contaminated sodium titanate after the heat treatment. The incorporated calcium ions suppress apatite formation of the surface of Ti metal in SBF as well as in the living body by inhibiting the Na⁺ ions release, and hence decrease bone-bonding ability (Kizuki et al., 2013).

On the other hand, when the Ti metal and its alloys are stored in a humid environment, the Na⁺ ions in the sodium titanate are liable to be released via exchange with the H₃O⁺ ions in the moisture, thus decreasing the Na⁺ ions in the sodium titanate decreasing the bone-bonding ability (Kawai et al., 2010). Ti metal and its alloys subjected to the modified alkali and heat treatment so as to form the Ca-deficient calcium titanate on their surfaces have no such problems with regard to these matters.

EXTENSION OF MODIFIED ALKALI AND HEAT TREATMENT

Certain ions such as Mg (Park et al., 2012), Sr (Bonnelye et al., 2008), and Zn (Alvarez et al., 2010) are known to promote bone



growth. It is expected that if these ions are slowly released from the bone-bonding bioactive Ti metal and its alloys, they can be bonded to the surrounding bone in a short period of time after implantation, since the surrounding bone grows to the apatite layer on the surface of the Ti metal in a short period. These ions can be incorporated into the Ca-deficient calcium titanate layer on the surface of the Ti metal and its alloys without disturbing their apatite-forming abilities by adding these ions into the CaCl₂ solution of the second treatment, and/or into the hot water of the final treatment of the modified alkali and heat treatments (Yamaguchi et al., 2013a,b, 2014). For example, when the Ti metal is heat-treated at 600°C after exposure to a mixed solution of 50 ml CaCl₂ and 50 ml SrCl₂ at 40°C for 24 h following to the NaOH solution, and then soaked in 1M SrCl₂ solution at 80°C for 24 h, the Sr²⁺ ions are incorporated into the Ca-deficient calcium titanate, as shown by depth profile of XPS near the surface of the Ti metal in **Figure 12** (Yamaguchi et al., 2014). It was confirmed that this Ti metal can form the apatite on its surface in SBF and that the Sr²⁺ ions are slowly released into the phosphate-buffered saline at 36.5°C (Yamaguchi et al., 2014).

The silver ion, which is known to exhibit antibacterial activity (Chen et al., 2008), also can be incorporated into the Ca-deficient calcium titanate layer of the Ti metal by replacing the final hot water of the modified alkali and heat treatment with 1M AgNO₃ solution (Kizuki et al., 2014). It was confirmed that this Ti metal also forms the apatite on its surface in SBF and that the Ag⁺ ions are slowly released into fetal bovine serum. This Ti metal exhibited a strong antibacterial effect against *Staphylococcus aureus*, as expected (Kizuki et al., 2014).

It is apparent from these results that bone-bonding bioactive Ti metal and its alloys possessing various functions can be obtained by forming Ca-deficient calcium titanate containing various ions on their surfaces by the modified alkali and heat treatment.

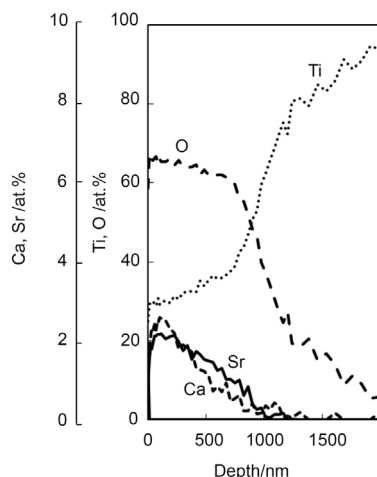


FIGURE 12 | Depth profile of XPS of Ti metal subjected to NaOH, $\text{CaCl}_2/\text{SrCl}_2$, heat, and SrCl_2 treatments. Reproduced from Yamaguchi et al. (2014) with permission Elsevier.

MODIFICATION OF THE ACID AND HEAT TREATMENT

The simple acid and heat treatment described above is not effective for many of the Ti-based alloys in inducing bone-bonding bioactivity, since the alloying elements are generally hardly released during the acid treatment and are enriched on the surface of the alloys during the subsequent heat treatment. For example, Al and V of the Ti-6Al-4V alloy are hardly released during the first $\text{H}_2\text{SO}_4/\text{HCl}$ acid treatment, and are segregated on the surface of the alloy during the subsequent heat treatment at 600°C . Consequently, the Ti-6Al-4V alloy subjected to the simple acid and heat treatment does not form the apatite on its surface in SBF (Yamaguchi et al., 2015).

On the other hand, the alloying elements Zr, Nb, and Ta are generally more or less selectively released from the surface of the Ti-based alloys during the NaOH treatment. Therefore, if the Ti-based alloys are subjected to the acid and heat treatment after the NaOH treatment, they form titanium oxide on their surfaces to become able to form the apatite on their surfaces in SBF and the body environment. For example, if the Ti-15Zr-4Nb-4T alloy is soaked in 0.5 or 50 mM HCl solution at 40°C for 24 h after the NaOH treatment and then subjected to heat treatment at 600°C for 1 h, it forms anatase and rutile on its surface and exhibits apatite formation on its surface in SBF (Yamaguchi et al., 2011). The acid and heat treatment after the NaOH treatment gives stable apatite formation in SBF compared with the simple alkali and heat treatment, even in the case of pure Ti metal. Its apatite-forming ability increases with an increasing concentration of the acid solution (Pattanayak et al., 2009a, 2011a,b).

This modified acid and heat treatment as well as the simple acid and heat treatment are especially useful when they are applied to porous Ti metal.

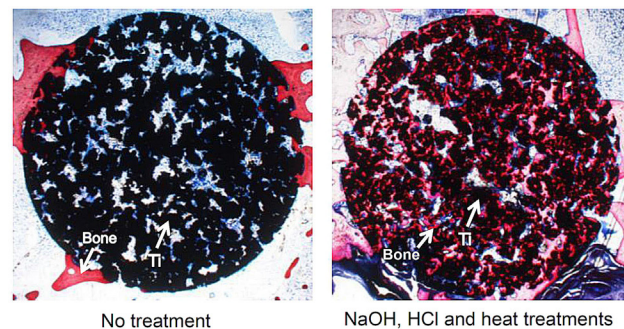


FIGURE 13 | Bone formation in porous Ti metals subjected to no treatment and NaOH, HCl, and heat treatments, 26 weeks after implantation into rabbit femur, after Takemoto et al. (2005) and Tanaka et al. (2009).

APPLICATION OF THE ACID AND HEAT TREATMENT TO POROUS Ti METAL

Natural bone consists of a cancellous portion and a cortical portion. The cancellous portion consists of three dimensionally connected pores. If such a porous structure is introduced into the Ti metal, its elastic modulus can be decreased down to the level of human bone, making the Ti metal mechanically compatible with the surrounding bone. In addition, the Ti metal with such a porous structure can be easily fixed to the surrounding bone by bone ingrowth into the pores.

Ti metal with a porous structure that is well controlled in terms of the size and arrangement of the pores can be fabricated by sintering with metal powder containing volatile substances (Pattanayak et al., 2009b), as well as by 3D-printing methods such as a selective melting of the metal powders with a laser or electron beam (Pattanayak et al., 2011c and Fukuda et al., 2011b).

However, bone ingrowth into the pores is limited to only a shallow region of the porous structure for the naturally porous Ti metal, as shown in **Figure 13** (Takemoto et al., 2005). In contrast, bone penetrates into a deeper region of the porous Ti metal subjected to the chemical and heat treatments for inducing the bone-bonding bioactivity described above, as shown in **Figure 13** (Tanaka et al., 2009; Kawai et al., 2013).

It should be noted here that the bioactive porous Ti metal forms bone tissue in the porous structure not only in the bone defect, but also in muscle, as shown in **Figure 14** (Fujibayashi et al., 2004; Takemoto et al., 2006). The former bone formation in bone defect is called osteoconduction, whereas the latter ectopic bone formation in muscle is called osteoinduction. It is interesting to note that the bioactive porous Ti metal forming the rutile on its surface by the simple (Kawai et al., 2014) or modified acid and heat treatment exhibit active osteoinductivity, while the bioactive porous Ti metal forming the sodium titanate or Ca-deficient calcium titanate on its surface by the simple or modified alkali and heat treatment exhibit only slight or no osteoinductivity. The latter poor osteoinductivity might be attributed to the adverse effect of the released Na^+ or Ca^{2+} ions on the activity of living cells in the narrow space of the pores by increasing the local pH in the environment.

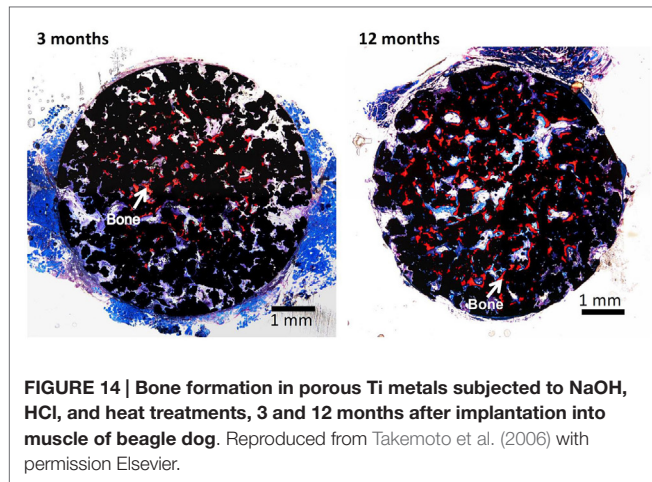


FIGURE 14 | Bone formation in porous Ti metals subjected to NaOH, HCl, and heat treatments, 3 and 12 months after implantation into muscle of beagle dog. Reproduced from Takemoto et al. (2006) with permission Elsevier.

It is expected that the osteoconductive and osteoinductive porous Ti metals prepared by the simple or modified acid and heat treatments will be used for various applications in orthopedics and dentistry.

CLINICAL APPLICATIONS OF OSTEOCONDUCTIVE AND OSTEOINDUCTIVE POROUS Ti METAL PREPARED BY ACID AND HEAT TREATMENT

Porous Ti metals with a three-dimensional porous structure analogous to human cancellous bone are prepared by the sintering or 3D-printing of metal powders, as described above. They exhibit osteoconductivity as well as osteoinductivity when subjected to simple or modified acid and heat treatment. These porous Ti metals can be used as important bone substitutes in many applications.

For example, a porous Ti metal that is 50% in porosity and 300 μm in average pore size prepared by the sintering method was subjected to 0.5 mM HCl and heat treatment after the NaOH treatment had formed anatase and rutile on its surface. It was implanted into a canine for spinal interbody fusion (Takemoto et al., 2007). Based on this successful result, it was subjected to clinical trials as a spinal fusion device in five human patients between November 2008 and June 2009, as shown in **Figure 15** (Fujibayashi et al., 2011). Conventional spinal fusion devices need an autograft for fixation to the surrounding bone, since they cannot bond to living bone, whereas the present device can be fixed without an autograft, as it does bond to living bone. All of the clinical cases to date have resulted in a successful outcome.

REFERENCES

Alvarez, K., Fukuda, M., and Yamamoto, O. (2010). Titanium implants after alkali heating treatment with a $[\text{Zn}(\text{OH})_4]_2$ -complex: analysis of interfacial bond strength using push-out tests. *Clin. Implant Dent. Relat. Res.* 12, e114–e125. doi:10.1111/j.1708-8208.2010.00278.x

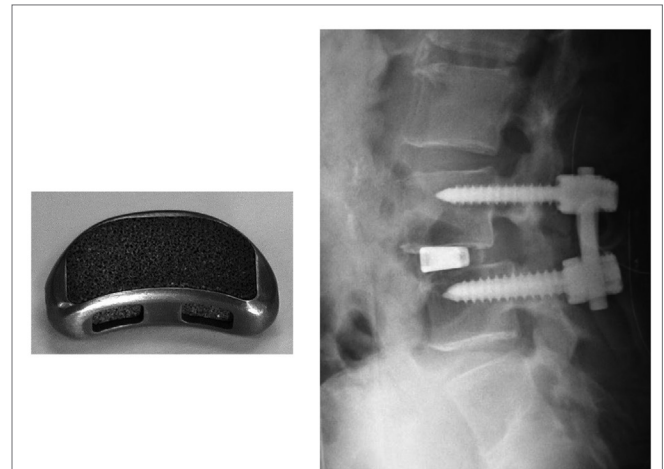


FIGURE 15 | Spinal fusion device of porous Ti metal subjected to NaOH, HCl and heat treatments (left hand side) and its clinical application (right hand side). Reproduced from Fujibayashi et al. (2011) with permission Springer.

CONCLUSION

A positively charged titanium oxide layer was grown on Ti metal, when it was heat-treated after exposure to strong acid solution, whereas negatively charged sodium titanate layer was grown on Ti metal, when it was heat-treated after exposure to strong alkali solution. Both the resultant products formed an apatite on their surfaces in a SBF and bonded to the living bone in the rabbit tibia. The latter product was successfully clinically applied to artificial hip joint.

A negatively charged calcium-deficient calcium titanate layer was formed on Ti metal and its alloys, when they were heat-treated after exposure to NaOH and CaCl_2 solutions and finally soaked in a hot water. They also formed the apatite on their surfaces in SBF and tightly bonded to the living bone. Bone growth promoting ions such as Mg, Sr, and Zn, as well as antibacterial ions such as Ag were incorporated into the calcium titanate surface layers, in order to be slowly released in the living body.

Porous Ti metal grown with the positively charged titanium oxide on its surface exhibited not only osteoconduction but also osteoinduction. The resultant product is being subjected to clinical trials as a spinal fusion device.

This kind of novel bioactive materials exhibiting various kinds of biological functions as well as intrinsic high mechanical strength likely to play an increasingly more important role in repairing damaged bone tissues.

Armitage, D. A., Mihoc, R., Tate, T. J., McPhail, D. S., Chater, R., Hobkirk, J. A., et al. (2007). The oxidation of calcium implanted titanium in water: a depth profiling study. *Appl. Surf. Sci.* 253, 4085–4093. doi:10.1016/j.apsusc.2006.09.006

Bjursten, L. M., Rasmusson, L., Oh, S., Smith, G. C., Brammer, K. S., and Jin, S. (2010). Titanium dioxide nanotubes enhance bone bonding in vivo. *J. Biomed. Mater. Res.* 92A, 1218–1224. doi:10.1002/jbm.a.32463

- Bonnelye, E., Chabadel, A., Saltel, F., and Jurdic, P. (2008). Dual effect of strontium ranelate: simulation of osteoblast differentiation and inhibition of osteoclast formation and resorption in vitro. *Bone* 42, 129–138. doi:10.1016/j.bone.2007.08.043
- Chen, X.-B., Li, Y. C., Plessis, J. D., Hodgson, P. D., and Wen, C. (2009). Influence of calcium ion deposition on apatite-inducing ability of porous titanium for biomedical applications. *Acta Biomater.* 5, 1808–1820. doi:10.1016/j.actbio.2009.01.015
- Chen, Y. K., Zheng, X. B., Xie, Y. T., Ding, C. X., Ruan, H. J., and Fan, C. Y. (2008). Anti-bacterial and cytotoxic properties of plasma sprayed silver-containing HA coating. *J. Mater. Sci. Mater. Med.* 19, 3603–3609. doi:10.1007/s10856-008-3529-8
- Coelho, P. G., Granjeiro, J. M., Romanos, G. E., Suzuki, M., Silva, N. R. F., Cardaropoli, G., et al. (2009). Basic research methods and current trends of dental implant surfaces. *J. Biomed. Mater. Res. B Appl. Biomater* 88B, 579–596. doi:10.1002/jbm.b.31264
- Cooper, L. F., Zhou, Y., Takebe, J., Guo, J., Abron, A., Holmen, A., et al. (2006). Fluoride modification effects on osteoblast behavior and bone formation at TiO₂ grit-blasted c.p. titanium endosseous implants. *Biomaterials* 27, 926–936. doi:10.1016/j.biomaterials.2005.07.009
- Diefenback, M., Muckley, T., Shrader, C., Schmidt, J., Zankovych, S., Bossert, J., et al. (2011). The effect of plasma chemical oxidation of titanium alloy on bone-implant contact in rats. *Biomaterials* 32, 8041–8047. doi:10.1016/j.biomaterials.2011.07.046
- Dong, W., Zhang, T., Epstein, J., Cooney, L., Wang, H., Li, Y., et al. (2007). Multifunctional nanowire bioscaffolds on titanium. *Chem. Mater.* 19, 4454–4459. doi:10.1021/cm070845a
- Ferraris, S., Spriano, S., Pan, G., Venturello, A., Bianchi, C. L., Chiesa, R., et al. (2011). Surface modification of T-6Al-4V alloy for biomineralization and specific biological response: part 1, inorganic modification. *J. Mater. Sci. Mater. Med.* 22, 533–545. doi:10.1007/s10856-011-4246-2
- Fujibayashi, S., Neo, M., Kim, H.-M., Kokubo, T., and Nakamura, T. (2004). Osteoinduction of porous bioactive titanium metal. *Biomaterials* 25, 443–450. doi:10.1016/S0142-9612(03)00551-9
- Fujibayashi, S., Takemoto, M., Neo, M., Matsushita, T., Kokubo, T., Doi, K., et al. (2011). A novel synthetic material for spinal fusion: a prospective clinical trial of porous bioactive titanium metal for lumbar interbody fusion. *Eur. Spine J.* 20, 1486–1495. doi:10.1007/s00586-011-1728-3
- Fukuda, A., Takemoto, M., Saito, T., Fujibayashi, S., Neo, M., Yamaguchi, S., et al. (2011a). Bone bonding bioactivity of Ti metal and Ti-Zr-Nb-Ta alloys with Ca ions incorporated on their surfaces by simple chemical and heat treatments. *Acta Biomater.* 7, 1379–1386. doi:10.1016/j.actbio.2010.09.026
- Fukuda, A., Takemoto, M., Saito, T., Fujibayashi, S., Neo, M., Pattanayak, D. K., et al. (2011b). Osteoinduction of porous Ti implants with a channel structure fabricated by selective laser melting. *Acta Biomater.* 7, 2327–2336. doi:10.1016/j.actbio.2011.01.037
- Gold, J. M., Schmidt, M., and Steinmann, S. G. (1989). XPS study of amino acid adsorption to titanium surfaces. *Helv. Phys. Acta* 62, 246–249.
- Hacking, S. A., Tanzer, M., Harvey, E. J., Krygier, J. J., and Bobyn, J. D. (2002). Relative contribution of chemistry and topography to the osseointegration of hydroxyapatite coating. *Clin. Orthop. Relat. Res.* 405, 24–38. doi:10.1097/00003086-200212000-00004
- Isaac, J., Galtayries, A., Kizuki, T., Kokubo, T., Berdal, A., and Sautier, J.-M. (2010). Bioengineered titanium surfaces affect the gene-expression and phenotypic response of osteoprogenitor cells derived from mouse calvarial bones. *Eur. Cell. Mater.* 20, 178–196.
- Isaac, J., Loty, S., Hamdan, A., Kokubo, T., Kim, H.-M., Berdal, A., et al. (2009). Bone-like tissue formation on a biomimetic titanium surface in an explant model of osteoconduction. *J. Biomed. Mater. Res.* 89A, 585–593. doi:10.1002/jbm.a.31993
- Karthega, M., and Rajendran, N. (2010). Hydrogen peroxide treatment on Ti-6Al-4V alloy: a promising surface modification technique for orthopaedic application. *Appl. Surf. Sci.* 256, 2176–2183. doi:10.1016/j.apsusc.2009.09.069
- Kawai, T., Kizuki, T., Takadama, H., Matsushita, T., Unuma, T., Nakamura, T., et al. (2010). Apatite formation on surface titanate layer with different Na content on Ti metal. *J. Ceram. Soc. Jpn.* 118, 19–24. doi:10.2109/jcersj.2.118.19
- Kawai, T., Takemoto, M., Fujibayashi, S., Akiyama, H., Tanaka, S., Yamaguchi, S., et al. (2014). Osteoinduction on acid and heat treated porous Ti metal samples in canine muscle. *PLoS ONE* 9:e88366. doi:10.1371/journal.pone.0088366
- Kawai, T., Takemoto, M., Fujibayashi, S., Akiyama, H., Yamaguchi, S., Pattanayak, D. K., et al. (2013). Osteoconduction of porous Ti metal enhanced by acid and heat treatments. *J. Mater. Sci. Mater. Med.* 24, 1701–1715. doi:10.1007/s10856-013-4919-0
- Kawai, T., Takemoto, M., Fujibayashi, S., Neo, M., Akiyama, H., Yamaguchi, S., et al. (2012). Bone-bonding properties of Ti metal subjected to acid and heat treatments. *J. Mater. Sci. Mater. Med.* 23, 2981–2992. doi:10.1007/s10856-012-4758-4
- Kawai, T., Takemoto, M., Fujibayashi, S., Tanaka, M., Akiyama, H., Nakamura, T., et al. (2015). Comparison between alkali heat treatment and sprayed hydroxy-apatite coating on thermally-sprayed rough Ti surface in rabbit model: effects on bone bonding ability and osteoconductivity. *J. Biomed. Mater. Res. B* 103B, 1069–1081. doi:10.1002/jbm.b.33281
- Kawanae, K., Ise, K., Goto, K., Akiyama, H., Nakamura, T., Kaneuji, A., et al. (2009). A new cementless total hip arthroplasty with bioactive titanium porous-coating by alkaline and heat treatments: average 4.8-year results. *J. Biomed. Mater. Res. B Appl. Biomater.* 90B, 476–481. doi:10.1002/jbm.b.31309
- Kim, H.-M., Himeno, T., Kawashita, M., Lee, J.-H., Kokubo, T., and Nakamura, T. (2003). Surface potential change in bioactive titanium metal during the process of apatite formation in simulated body fluid. *J. Biomed. Mater. Res. A* 67A, 1305–1309. doi:10.1002/jbm.a.20039
- Kim, H.-M., Miyaji, F., Kokubo, T., and Nakamura, T. (1996). Preparation of bioactive Ti and its alloys via simple chemical surface treatment. *J. Biomed. Mater. Res.* 32, 409–417. doi:10.1002/(SICI)1097-4636(199611)32:3<409::AID-JBM14>3.0.CO;2-B
- Kim, H.-M., Miyaji, F., Kokubo, T., Nishiguchi, S., and Nakamura, T. (1999). Graded surface structure of bioactive titanium prepared by chemical treatment. *J. Biomed. Mater. Res.* 45, 100–107. doi:10.1002/(SICI)1097-4636(199905)45:2<100::AID-JBM4>3.0.CO;2-0
- Kim, H.-M., Takadama, H., Miyaji, F., Kokubo, T., Nishiguchi, S., and Nakamura, T. (2000a). Formation of bioactive functionally graded structure on Ti-6Al-4V alloy by chemical surface treatment. *J. Mater. Sci. Mater. Med.* 11, 555–559. doi:10.1023/A:1008924102096
- Kim, H.-M., Takadama, H., Kokubo, T., Nishiguchi, S., and Nakamura, T. (2000b). Formation of bioactive graded surface structure on Ti-15Mo-5Zr-3Al alloys by chemical treatment. *Biomaterials* 21, 353–358. doi:10.1016/S0142-9612(99)00190-8
- Kim, H.-M., Kokubo, T., Fujibayashi, S., Nishiguchi, S., and Nakamura, T. (2000c). Bioactive macroporous titanium layer on titanium substrate. *J. Biomed. Mater. Res.* 52, 553–557. doi:10.1002/1097-4636(20001205)52:3<553::AID-JBM14>3.0.CO;2-X
- Kizuki, T., Matsushita, T., and Kokubo, T. (2014). Antibacterial and bioactive calcium titanate layers formed on Ti metal and its alloys. *J. Mater. Sci. Mater. Med.* 25, 1737–1746. doi:10.1007/s10856-014-5201-9
- Kizuki, T., Takadama, H., Matsushita, T., Nakamura, T., and Kokubo, T. (2010). Preparation of bioactive Ti metal surface enriched with calcium ions by chemical treatment. *Acta Biomater.* 6, 2836–2842. doi:10.1016/j.actbio.2010.01.007
- Kizuki, T., Takadama, H., Matsushita, T., Nakamura, T., and Kokubo, T. (2013). Effect of Ca contamination on apatite formation in a Ti metal subjected to NaOH and heat treatments. *J. Mater. Sci. Mater. Med.* 24, 635–644. doi:10.1007/s10856-012-4837-6
- Kokubo, T. (2008). *Bioceramics and Their Clinical Applications*. Cambridge: Woodhead.
- Kokubo, T., Pattanayak, D. K., Yamaguchi, S., Takadama, H., Matsushita, T., Kawai, T., et al. (2010). Positively charged bioactive charged bioactive Ti metal prepared by simple chemical and heat treatments. *J. R. Soc. Interface* 7, S503–S513. doi:10.1098/rsif.2010.0129.focus
- Kokubo, T., and Takadama, H. (2006). How useful is SBF in predicting in vivo bone bioactivity? *Biomaterials* 15, 2907–2915. doi:10.1016/j.biomaterials.2006.01.017
- Kokubo, T., and Yamaguchi, S. (2015). “Biomimetic surface modification of metallic biomaterials,” in *Surface Coating and Modification of Metallic Biomaterials*, ed. Wen C. (Cambridge: Woodhead), 219–246.
- Lee, M.-H., Park, H.-S., Min, K.-S., Ahn, S.-G., Park, J.-M., Song, K.-Y., et al. (2007). Evaluation of in vitro tests for surface-modified titanium by H₂SO₄ and H₂O₂ treatment. *Met. Mater. Int.* 13, 109–115. doi:10.1007/BF03027560
- Leeuwenburgh, S. C. G., Wolke, J. G. C., Jansen, J. A., and de Groot, K. (2008). “Calcium phosphate coatings,” in *Bioceramics and Their Clinical Applications*, ed. Kokubo T. (Cambridge: Woodhead), 464–484.

- Li, P., Ohtsuki, C., Kokubo, T., Nakanishi, K., Soga, N., and de Groot, K. (1994). The role of hydrated silica, titania, and alumina in inducing apatite on implants. *J. Biomed. Mater. Res.* 28, 7–15. doi:10.1002/jbm.b.820280103
- Li, Y., Zou, S., Wang, D., Feng, G., Bao, C., and Hu, J. (2010). The effect of hydrofluoric acid treatment on titanium implant osseointegration in ovariectomized rats. *Biomaterials* 31, 3266–3273. doi:10.1016/j.biomaterials.2010.01.028
- Liu, X., Zhao, Z., and Leng, Y. (2007). Biomimetic calcium phosphate coatings on nitric-acid-treated titanium surfaces. *Mater. Sci. Eng. C* 27, 700–708. doi:10.1016/j.msec.2006.06.030
- Minagar, S., Wang, J., Barndt, C. C., Ivanova, E. P., and Wen, C. (2013). Cell response of anodized nanotubes on titanium and titanium alloys. *J. Biomed. Mater. Res. A* 101A, 2726–2739. doi:10.1002/jbm.a.34575
- Nayab, S.N., Jones, F. H., and Olsen, I. (2007). Enhancement of Effects of calcium ion-implantation of titanium on bone cell function in vitro. *J. Biomed. Mater. Res. A* 83A, 292–302. doi:10.1002/jbm.a.31218
- Nishiguchi, S., Fujibayashi, S., Kim, H.-M., Kokubo, T., and Nakamura, T. (2003). Biology of alkali- and heat-treated titanium implants. *J. Biomed. Mater. Res. A* 67A, 26–35. doi:10.1002/jbm.a.10540
- Nishiguchi, S., Kato, H., Fujita, H., Kim, H.-M., Miyaji, F., Kokubo, T., et al. (1999). Enhancement of Bone-bonding strengths of titanium alloy implants by alkali and heat treatments. *J. Biomed. Mater. Res. (Appl. Biomater.)* 48, 689–696. doi:10.1002/(SICI)1097-4636(1999)48:5<689::AID-JBM13>3.0.CO;2-C
- Nishiguchi, S., Kato, H., Fujita, H., Oka, M., Kim, H.-M., Kokubo, T., et al. (2001). Titanium metals form direct bonding to bone after alkali and heat treatments. *Biomaterials* 22, 2525–2533. doi:10.1016/S0142-9612(00)00443-9
- Nishio, K., Neo, M., Akiyama, H., Nishiguchi, S., Kim, H.-M., Kokubo, T., et al. (2000). The effect of alkali- and heat-treated titanium and apatite-formed titanium on osteoblastic differentiation of bone marrow cells. *J. Biomed. Mater. Res.* 52, 652–661. doi:10.1002/1097-4636(20001215)52:4<652::AID-JBM9>3.0.CO;2-W
- Park, J. B., and Lakes, R. S. (1992). *Biomaterials, An Introduction*, Second Edn. New York, NY: Plenum, 231–236.
- Park, J.-W., Kim, Y.-J., Jang, J.-H., Kwon, T. G., Bae, Y.-C., and Suh, J.-Y. (2010). Effects of phosphoric acid treatment of titanium surface on surface properties, osteoblast response and removal of torque forces. *Acta Biomater.* 6, 1661–1670. doi:10.1016/j.actbio.2009.10.011
- Park, J.-W., Ko, H.-J., Jang, J.-H., Kang, H., and Suh, J.-Y. (2012). Increased new bone formation with a surface magnesium-incorporated deproteinized porcine bone substitute in rabbit calvarial defects. *J. Biomed. Mater. Res. A* 100A, 834–840. doi:10.1002/jbm.a.34017
- Park, J.-W., Park, K. B., and Suh, J.-Y. (2007). Effects of calcium ion incorporation on bone healing of Ti6Al4V alloy implants in rabbit tibia. *Biomaterials* 28, 3306–3313. doi:10.1016/j.biomaterials.2007.04.007
- Pattanayak, D. K., Kawai, T., Matsushita, T., Takadama, H., Nakamura, T., and Kokubo, T. (2009a). Effect of HCl concentrations on apatite-forming ability of NaOH-HCl- and heat-treated titanium metal. *J. Mater. Sci. Mater. Med.* 20, 2401–2411. doi:10.1007/s10856-009-3815-0
- Pattanayak, D. K., Matsushita, T., Ooi, K., Takadama, H., Nakamura, T., and Kokubo, T. (2009b). Effect of oxygen content of porous titanium metal on its apatite-forming ability and compressive strength. *Mater. Sci. Eng. C* 29, 1974–1978. doi:10.1016/j.msec.2009.03.014
- Pattanayak, D. K., Yamaguchi, S., Matsushita, T., and Kokubo, T. (2011a). Effect of heat treatments on apatite-forming ability of NaOH- and HCl-treated titanium metal. *J. Mater. Sci. Mater. Med.* 22, 273–278. doi:10.1007/s10856-010-4218-y
- Pattanayak, D. K., Yamaguchi, S., Matsushita, T., and Kokubo, T. (2011b). Nanostructured positively charged bioactive TiO₂ layer formed on Ti metal by NaOH, acid and heat treatments. *J. Mater. Sci. Mater. Med.* 22, 1803–1812. doi:10.1007/s10856-011-4372-x
- Pattanayak, D. K., Fukuda, A., Matsushita, T., Takemoto, M., Fujibayashi, S., and Sasaki, K. (2011c). Bioactive Ti metal analogous to human cancellous bone: fabrication by selective laser melting and chemical treatments. *Acta Biomater.* 7, 1398–1406. doi:10.1016/j.actbio.2010.09.034
- Pattanayak, D. K., Yamaguchi, S., Matsushita, T., Nakamura, T., and Kokubo, T. (2012). Apatite-forming ability of titanium in terms of pH of the exposed solution. *J. R. Soc. Interface* 9, 2145–2155. doi:10.1098/rsif.2012.0107
- Rautray, T. R., Narayanan, R., Kwon, T.-Y., and Kim, K.-H. (2010). Surface modification of titanium and titanium alloys by ion implantation. *J. Biomed. Mater. Res. B Appl. Biomater.* 93B, 581–591. doi:10.1002/jbm.b.31596
- Shibata, Y., Suzuki, D., Omori, S., Tanaka, R., Murakami, A., Kataoka, Y., et al. (2010). The characteristics of in vitro biological activity of titanium surfaces anodically oxidized in chloride solution. *Biomaterials* 31, 8546–8555. doi:10.1016/j.biomaterials.2010.07.098
- So, K., Kaneuji, A., Matsumoto, T., Matsuda, S., and Akiyama, H. (2013). Is the bone-bonding ability of a cementless total hip prosthesis enhanced by alkaline and heat treatments. *Clin. Orthop. Relat. Res.* 471, 3847–3855. doi:10.1007/s11999-013-2945-3
- Sugino, A., Ohtsuki, C., Tsuru, K., Hayakawa, S., Nakano, T., Okazaki, Y., et al. (2009). Effect of spatial design and thermal oxidation on apatite formation on Ti-15Zr-4Ta-4Nb alloy. *Acta Biomater.* 5, 298–304. doi:10.1016/j.actbio.2008.07.014
- Suh, Y.-T. (2003). The significance of the surface properties of oxidized titanium to the bone response: special emphasis on potential biochemical bonding of oxidized titanium implant. *Biomaterials* 24, 3893–3907. doi:10.1016/S0142-9612(03)00261-8
- Taguchi, T., Muraoka, Y., Matasuyama, H., and Akashi, M. (2001). Apatite coating on hydrophilic polymer-grafted poly(ethylene) films using an alternative soaking process. *Biomaterials* 22, 53–58. doi:10.1016/S0142-9612(00)00162-9
- Takadama, H., Kim, H.-M., Kokubo, T., and Nakamura, T. (2001a). An X-ray photoelectron spectroscopy study of the process of apatite formation on bioactive titanium metal. *J. Biomed. Mater. Res.* 55, 185–193. doi:10.1002/1097-4636(200105)55:2<185::AID-JBM1005>3.0.CO;2-P
- Takadama, H., Kim, H.-M., Kokubo, T., and Nakamura, T. (2001b). TEM-EDX study of mechanism of bone-like apatite formation on bioactive titanium metal in simulated body fluid. *J. Biomed. Mater. Res.* 57, 441–448. doi:10.1002/1097-4636(20011205)57:3<441::AID-JBM1187>3.0.CO;2-B
- Takemoto, M., Fujibayashi, S., Neo, M., So, K., Akiyama, N., Matsushita, T., et al. (2007). A porous bioactive titanium implant for spinal interbody fusion: an experimental study using a canine model. *J. Neurosurg. Spine* 7, 435–443. doi:10.3171/SPI-07/10/435
- Takemoto, M., Fujibayashi, S., Neo, M., Suzuki, J., Kokubo, T., and Nakamura, T. (2005). Mechanical properties and osteoconductivity of porous bioactive titanium. *Biomaterials* 26, 6014–6023. doi:10.1016/j.biomaterials.2005.03.019
- Takemoto, M., Fujibayashi, S., Neo, M., Suzuki, J., Matsushita, T., Kokubo, T., et al. (2006). Osteoinductive porous titanium implants: effect of sodium removal by dilute HCl treatment. *Biomaterials* 27, 2682–2691. doi:10.1016/j.biomaterials.2005.12.014
- Takeuchi, K., Saruwatari, L., Nakamura, H., Yang, J.-M., and Ogawa, T. (2005). Enhanced intrinsic biomechanical properties of osteoblastic mineralized tissue on roughened titanium surface. *J. Biomed. Mater. Res. A* 72A, 296–305. doi:10.1002/jbm.a.30227
- Tanaka, K., Takemoto, M., Fujibayashi, S., Kawanabe, K., Matsushita, T., Kokubo, T., et al. (2009). Long term study of osteoconductivity of bioactive porous titanium metals: effects of sodium removal by dilute HCl treatment. *Key Eng. Mater.* 396–398, 353–356. doi:10.4028/www.scientific.net/KEM.396-398.353
- Tanaka, M., Takemoto, M., Fujibayashi, S., Kawai, T., Yamaguchi, S., Kizuki, T., et al. (2014). Bone bonding ability of a chemically treated low elastic modulus Ti alloy; gum metal. *J. Mater. Sci. Mater. Med.* 25, 635–643. doi:10.1007/s10856-013-5101-4
- Tsukanaga, M., Yamamoto, K., Fujibayashi, S., Pattanayak, D. K., Matsushita, T., Kokubo, T., et al. (2013). Evaluation of bioactivity of alkali- and heat-treated titanium using fluorescent mouse osteoblasts. *J. Bone Miner. Metab.* 32, 660–670. doi:10.1007/s00774-013-0544-8
- Turkan, U., and Guden, M. (2010). The effect of nitric acid surface treatment on CaP deposition on Ti6Al4V open-cell foams in SBF solution. *Surf. Coat. Technol.* 205, 1904–1916. doi:10.1016/j.surfcoat.2010.08.071
- Ueda, M., Ikeda, M., and Ogawa, M. (2009). Chemical-hydrothermal combined surface modification of titanium for improvement of osteointegration. *Mater. Sci. Eng. C* 29, 994–1000. doi:10.1016/j.msec.2008.09.002
- Ueno, T., Tsukimura, N., Yamada, M., and Ogawa, T. (2011). Enhanced bone-integration capability of alkali- and heat-treated nanopolymorphic titanium in micro-to-nanoscale hierarchy. *Biomaterials* 32, 7297–7308. doi:10.1016/j.biomaterials.2011.06.033
- Wang, X.-X., Hayakawa, S., Tsuru, K., and Osaka, A. (2002). Bioactive titania gel layers formed by chemical treatment of Ti substrate with H₂O₂/HCl solution. *Biomaterials* 23, 1353–1357. doi:10.1016/S0142-9612(01)00254-X
- Whiteside, P., Matykina, E., Gough, J. E., Skeldon, P., and Thompson, G. E. (2010). In vitro evaluation of cell proliferation and collagen synthesis on titanium

- following plasma electrolytic oxidation. *J. Biomed. Mater. Res. A* 94A, 38–46. doi:10.1002/jbm.a.32664
- Wu, J.-M., Hayakawa, S., Tsuru, K., and Osaka, A. (2004). Low-temperature preparation of anatase and rutile layers on titanium substrates and their ability to induce vitro apatite deposition. *J. Am. Ceram. Soc.* 87, 1635–1642. doi:10.1111/j.1551-2916.2004.01635.x
- Xie, L., Liao, X., Yin, G., Huang, Z., Yan, D., Yao, D., et al. (2011). Preparation, characterization, in vitro bioactivity, and osteoblast adhesion of multi-level porous titania layer on titanium by two-step anodization treatment. *J. Biomed. Mater. Res. A* 98A, 312–320. doi:10.1002/jbm.a.33120
- Yamaguchi, S., Akeda, K., Murata, K., Takegami, N., Goto, M., Sudo, A., et al. (2015). Chemical and heat treatments for inducing bone-bonding ability of Ti-6Al-4V pedicle screw. *Key Eng. Mater.* 631, 225–230. doi:10.4028/www.scientific.net/KEM.631.225
- Yamaguchi, S., Kizuki, T., Takadama, H., Matsushita, T., Nakamura, T., and Kokubo, T. (2012). Formation of a bioactive calcium titanate layer on gum metal by chemical treatment. *J. Mater. Sci. Mater. Med.* 23, 873–883. doi:10.1007/s10856-012-4569-7
- Yamaguchi, S., Matsushita, T., and Kokubo, T. (2013a). A bioactive Ti metal with a Ca-enriched surface layer releases Mg ions. *RSC Adv.* 3, 11274–11282. doi:10.1039/c3ra00054k
- Yamaguchi, S., Matsushita, T., Nakamura, T., and Kokubo, T. (2013b). Bioactive Ti metal with Ca-enriched surface layer able to release Zn ion. *Key Eng. Mater.* 52, 547–552. doi:10.4028/www.scientific.net/KEM.529-530.547
- Yamaguchi, S., Nath, S., Matsushita, T., and Kokubo, T. (2014). Controlled release of strontium ions from a bioactive Ti metal with a Ca-enriched surface layer. *Acta Biomater.* 10, 2282–2289. doi:10.1016/j.actbio.2014.01.026
- Yamaguchi, S., Takadama, H., Matsushita, T., Nakamura, T., and Kokubo, T. (2009). Cross-sectional analysis of the surface ceramic layer developed on Ti metal by NaOH-heat treatment and soaking in SBF. *J. Ceram. Soc. Jpn.* 117, 1126–1130. doi:10.2109/jcersj2.117.1126
- Yamaguchi, S., Takadama, H., Matsushita, T., Nakamura, T., and Kokubo, T. (2010). Apatite-forming ability of Ti-15Zr-4Nb-4Ta alloy induced by calcium solution treatment. *J. Mater. Sci. Mater. Med.* 21, 439–444. doi:10.1007/s10856-009-3904-0
- Yamaguchi, S., Takadama, H., Matsushita, T., Nakamura, T., and Kokubo, T. (2011). Preparation of bioactive Ti-15Zr-4Nb-4Ta alloy from HCl and heat treatments after an NaOH treatment. *J. Biomed. Mater. Res. A* 97A, 135–144. doi:10.1002/jbm.a.33036
- Yan, W.-Q., Nakamura, T., Kobayashi, M., Kim, H.-M., Miyaji, F., and Kokubo, T. (1997). Bonding of chemically treated titanium implants to bone. *J. Biomed. Mater. Res.* 37, 267–275. doi:10.1002/(SICI)1097-4636(199711)37:2<267::AID-JBM17>3.0.CO;2-B
- Zhang, L., Ayukawa, Y., LeGeros, R. Z., Matsuya, S., Koyano, K., and Ishikawa, K. (2010). Tissue-response to calcium-bonded titanium surface. *J. Biomed. Mater. Res. A* 95A, 33–39. doi:10.1002/jbm.a.32763
- Zhang, P., Zhang, Z., Li, W., and Zhu, M. (2013). Effect of Ti-OH groups on micro-structure and bioactivity of TiO₂ coating prepared by micro-arc oxidation. *Appl. Surf. Sci.* 268, 381–386. doi:10.1016/j.apsusc.2013.09.163
- Zhao, L., Mei, S., Chu, P. K., Zhang, Y., and Wu, Z. (2010). The influence of hierarchical hybrid micro/nano-textured titanium surface with titania nanotubes on osteoblast functions. *Biomaterials* 31, 5072–5082. doi:10.1016/j.biomaterials.2010.03.014
- Zhao, X., Liu, X., and Ding, C. (2005). Acid-induced bioactive titania surface. *J. Biomed. Mater. Res. A* 75A, 888–894. doi:10.1002/jbm.a.30485
- Zhao, X., Liu, X., You, J., Chen, Z., and Ding, C. (2008). Bioactivity and cytocompatibility of plasma-sprayed titania coating treated by sulfuric acid treatment. *Surf. Coat. Technol.* 202, 3221–3226. doi:10.1016/j.surfcoat.2007.11.026
- Zhou, R., Wei, D., Yang, H., Cheng, S., Feng, W., Li, B., et al. (2014). Osseointegration of bioactive microarc oxidized amorphous phase/TiO₂ nanocrystals composite coatings on titanium after implantation into rabbit tibia. *Mater. Sci. Mater. Med.* 25, 1307–1318. doi:10.1007/s10856-014-5154-z
- Zhou, W., Zhou, X., Wu, X., Yuan, L., Shu, Q., Xia, Y., et al. (2007). Plasma-controlled nanocrystallinity and phase composition of TiO₂: a smart way to enhance biomimetic response. *J. Biomed. Mater. Res. A* 81A, 453–464. doi:10.1002/jbm.a.30987

Conflict of Interest Statement: The authors declare that the research was conducted in the absence of any commercial or financial relationships that could be construed as a potential conflict of interest.

Copyright © 2015 Kokubo and Yamaguchi. This is an open-access article distributed under the terms of the Creative Commons Attribution License (CC BY). The use, distribution or reproduction in other forums is permitted, provided the original author(s) or licensor are credited and that the original publication in this journal is cited, in accordance with accepted academic practice. No use, distribution or reproduction is permitted which does not comply with these terms.



Electrophoretic deposition of chitosan/45S5 bioactive glass composite coatings doped with Zn and Sr

OPEN ACCESS

Edited by:

Hae-Won Kim,
Institute of Tissue Regeneration
Engineering, South Korea

Reviewed by:

Ashutosh Goel,
Rutgers, The State University of
New Jersey, USA
Kapil Dev Patel,
Dankook University, South Korea

*Correspondence:

Enrica Verné
enrica.verne@polito.it

[†]Present address:

Marta Miola,
Department of Health Sciences,
Università degli Studi del Piemonte
Orientale "Amedeo Avogadro",
Novara, Italy

Specialty section:

This article was submitted to
Biomaterials, a section of the journal
Frontiers in Bioengineering and
Biotechnology

Received: 11 August 2015

Accepted: 28 September 2015

Published: 19 October 2015

Citation:

Miola M, Verné E, Ciraldo FE,
Cordero-Arias L and Boccaccini AR
(2015) Electrophoretic deposition of
chitosan/45S5 bioactive glass
composite coatings
doped with Zn and Sr.
Front. Bioeng. Biotechnol. 3:159.
doi: 10.3389/fbioe.2015.00159

Marta Miola^{1†}, Enrica Verné^{1*}, Francesca Elisa Ciraldo¹, Luis Cordero-Arias² and Aldo R. Boccaccini²

¹ Department of Applied Science and Technology, Politecnico di Torino, Turin, Italy, ² Department of Materials Science and Engineering, Institute of Biomaterials, University of Erlangen-Nuremberg, Erlangen, Germany

In this research work, the original 45S5 bioactive glass was modified by introducing zinc and/or strontium oxide (6 mol%) in place of calcium oxide. Sr was added for its ability to stimulate bone formation and Zn for its role in bone metabolism, antibacterial properties, and anti-inflammatory effect. The glasses were produced by means of melting and quenching process. SEM and XRD analyses evidenced that Zr and Sr introduction did not modify the glass structure and morphology while compositional analysis (EDS) demonstrated the effective incorporation of these elements in the glass network. Bioactivity test in simulated body fluid (SBF) up to 1 month evidenced a reduced bioactivity kinetics for Zn-doped glasses. Doped glasses were combined with chitosan to produce organic/inorganic composite coatings on stainless steel AISI 316L by electrophoretic deposition (EPD). Two EPD processes were considered for coating development, namely direct current EPD (DC-EPD) and alternating current EPD (AC-EPD). The stability of the suspension was analyzed and the deposition parameters were optimized. Tape and bending tests demonstrated a good coating-substrate adhesion for coatings containing 45S5-Sr and 45S5-ZnSr glasses, whereas the adhesion to the substrate decreased by using 45S5-Zn glass. FTIR analyses demonstrated the composite nature of coatings and SEM observations indicated that glass particles were well integrated in the polymeric matrix, the coatings were fairly homogeneous and free of cracks; moreover, the AC-EPD technique provided better results than DC-EPD in terms of coating quality. SEM, XRD analyses, and Raman spectroscopy, performed after bioactivity test in SBF solution, confirmed the bioactive behavior of 45S5-Sr-containing coating while coatings containing Zn exhibited no hydroxyapatite formation.

Keywords: electrophoretic deposition, bioactive glasses, composite coatings, therapeutic ions, chitosan

INTRODUCTION

Metallic alloys (such as Ti alloys, stainless steel, or Co–Cr alloys) are the materials of choice for bone implants where good mechanical properties and load-carrying ability are required (Niinomi, 2002; Chen and Thouas, 2015). These materials generally are osteointegrated by morphological fixation, i.e., by bone ingrowth on their surface irregularities by press fitting into a bone defect or by cementing the implant with acrylic bone cement. Metallic alloys generally lack osteoinductive properties and, if the bone ingrowth is not effective, they could develop a fast formation of a non-adherent fibrous capsule at the interface which, in turn, can cause bone interfacial loosening and the failure of the implant. A better behavior can be achieved if a bioactive fixation is induced, i.e., a direct chemical bonding with the bone (Drnovšek et al., 2012). For this purpose, the modification of the implant surface with a bioactive coating (i.e., a coating with the ability of forming a biologically active hydroxyapatite layer on its surface) can lead to a significant improvement of its osteointegration. Bioactive glasses (BGs) and glass-ceramics can be successfully used with this purpose (Rahaman et al., 2012; Jones, 2013; Hench, 2015) due to their peculiar ability of inducing bone ingrowth. BGs have been studied and developed during the last 40 years for a vast number of medical applications, including powders, granules, 3D scaffolds, additive for injectable or putty-like bone substitutes, second phases in bone cements, as well as dense coatings on metallic and ceramic substrates (Gerhardt and Boccaccini, 2010; Jones, 2013). Moreover, BG compositions can be easily modified by introducing several elements with therapeutic effect (Mouriño et al., 2012); for example, Ag, Cu, and Ga have been added for their antimicrobial effect, Cu was used for its ability to stimulate angiogenesis and bone (Miola et al., 2014), and Mn for its role in the metabolism of muscle and bone (Rath et al., 2014). Among the investigated elements, also Zn and Sr have drawn the attention of the researchers for their role in bone metabolism and the Zn antibacterial effect (Balamurugan et al., 2007; Gentleman et al., 2010; Jaiswala et al., 2012; Balasubramanian et al., 2015).

Bioactive ceramic coatings can be applied on the bioinert implant surface by means of several methods, such as glazing, enameling, plasma spraying, electrophoretic deposition (EPD), RF-magnetron sputtering, and pulsed laser deposition (Verné, 2012).

Electrophoretic deposition (Besra and Liu, 2007) has been gaining interest in different sectors for its versatility and its cost-effectiveness and EPD of biomaterials is being increasingly investigated (Boccaccini et al., 2010). In particular, the advantages of EPD are its applicability to a wide range of materials (ceramics, polymers, metals, and composites), the use of simple equipment, and the possibility to deposit homogenous thin or thick coatings on substrates with different shapes and dimensions in a matter of minutes. Moreover, EPD can be carried out using aqueous and non-aqueous solvents (Besra and Liu, 2007). Even if water-based EPD implies some problems due to the electrolysis phenomenon, it has been shown that using relatively high voltages and alternating current EPD (AC-EPD), it is possible to obtain high-quality coatings and films (Neirincx et al., 2009; Chávez-Valdez and Boccaccini, 2012).

Since the deposition of pure ceramics can lead to the formation of a brittle coating, they often are codeposited with polymers, especially natural polymers (Cordero-Arias et al., 2014). Among biopolymers, chitosan, a linear, semicrystalline polysaccharide, shows outstanding properties: biocompatibility, the ability to complexes various species such as metal ions, pH-dependant solubility, low cost, and antibacterial activity. Moreover, chitosan is a suitable film-forming polymer that does not require further heat treatment (Croisier and Jérôme, 2013). For these reasons, chitosan is often used in EPD process to realize coatings suitable for orthopedic applications and bone tissue engineering (Pishbin et al., 2011; Cordero-Arias et al., 2013).

In this article, 45S5-base BGs doped with Zn and Sr were combined with chitosan to produce organic/inorganic composite coatings on stainless steel AISI 316L by direct current (DC)-EPD and AC-EPD. The effects of the added ions on the glass and coatings bioactivity combined with the influence of the two EPD methods on coating properties were investigated.

MATERIALS AND METHODS

Glasses Synthesis and Characterization

Zinc oxide (6 mol%), strontium oxide (6 mol%), and both Zn and Sr oxide (ZnO, 3 mol%; SrO, 3 mol%) were added to the original 45S5 BG composition (Hench, 2006) by replacing calcium oxide; the doped glasses were named 45S5-Zn, 45S5-Sr, and 45S5-ZnSr and their compositions are presented in **Table 1**.

All the glasses were produced by means of melting and quenching process: the reactants were accurately mixed and subsequently put in a Pt crucible maintained at 1500°C for 30 min. The melt was then poured in water obtaining a frit, which was dried at room temperature overnight and then milled and sieved to reach a grain size <20 µm.

The influence of Zn and Sr on the glass structure was evaluated by X-ray diffraction (XRD – X’Pert Philips diffractometer), using the Bragg Brentano camera geometry and the Cu-Kα incident radiation; the obtained pattern was analyzed with X’Pert High Score software and the PCPDF data bank. All glasses were also analyzed from the morphological and compositional points of view by Field Emission Scanning Electron Microscopy (FESEM – SUPRATM 40, Zeiss) equipped with energy-dispersive spectroscopy (EDS).

In order to assess the effect of the introduced oxides on the mechanism of bioactivity, glass powders were immersed in SBF (Kokubo and Takadama, 2006) for different time periods (1, 3, 7, 14, 21, and 28 days). The test was performed in an orbital shaker (KS 4000i control, IKA®) at 37°C using a glass powder (mg)/SBF (ml) ratio of 1 and an agitation rate of 120 rpm (Magallanes-Perdomo et al., 2012). At the end of the incubation time, the powders were washed with water and acetone, filtered, dried during 3 h at 60°C, and analyzed by means of XRD and FESEM-EDS. For comparison, the bioactivity of the original 45S5 BG was evaluated for up to 3 days.

Suspension Preparation and Stability Evaluation

Doped glass powders and chitosan were used to produce organic/inorganic composite coatings on AISI 316L stainless steel

substrate (15 mm × 20 mm) by EPD, using both direct current (DC) and alternating current (AC). Suspensions containing 0.5 g/L chitosan (80 kDa, 85% deacetylation, Sigma) and 1.5 g/L glass powders were prepared in a solvent mixture of 1 vol% acetic acid (Sigma-Aldrich), 20 vol% pure water (Purelab Option R7BP, ELGA), and 79 vol% ethanol (VWR). These experimental parameters were chosen according to previously reported results (Grandfield and Zhitomirsky, 2008; Cordero-Arias et al., 2013). Before the EPD process, the suspensions were sonicated with a VWR USC 300 sonicator for 1 h and stirred during 5 min to avoid particle sedimentation. Suspension stability was evaluated by measuring the ζ -potential, using a Zetasizer nano ZS equipment (Malvern Instrument, UK).

Coatings Deposition and Characterization

Different deposition parameters were investigated. For the DC-EPD process, the deposition time varied between 30 s and 2 min and the electric potential in a range of 20–80 V. Regarding the AC-EPD, the voltage varied in the range of 8–20 V and the deposition time between 1 and 2 min; moreover, a frequency range of 4–10 KHz and a duty cycle of 70–80% were considered. For both, DC- and AC-EPD procedures, the distance between the deposition and counter electrodes was kept constant at 10 mm. The choice of the optimal parameters was carried out on the basis of morphological analysis of the samples by means of the coating homogeneity in preliminary experiments. Coating microstructure was evaluated by SEM (Hitachi S4800) while FTIR (Nicolet 6700) analysis was carried out to determine the presence of chitosan and the different glass particles in the coating.

The mechanical characterization of the coatings was performed through the tape test (four samples for each composition), in accordance with ASTM D3359-09 standard, and a qualitative flexural bend test by manually flexing the sample up to an angle of 180° according to previous studies (two samples for each composition) (Chen et al., 2013; Cordero-Arias et al., 2013, 2014). The deposited mass was calculated by weighing the samples before and after the deposition process, both using AC- and DC-EPD methods. Chitosan/45S5-Sr coatings were selected as an example, and 10 measures were performed for each deposition by means of a precision balance (0.0001 g).

The surface roughness (R_a) of all coatings, synthesized both using AC-EPD and DC-EPD, was measured by means of a laser profilometer (UBM, ISC-2); the analysis was performed in triplicate. The coating wettability was estimated through static contact angle measurements using a DSA30 instrument (Kruess GmbH,

Germany). Five measurements for each sample were carried out using distilled water.

Bioactivity test in SBF was performed according to Kokubo's protocol (Kokubo and Takadama, 2006) to evaluate the influence of the doping elements on the final bioactivity of the coating. Coated samples were immersed in 40 ml of SBF solution maintained at 37°C for 1, 3, 7, 14, 21, and 28 days. Every 7 days, the SBF solution was refreshed. After the immersion period, samples were analyzed by means of SEM, XRD, and Raman spectroscopy (LabRAM HR800, Horiba Jobin Yvon) to evaluate the formation of hydroxyapatite (HAp) or its precursor on the samples surfaces.

RESULTS

Glasses Synthesis and Characterization

The structural analyses of Zn- and/or Sr-doped glasses (**Figure 1**) demonstrated that all glass powders were amorphous; therefore, the introduction of Zn and Sr oxides did not induce nucleation of crystalline phases. Also from the morphological point of view, no significant differences were evidenced by FESEM analyses while the presence of doping elements was verified by means of EDS analysis (data not shown here).

Immersion tests in SBF solution revealed the influence of Sr and Zn on bioactivity of the glasses. In particular, Zn-containing glasses showed a delay in the nucleation of HAp, even if the silica gel formation and its enrichment in Ca and P were observed after few days of SBF immersion.

Figure 1 reports the XRD patterns of all glasses before and after SBF treatment up to 1 month; as it can be noticed, no crystallization peaks were observed for 45S5-Zn glasses (**Figure 1A**), but only the typical silica-gel halo at about $2\theta = 20^\circ$ – 25° after 3 days of immersion in SBF was noticed. XRD analyses of 45S5-Sr glasses (**Figure 1B**) showed always the presence of the silica-gel halo after 1 day of treatment and the appearance of HAp peaks after 7 days of immersion in SBF; then in this case only a slight delay, in comparison to the pristine glass (45S5 BG, **Figure 2**), in the HAp crystallization was observed. Glasses containing both Zn and Sr showed an intermediate behavior: silica gel was present after 3 days of SBF immersion, but the HAp peaks appeared only after 1 month of treatment.

The results obtained by means of XRD analyses were confirmed by FESEM observation and EDS analyses, reported in **Figures 3** and **4** respectively. Regarding 45S5-Zn glass powders, no formation of crystals with the typical globular shape of HAp was evidenced up to 1 month, even if a reaction layer can be noticed on SEM images (**Figure 3A**) and an increase of Ca and most of all P was evidenced by EDS analysis (**Figure 4A**). A noticeable increase of Ca and P concentration together with the decrease of Na were also evidenced for 45S5-Sr glass (**Figure 4B**). SEM analyses revealed the presence of globular agglomerates with the typical morphology of *in vitro* self-grown HAp (Kaur et al., 2014) after 7 days of SBF treatment. Also in this case, 45S5-ZnSr presents an intermediate performance: EDS analysis showed a significant increase of Ca and P and a reduction of Na concentrations, which are intermediate between those of 45S5-Sr and 45S5-Zn. Moreover, globular precipitates

TABLE 1 | Compositions of the 45S5-based bioactive glasses investigated.

%wt	45S5	45S5-Sr	45S5-Zn	45S5-Sr-Zn
SiO ₂	45.00	43.01	43.92	43.46
Na ₂ O	24.50	23.42	23.91	23.66
P ₂ O ₅	6.00	5.73	5.86	5.79
CaO	24.50	18.19	18.58	18.38
SrO	0.00	9.65	0.00	4.87
ZnO	0.00	0.00	7.74	3.83

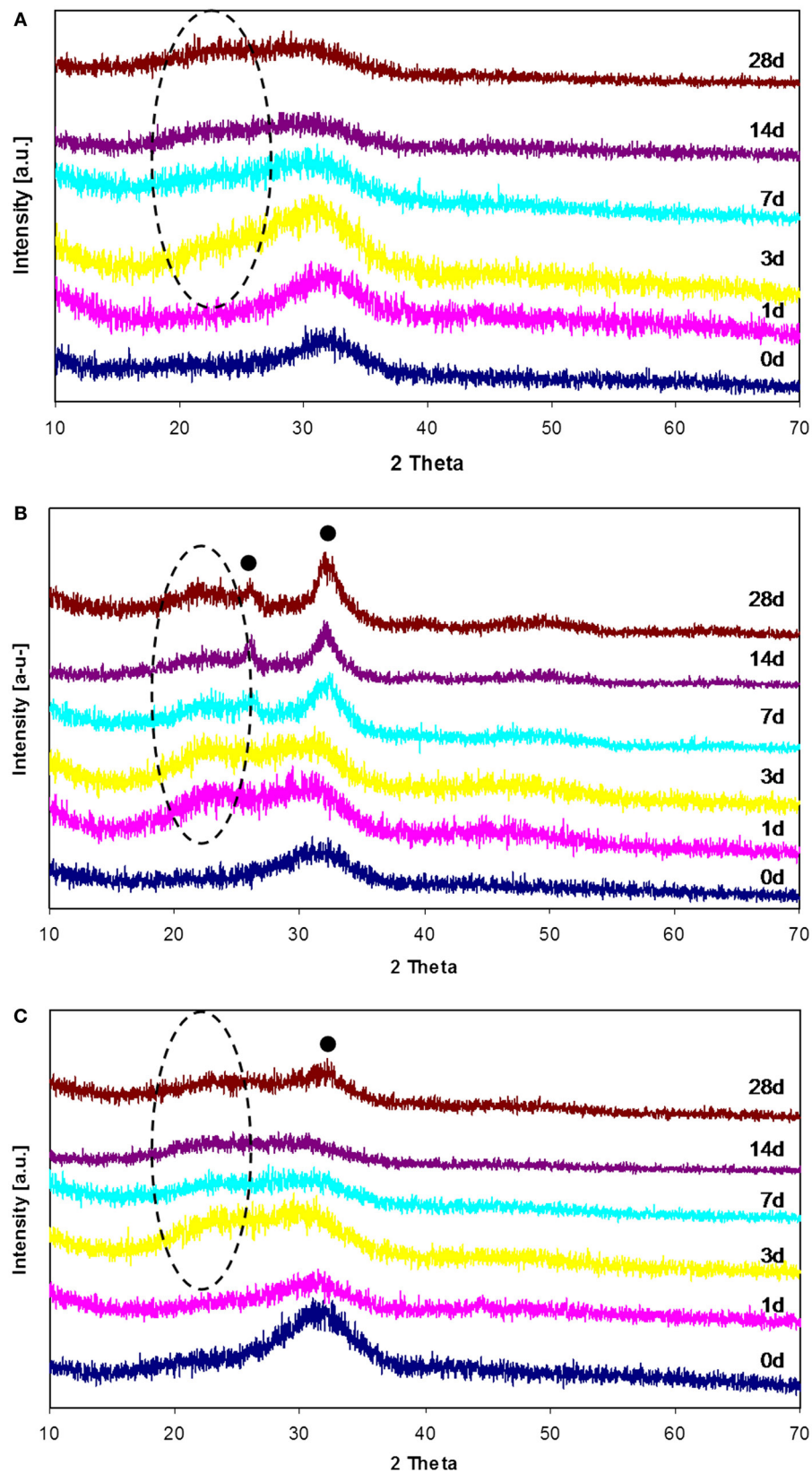


FIGURE 1 | XRD patterns of 45S5-Zn (A), 45S5-Sr (B), and 45S5-ZnSr (C) before and after SBF treatment up to 1 month. (•) Hydroxyapatite, (–) silica gel.

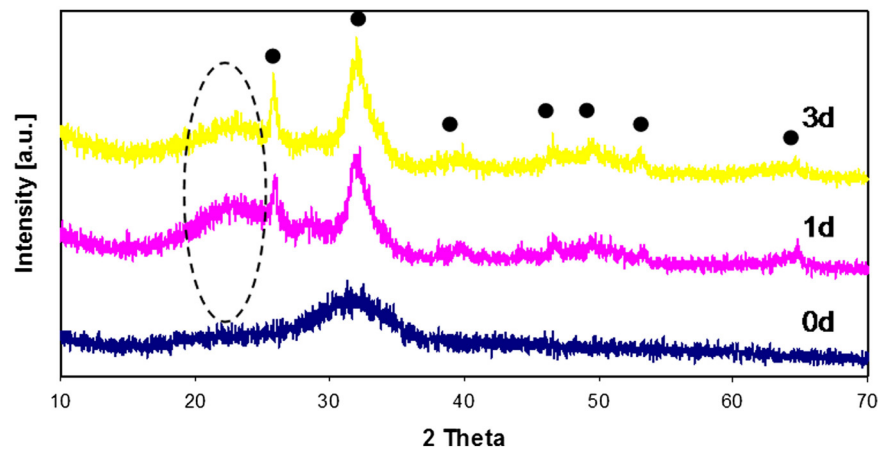


FIGURE 2 | XRD patterns of 45S5 (BG) before and after SBF treatment up to 3 days. (•) Hydroxyapatite, (–) silica gel.

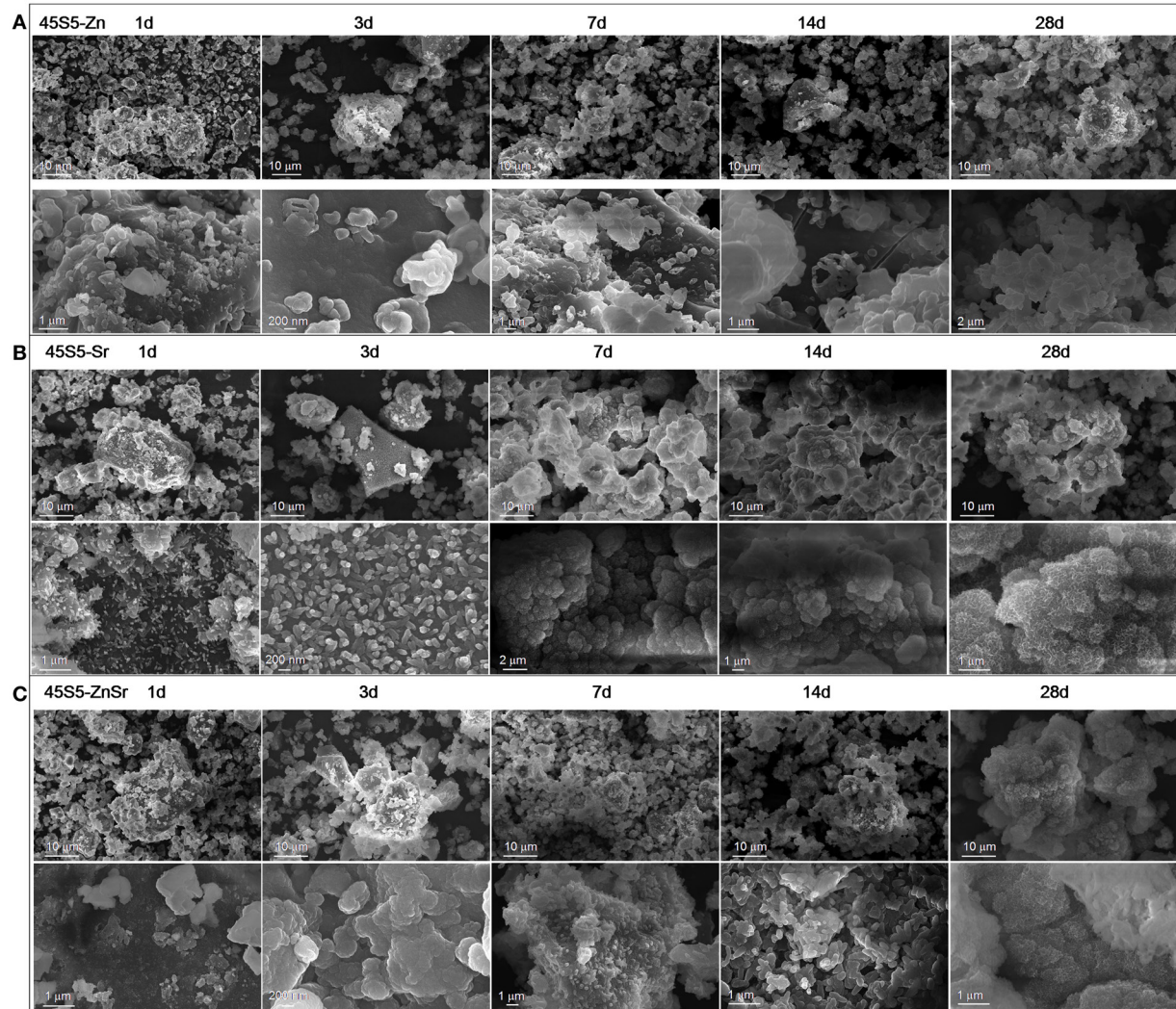


FIGURE 3 | SEM micrographs of 45S5-Zn (A), 45S5-Sr (B), and 45S5-ZnSr (C) after different times of immersion in SBF.

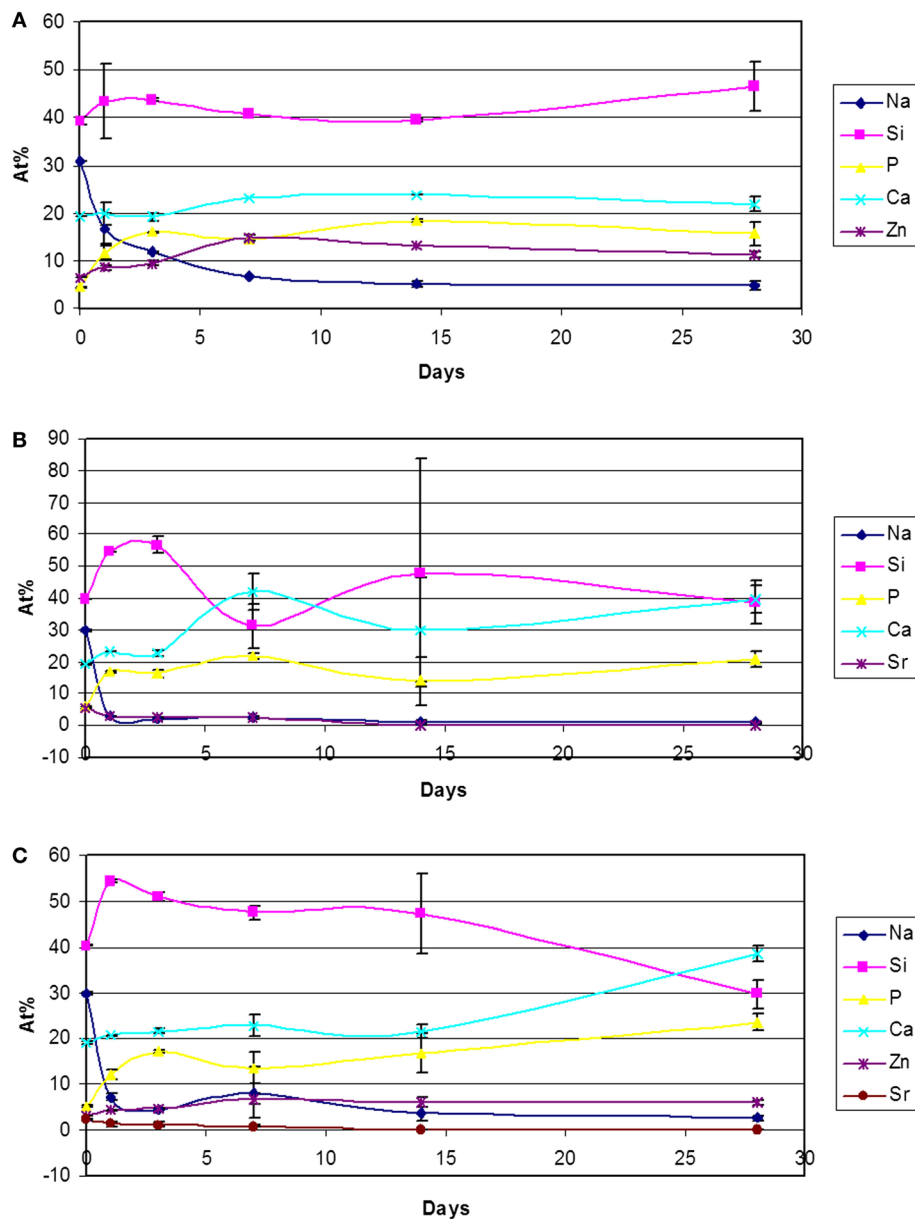


FIGURE 4 | Atomic percentages variation (EDS analyses of 500x area) of 45S5-Zn (A), 45S5-Sr (B), and 45S5-ZnSr (C) after immersion in SBF.

were confirmed to form after 28 days of immersion by means of SEM observation.

Suspension Stability

The ζ -potential results for BG suspension stability are presented in **Table 2**. For the Sr- and Zn-doped BGs/chitosan suspensions, the ζ -potential results show a similar value. All systems exhibit a relative high standard deviation (14 mV), and this result can be related to the large size of the glass particles decreasing the suspension stability. Nevertheless, a cathodic deposition is predicted for all the systems. It can be assumed that deposition is controlled by the chitosan molecules, which move the potential from a negative

value for the BG to a positive value when chitosan is incorporated, this occurs by the esterification that the polymer chain has on the surface of the BG particles, as discussed in previous studies (Zhitomirsky et al., 2009; Pishbin et al., 2011; Chen et al., 2013; Cordero-Arias et al., 2013).

The fresh prepared suspensions exhibited a pH value in the range of 3–4.5 for all suspensions. Under those conditions, the suspensions were used for EPD.

Coating Synthesis and Characterization

Using the DC-EPD technique, homogeneous and well-attached coatings were obtained for the 45S5-Sr- and 45S5-ZnSr-based

coatings using 75 V and 1 min of deposition potential and time, respectively (**Figures 5B,C**). In the case of the 45S5-Zn/Ch system, the coatings presented a higher porosity and microcracks, which are likely due to a stronger hydrolysis during the deposition (**Figure 5A**). When AC-EPD was used, homogeneous and well-attached coatings were obtained for the different glasses using 20 V of deposition potential, 2 min of deposition time, 10 kHz of frequency, and a duty charge of 80% (**Figures 5D–F**). Comparing the 45S5-Zn/Ch produced by DC-EPD and AC-EPD, better coatings were produced using the AC-EPD method since the voltage is periodically inverted, the supplied energy is not sufficient to cause water hydrolysis, and the coatings appeared more homogeneous. These results are in accordance with previously reported data (Neirinck et al., 2009; Chávez-Valdez and Boccaccini, 2012; Chen et al., 2013). The used voltage did not have influence on the deposition of 45S5-Sr powders, allowing a uniform deposition both in AC and DC processes. Finally, in 45S5-ZnSr-containing coating, a low amount of bubbles was detected, but there were no differences between AC and DC deposition.

The qualitative bending test demonstrated an optimal adhesion of all coatings on the substrates, without the formation of cracks or detachments (**Figure 6**).

Concerning the measurement of deposited mass, AC-EPD led to a deposited mass of 1.3 ± 0.2 mg/cm² while 0.8 ± 0.2 mg/cm² was calculated for DC-EPD coatings.

The tape test (**Figure 7**), performed in accordance with ASTM D3359-09, evidenced some differences among the various coatings; the 45S5-Zn coatings showed a damage classified as 2B

for AC-EPD (65% of the coating removed) and 3B for DC-EPD (25% of the coating removed). 45S5-Sr coatings revealed a damage <5% for both deposition modes and were classified as 4B. Finally, 45S5-ZnSr coatings showed a significant damage both for AC-EPD (classified as 1B, more than 65% of the coating removed) and for DC-EPD (classified as 2B, 65% of the coating removed).

The morphological analysis of the coatings is reported in **Figure 8**. As it can be observed, the 45S5-Zn coatings exhibit poor homogeneity, and the glass particles formed clusters which are well embedded in the polymeric matrix. Regarding the deposition process, AC-EPD allowed depositing glass particles/clusters with greater dimensions than the DC-EPD process, covering more of the substrate surface. 45S5-Sr coatings appear relatively more homogenous and uniform with glass particles well integrated in the chitosan matrix. No substantial difference between DC- and AC-EPD is observed in terms of microstructure. Concerning the 45S5-ZnSr coatings, a more pronounced difference was noticed between DC and AC deposition; the coatings obtained with DC-EPD are clearly less consistent and homogenous in comparison to those synthesized with AC-EPD, similar results for DC- and AC-EPD for organic/inorganic coatings have been previously reported (Chen et al., 2013).

Figure 9 shows as example the FTIR spectrum of an Sr-containing coating. In order to verify the presence of chitosan, the FTIR spectrum of pure chitosan powder was obtained together with that of pure glass powder (45S5-Sr). Moreover, also the spectrum of a chitosan coating was obtained.

FTIR analysis evidenced the composite nature of all coatings. The chitosan characteristic peaks were present in all spectra, in particular the peaks around 891 cm⁻¹ and 1150 cm⁻¹, which correspond to the saccharide structure and are due to the vibrations of the glycosidic bonding (–C–O–C–). The stretching of the C=O group in the glucosamine unit appears at about 1650 cm⁻¹ and corresponds to the amide I band. The band at 1570 cm⁻¹ corresponds to the amide II band, indicating the NH-bending vibrations in the amide group (Gebhardt et al., 2012). Finally, the peak at 1350 cm⁻¹ is ascribable to the vibration of the C–H/N–H

TABLE 2 | ζ -potential results for suspensions containing the different doped bioactive glasses in a mixture with chitosan.

Suspension	ζ -Potential (mV)
45S5-Sr/Ch	+29 ± 14
45S5-Zn/Ch	+31 ± 15
45S5-ZnSr/Ch	+36 ± 14

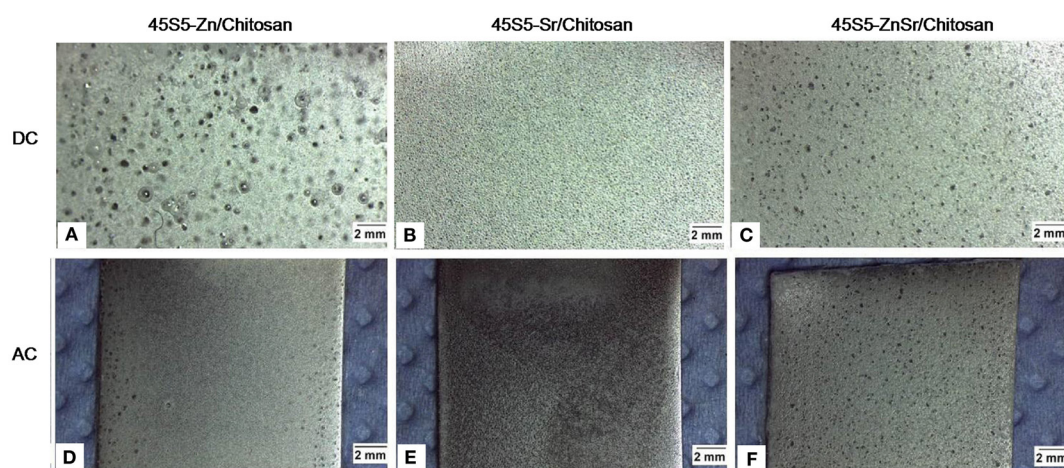


FIGURE 5 | Images of the electrophoretic coatings using both DC (A–C) and AC-EPD (D–F) for the different chitosan/BG systems investigated.

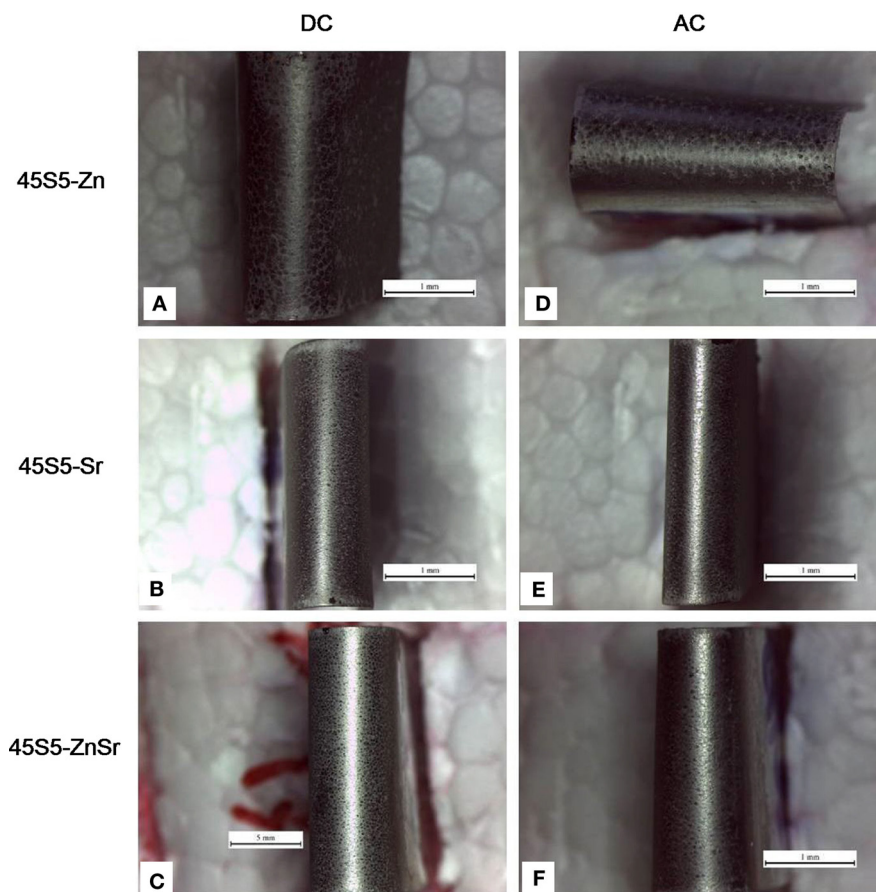


FIGURE 6 | Digital camera images of the surface of coatings after bending tests. Coatings produced by means of DC-EPD (A–C) and AC-EPD (D–F). Scale bar: 1 mm.

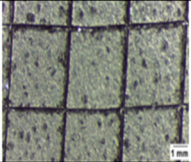
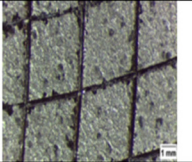
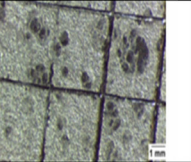
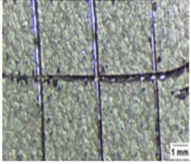
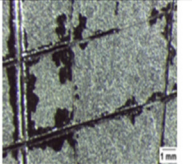
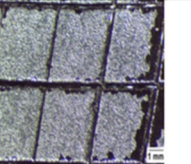
	45S5-Sr	45S5-Zn	45S5-ZnSr
DC-EPD			
Classification	4B	3B	2B
AC-EPD			
Classification	4B	2B	1B

FIGURE 7 | Tape test results for the different chitosan/45S5-doped BG coatings on stainless steel AISI 316L substrate confirming different adhesion behavior of coatings depending on deposition mode (AC- or DC-EPD).

group. Instead, the characteristic bands of BG are located at about 916 cm^{-1} and 496 cm^{-1} and correspond to the vibration of Si–O–Si and P–O groups, respectively.

The roughness of the coatings was evaluated and the obtained values are reported in **Table 3**. As it can be observed, the roughness values are generally higher for coatings obtained by AC-EPD

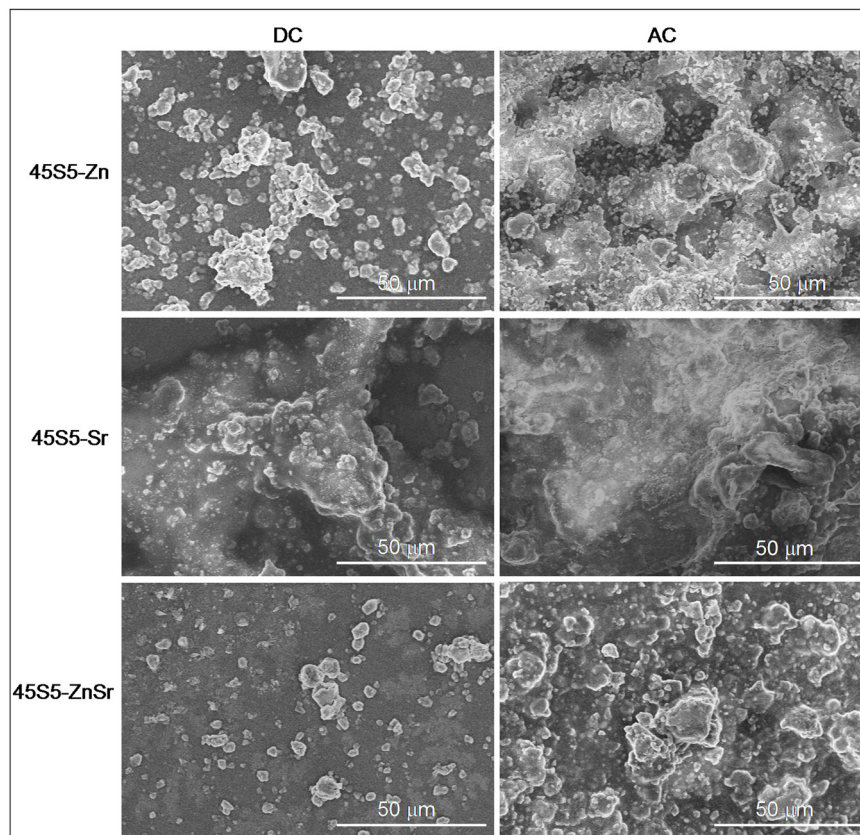


FIGURE 8 | SEM images of AC- and DC-EPD-obtained coatings showing glass particles in chitosan matrix.

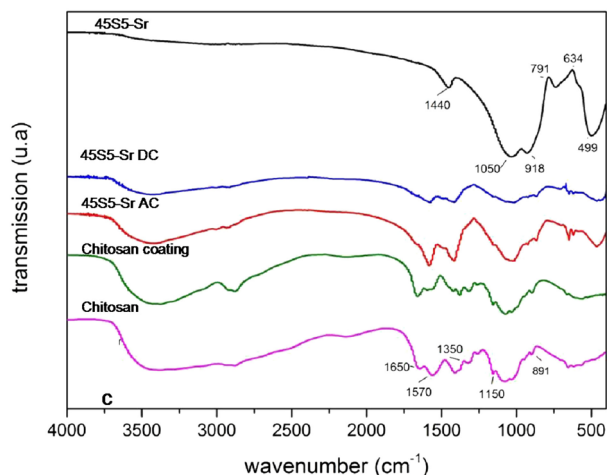


FIGURE 9 | FTIR spectra of chitosan/45S5-Sr. The relevant peaks are explained in the text.

process. This behavior is probably due to the greater amount of material deposited.

Table 3 reports also the results of wettability test; the values of the contact angle measurements varied between 35° and 80°. As

reported in the literature (Chen et al., 2013), the presence of BG should lead to hydrophilic properties, and hydrophilic surfaces are promising for the *in vitro/in vivo* cells interaction.

Figure 10 shows the results obtained for 45S5-Zn-containing coating upon immersion in SBF. SEM images confirmed the results obtained on glass powders: the Zn presence causes a pronounced inhibition of the precipitation of HAp. No differences were evidenced between AC- and DC-EPD modes at any time of immersion in SBF.

On the contrary, Sr-containing coatings were able to induce the precipitation of HAp after 1 day for AC-EPD and 3 days for DC-EPD coatings. **Figure 11** shows SEM micrographs, XRD, and Raman analyses of the samples: globular agglomerates similar to *in vitro* grown HAp are visible after few days of treatment; the HAp presence is confirmed by XRD up to 7 days and Raman analyses from 7 to 28 days (Koutsopoulos, 2002; Li et al., 2004).

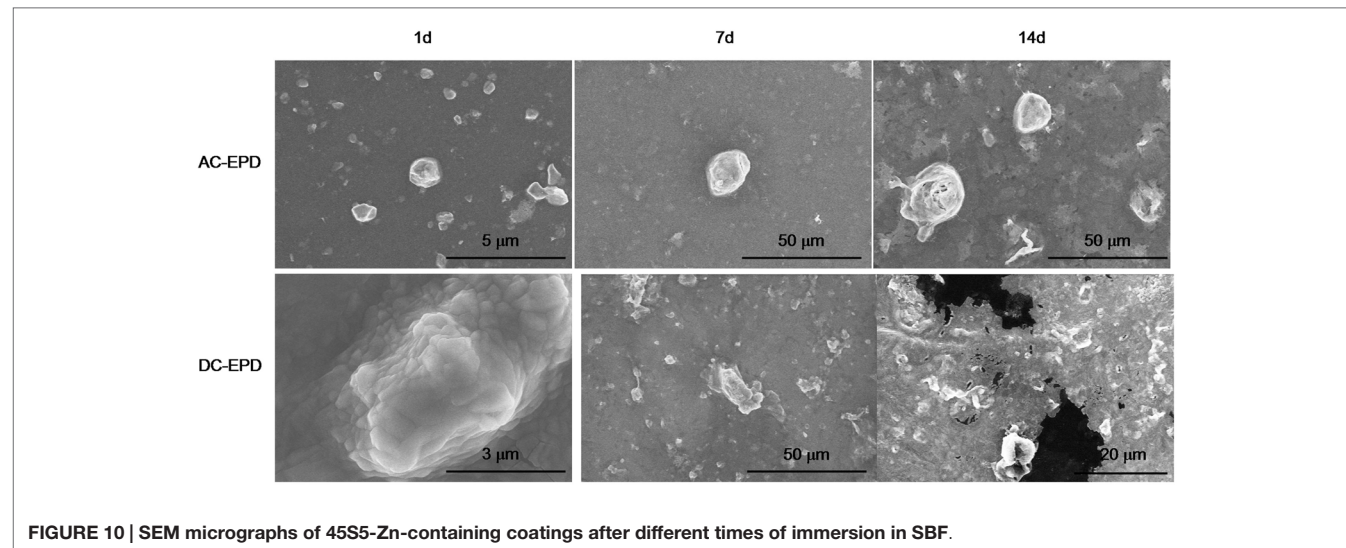
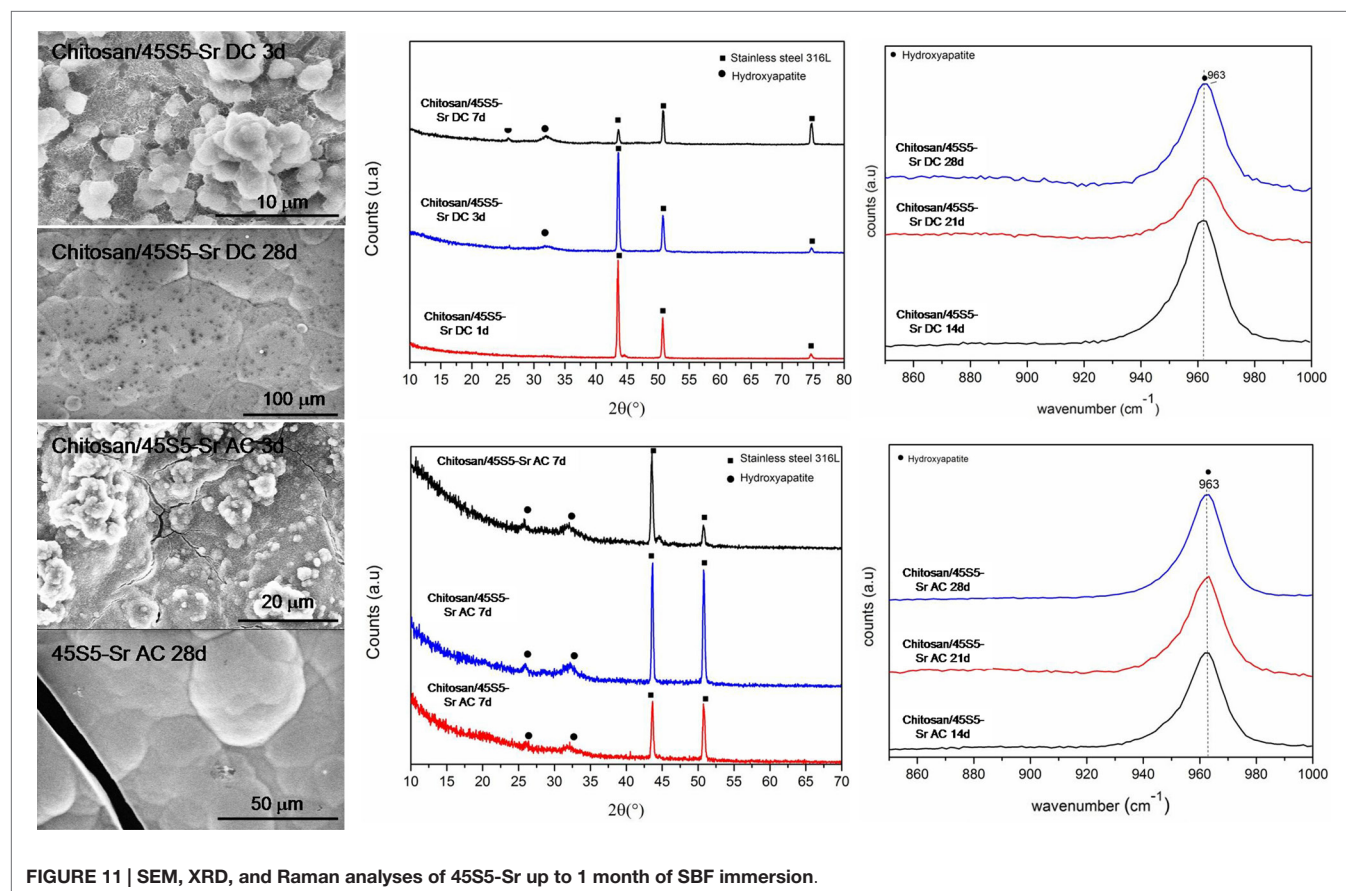
Finally, a reduced bioactivity was also evidenced for 45S5-ZnSr-containing coatings, since up to 14 days no HAp precipitation was detected both with SEM and XRD analyses (**Figure 12**).

DISCUSSION

This research has considered the synthesis of Zn- and Sr-doped glasses and their use to develop chitosan/glass composite coatings

TABLE 3 | Roughness (Ra) and contact angle values of the different produced coatings.

	45S5-Zn AC	45S5-Zn DC	45S5-Sr AC	45S5-Sr DC	45S5-ZnSr AC	45S5-ZnSr DC
Ra (μm)	1.8 ± 0.2	1.6 ± 0.08	2.2 ± 0.4	1.2 ± 0.1	1.6 ± 0.04	1.7 ± 0.2
Contact angle	$47^\circ \pm 5^\circ$	$54^\circ \pm 9^\circ$	$41^\circ \pm 6^\circ$	$62^\circ \pm 12^\circ$	$73^\circ \pm 7^\circ$	$59^\circ \pm 8^\circ$

**FIGURE 10 |** SEM micrographs of 45S5-Zn-containing coatings after different times of immersion in SBF.**FIGURE 11 |** SEM, XRD, and Raman analyses of 45S5-Sr up to 1 month of SBF immersion.

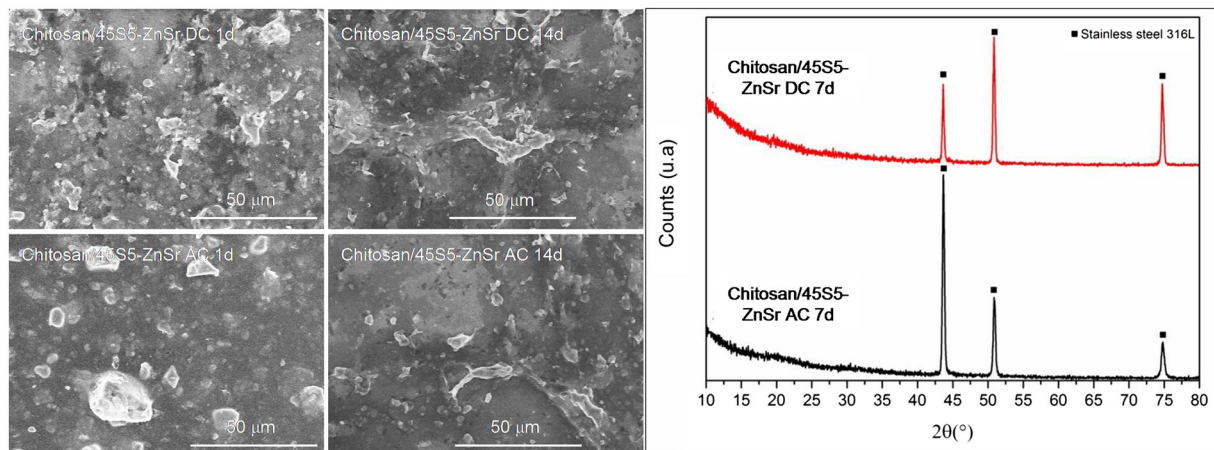


FIGURE 12 | SEM micrographs and XRD analyses of 45S5-ZnSr after immersion in SBF solution.

by means of EPD. In particular, the influence of Zn, Sr, and their combination on the bioactivity process was investigated from both glass powders and coatings. Moreover, the effect of these ions in the EPD process was also evaluated.

Regarding the glass powders, both Zn and Sr introduction did not change the structure of the pristine glass (45S5), since no crystallization peaks were detected in XRD spectra. However, the incorporation of these elements, especially Zn, generated differences on the kinetics of bioactivity. In fact, Zn-doped glass (45S5-Zn) did not show the precipitation of crystalline HAp up to 1 month of immersion in SBF solution (**Figure 1A**). The influence of Zn on the bioactivity process and its role in glass structure have been extensively debated in literature, as reviewed recently (Balasubramanian et al., 2015). It has been reported that ZnO can act as a modifier (Anand et al., 2014; Balasubramanian et al., 2015), leading to the decrease in surface area and pore size of glass. Moreover, when present in higher amount, ZnO can also act as an intermediate oxide, thus creating a more stable glass structure by forming covalent links between adjacent SiO_4 tetrahedra (El-Kady and Ali, 2012; Balasubramanian et al., 2015). Regarding ZnO role in glass bioactivity and degradation, Kamitakahara et al. (2006) reported that the introduction of ZnO (replacing CaO) in a bioactive apatite-wollastonite containing glass-ceramic decreases the glass-ceramic bioactivity. They reported that the glass-ceramic chemical durability was improved by adding ZnO because ZnO is an amphoteric oxide and shows very low solubility in SBF. Similar results were obtained by Goel et al. (2013). The silicon release of the glass-ceramic decreased with increasing ZnO content, and as a consequence, the formation of silanol groups was suppressed. It has been observed that the presence of zinc causes a general reduction in ion leaching in the 45S5 BG composition (Lusvardi et al., 2009). This behavior was also confirmed by Aina et al. (2009); in this study, it is proven that high level of ZnO (20 mol%) caused a drastic reduction of 45S5 glass leaching activity and so HAp formation. A 5 mol% of ZnO addition causes only a delay in the HAp precipitation; however, in this case, Zn substituted all glass elements. Oudadesse et al. (2011) reported that only 0.1 wt%

of Zn (replacing Ca and Na) inhibited the glass dissolution, limiting the formation of silica gel layer and generating a delay in the HAp formation.

The present study confirms that Zn introduction retards the glass degradation and the crystal nucleation of HAp, even if for glass powders the silica gel formation and its enrichment in Ca and P were observed after few days of SBF immersion.

Data regarding Sr introduction in glasses has shown that its addition does not result in any structural alteration of the glass network (Fredholm et al., 2010), since its role is similar to the calcium one. Moreover, in general, this element does not modify or even enhances the bioactivity of the pristine glass (Lao et al., 2008, 2009). Only few studies reported a negative influence of Sr in HAp nucleation. Hoppe et al. (2014) reported that Sr-containing BG (type 1393) nanoparticles showed a delay in the bioactivity mechanism by increasing the Sr content, and Goel et al. (2011) showed that increasing the $\text{Sr}^{2+}/\text{Ca}^{2+}$ ratio in the glasses does not affect their structure significantly, but the apatite-forming ability is decreased considerably. In the present study, Sr introduction entails a slight delay in the bioactivity kinetics, but XRD (**Figure 1B**) and FESEM-EDS analyses (**Figures 3B** and **4B**) demonstrated that after 3 days of SBF immersion, HAp crystals were present on the surface of the glass powders. It must be underlined that in the literature there are some controversies about the effect of Sr/Ca substitution on the dissolution mechanism of the glasses. These controversies seem to be due to the mixed use of weight instead of mole percent in glasses composition design (O'Donnell and Hill, 2010; Du and Xiang, 2012). In fact, if weight percentage is used, the higher molecular weight of SrO than CaO can lead to an actual increase of SiO_2 content in mole percent, which involves an increase of network connectivity and a decrease of dissolution rate. Instead, if Sr is substituted in mole percent, the network structure of the glass does not significantly change and a higher dissolution rate is usually observed (Neel et al., 2009; O'Donnell and Hill, 2010).

Finally, the substitution of both Zn and Sr leads to an intermediate behavior; the bioactivity process of 45S5-ZnSr glass is

obviously delayed; however, after 1 month in SBF solution, the performed XRD and FESEM-EDS analyses (Figures 1C and 4C) demonstrated the formation of a crystalline HAp layer on glass powders surface. Differently, Kapoor et al. evidenced HAp formation in few hours on Sr- and Zn-doped alkali-free glass, however with very different composition respect to the ones of the glasses investigated here (Kapoor et al., 2014).

The bioactivity test of composite coatings produced by EPD leads to the same observations: Zn introduction significantly modified the glass reactivity toward SBF solution while Sr introduction allows maintaining the bioactivity of the coatings.

By tuning the EPD parameters, it was possible to obtain composite coatings using all doped glasses with glass particles or clusters well embedded in the chitosan matrix; however, the glass composition seems to have an effect not only on the coating bioactivity but also on their deposition and adhesion to the metallic substrate; in fact, Zn-containing coatings showed qualitative low adhesion with respect to Sr-containing ones (Figure 7).

Moreover, some differences were observed between AC and DC deposition; usually, the AC-EPD technique allowed deposition of composite coating without the formation of cracks and bubbles while some bubbles were observed using DC-EPD, specially for Zn-containing coatings. When water is used as solvent, the use of DC can originate water electrolysis, which leads to the formation of oxygen or hydrogen bubbles formation and their entrapment in the coating; in the AC-EPD technique, the voltage is periodically inverted, so the supplied energy is not sufficient to cause water hydrolysis, and consequent bubble formation, and the coatings appeared more homogeneous (Neirincx et al., 2009; Chávez-Valdez and Boccaccini, 2012; Chen et al., 2013). Moreover, AC-EPD allowed the deposition of a slightly greater amount of material than DC-EPD. As confirmed by Kollatha et al. (2013), AC-EPD is advantageous in depositing denser and less cracked coatings in comparison to DC-EPD. The bubble formation can also have some influence on the roughness of the coatings; nevertheless, the observed difference among roughness values can be due to the greater amount of material deposited on the substrates using AC-EPD.

REFERENCES

- Aina, V., Malavasi, G., Fiorio Pla, A., Munaron, L., and Morterra, C. (2009). Zinc-containing bioactive glasses: surface reactivity and behaviour towards endothelial cells. *Acta Biomater.* 5, 1211–1222. doi:10.1016/j.actbio.2008.10.020
- Anand, V., Singh, K. J., and Kaur, K. (2014). Evaluation of zinc and magnesium doped 45S5 mesoporous bioactive glass system for the growth of hydroxyl apatite layer. *J. Non Cryst. Solids* 406, 88–94. doi:10.1016/j.jnoncrsol.2014.09.050
- Balamurugan, A., Balossier, G., Kannan, S., Michel, J., Rebelo, A. H. S., and Ferreira, J. M. F. (2007). Development and in vitro characterization of sol-gel derived CaO-P2O5-SiO2-ZnO bioglass. *Acta Biomater.* 3, 255–262. doi:10.1016/j.actbio.2006.09.005
- Balasubramanian, P., Strobel, L. A., Kneser, U., and Boccaccini, A. R. (2015). Zinc-containing bioactive glasses for bone regeneration, dental and orthopedic applications. *Biomed. Glasses* 1, 51–69. doi:10.1515/bglass-2015-0006
- Besra, L., and Liu, M. (2007). A review on fundamentals and applications of electrophoretic deposition (EPD). *Prog. Mater. Sci.* 52, 1–61. doi:10.1016/j.pmatsci.2006.07.001
- Boccaccini, A. R., Keim, S., Ma, R., Li, Y., and Zhitomirsky, I. (2010). Electrophoretic deposition of biomaterials. *J. R. Soc. Interface* 7, 581–613. doi:10.1098/rsif.2010.0156.focus

CONCLUSION

The introduction of Zn and Sr in the 45S5 BG composition leads to a different behavior in terms of bioactivity, both for glass powders and composite coatings. The presence of ZnO allowed silica gel formation and its enrichment in Ca and P after few days of SBF immersion but inhibited the formation and precipitation of HAp while SrO introduction allowed the formation of a crystalline HAp after 1–3 days of SBF treatment. All glasses were successfully used to synthesize composite coatings by means of EPD with chitosan as the biopolymer component by adjusting the process parameters; however, Zn-containing coatings showed low adhesion to the substrate in comparison with 45S5-Sr/chitosan coatings. The deposition using AC revealed better coating quality than DC-EPD technique, since it allowed the realization of compact coatings, reducing bubbles and cracks formation. In conclusion, Zn concentration in 45S5 BG should be tailored to not completely inhibit the bioactivity process but at the same time to allow its antibacterial and anti-inflammatory effect and its role in bone metabolism while Sr-containing coatings, due to the bioactivity and biological effect of Sr, are promising materials for orthopedic coatings. A deeper investigation should be carried out in future work to evaluate the Sr ability to stimulate bone formation through *in vitro* biological tests.

ACKNOWLEDGMENTS

The authors thank Prof. S. Virtanen and Prof. W. Peukert (University of Erlangen-Nuremberg) for their support to facilitate SEM and ζ -potential measurements at their institutes, respectively. Dr. Sandra Cabanas-Polo is acknowledged for carrying out the ζ -potential measurements. LC-A acknowledges support from the German Academic Exchange Service (DAAD). Politecnico di Torino is acknowledged for funding a six months period of study at Institute for Biomaterials, Department of Materials Science and Engineering, University of Erlangen-Nuremberg with a Mobility Grant (2013-2104) for MS degree thesis.

- Chávez-Valdez, A., and Boccaccini, A. R. (2012). Innovations in electrophoretic deposition: alternating current and pulsed direct current methods. *Electrochim. Acta* 65, 70–89. doi:10.1016/j.electacta.2012.01.015
- Chen, Q., Cordero-Arias, L., Roether, J. A., Cabanas-Polo, S., Virtanen, S., and Boccaccini, A. R. (2013). Alginate/bioglass® composite coatings on stainless steel deposited by direct current and alternating current electrophoretic deposition. *Surf. Coat. Technol.* 233, 49–56. doi:10.1016/j.surfcoat.2013.01.042
- Chen, Q., and Thouas, G. A. (2015). Metallic implant biomaterials. *Mater. Sci. Eng. R Rep.* 87, 1–57. doi:10.1016/j.msea.2015.07.046
- Cordero-Arias, L., Cabanas-Polo, S., Gao, H. X., Gilbert, J., Sanchez, E., Roether, J. A., et al. (2013). Electrophoretic deposition of nanostructured-TiO2/chitosan composite coatings on stainless steel. *RSC Adv.* 3, 39–41. doi:10.1039/c3ra40535d
- Cordero-Arias, L., Cabanas-Polo, S., Gilbert, J., Goudouri, O. M., Sanchez, E., Virtanen, S., et al. (2014). Electrophoretic deposition of nanostructured TiO2/alginate and TiO2-bioactive glass/alginate composite coatings on stainless steel. *Adv. Appl. Ceram.* 113, 42–49. doi:10.1179/1743676113Y.0000000096
- Croisier, F., and Jérôme, C. (2013). Chitosan-based biomaterials for tissue engineering. *Eur. Polym. J.* 49, 780–792. doi:10.1016/j.eurpolymj.2012.12.009
- Drnovšek, N., Novak, S., Dragin, U., Čeh, M., Gorenšek, M., and Gradišar, M. (2012). Bioactive glass enhances bone ingrowth into the porous titanium

- coating on orthopaedic implants. *Int. Orthop.* 36, 1739–1745. doi:10.1007/s00264-012-1520-y
- Du, J., and Xiang, Y. (2012). Effect of strontium substitution on the structure, ionic diffusion and dynamic properties of 45S5 bioactive glasses. *J. Non Cryst. Solids* 358, 1059–1071. doi:10.1016/j.jnoncrysol.2011.12.114
- El-Kady, A. M., and Ali, A. F. (2012). Fabrication and characterization of ZnO modified bioactive glass nanoparticles. *Ceram. Int.* 38, 1195–1204. doi:10.1016/j.ceramint.2011.07.069
- Fredholm, Y. C., Karpukhina, N., Law, R. V., and Hill, R. G. (2010). Strontium containing bioactive glasses: glass structure and physical properties. *J. Non Cryst. Solids* 356, 2546–2551. doi:10.1016/j.jnoncrysol.2010.06.078
- Gebhardt, F., Seuss, S., Turhan, M. C., Hornberger, H., Virtanen, S., and Boccaccini, R. (2012). Characterization of electrophoretic chitosan coatings on stainless steel. *Mater. Lett.* 66, 302–304. doi:10.1016/j.matlet.2011.12.031
- Gentleman, E., Fredholm, Y. C., Jell, G., Lotfibakhshaiesh, N., O'Donnell, M. D., Hill, R. G., et al. (2010). The effects of strontium-substituted bioactive glasses on osteoblasts and osteoclasts in vitro. *Biomaterials* 31, 3949–3956. doi:10.1016/j.biomaterials.2010.01.121
- Gerhardt, L. C., and Boccaccini, A. R. (2010). Bioactive glass and glass-ceramic scaffolds for bone tissue engineering. *Materials* 3, 3867–3910. doi:10.3390/ma3073867
- Goel, A., Kapoor, S., Tilocca, A., Rajagopal, R. R., and Ferreira, J. M. F. (2013). Structural role of zinc in biodegradation of alkali-free bioactive glasses. *J. Mater. Chem. B* 1, 3073–3082. doi:10.1039/c3tb20163e
- Goel, A., Rajagopal, R. R., and Ferreira, J. M. F. (2011). Influence of strontium on structure, sintering and biodegradation behaviour of CaO-MgO-SrO-SiO₂-P₂O₅-CaF₂ glasses. *Acta Biomater.* 7, 4071–4080. doi:10.1016/j.actbio.2011.06.047
- Grandfield, K., and Zhitomirsky, I. (2008). Electrophoretic deposition of composite hydroxyapatite-silica-chitosan coatings. *Mater. Charact.* 59, 61–67. doi:10.1016/j.matchar.2006.10.016
- Hench, L. L. (2006). The story of bioglass®. *J. Mater. Sci. Mater. Med.* 17, 967–978. doi:10.1007/s10856-006-0432-z
- Hench, L. L. (2015). Opening paper 2015 – some comments on bioglass: four eras of discovery and development. *Biomed. Glasses* 1, 1–11. doi:10.1515/bglass-2015-0001
- Hoppe, A., Sarker, B., Detsch, R., Hild, N., Mohn, D., Stark, W. J., et al. (2014). In vitro reactivity of Sr-containing bioactive glass (type 1393) nanoparticles. *J. Non Cryst. Solids* 387, 41–46. doi:10.1016/j.jnoncrysol.2013.12.010
- Jaiswala, S., McHale, P., and Duffy, B. (2012). Preparation and rapid analysis of antibacterial silver, copper and zinc doped sol-gel surfaces. *Colloids Surf. B Biointerfaces* 94, 170–176. doi:10.1016/j.colsurfb.2012.01.035
- Jones, J. R. (2013). Review of bioactive glass: from hench to hybrids. *Acta Biomater.* 9, 4457–4486. doi:10.1016/j.actbio.2012.08.023
- Kamitakahara, M., Ohtsuki, C., Inada, H., Tanihara, M., and Miyazaki, T. (2006). Effect of ZnO addition on bioactive CaO-SiO₂-P₂O₅-CaF₂ glass-ceramics containing apatite and wollastonite. *Acta Biomater.* 2, 467–471. doi:10.1016/j.actbio.2006.03.001
- Kapoor, S., Goel, A., Tilocca, A., Dhunad, V., Bhatia, G., Dhunae, K., et al. (2014). Role of glass structure in defining the chemical dissolution behavior, bioactivity and antioxidant properties of zinc and strontium co-doped alkali-free phosphosilicate glasses. *Acta Biomater.* 10, 3264–3327. doi:10.1016/j.actbio.2014.03.033
- Kaur, G., Pandey, O. P., Singh, K., Homa, D., Scott, B., and Pickrell, G. (2014). A review of bioactive glasses: their structure, properties, fabrication and apatite formation. *J. Biomed. Mater. Res. A* 102, 254–274. doi:10.1002/jbm.a.34690
- Kokubo, T., and Takadama, H. (2006). How useful is SBF in predicting in vivo bone bioactivity? *Biomaterials* 27, 2907–2915. doi:10.1016/j.biomaterials.2006.01.017
- Kollatha, V. O., Chen, Q., Closset, R., Luyten, J., Traina, K., Mullens, S., et al. (2013). AC vs. DC electrophoretic deposition of hydroxyapatite on titanium. *J. Eur. Ceram. Soc.* 33, 2715–2721. doi:10.1016/j.jeurceramsoc.2013.04.030
- Koutsopoulos, S. (2002). Synthesis and characterization of hydroxyapatite crystals: a review study on the analytical methods. *J. Biomed. Mater. Res.* 62, 600–612. doi:10.1002/jbm.10280
- Lao, J., Jallot, E., and Nedelec, J. M. (2008). Strontium-delivering glasses with enhanced bioactivity: a new biomaterial for antiosteoporotic applications? *Chem. Mater.* 20, 4969–4973. doi:10.1021/cm800993s
- Lao, J., Nedelec, J. M., and Jallot, J. (2009). New strontium-based bioactive glasses: physicochemical reactivity and delivering capability of biologically active dissolution products. *J. Mater. Chem.* 19, 2940–2949. doi:10.1039/b822214b
- Li, H., Ng, B., Khor, K., Cheang, P., and Clyne, T. (2004). Raman spectroscopy determination of phases within thermal sprayed hydroxyapatite splats and subsequent in vitro dissolution examination. *Acta Mater.* 52, 445–453. doi:10.1016/j.actamat.2003.09.046
- Lusvardi, G., Zaffe, D., Menabue, L., Bertoldi, C., Malavasi, G., and Consolo, U. (2009). In vitro and in vivo behaviour of zinc-doped phosphosilicate glasses. *Acta Biomater.* 5, 419–428. doi:10.1016/j.actbio.2008.07.007
- Magallanes-Perdomo, M., Meille, S., Chenal, J. M., Pacard, E., and Chevalier, J. (2012). Bioactivity modulation of bioglass® powder by thermal treatment. *J. Eur. Ceram. Soc.* 32, 2765–2775. doi:10.1016/j.jeurceramsoc.2012.03.018
- Miola, M., Vitale Brovarone, C., Maina, G., Rossi, F., Bergandi, L., Ghigo, D., et al. (2014). In vitro study of manganese-doped bioactive glasses for bone regeneration. *Mater. Sci. Eng. C* 38, 107–118. doi:10.1016/j.msec.2014.01.045
- Mouriño, V., Cattalini, J. P., and Boccaccini, A. R. (2012). Metallic ions as therapeutic agents in tissue engineering scaffolds: an overview of their biological applications and strategies for new developments. *J. R. Soc. Interface* 9, 401–419. doi:10.1098/rsif.2011.0611
- Neel, E. A., Chrzanowski, W., Pickup, D. M., O'Dell, L. A., Mordan, N. J., Newport, R. J., et al. (2009). Structure and properties of strontium-doped phosphate-based glasses. *J. R. Soc. Interface* 6, 435–446. doi:10.1098/rsif.2008.0348
- Neirincx, B., Franssaer, J., Van der Biest, O., and Vleugels, J. (2009). Aqueous electrophoretic deposition in asymmetric AC electric fields (AC-EPD). *Electrochem. Commun.* 11, 57–60. doi:10.1016/j.elecom.2008.10.028
- Niinomi, M. (2002). Recent metallic materials for biomedical applications. *Metall. Mater. Trans. A* 33, 477–486. doi:10.1007/s11661-002-0109-2
- O'Donnell, M. D., and Hill, R. G. (2010). Influence of strontium and the importance of glass chemistry and structure when designing bioactive glasses for bone regeneration. *Acta Biomater.* 6, 2382–2385. doi:10.1016/j.actbio.2010.01.006
- Oudadesse, H., Dietrich, E., Gal, Y. L., Pellen, P., Bureau, B., Mostafa, A. A., et al. (2011). Apatite forming ability and cytocompatibility of pure and Zn-doped bioactive glasses. *Biomed. Mater.* 6, 1–9. doi:10.1088/1748-6041/6/3/035006
- Pishbin, F., Simchi, A., Ryan, M. P., and Boccaccini, A. R. (2011). Electrophoretic deposition of chitosan/45S5 bioglass® composite coatings for orthopaedic applications. *Surf. Coat. Technol.* 205, 5260–5268. doi:10.1016/j.surfcoat.2011.05.026
- Rahaman, M. N., Day, D. E., Bal, B. S., Fu, Q., Jung, S. B., Bonewald, L. F., et al. (2012). Bioactive glass in tissue engineering. *Acta Biomater.* 7, 2355–2373. doi:10.1016/j.actbio.2011.03.016
- Rath, S. N., Brandl, A., Hiller, D., Hoppe, A., Gbureck, U., Horch, R. E., et al. (2014). Bioactive copper-doped glass scaffolds can stimulate endothelial cells in co-culture in combination with mesenchymal stem cells. *PLoS ONE* 9:e113319. doi:10.1371/journal.pone.0113319
- Verné, E. (2012). “Bioactive glass and glass-ceramic coatings,” in *Bio-Glasses – An Introduction*, eds Jones R. J. and Clare A. G. (Chichester, UK: John Wiley & Sons, Ltd), 107–119. doi:10.1002/9781118346457.ch8
- Zhitomirsky, D., Roether, J. A., Boccaccini, A. R., and Zhitomirsky, I. (2009). Electrophoretic deposition of bioactive glass/polymer composite coatings with and without HA nanoparticle inclusions for biomedical applications. *J. Mater. Process. Technol.* 209, 1853–1860. doi:10.1016/j.jmatprotec.2008.04.034

Conflict of Interest Statement: The authors declare that the research was conducted in the absence of any commercial or financial relationships that could be construed as a potential conflict of interest.

Copyright © 2015 Miola, Verné, Cirraldo, Cordero-Arias and Boccaccini. This is an open-access article distributed under the terms of the Creative Commons Attribution License (CC BY). The use, distribution or reproduction in other forums is permitted, provided the original author(s) or licensor are credited and that the original publication in this journal is cited, in accordance with accepted academic practice. No use, distribution or reproduction is permitted which does not comply with these terms.



Uniform surface modification of 3D Bioglass[®]-based scaffolds with mesoporous silica particles (MCM-41) for enhancing drug delivery capability

Elena Boccardi¹, Anahí Philippart¹, Judith A. Juhasz-Bortuzzo¹, Ana M. Beltrán^{2†},
Giorgia Novajra³, Chiara Vitale-Brovarone³, Erdmann Spiecker² and Aldo R. Boccaccini^{1*}

OPEN ACCESS

Edited by:

Malcolm Xing,
University of Manitoba, Canada

Reviewed by:

Hélder A. Santos,
University of Helsinki, Finland
Ahmed El-Fiqi,
Dankook University, South Korea

*Correspondence:

Aldo R. Boccaccini
aldo.boccaccini@uni-erlangen.de

[†]Present address:

Ana M. Beltrán,
Instituto de Ciencia de Materiales de
Sevilla (ICMS), CSIC-Universidad de
Sevilla, Sevilla, Spain

Specialty section:

This article was submitted to
Biomaterials, a section of the
journal *Frontiers in Bioengineering
and Biotechnology*

Received: 14 August 2015

Accepted: 15 October 2015

Published: 06 November 2015

Citation:

Boccardi E, Philippart A, Juhasz-Bortuzzo JA, Beltrán AM, Novajra G, Vitale-Brovarone C, Spiecker E and Boccaccini AR (2015) Uniform surface modification of 3D Bioglass[®]-based scaffolds with mesoporous silica particles (MCM-41) for enhancing drug delivery capability. *Front. Bioeng. Biotechnol.* 3:177. doi: 10.3389/fbioe.2015.00177

¹ Institute of Biomaterials, Department of Materials Science and Engineering, Friedrich-Alexander University Erlangen-Nürnberg, Erlangen, Germany, ² Center for Nanoanalysis and Electron Microscopy (CENEM), Institute of Micro- and Nanostructure Research, Department of Materials Science and Engineering, Friedrich-Alexander University Erlangen-Nürnberg, Erlangen, Germany, ³ Institute of Materials Physics and Engineering, Applied Science and Technology Department, Politecnico di Torino, Turin, Italy

The design and characterization of a new family of multifunctional scaffolds based on bioactive glass (BG) of 45S5 composition for bone tissue engineering and drug delivery applications are presented. These BG-based scaffolds are developed via a replication method of polyurethane packaging foam. In order to increase the therapeutic functionality, the scaffolds were coated with mesoporous silica particles (MCM-41), which act as an *in situ* drug delivery system. These sub-micron spheres are characterized by large surface area and pore volume with a narrow pore diameter distribution. The solution used for the synthesis of the silica mesoporous particles was designed to obtain a high-ordered mesoporous structure and spherical shape – both are key factors for achieving the desired controlled drug release. The MCM-41 particles were synthesized directly inside the BG-based scaffolds, and the drug-release capability of this combined system was evaluated. Moreover, the effect of MCM-41 particle coating on the bioactivity of the BG-based scaffolds was assessed. The results indicate that it is possible to obtain a multifunctional scaffold system characterized by high and interconnected porosity, high bioactivity, and sustained drug delivery capability.

Keywords: ordered mesoporosity, silica, MCM-41, bioactive glass, scaffolds, drug release, ibuprofen

INTRODUCTION

One of the most promising fields of tissue engineering is the development of porous 3D engineered scaffolds to enhance bone regeneration and neovascularization (Porter et al., 2009). The main challenge is the design of materials able to match at the same time the biological and the mechanical properties of the natural bone tissue (Mastrogiacomo et al., 2006; Stevens, 2008; Philippart et al., 2015). However, the design of the scaffolds is not the only challenge, in fact the first problem after implantation is the exposure to inflammatory and infection risks with further complications, e.g., septicemia and potential implant failure (Misch and Wang, 2008). To avoid these consequences,

a large amount of antibiotics and anti-inflammatory drugs are administered to the patient, which can increase the healing time, the stay at the hospital, and costs (Neut et al., 2003). Nowadays, the most popular ways for drug intake are oral administration and injection. However, these methods may be affected by a lack of efficiency especially since the release of the drug is not targeted to the area that needs to be treated (Vallet-Regí et al., 2012a). For all these reasons, the development of local drug-release systems, which enable controlled release kinetics, has increased considerably during the past few years (Vallet-Regí, 2006a; Slowing et al., 2007; Cotí et al., 2009; Vitale-Brovarone et al., 2009; Wu et al., 2013). In this context, the combination of bioactive scaffolds with local drug delivery carriers is gaining increasing research efforts in the bone tissue engineering field (Philippart et al., 2015). Several matrices have been tested so far, such as organic polymers, organic–inorganic hybrid materials, bioactive glasses (BG), and ceramics (Wu and Chang, 2014). One approach gaining increasing interest involves obtaining drug carriers that are structured at the nanoscale. Since 1992, when silica-based MCM-41 was developed (Mobil Composition of Matter No. 41) (Beck et al., 1992), highly ordered mesoporous materials have attracted the attention of many scientists and in 2001 they were proposed as drug delivery system (Vallet-Regí et al., 2001). The most interesting features of these materials are the regular pore system, high specific surface area and high pore volume (Vallet-Regí et al., 2001, 2012a,b; Vallet-Regí, 2006b; Zhao et al., 2013). These silica-based mesoporous materials are able to incorporate relatively high content of drugs into the mesopores. Moreover, their silanol groups can be functionalized (**Figure 1**) and the pore diameter can be modulated, allowing a better control of the drug-release kinetic (Grün et al., 1997; Vallet-Regí et al., 2001, 2012b; Vallet-Regí, 2006b; Wu and Chang, 2014). Two mechanisms have been proposed to describe mesoporous silica material formation. The first model describes the addition

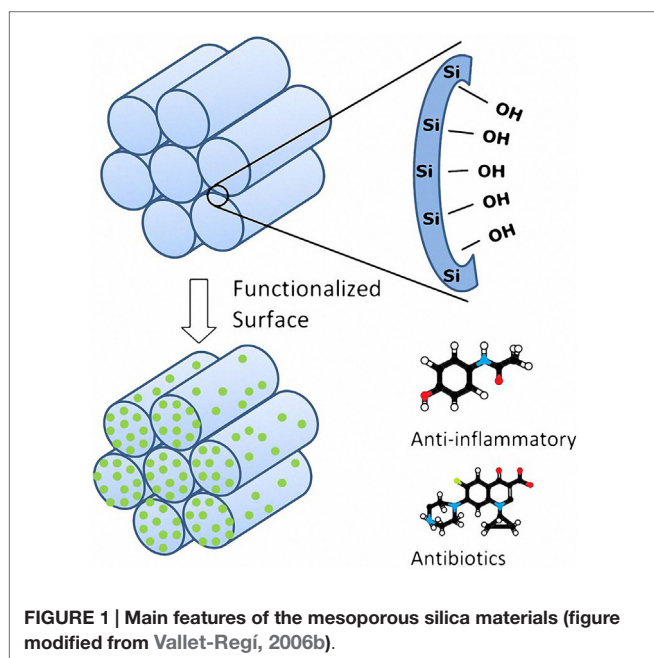
of silicate to micelles formed using *n*-decyltrimethylammonium bromide. In this way, the silica precursor polymerizes around the already formed micelles (Zhao et al., 2013). The second proposed mechanism is that the addition of the silica precursor to an aqueous *n*-decyltrimethylammonium bromide solution induces the ordering of silica-encased surfactant micelles simultaneously. In this case, the micelle formation requires the silica precursor to be present (Vallet-Regí et al., 2012a; Zhao et al., 2013).

MCM-41 has become the most popular member of the mesoporous silicate materials family, and it has been considered also as drug carrier (Vallet-Regí et al., 2012b). Nowadays, it is possible to find in literature different approaches for the synthesis of spherical MCM-41 (Grün et al., 1999; Cai et al., 2001; Zelenák et al., 2008; Liu et al., 2009). Grün et al. (1997, 1999) proposed a novel pathway for the production of spherical MCM-41 applying a modification of the Stöber reaction (Stober and Fink, 1968) for the synthesis of spherical non-porous silica particles. The approach involves introducing a low-boiling alcohol, such as ethanol or isopropanol, as co-solvent for the silica source in order to get a more homogeneous solution (Grün et al., 1999). Starting from the work of Grün et al. (1999), it is possible to obtain well-shaped spherical particles; however, the mesoporosity is not homogeneously present. On the other hand, following a standard procedure reported by Zelenák et al. (2008), it is possible to obtain well-ordered mesoporous structures; however, the particles are not spherical and the size distribution is usually broad. Combining these two synthesis pathways, a new solution for the synthesis of spherical mesoporous silica particles has been proposed in this study. Thus, the aim of the present work is the synthesis of spherical silica mesoporous particles (MCM-41) inside porous BG-based scaffolds [45S5 BG composition (Hench, 2015)] to combine in the same system the drug uptake and release capabilities of this mesoporous material with the bioactivity properties of the BG. The concept of incorporating a silica drug carrier into bioactive silicate scaffolds has been previously explored (Mortera et al., 2008); however, the main advantage of the approach introduced in this paper is the possibility to obtain a highly homogeneous coating of the BG scaffold struts with highly ordered mesoporous silica particles without affecting the BG bioactivity. Moreover, the total amount of produced particles obtained per single batch increases by ~60% combining the two standard procedures reported in literature (Grün et al., 1999; Zelenák et al., 2008), which represents another advantage of the present approach.

MATERIALS AND METHODS

MCM-41 Particle Synthesis

The procedure adopted to prepare MCM-41 was a combination of the standard pathway for the production of mesoporous silica particles and a modification of the Stöber reaction (Stober and Fink, 1968) for the preparation of non-porous silica spheres proposed by Grün et al. (1999). In this way, the reaction took place in a more homogeneous environment, resulting in the formation of sub-micron sized spherical MCM-41 particles and the total amount of the cationic surfactant, which is extremely toxic, can be



reduced (Grün et al., 1999). A low-boiling alcohol such as ethanol was added as co-solvent for the tetra-*n*-alkoxysilane to make it soluble. The reactants were ammonia (catalyst of the reaction), *n*-hexadecyltrimethylammonium bromide (CTAB, surfactant), pure ethanol (co-solvent of silica source), and tetraethyl orthosilicate (TEOS), all purchased from Sigma-Aldrich (Germany). Pure ethanol and ammonia (28–30 wt.%) solution were mixed with deionized water. The cationic surfactant was added to the solution under continuous stirring for 20 min. Once the solution was clear, TEOS was added (0.25 mL min⁻¹). All synthesis steps were carried out at room temperature (RT), which is the optimal temperature condition for the reaction with cationic surfactant in basic conditions as reported by Zhao et al. (2013). After 2 h of stirring, the resulting dispersion was centrifuged and washed once with deionized water and twice with ethanol in order to remove completely every trace of ammonia, collected in a ceramic crucible, dried, and calcined in air. The solutions used are reported in Table 1. For samples MCM-41_A (Zeleňák et al., 2008), MCM-41_B, and MCM-41_C, the thermal treatment was 60°C (2°C min⁻¹) for 12 h and 550°C (2°C min⁻¹) for 6 h; for sample MCM-41_D (Grün et al., 1999), the thermal treatment was 90°C (2°C min⁻¹) for 12 h and 550°C (1°C min⁻¹) for 5 h.

Scaffolds Preparation

The template used to prepare 3D porous scaffolds was polyurethane (PU) packaging foams (45 ppi) (Eurofoam Deutschland GmbH Schaumstoffe). BG powder (particle size 5 µm of 45S5 composition) was used. 45S5 BG-based scaffolds were produced by the replica technique, according to the method described by Chen et al. (2006). Briefly, the slurry for the scaffolds fabrication was prepared by dissolving polyvinyl alcohol (PVA) in deionized water at 80°C for 1 h, the concentration being 0.01 mol L⁻¹. Then, 45S5 BG powder was added to 25 mL PVA–water solution to obtain a concentration of 40 wt.%. Each procedure was carried out under vigorous stirring using a magnetic stirrer for 1 h. The sacrificial PU templates, cut to cylinders (7 mm in height and 5 mm in diameter), were immersed in the slurry for 10 min. The foams were retrieved and the extra slurry was completely squeezed out manually. The samples were then dried at RT for at least 12 h. The dip coating in the slurry was repeated three times to increase the coating thickness and consequently the mechanical properties. After the second and third coating, the extra slurry was completely removed using compressed air as explained elsewhere (Boccardi et al., 2015). Post-foaming heat treatment for the burning-out of the sacrificial template

and sintering of the BG structure was programmed. The burning and sintering conditions were: 400°C for 1 h and 1050°C for 1 h, respectively. The heating and cooling rates were 2 and 5°C min⁻¹, respectively.

Composite System Preparation

MCM-41_A, MCM-41_B, and MCM-41_D samples were used for the preparation of BG_MCM-41 composite scaffolds. MCM-41_C solution was not used because it did not show any ordered mesoporosity. The coating procedure used here was similar to the one reported by Mortera et al. (2008). The procedure consisted of four steps, i.e., hydrolysis of TEOS in MCM-41-synthesis solution, dipping of scaffolds for particles impregnation, drying of the scaffolds, and calcination (heat treatment) for the removal of the surfactant. After TEOS addition, the solution was stirred for 10 min to promote the hydrolysis of the silica precursor. Scaffolds were then immersed in the silica synthesis batch for 10 min and meanwhile the solution was kept under vigorous stirring in order to enhance the coating of the inner core of the BG scaffolds. The resulting BG-based scaffolds coated with the MCM-41 particles were heat-treated at 60°C (2°C min⁻¹) for 12 h for drying and at 550°C (2°C min⁻¹) for 6 h in air as reported in Figure 2.

Drug-Release Test

To load silica particles with a drug, Ibuprofen (>98%, purchased from Sigma-Aldrich) as model drug was dissolved in hexane (33 mg mL⁻¹) and MCM-41 particles were added to the drug solution (33 mg mL⁻¹) at RT following the procedure presented in literature (Vallet-Regí et al., 2001). The samples with the drug solution were then placed in a vacuum hood at RT at 300 mbar for 10 min in order to enhance the drug infiltration inside the mesoporosity. After 12 h, this procedure was repeated, the drug solution was removed and the particles were dried in a vacuum

TABLE 1 | Composition of four different synthesis solutions used for the preparation of mesoporous silica particles.

Sample	H ₂ O (mL)	EtOH (mL)	NH ₃ (mL)	CTAB (g)	TEOS (mL)
MCM-41_A (Zeleňák et al., 2008)	29	–	18.5	0.2	1
MCM-41_B	11	18	18.5	0.2	1
MCM-41_C	4	25	18.5	0.2	1
MCM-41_D (Grün et al., 1999)	11	19	3.3	0.62	1.25

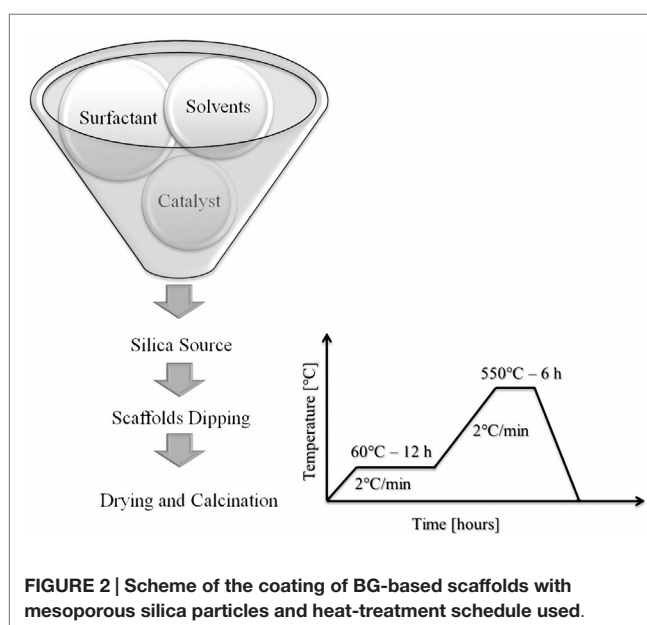


FIGURE 2 | Scheme of the coating of BG-based scaffolds with mesoporous silica particles and heat-treatment schedule used.

hood at RT. All the particle synthesis solutions were tested for their drug-releasing capability.

The scaffolds coated with MCM-41_B were in contact with the drug solution for 3 days (10 mg mL^{-1}) before the starting of the drug-release test, in order to get a better infiltration of the drug. Only the scaffolds coated with MCM-41_B particles were considered for the test, because the resulting particles were still spherical and with ordered mesoporosity and the results were compared with those obtained on scaffolds not coated with MCM-41.

The drug-release kinetics from all samples, particles (10 mg each sample), and scaffolds was assessed by soaking the samples in 4 mL of PBS, kept at 37°C until the complete release of ibuprofen. At every time point, 1 mL of solution was uptake for the drug-release analysis and substituted with 1 mL of fresh PBS. A UV-vis spectrophotometer was used to evaluate the amount of released drug. The calibration curve was calculated using a solution of ibuprofen in PBS with different known concentrations, on the basis of the absorption at 273 nm , typical of this molecule (Vallet-Regí et al., 2001).

Bioactivity and Stability of the Composite System

Simulated body fluid (SBF) was prepared by dissolving reagent-grade $8.035 \text{ g L}^{-1} \text{ NaCl}$, $0.355 \text{ g L}^{-1} \text{ NaHCO}_3$, $0.225 \text{ g L}^{-1} \text{ KCl}$, $0.231 \text{ g L}^{-1} \text{ K}_2\text{HPO}_4 (3\text{H}_2\text{O})$, $0.311 \text{ g L}^{-1} \text{ MgCl}_2 (6\text{H}_2\text{O})$, $0.292 \text{ g L}^{-1} \text{ CaCl}_2$, and $0.072 \text{ g L}^{-1} \text{ Na}_2\text{SO}_4$ in deionized water and buffered at $\text{pH } 7.4$ at 36.5°C with 6.118 g L^{-1} tris(hydroxymethyl) aminomethane $[(\text{CH}_2\text{OH})_3\text{CNH}_2]$ and 1 M HCl , as previously reported by Kokubo and Takadama (2007). Cylindrical BG foams coated and not coated with mesoporous silica particles were immersed in SBF at a 1.5 g L^{-1} ratio (Cerruti et al., 2005). The stability of the MCM-41 coating was evaluated in Tris-buffered solution [tris(hydroxymethyl) aminomethane]. Only the scaffolds coated with MCM-41_B were tested, because the silica particles showed suitable features in terms of homogeneous coating, shape, and ordered mesoporosity. In both cases, the solution was kept in a polystyrene container at 37°C in a shaking incubator (90 rpm) up to 1 week. The solution was renewed every 2 days in order to better mimic the *in vivo* behavior, as carried out also in previous studies (Chen et al., 2006). At the end of the incubator period, the foams were washed with deionized water, dried, and stored for further characterizations.

Characterization Techniques

The shape and the surface structure of the resulting MCM-41 particles and BG_MCM-41 were evaluated by means of scanning electron microscope (SEM) (Auriga 0750 from ZEISS). The porous structure of the particles was assessed with high-resolution transmission electron microscopy (HRTEM) (Phillips CM30) operating at an acceleration voltage of 300 kV . For the TEM observation, the samples were dispersed with ethanol on a lacey carbon film. The pore diameter analyses were conducted on HRTEM images with ImageJ analysis software. Small angle X-ray diffraction (SAXRD), carried out using Philips Xpert Diffractometer, was used to analyze the porous structure and the pore diameter of the silica particles. Diffraction data were

recorded between 1 and $10^\circ 2\theta$ at an interval of $0.02^\circ 2\theta$. Nitrogen adsorption desorption analysis was conducted at 77 K in a Quantachrome Autosorb Instrument to assess the specific surface area and the pore size of the particles. Prior to the measurements, the samples were outgassed for 12 h at 300°C under vacuum. The specific surface area and pore size of MCM-41 microspheres were evaluated, respectively, with BET method and BJH method.

RESULTS

MCM-41 Particles

The morphology and the microstructure of the obtained MCM-41 particles were assessed by HRTEM micrographs. HRTEM images of sample MCM-41_A and MCM-41_B showed the existence of highly ordered hexagonal array and streaks structural features (Figures 3a–d). The hexagonal array and the streaks are the view of the crystals whose axes are, respectively, parallel and perpendicular to the line of vision. Sample MCM-41_C, which was prepared with a high concentration of ethanol in the synthesis solution, was porous however the porosity was not ordered (Figures 3e,f). Moreover MCM-41_D particles were porous but the porosity was not completely ordered, in contrast with the results reported in literature (Grün et al., 1999) (Figures 3g,h). From the analysis of the HRTEM images with ImageJ analysis software, the dimension of the pores was evaluated, which was found to be around 3 nm for all samples (Figure 4). The analysis has been done applying the Fast Fourier Transform (FFT) and the inverse FFT (Figure 4A) to the image, and the plug in plot (Figure 4B) has been used to evaluate the distance between the pore channels.

The pore size dimensions were confirmed also by SAXRD analysis. The spectra of sample MCM-41_A exhibited three sharp peaks, called Bragg peaks, indicating the long-range order present in the material, which is typical of MCM-41 materials (Vallet-Regí et al., 2001) (Figure 5A) in agreement with literature (Grün et al., 1999). These peaks arise from the quasi-regular arrangement of the mesopores in the bulk material (Grün et al., 1999; Vallet-Regí et al., 2001). The Bragg peaks can be indexed assuming a hexagonal symmetry. 2θ values of sample MCM-41_A namely 2.75 , 4.65 , and 5.10 can be indexed as (100), (110), and (200) reflections, respectively. These values were close to those reported by Grün et al. (1999). The repeating distance, a_0 , between two pore centers may be calculated by $a_0 = (2/\sqrt{3})d_{100}$. The pore diameter can be evaluated from a_0 subtracting 1.0 nm , which is approximately the value of the pore wall thickness (Grün et al., 1999). For MCM-41_B particles, it was possible to identify unequivocally only the main peak (100) (Figure 5B), meanwhile the 110 and 200 peaks were less pronounced but still visible. The SAXRD results combined with HRTEM results confirm thus the mesoporous ordered structures of MCM-41_A and MCM-41_B particles.

For samples MCM-41_C and MCM-41_D, only the main peak (100) was identified, in agreement with the HRTEM analysis (Figures 5C,D). The first peak is in fact an indicator of the presence of mesoporosity in the sample. Also in this case, it was

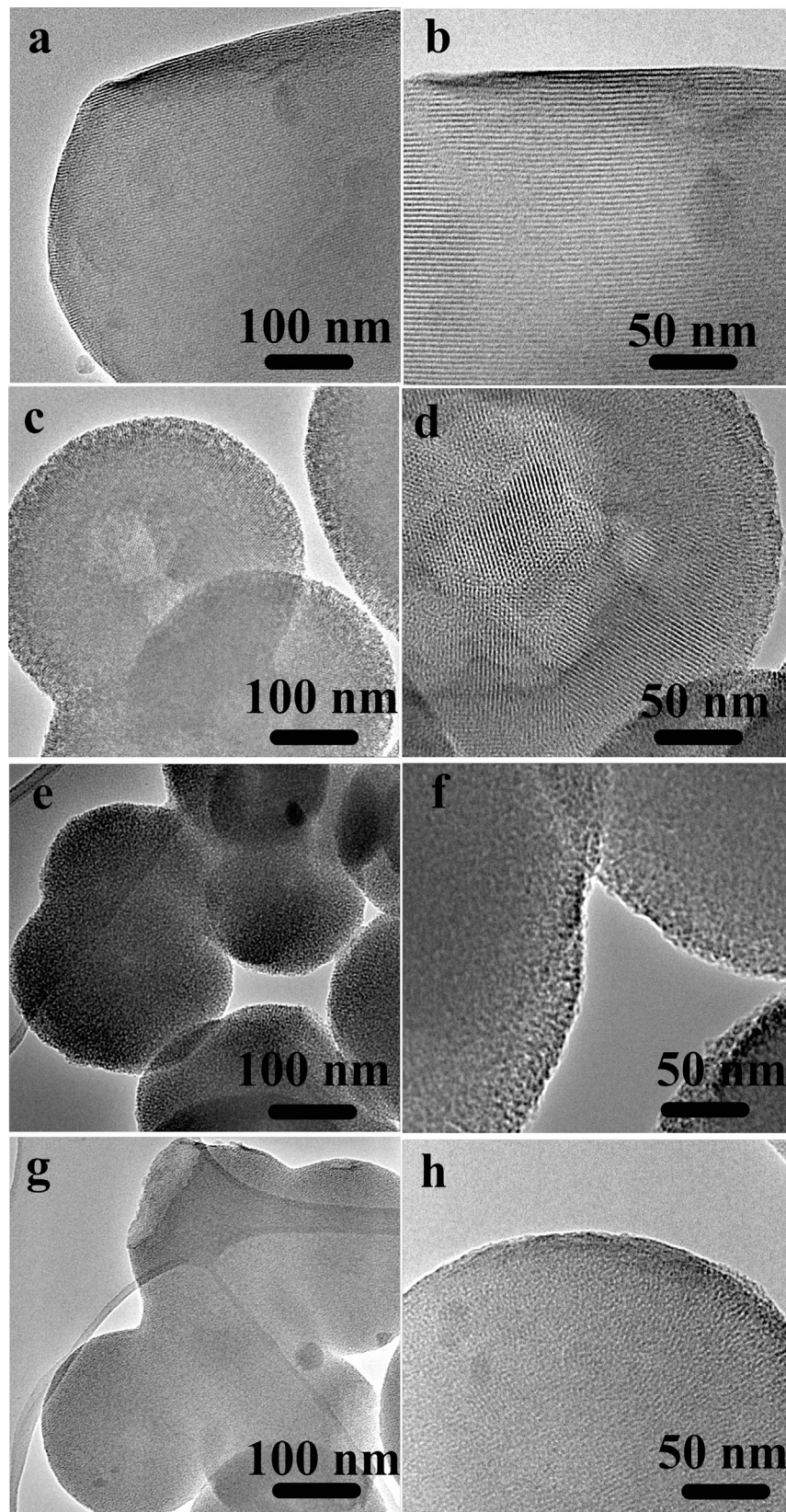


FIGURE 3 | HRTEM images of sample MCM-41_A (a,b) and sample MCM-41_B (c,d), which are characterized by ordered mesoporosity, sample MCM-41_C (e,f) and MCM-41_D (g,h), which are characterized by a disordered porosity.

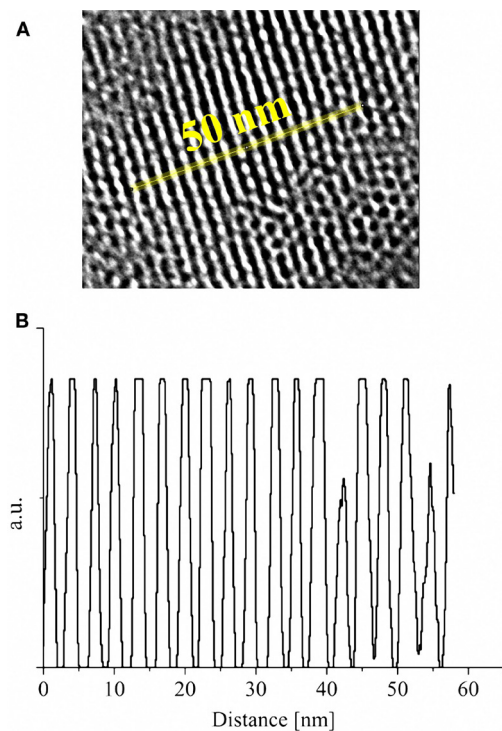


FIGURE 4 | High-resolution image of the ordered mesoporous structure of MCM-41_B after analysis with FFT and inverse FFT (A); plot of the distance between the pore channels obtained with ImageJ plug in plot applied along the yellow line (B).

possible to evaluate the pore diameter with the Bragg's law and the resulting values were in agreement with the ImageJ analysis.

The nitrogen isotherms of sample MCM-41_B are shown in **Figure 6**. The isotherms can be classified as type IV isotherms according to the IUPAC nomenclature for MCM-41 (Vallet-Regí et al., 2012a; Zhao et al., 2013), which is typical of mesoporous material with pore diameter in the range of 2–10 nm. MCM-41_B particles were characterized by a specific surface area of $951 \text{ m}^2 \text{ g}^{-1}$ and a pore volume of $0.24 \text{ cm}^3 \text{ g}^{-1}$. From **Figure 7**, it was possible to observe how the different amounts of solvent influenced the final shape and mesostructure of the resulting MCM-41 particles. The particles produced with only deionized water (**Figures 7a,b**) as solvent were characterized by hexagonal and not spherical geometry (MCM-41_A). Progressively increasing the amount of ethanol as co-solvent, it was possible to produce spherical particles, which exhibited a fairly homogeneous distribution of particle size but reduced mesoporosity order (**Figures 7e,f**).

Composite Scaffold System

From SEM analysis, it was possible to observe that the surface of scaffolds was completely coated after immersion in the MCM-41 synthesis batch maintaining an open porosity. In the case of the synthesis solution of MCM-41_A (Zeleňák et al., 2008) (**Figures 8a,b**), the one without ethanol as co-solvent, the shape of the resulting MCM-41 particles was seen to be completely changed. The presence of the scaffold affected the formation of the particles, probably due to a reduction in the homogeneity of the solution. Moreover, with this solution,

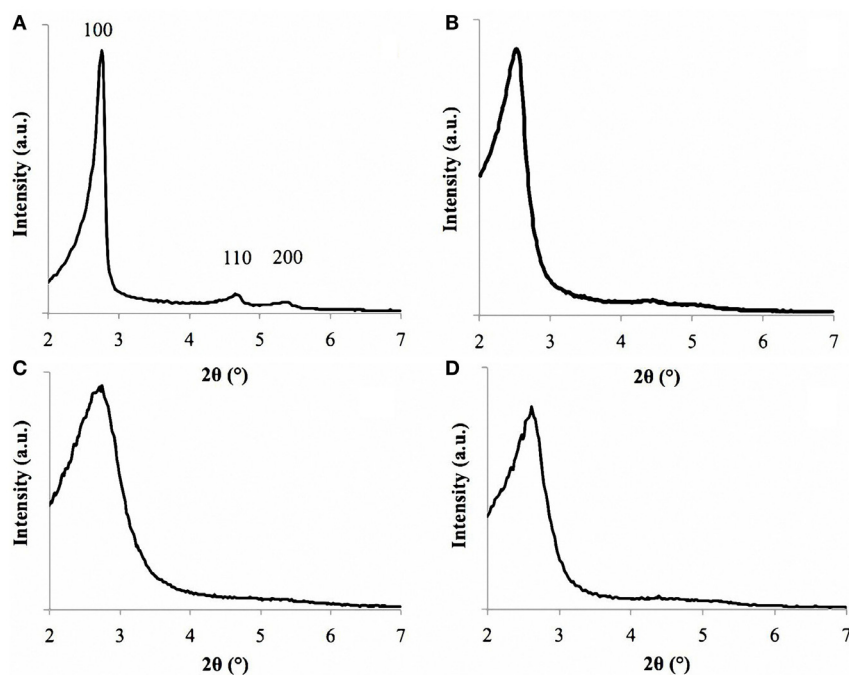


FIGURE 5 | SAXRD of sample MCM-41_A (A), MCM-41_B (B), MCM-41_C (C), and MCM-41_D (D). Sample MCM-41_A is characterized by the three peaks, labeled as 100, 110, and 200.

it was not possible to obtain a homogenous coverage of the BG scaffold surface. With the synthesis solution of samples MCM-41_B (Figures 8c,d) and MCM-41_D (Grün et al., 1999) (Figures 8e,f), the resulting particles on the surface of the BG scaffolds were still perfectly spherical and they covered completely the surface of the scaffold struts. By means of HRTEM analysis, it was also possible to confirm that the MCM-41_B particles still exhibited ordered mesoporosity, as shown in Figure 9.

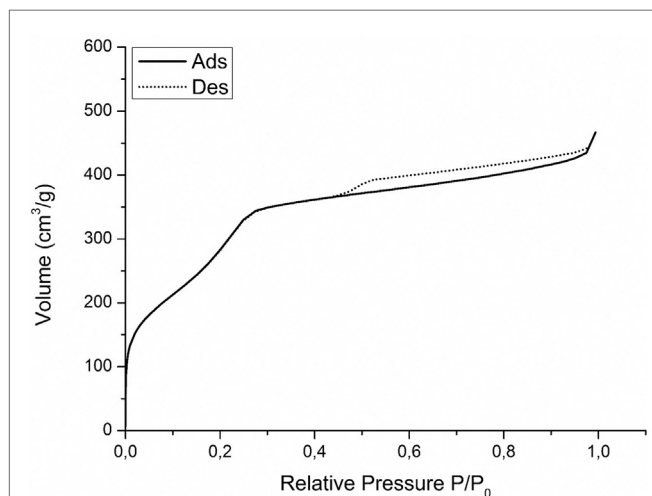


FIGURE 6 | Nitrogen adsorption-desorption isotherms on MCM-41_B.

Drug-Release Capability of MCM-41 Particles

The drug-release capability of the different mesoporous silica particles was evaluated and the released profiles are reported in Figure 10. Both samples MCM-41_A (Figure 10A) and MCM-41_D (Figure 10D) were characterized by a burst release and it was confirmed that after 1 h of test, the 80% of the loaded drug was released. The rest 20% of the drug was released within the next 7 days. The particles prepared with solutions MCM-41_B and MCM-41_C showed the best drug-release profile (Figures 10B,C), in terms of lack of uncontrolled burst release. Especially MCM-41_B, which was characterized by high-ordered mesoporosity, did not show any burst release during the first hours of the test. Eighty percent of the loaded drug was in fact released only after 30 h and the rest of the ibuprofen was released within the seven following days. It should be pointed out that ibuprofen solubility in water at 25°C is 21 mg L⁻¹ (Vallet-Regí et al., 2001). During the present release test, the highest concentrations of ibuprofen were lower than its solubility, also after the first hours of release. At every time point, 1 mL of fresh PBS was added to every sample to keep constant the PBS volume and for this reason the solution was highly diluted.

Drug-Release Capability of Composite Scaffold System

The amounts of released ibuprofen from the BG and BG_MCM-41_B scaffolds are shown in Figure 11. The presence of the

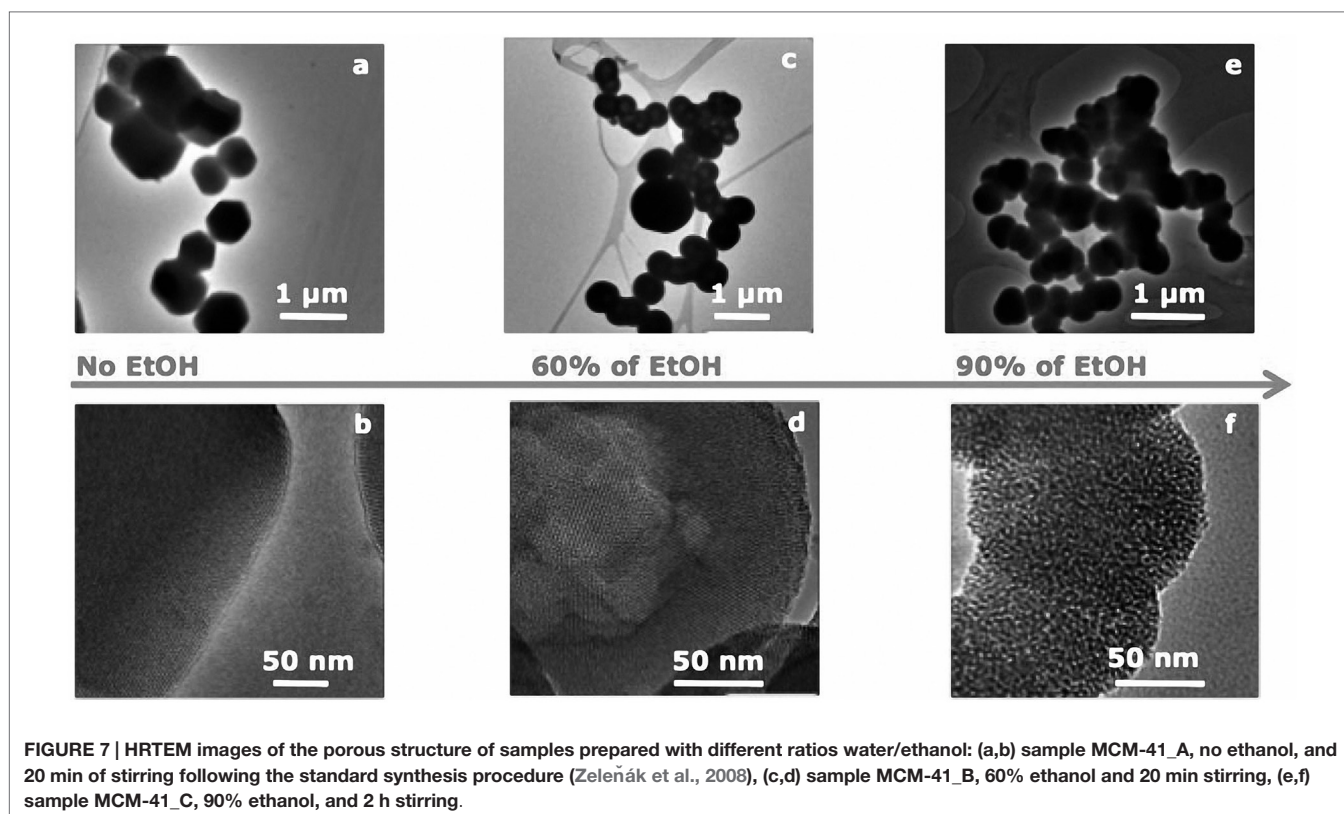


FIGURE 7 | HRTEM images of the porous structure of samples prepared with different ratios water/ethanol: (a,b) sample MCM-41_A, no ethanol, and 20 min of stirring following the standard synthesis procedure (Zeleňák et al., 2008), (c,d) sample MCM-41_B, 60% ethanol and 20 min stirring, (e,f) sample MCM-41_C, 90% ethanol, and 2 h stirring.

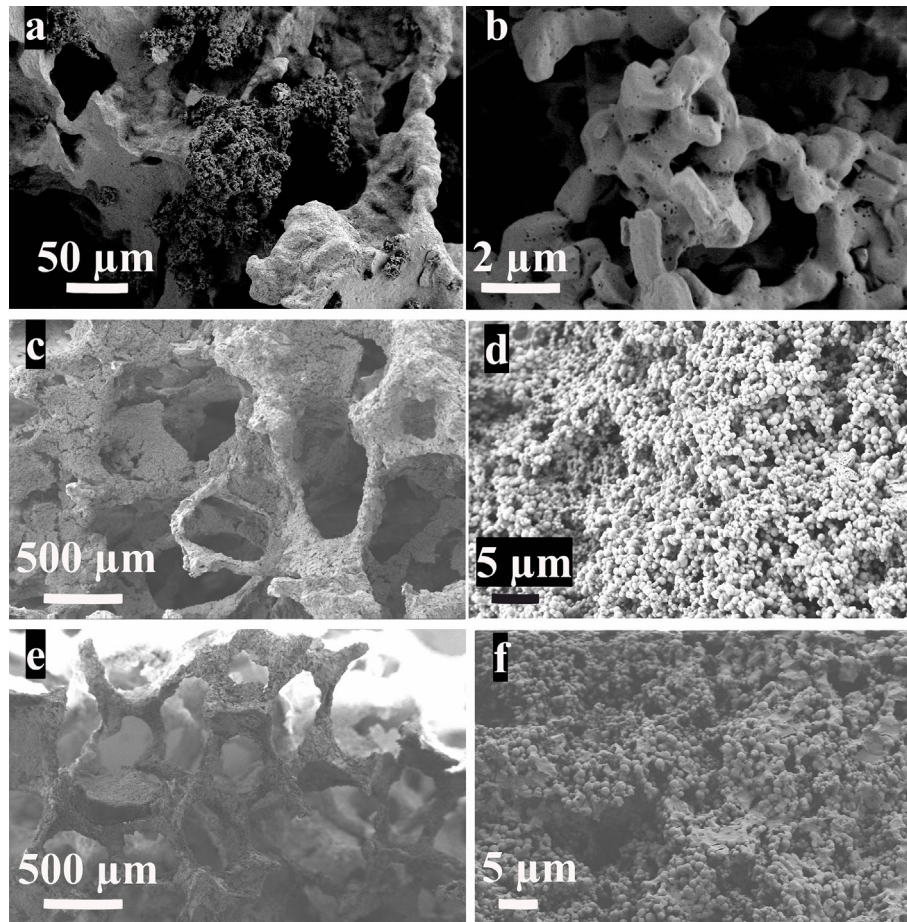


FIGURE 8 | BG-based scaffolds coated with MCM-41_A (Zeleňák et al., 2008) (a,b), MCM-41_B (c,d), and MCM-41_D (Grün et al., 1999) (e,f).

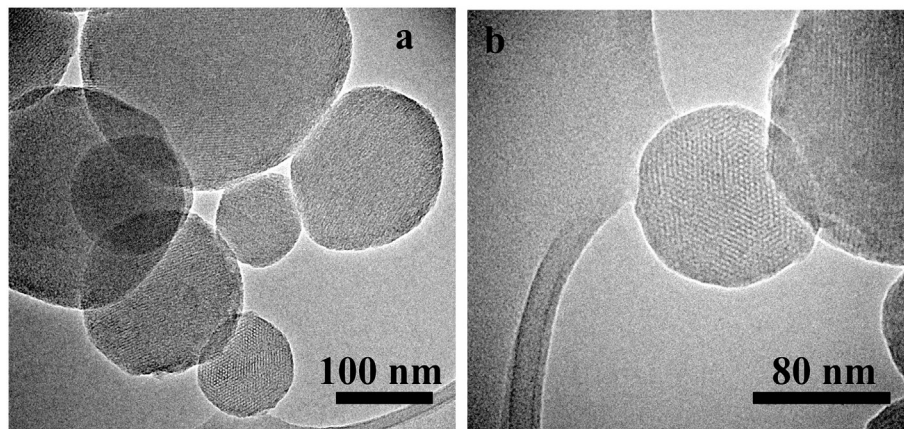


FIGURE 9 | HRTEM images of the MCM-41_B particles coating of BG-based scaffolds at different magnifications. TEM images of few MCM-41_B particles (a) and HRTEM image of a single particle where the ordered mesoporosity was observed (b).

mesoporous silica particles increased the drug incorporation capability, but in both cases most of the drug was released during the first hours of the test. The uncoated BG scaffolds were able to uptake 31 mg_{IBU}/g_{bioglass}, the scaffolds coated with MCM-41_B could uptake 43 mg_{IBU}/g_{bioglass}.

Immersion Test

BG-based scaffolds both uncoated and coated with MCM-41_B particles were immersed in SBF at 37°C. After 1 week of immersion, it was possible to observe that the presence of the silica particles did not affect the bioactivity of the (crystallized)

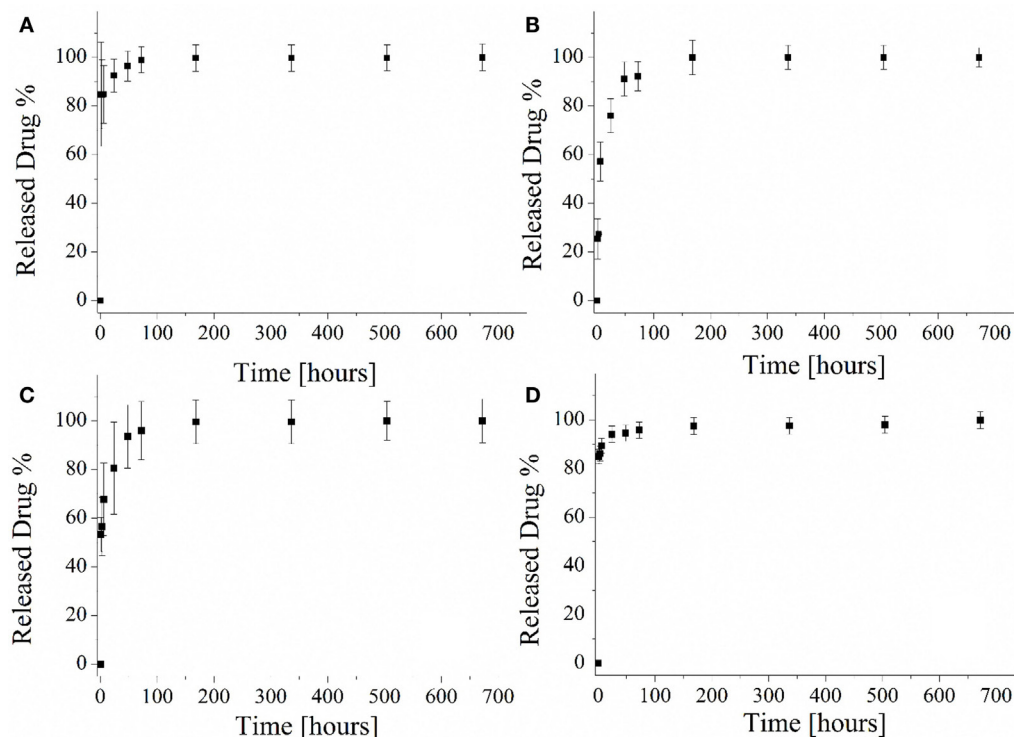


FIGURE 10 | Ibuprofen released profile from MCM-41_A (A), MCM-41_B (B), MCM-41_C (C), and MCM-41_D (D).

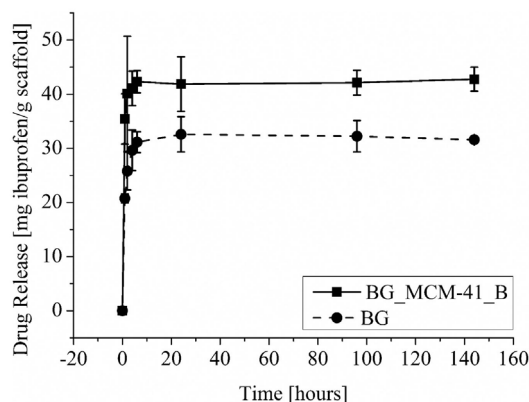


FIGURE 11 | Drug-release profile from BG scaffolds coated with mesoporous silica particles BG_MCM-41 (■) and uncoated (●).

BG struts. In fact on both samples, coated and not coated (Figure 12a), a hydroxycarbonate apatite (HCA) layer formation was seen to form (Figures 12c,d). Moreover, it was possible to confirm the stability of the MCM-41 coating: after 10 days in Tris buffered solution, it was possible to identify the layer of MCM-41 particles covered with the HCA deposit (Figure 12e). The HCA layer was well developed and a deposit was also seen to have formed on the surface of the silica particles (Figures 12f,g, black circle).

DISCUSSION

One of the most investigated areas in the bone tissue engineering field is related to the development and characterization of mechanically robust and porous 3D scaffolds. The main challenge is the design of a material able to match at the same time the biological and mechanical properties of the natural bone and also release ions or drugs able to reduce the risk of inflammation and infections after the implantation. In a previous work of Mortera et al. (2008), the possibility to increase the functionality of BG-based porous scaffolds was considered using a coating with MCM-41 particles as drug delivery system. In this way, it was possible to combine in a single system the drug uptake and release capability of mesoporous materials with the bioactivity of BG. In the present work, a further development of this idea was presented, improving the homogeneity of the coating, assessing the bioactivity and stability of the composite system BG_MCM-41. Four different solutions were evaluated for the preparation of mesoporous silica particles, and an optimal synthesis procedure was found (MCM-41_B). In fact, by combining two different synthesis pathways, both well known in literature (Grün et al., 1999; Zelenák et al., 2008), it was possible to obtain particles characterized by spherical shape and high-ordered mesoporosity as confirmed by HRTEM, SAXRD, and Nitrogen adsorption/desorption analysis (specific surface area $951 \text{ m}^2 \text{ g}^{-1}$, pore volume $0.24 \text{ cm}^3 \text{ g}^{-1}$). Moreover, the efficiency of the synthesis was increased and the total amount of produced particles obtained per single batch increased up to 60% compared to the previous

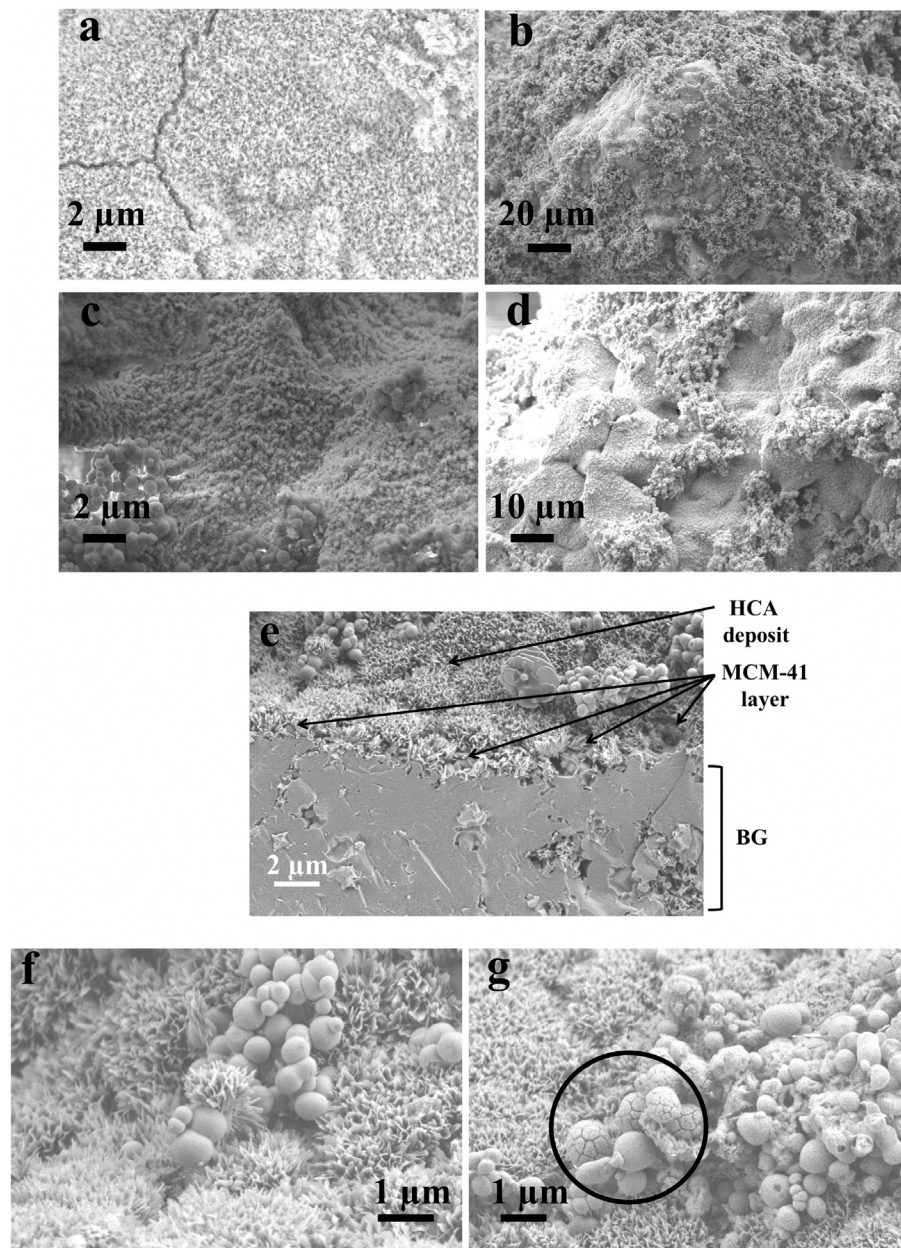


FIGURE 12 | SEM micrographs of BG-based scaffolds uncoated (a) and coated with MCM-41 (b–d) after 1 week in SBF; BG_MCM-41_B scaffolds after immersion in Tris buffered solution for 10 days (e–g).

synthesis procedure: every 500 mL of solution, 4 g of MCM-41_B were produced. MCM-41_B showed the best drug-release profile not exhibiting any burst release during the first hours of the test. The 80% of the loaded drug was in fact released only after 30 h and the rest of the ibuprofen was released within the seven following days. The drug-release times obtained during this work are in agreement with previous studies on drug-release capability of mesoporous silica particles (Vallet-Regí et al., 2001). These novel synthesis solution was used for the coating of 3D BG scaffolds. Due to the high amount of particles produced during

the synthesis, a highly homogeneous coating of the scaffolds was obtained. After the coating procedure, the particles were still spherical in shape and also the ordered mesoporosity was not affected. This was an improvement compared to previous works, in which the coatings were not homogeneously distributed on the surface of the scaffolds and the particles were not characterized by ordered mesoporosity (Mortera et al., 2008). The system BG_MCM-41 was assessed to be bioactive. In fact after 1 week of immersion in SBF on the surface of both coated and not coated scaffolds, a layer of HCA was observed. It has been

reported in literature that MCM-41 particles are not bioactive and formation of HCA on their surface was not observed after 2 months of immersion in SBF due to the small pore size and the lower concentration of silanol groups ($\sim 2 \text{ mmol SiOH m}^{-2}$) in comparison to other silica particles such as SBA-15 and MCM-48 (Vallet-Regí et al., 2006), which can act as nucleation sites for the apatite layer. This behavior confirms that MCM-41 particles did not have a negative effect on the bioactivity of the BG scaffolds, on the contrary, combined with BG, they seem to enhance the bioactivity. Moreover, most of the MCM-41 particles were still on the surface of the scaffold and some of them are seen to be also coated with HCA in SEM images (Figures 12f–g). The MCM-41 particles were in fact adhered to the glass surface due to the thermal treatment: the calcination at 550°C is likely to induce softening of the glass (Lefebvre et al., 2007) which should facilitate adhesion of the MCM-41 spheres. For this reason, the MCM-41 particles coating was stable on the surface of the BG scaffold also after immersion in SBF. Moreover, the presence of the particles on the surface of the BG scaffolds increased the drug uptake capability of the scaffolds compared to the not

coated ones. Thanks to the ordered mesoporosity and the pore size in the range of 3 nm, MCM-41 particles were thus confirmed to be an optimal drug delivery carrier.

ACKNOWLEDGMENTS

The authors would like to thank Dipl.-Ing Jürgen Vargas Schmitz (Chair of Separation Science and Technology, University of Erlangen-Nuremberg, Germany) and Dr. Alexandra Inayat (Institute of Chemical Reaction Engineering, University of Erlangen-Nuremberg, Germany) for assistance in N_2 physisorption measurements and Lucia Pontiroli (Applied Science and Technology Department, Politecnico di Torino, Italy) for SAXRD analysis.

FUNDING

This research was carried out in the framework of the EU ITN FP-7 project “GlaCERCo.” The authors would like to acknowledge its financial support.

REFERENCES

- Beck, J. S., Chu, C. T.-W., Johnson, I. D., Kresge, C. T., Leonowicz, M. E., Roth, W. J., (1992). *U.S. Patent* 5 108 725.
- Boccardi, E., Philippart, A., Juhasz-Bortuzzo, J. A., Novajra, G., Vitale-Brovarone, C., and Boccaccini, A. R. (2015). Characterisation of Bioglass®-based foams developed via replication of natural marine sponges. *Adv. Appl. Ceram.* doi:10.1179/1743676115Y.0000000036
- Cai, Q., Luo, Z., Pang, W., Fan, Y., Chen, X., and Cui, F. (2001). Dilute solution routes to various controllable morphologies of MCM-41 silica with a basic medium. *Chem. Mater.* 10, 258–263. doi:10.1021/cm990661z
- Cerruti, M., Greenspan, D., and Powers, K. (2005). Effect of pH and ionic strength on the reactivity of Bioglass® 45S5. *Biomaterials* 26, 1665–1674. doi:10.1016/j.biomaterials.2004.07.009
- Chen, Q., Thompson, I., and Boccaccini, A. R. (2006). 45S5 Bioglass-derived glass-ceramic scaffolds for bone tissue engineering. *Biomaterials* 27, 2414–2425. doi:10.1016/j.biomaterials.2005.11.025
- Coti, K. K., Belowich, M. E., Liong, M., Ambrogio, M. W., Lau, Y. A., Khatib, H. A., et al. (2009). Mechanised nanoparticles for drug delivery. *Nanoscale* 1, 16–39. doi:10.1039/b9nr00162j
- Grün, M., Lauer, I., and Unger, K. K. (1997). The synthesis of micrometer- and submicrometer-size spheres of ordered mesoporous oxide MCM-41. *Adv. Mater.* 3, 254–257. doi:10.1002/adma.19970090317
- Grün, M., Unger, K. K., Matsumoto, A., and Tsutsumi, K. (1999). Novel pathways for the preparation of mesoporous MCM-41 materials: control of porosity and morphology. *Microporous Mesoporous Mater.* 27, 207–216. doi:10.1016/S1387-1811(98)00255-8
- Hench, L. L. (2015). Opening paper 2015 – some comments on Bioglass: four eras of discovery and development. *Biomed. Glasses* 1, 1–11. doi:10.1515/bglass-2015-0001
- Kokubo, T., and Takadama, H. (2007). How useful is SBF in predicting in vivo bone bioactivity? *Biomaterials* 27, 2907–2915. doi:10.1016/j.biomaterials.2006.01.017
- Lefebvre, L., Chevalier, J., Gremillard, L., Zenait, R., Thollet, G., Bernache-Assolant, D., et al. (2007). Structural transformation of bioactive glass 45S5 with thermal treatments. *Acta Biomater.* 55, 3305–3313. doi:10.1016/j.actamat.2007.01.029
- Liu, X., Sun, H., Chen, Y., Yang, Y., and Borgna, A. (2009). Preparation of spherical large-particle MCM-41 with a broad particle-size distribution by a modified pseudomorphic transformation. *Microporous Mesoporous Mater.* 121, 73–78. doi:10.1016/j.micromeso.2009.01.018
- Mastrogioacomo, M., Scaglione, S., Martinetti, R., Dolcini, L., Beltrame, F., Cancedda, R., et al. (2006). Role of scaffold internal structure on in vivo bone formation in macroporous calcium phosphate bioceramics. *Biomaterials* 27, 3230–3237. doi:10.1016/j.biomaterials.2006.01.031
- Misch, K., and Wang, H. L. (2008). Implant surgery complications: etiology and treatment. *Implant Dent.* 17, 159–168. doi:10.1097/ID.0b013e3181752f61
- Mortera, R., Onida, B., Fiorilli, S., Cauda, V., Brovarone, C. V., Baines, F., et al. (2008). Synthesis and characterization of MCM-41 spheres inside bioactive glass-ceramic scaffold. *Chem. Eng. J.* 137, 54–61. doi:10.1016/j.cej.2007.07.094
- Neut, D., Jim, R., Theo, G., Henny, C., and Henk, J. (2003). Detection of biomaterial-associated infections in orthopaedic joint implants. *Clin. Orthop. Relat. Res.* 413, 261–268. doi:10.1097/01.blo.0000073345.50837.84
- Philippart, A., Boccaccini, A. R., Fleck, C., Schubert, D. W., and Roether, J. A. (2015). Toughening and functionalization of bioactive ceramic and glass bone scaffolds by biopolymer coatings and infiltration: a review of the last 5 years. *Expert Rev. Med. Devices* 12, 93–111. doi:10.1586/17434440.2015.958075
- Porter, J. R., Ruckh, T. T., and Popat, K. C. (2009). Bone tissue engineering: a review in bone biomimetics and drug delivery strategies. *Biotechnol. Prog.* 25, 1539–1560. doi:10.1002/btpr.246
- Slowing, I. I., Trewyn, B. G., Giri, S., and Lin, V. S. Y. (2007). Mesoporous silica nanoparticles for drug delivery and biosensing applications. *Adv. Funct. Mater.* 17, 1225–1236. doi:10.1002/adfm.200601191
- Stevens, M. M. (2008). Biomaterials for bone tissue engineering. *Mater. Today* 11, 18–25. doi:10.1016/S1369-7021(08)70086-5
- Stober, W., and Fink, A. (1968). Controlled growth of monodisperse silica spheres in the micron size range. *J. Colloid Interface Sci.* 69, 62–69. doi:10.1016/0021-9797(68)90272-5
- Vallet-Regí, M. (2006a). Revisiting ceramics for medical applications. *Dalton Trans.* 28, 5211–5220. doi:10.1039/b610219k
- Vallet-Regí, M. (2006b). Ordered mesoporous materials in the context of drug delivery systems and bone tissue engineering. *Chemistry* 12, 5934–5943. doi:10.1002/chem.200600226
- Vallet-Regí, M., Manzano-García, M., and Colilla, M. (2012a). *Biomedical Applications of Mesoporous Ceramics*. Boca Raton: CRC Press.
- Vallet-Regí, M., Izquierdo-Barba, I., and Colilla, M. (2012b). Structure and functionalization of mesoporous bioceramics for bone tissue regeneration and local drug delivery. *Philos. Trans. A Math. Phys. Eng. Sci.* 370, 1400–1421. doi:10.1098/rsta.2011.0258
- Vallet-Regí, M., Ramila, A., del Real, R. P., and Perez-Periente, J. (2001). A new property of MCM-41: drug delivery system. *Chem. Mater.* 13, 308–311. doi:10.1021/cm0011559
- Vallet-Regí, M., Ruiz-Gonzalez, L., Izquierdo-Barba, I., and Gonzalez-Calbet, J. M. (2006). Revisiting silica based ordered mesoporous materials: medical applications. *J. Mater. Chem.* 16, 26–31. doi:10.1039/B509744D
- Vitale-Brovarone, C., Baines, F., Miola, M., Mortera, R., Onida, B., and Verné, E. (2009). Glass-ceramic scaffolds containing silica mesophases for bone grafting and drug delivery. *J. Mater. Sci. Mater. Med.* 20, 809–820. doi:10.1007/s10856-008-3635-7

- Wu, C., and Chang, J. (2014). Multifunctional mesoporous bioactive glasses for effective delivery of therapeutic ions and drug/growth factors. *J. Control. Release* 193, 282–295. doi:10.1016/j.jconrel.2014.04.026
- Wu, C., Zhou, Y., Chang, J., and Xiao, Y. (2013). Delivery of dimethyloxallyl glycine in mesoporous bioactive glass scaffolds to improve angiogenesis and osteogenesis of human bone marrow stromal cells. *Acta Biomater.* 9, 9159–9168. doi:10.1016/j.actbio.2013.06.026
- Zelenák, V., Badaničová, M., Halamová, D., Čejka, J., Zukal, A., Murafa, N., et al. (2008). Amine-modified ordered mesoporous silica: effect of pore size on carbon dioxide capture. *Chem. Eng. J.* 144, 336–342. doi:10.1016/j.cej.2008.07.025
- Zhao, D., Wan, Y., and Zhou, W. (2013). *Ordered Mesoporous Materials*. Wiley-VCH Verlag GmbH & Co. KGaA.

Conflict of Interest Statement: The authors declare that the research was conducted in the absence of any commercial or financial relationships that could be construed as a potential conflict of interest.

Copyright © 2015 Boccardi, Philippart, Juhasz-Bortuzzo, Beltrán, Novajra, Vitale-Brovarone, Spiecker and Boccaccini. This is an open-access article distributed under the terms of the Creative Commons Attribution License (CC BY). The use, distribution or reproduction in other forums is permitted, provided the original author(s) or licensor are credited and that the original publication in this journal is cited, in accordance with accepted academic practice. No use, distribution or reproduction is permitted which does not comply with these terms.



Effect of ceramic scaffold architectural parameters on biological response

Maria Isabella Gariboldi* and Serena M. Best

Department of Materials Science and Metallurgy, Cambridge Centre for Medical Materials, University of Cambridge, Cambridge, UK

OPEN ACCESS

Edited by:

Wolfram Höland,
Ivoclar Vivadent AG, Liechtenstein

Reviewed by:

Rajendra K. Singh,
Dankook University, South Korea
Marc Bohner,
RMS Foundation, Switzerland

*Correspondence:

Maria Isabella Gariboldi,
Department of Materials Science and
Metallurgy, Cambridge Centre for
Medical Materials, University of
Cambridge, 27 Charles Babbage
Road, Cambridge CB3 0FS, UK
mig29@cam.ac.uk

Specialty section:

This article was submitted to
Biomaterials, a section of the
journal *Frontiers in Bioengineering
and Biotechnology*

Received: 31 July 2015

Accepted: 18 September 2015

Published: 09 October 2015

Citation:

Gariboldi MI and Best SM (2015)
Effect of ceramic scaffold
architectural parameters on
biological response.
Front. Bioeng. Biotechnol. 3:151.
doi: 10.3389/fbioe.2015.00151

Numerous studies have focused on the optimization of ceramic architectures to fulfill a variety of scaffold functional requirements and improve biological response. Conventional fabrication techniques, however, do not allow for the production of geometrically controlled, reproducible structures and often fail to allow the independent variation of individual geometric parameters. Current developments in additive manufacturing technologies suggest that 3D printing will allow a more controlled and systematic exploration of scaffold architectures. This more direct translation of design into structure requires a pipeline for design-driven optimization. A theoretical framework for systematic design and evaluation of architectural parameters on biological response is presented. Four levels of architecture are considered, namely (1) surface topography, (2) pore size and geometry, (3) porous networks, and (4) macroscopic pore arrangement, including the potential for spatially varied architectures. Studies exploring the effect of various parameters within these levels are reviewed. This framework will hopefully allow uncovering of new relationships between architecture and biological response in a more systematic way as well as inform future refinement of fabrication techniques to fulfill architectural necessities with a consideration of biological implications.

Keywords: scaffold architecture, ceramic scaffolds, bone tissue engineering, 3D printing, graded materials, scaffold design

Introduction

Ceramic scaffold architecture has long been explored as a factor to optimize for bone tissue engineering. While architecture has been shown to affect scaffold performance and biological response, a single optimal scaffold architecture does not exist (Bohner et al., 2011). Different functional necessities, such as mechanical performance and permeability, will often require competing properties (Hollister et al., 2002). Optimized structures will also vary according to defect site due to differences in functional requirements and site-specific aspects, such as location of fluid supply (Bohner et al., 2011). Further, while a range of imaging techniques have been adapted to tissue engineering constructs (Vielreicher et al., 2013), designing and characterizing scaffold geometries systematically remain challenging due to limitations of fabrication techniques and the absence of fully descriptive standardized characterization methods (Bohner et al., 2011; Ashworth et al., 2014). Despite these limitations, the authors believe that a controlled study of the effects of architecture at different length scales on biological response would allow developing an integrated model to optimize scaffold architecture based on the requirements of the patient and the specific defect site.

Studies on the effect of scaffold architecture on biological response have been limited by the inability of conventional fabrication techniques, such as gas foaming and porogen leaching, to vary single parameters independently (Bohner and Baumgart, 2004) as well as issues with consistency of the produced structures (Leong et al., 2003). Some improvements to porogen leaching allow independent variation of pore size and interconnections (Descamps et al., 2008). Recent advances in solid freeform fabrication (SFF) have allowed for the production of precise geometries (Chu et al., 2002; Dunlop et al., 2010; Bidan et al., 2012, 2013a), increasing the control on architecture and allowing for the exploration of previously inaccessible geometries. New theoretical frameworks not hindered by the limited capabilities of fabrication techniques are, therefore, needed to design architectures and quantitatively evaluate their performance in terms of specific functional requirements. This systematic evaluation would allow developing a toolkit of architecture-performance relations to tailor scaffold architecture for specific functional specifications.

Discrepancies between *in vitro* and *in vivo* effects of scaffold architecture, for example, due to cell aggregation *in vitro* (Karageorgiou and Kaplan, 2005), have been a challenge in the field. Further, the adaptation of various additive manufacturing techniques for ceramic scaffolds (Leukers et al., 2005; Michna et al., 2005; Seitz et al., 2005), including the use of 3D printing of sacrificial negative molds (Woesz et al., 2005), remains limited by resolution. Features with sizes on the scale of a single cell cannot yet be achieved. However, rapid improvements in resolution of additive manufacturing technologies have occurred for other industrial applications (Chia and Wu, 2015) and their adaptation to the printing of ceramics and other biomaterials is expected to greatly reduce this limitation.

This review aims to develop a new framework for thinking of scaffold architectures and summarize some of the key findings concerning their biological effect (**Figure 1**). The influence of four levels of architecture, representing different length scales, on biological response will be discussed: (1) surface topography, (2) pore size and geometry, (3) porous networks, and (4) macroscopic pore arrangement.

Surface Topography

Cells have been shown to sense and react to mechanical cues, such as stiffness (Discher et al., 2005; Engler et al., 2006; Shih et al., 2011), tension (Zhang et al., 2011), and compression (Ramage et al., 2009), through mechanotransduction pathways. A wealth of studies have focused on the effects of surface microtopography on cell response *in vitro* and bone formation *in vivo* with often conflicting results. Microtopography is a poorly defined parameter encompassing features, such as surface roughness and microporosity. Microporosity is commonly defined as the presence of pores with diameters lower than 10 μm (Rosa et al., 2003; Habibovic et al., 2005; Rouahi et al., 2006). Within ceramic struts, micropores can be closed or open (Hing et al., 2005), with closed pores not contributing to the cell microenvironment but affecting the mechanical properties of the struts.

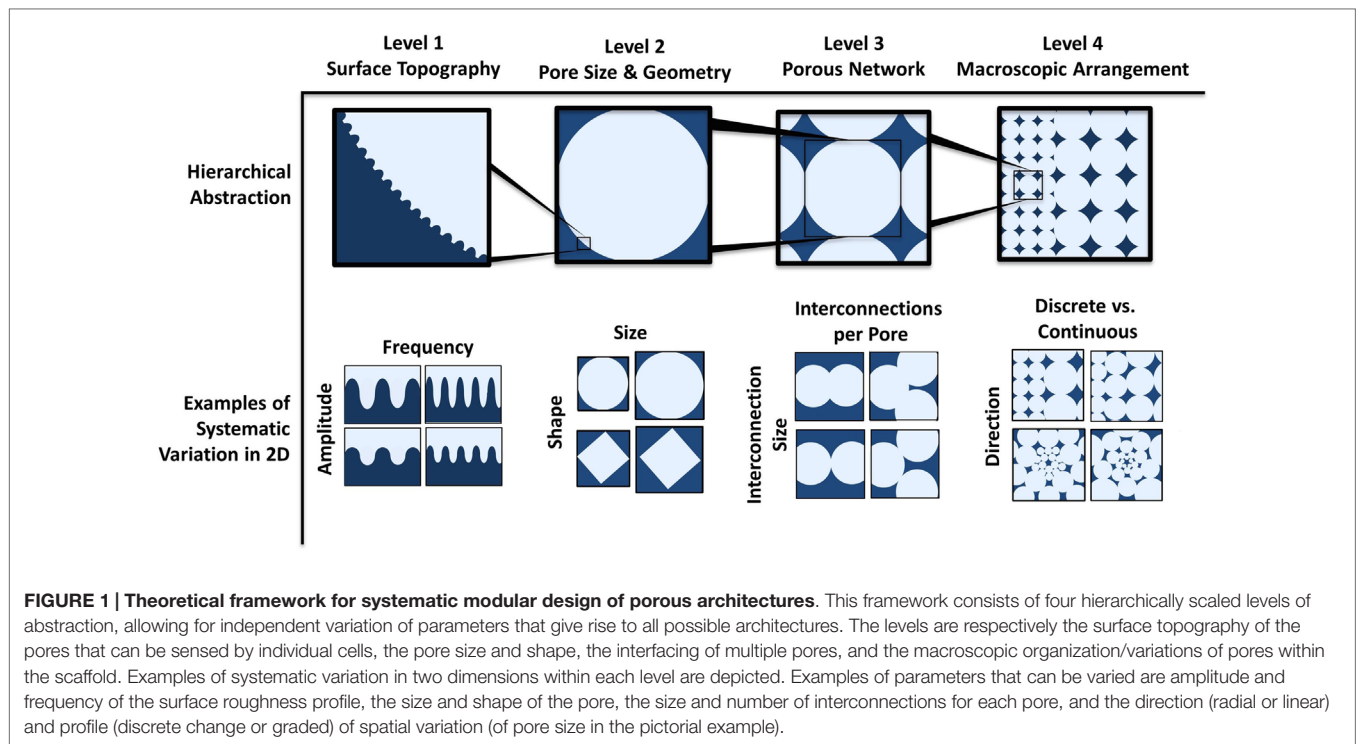
Control over surface roughness and microporosity in bioceramics has been achieved by varying sintering conditions (Bignon et al., 2003; Habibovic et al., 2005), changing processing parameters, such as uniaxial powder pressing load (Rosa et al., 2003) and polishing (Deligianni et al., 2001; Rouahi et al., 2006). Single parameter variations using conventional fabrication techniques, however, remain a challenge. Malmström et al. (2007) produced hydroxyapatite scaffolds by slip casting of 3D-printed sacrificial molds, adding a binder to the slurry to obtain microporosity. This method was proposed to avoid secondary effects that varying microporosity by sintering may have, such as changes in grain size, phase, and chemical composition of the calcium phosphate material.

While conclusions drawn by different studies on the effect of microporosity on bone formation and cell behavior are conflicting, multiple *in vivo* studies have shown positive effects of microporosity in implanted ceramic scaffolds. Comparing identical hydroxyapatite structures differing only by the presence or absence of microporosity demonstrated increased bone ingrowth and bone contact in microporous structures compared to non-microporous hydroxyapatite implants (Malmström et al., 2007). Further, comparing different levels of microporosity has shown that increased levels of microporosity resulted in higher volumes of denser bone at early time points (Hing et al., 2005). A study by Habibovic et al. (2005) on biphasic calcium phosphate (BCP) and hydroxyapatite structures with different levels of microporosity showed that a minimum amount of microporosity is required for osteoinduction.

Various mechanisms have been proposed for microporosity effects on cell and tissue behavior. Microporosity has been proposed to provide anchoring sites for cell extensions (filopodia), thus permitting them to spread and invade the material (Bignon et al., 2003; Annaz et al., 2004). By this mechanism, however, microporosity is not deemed necessary, as demonstrated by ingrowth taking place in low microporosity materials (Bignon et al., 2003) and its effect is seen as important at early time points for initial cell attachment with no notable effect on cell morphology later on (Annaz et al., 2004).

Another proposed mechanism deals with the effect of microtopography on adhesion protein adsorption (Deligianni et al., 2001; Annaz et al., 2004). Deligianni et al. (2001) propose that surface roughness affects the selective adsorption of serum proteins, which in turn affects cell-substrate interaction resulting in improved cell behavior *in vitro* (increasing their adhesion, proliferation, and their detachment strength). Surface roughness was found not to have an effect on alkaline phosphatase (ALP) activity but to delay its expression. Rouahi et al. (2006) have shown a 10-fold increase in protein adsorbed on microporous hydroxyapatite compared to non-microporous hydroxyapatite after 30 min of immersion in complete culture medium. The increased protein adsorption was correlated with a higher initial attachment on microporous hydroxyapatite (within the first 24 h) of osteosarcoma cells (Saos-2), but with a significantly lower proliferation potential after 4 days, possibly due to a closer interaction of cells with the substrate.

Habibovic et al. (2005) propose that increased microporosity and decreased crystal size with lower sintering temperatures



increase the specific surface area of the material, favoring the dissolution and reprecipitation of calcium and phosphate ions inducing the formation of biological apatite. Proteins that are co-precipitated in this process induce the differentiation of cells into the osteogenic lineage. Hing et al. (2005) link positive effects of microporosity at early time points after implantation to an increased vascularization of the scaffold, potentially due to increased nutrient permeability or to increased protein adsorption and cell attachment. At later time points, the most significant factor was hypothesized to be strut porosity's effect on the mechanics of the scaffold with implications for cell mechanotransduction. This proposition was supported by lower total porosity scaffolds resulting in similar bone volume as ones with higher porosity.

Other studies have contradicted these results. An *in vitro* study conducted by Rosa et al. (2003) reported that surface topography of hydroxyapatite did not affect initial stages of cell attachment and that proliferation, protein synthesis, ALP activity, and bone-like nodule formation were increased on surfaces with lower levels of microporosity. Differences in experimental results, particularly *in vitro*, can be ascribed to different experimental design, such as processing techniques, experimental set up, and material chemistry (Malmström et al., 2007). Microtopography and microporosity still remain loosely defined parameters, reported, for example, through roughness values (Deligianni et al., 2001) or as percentages (Hing et al., 2005). New methods of characterizing microtopography with more emphasis on geometric and/or topographical aspects that affect cell contact and morphology could be beneficial. A more systematic characterization is proposed taking into account defined surface profile parameters, such as spatial frequency and amplitude of surface roughness (depicted in level 1 in **Figure 1**). Further, exploring new scaffold surface topographies

could allow new functionality. For example, patterning surfaces with grooves could allow spatially controlling cell orientation by contact guidance (Brunette, 1986; Oakley and Brunette, 1993; Anselme et al., 2002; Chen et al., 2009) within the scaffold, which could allow control over tissue deposition orientation (Wang et al., 2003; Engelmayer et al., 2006).

Pore Size and Geometry

Macropore size and shape (level 2 in **Figure 1**) play a key role in tissue formation inside ceramic scaffolds. Karageorgiou and Kaplan (2005) have reviewed the pore size requirements of biomaterials. The minimum pore size requirement for bone ingrowth, however, still remains a highly contested topic. Based on the work of Hulbert et al. (1970), pore size should not be smaller than 75–100 μm . Osteogenesis has been shown by other studies to be enhanced with pore sizes larger than 300 μm (Tsuruga et al., 1997; Kuboki et al., 2001) due to higher permeability and potential for vascularization although higher porosity results in diminished mechanical strength. However, multiple recent studies have shown both bone ingrowth and the presence of cells in micropores (Lan Levengood et al., 2010; Bernstein et al., 2013; Polak et al., 2013). Regardless, pore shapes produced by conventional fabrication techniques being largely irregular results in difficulty in defining pore size. Pore size can be analyzed using different quantitative analytical techniques, such as mercury intrusion porosimetry or imaging techniques including X-ray microtomography (Atwood et al., 2004; Jones et al., 2007) combined with various analytical methods. A single pore size value or pore size distribution is insufficient for describing a porous architecture. Results greatly differ depending on the analytical model used, such as a continuous

or discrete approach, for the analysis of pore size distributions (Münch and Holzer, 2008). Further, incongruence in analytical approaches results in discrepancies in the literature and generates results that cannot be compared to yield definitive conclusions.

Macropore geometry has been found to modulate cell-network formation and tissue growth. A thorough review on this topic has been carried out by Zadpoor (2014). Cells have been found to respond to radii of curvature far larger than the cells themselves (Rumpler et al., 2008). Murine osteoblast-like cells cultured on hydroxyapatite channels with controlled cross-sections of different geometries (triangular, square, hexagonal, and circular) were shown to have initial tissue formation occur at corners, with cells on edges not growing until growth of adjacent tissue resulted in a curved environment (Rumpler et al., 2008) (Figure 2). Tissue growth is proposed to be curvature-driven, with growth increasing with local curvature resulting in a round opening regardless of the initial substrate shape. High curvature is thought to result in mechanical forces in cells, as evident by the formation of actin stress fibers along the tissue-fluid interface, which drives further tissue growth (Nelson et al., 2005). Overall tissue growth was independent of shape, but dependent on the cross-sectional perimeter (or channel surface area), with shorter perimeters resulting in more tissue at any given time point, consistent with Fenchel's theorem (Fenchel, 1929) that states that the average curvature of a closed convex plane is only dependent on perimeter. The model was confirmed to accurately predict the change in curvature profiles and the amount of tissue produced in pores with more complex geometries (Bidan et al., 2013a), with both experimental and computational results showing that at early time points, growth rates for cross shaped pores are almost twice those of square-shaped pores regardless of their size.

Observation of tissue growth on physiologically relevant geometries has shown that the curvature-driven growth model likely regulates bone architecture emerging after bone remodeling. Tissue

growth in circular pores, simulating cavities preceding osteon formation, proceeds with a concentric tissue front, while growth in semi-circular trenches, mimicking ridges preceding hemi-osteon formation, results in a pinned tissue front and an eventual termination of growth upon flattening out (zero curvature) (Bidan et al., 2012). This cell-network behavior is consistent with physiological observations of trabecular bone's three-dimensional curvature approaching zero (Jinnai et al., 2002; Bidan et al., 2012).

Various models have been developed to predict tissue growth in geometrically controlled environments. Dunlop et al. (2010) proposed a thermodynamically based model for tissue growth that successfully predicted experimental results by Rumpler et al. (2008) based on the theoretical models previously developed by Ambrosi and Guana (2005) and Ambrosi and Guillou (2007) on stress-modulated tissue growth and the biochemical energy in tissue growth respectively. Bidan et al. (2013a) developed a mathematical model to describe total tissue growth rate in a scaffold. The model includes factors representing cell activity, scaffold properties, and pore structure, including geometry. The model was extended to structures containing pore geometry heterogeneity.

Improvements to the curvature-driven growth model have included its refinement to explain differences in tissue growth on concave versus convex surfaces (Gamsjäger et al., 2013) and its extension to predict growth in three dimensions (Bidan et al., 2013b; Guyot et al., 2014). Tissue growth has been experimentally observed *in vivo* to be considerably increased on concave surfaces compared to convex and planar ones, with bone formation initiation occurring at concavities in hydroxyapatite-coated titanium implants (Ripamonti et al., 2012; Scarano et al., 2014). Gamsjäger et al. (2013) incorporate the role of surface stress in the curvature-driven growth model to allow predicting this phenomenon. An explanation for this behavior is the tensile nature of the cells that make up the tissue surface, as evidenced by actin and myosin

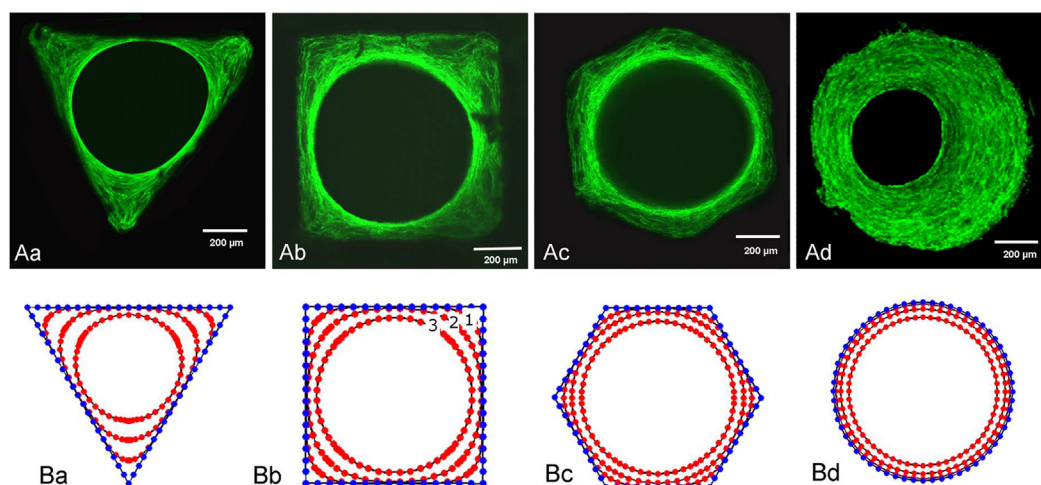


FIGURE 2 | Tissue growth in channels with controlled geometry. Tissue growth in channels with (i) triangular, (ii) square, (iii) hexagonal, and (iv) circular cross-sections. **(A)** Actin stress fibers stained with phalloidin-FITC after 21 days for (i)–(iii) and 30 days for (iv). **(B)** Computational simulation of tissue growth showing evolution of tissue front at different time points. Computational results closely agree with experimental results. Figure retrieved from Rumpler et al. (2008).

presence, that affects the growth of the cells underneath the interface differently depending on the nature of the underlying surface, as explained by the chord model developed by Bidan et al. (2012) (**Figure 3**).

Computational models have been developed for predicting curvature-driven growth of 3-dimensional geometries (Bidan et al., 2013b; Guyot et al., 2014). Guyot et al. (2014) developed a model that can be applied to highly complex and non-symmetrical scaffold geometries with minimal user input (**Figure 4**) and was validated *in vitro* on Ti6Al4V (Ti) scaffolds produced by selective laser melting. All simulations were found to eventually yield spherical or cylindrical tissue fronts. The authors of the study proposed that given scaling differences in experimental versus simulation times with pore size, integrating in the model the effects of mass transport and other mechanisms necessary for biological function may improve its predictive ability.

Pore geometry could also have large implications in regulating collagen fiber organization and orientation, with profound effects on the resulting tissue structure and mechanics (Engelmayr et al., 2006). Tissue growth in open rectangular pore slots with different widths in calcium phosphate bone cement plates showed that actin fibers were organized parallel to the pore length in slots of 200 and 300 μm thickness. Larger slots were found to have fibers forming larger angles with the longitudinal axis at the growth

front and thinner fibers oriented mainly normal to the pore wall in the bulk of the tissue (Knychala et al., 2013). The anisotropy created by the actin alignment was proposed to be encouraging tissue growth by migration and force transmission through cell-cell junctions (Tambe et al., 2011).

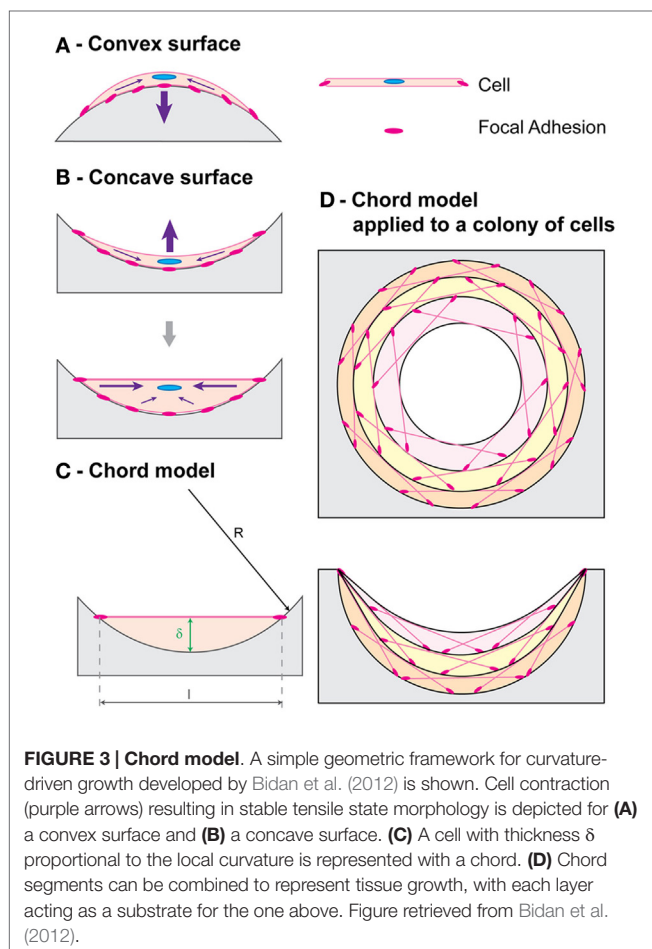
Given the findings of geometric effects on tissue growth, it is clear that additive manufacturing techniques currently being adapted for biomaterial scaffold fabrication are often inadequate. Many extrusion-based techniques, for example, produce arrays of cylindrical rods (Michna et al., 2005; Seitz et al., 2005; Carrel et al., 2014) that are inadequate given their convex geometry. Biological effects must be taken into consideration for further refinement of SFF methods for scaffold fabrication.

Porous Network

The interfacing of two or more pores to form a network (level 3 in **Figure 1**) affects the infiltration of nutrients and cells into the scaffold. The macroscopic structure produced by a network of pores is often described using porosity values. Overall scaffold porous structure is a key determinant of scaffold mechanical performance (Rodríguez-Lorenzo et al., 2002), resorption rate (De Groot, 1988; Böhner and Baumgart, 2004) as well as the surface area to volume ratio (SAV) of the scaffold (Ashworth et al., 2014). Scaffold SAV has been shown to influence the SAV of the formed tissue in silk fibroin implants (Hofmann et al., 2007). Porosity can be open, closed, or blind-ended, with only open porosity being directly conducive to tissue ingrowth (Ashworth et al., 2014).

Porosity alone, however, while widely used is a poor predictor of biological response. Other than pore size, the arrangement of two or more pores in space to form a porous network requires careful consideration of pore interconnection size and geometry that will affect overall scaffold permeability and accessibility to cells and nutrients. The shape of interconnections is likely an important factor given the curvature-driven growth model and the convex nature of interconnections in many traditional porous scaffolds although this aspect has not been systematically explored to the authors' knowledge. Two main factors affecting the accessibility of a scaffold to tissue growth are discussed: interconnectivity, which determines the accessibility of a porous network through fenestrations between pores to a finitely sized object, such as a cell, and tortuosity, which determines how long and winding a pathway of interconnected pores is.

Interconnectivity is often considered a binary property, with scaffolds frequently being described as "fully interconnected." This definition, however, fails to recognize the importance of interconnection size. Cells have been shown to penetrate porous networks with interconnections smaller than the cells themselves (Polak et al., 2013), with deformation of the nucleus being considered a major limitation to cell migration (Wolf et al., 2013). Interconnection size does, however, affect scaffold accessibility to cells. Fenestration size distribution or average interconnection sizes alone are not sufficiently informative parameters as a single small interconnection is enough to prevent accessibility to all downstream pores. Otsuki et al. (2006) showed that narrow pore throats, particularly in the shorter routes connecting a given pore to an implant's outer surface, compromise tissue differentiation



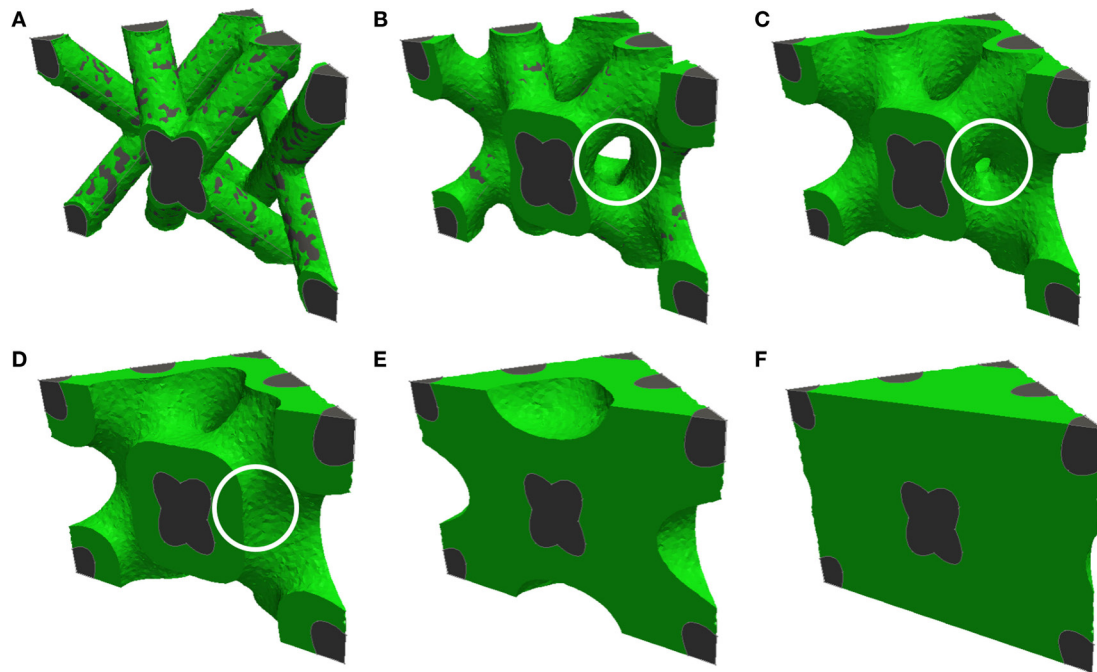


FIGURE 4 | Computational prediction of tissue growth on a complex 3-dimensional pore geometry. Cross-sections of diamond-shaped pores are shown, with increasing degrees of pore filling from (A) to (F). The white circle highlights bridging of tissue resulting from convergent growth from two local surfaces [reproduced from Figure 7 from Guyot et al. (2014) with kind permission from Springer Science and Business Media].

in that pore. They proposed two new indices to assess the effect of narrow pore throats on the entire implant's performance: the volume ratio of dead pores (those pores that do not connect to the implant's outer surface due to narrow pore throats) and the average detour index (the ratio of the shortest distance through interconnections of all pore voxels, excluding dead pores, to the distance from the implant periphery). Both indices are a function of the minimum pore throat size for bone ingrowth, a value that is dependent on implant properties, such as material type.

Ashworth et al. (2014) developed another solution to the problem of quantitatively describing an entire scaffold's interconnectivity by adapting the concept of percolation from geological research to describe the interconnectivity of porous networks. A percolating cluster of pores is defined as a cluster of interconnected pores that forms a path through the material. Ashworth et al. (2014) introduce the new scalable quantity of percolation diameter, i.e., the diameter of the largest "tracer" sphere that can percolate through an infinitely large porous structure (Figure 5).

While a percolation diameter allows the determination of whether an object with a specific size is able to fully traverse a scaffold, tortuosity describes how circuitous a route through a network of pores is. Tortuosity is commonly defined as the ratio of the path length through interconnected pores between two points to the length or shortest distance between them (Starly et al., 2007; Chang and Wang, 2011). Another commonly used definition for tortuosity is in terms of the ratio of the diffusivity of molecules in the bulk to the effective diffusivity (Hrabe et al.,

2004; Zalc et al., 2004). This second macroscopic definition, however, is only informative for symmetrical geometries (Starly et al., 2007). Tortuosity affects cell migration through the scaffold, nutrient diffusion, and waste removal. Since tortuosity affects permeability to nutrients necessary for cell proliferation, directed cell growth can be obtained by controlling tortuosity in different directions (Starly et al., 2007). Malda et al. (2004) studied the effect of scaffold architecture on oxygen supply, cell distribution, and cartilaginous matrix deposition. Botchwey et al. (2003) showed that tortuosity affects fluid and nutrient perfusion in scaffolds using dynamic culture conditions, with increased tortuosity resulting in decreased internal fluid flow rates. Random open porosity has also been shown to decrease cell penetration into the hydroxyapatite scaffold core when compared to open porous scaffolds with aligned channels both *in vivo* and *in vitro*, suggesting that tortuosity reduces cell penetration (Silva et al., 2006). On the other hand, tortuous channels have been proposed to increase the rate of osteoblast precursor growth (Leber et al., 2010). Starly et al. (2007) developed a tracer metric numerical model to obtain three tortuosity factors to describe tortuosity for each axis of a unit cell of the scaffold. The model is applicable to any geometry provided that a virtual model can be produced, for example, by use of X-ray microtomography. Tortuosity could also be measured as a function of the size of an object traveling through the scaffold, as is done with a percolation diameter, by using a "tracer" with finite dimension, resulting in a parameter similar to the average detour index proposed by Otsuki et al. (2006) (above).

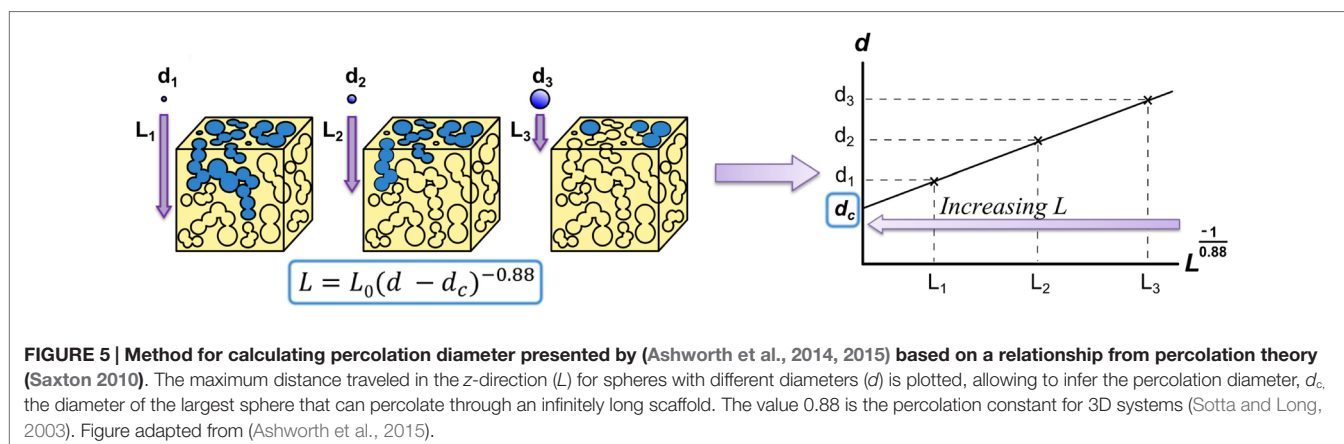


FIGURE 5 | Method for calculating percolation diameter presented by (Ashworth et al., 2014, 2015) based on a relationship from percolation theory (Saxton 2010). The maximum distance traveled in the z-direction (L) for spheres with different diameters (d) is plotted, allowing to infer the percolation diameter, d_c , the diameter of the largest sphere that can percolate through an infinitely long scaffold. The value 0.88 is the percolation constant for 3D systems (Sotta and Long, 2003). Figure adapted from (Ashworth et al., 2015).

Macroscopic Pore Arrangement

Porous scaffolds produced by conventional fabrication techniques are largely homogenous. Novel production techniques, such as SFF and freeze-casting, to some extent, have allowed for the production of porous networks with spatial control over architecture (Hutmacher, 2001) (level 4 in **Figure 1**). Macroscopic control of porous networks can allow locally tuning the scaffold properties and directing biological activity. This can be done, for example, by spatially controlling mechanical properties, tuning degradation behavior, or directing fluid and nutrient flow. Three different ways of macroscopically controlling scaffold architectural properties are discussed: pore network orientation, architectural gradients, and patterning.

Both macroscopic architectural features (such as osteonal and trabecule orientation) and microscopic ones (such as collagen and lamellar orientation) contribute to bone anisotropy (Majumdar et al., 1998; Takano et al., 1999; Doblaré et al., 2004). Bone anisotropy is both necessary for biomechanical function and maintained through bone turnover thanks to cell mechanosensitivity guiding bone remodeling. This results in osteons produced by the cutting cone resorption process being aligned with the major stress axis (Lanyon and Bourn, 1979; Burr and Martin, 1989; Petrtyl et al., 1996). Isotropic pore structures in biomaterials result in tissue that differs from native tissue structurally and functionally (De Mulder et al., 2009). Thus, in order to regenerate anisotropic tissue, anisotropy must be incorporated in the scaffold porous structure (Engelmayr et al., 2008), reducing the need for a second remodeling step (De Mulder et al., 2009). Other than to tune mechanical performance, porous structure anisotropy can be used to guide tissue growth and nutrient flow direction. Optimal pore orientation, therefore, requires defect site-specific considerations to tailor the structure, for example, to the location and direction of fluid supply (Bohner et al., 2011).

Multiple studies have produced anisotropic structures, for example, through ionotropic gelation of alginate-hydroxyapatite slurries (Despang and Bernhardt, 2013) or unidirectional freezing producing columnar or lamellar microstructures (Fu et al., 2009). Ice-templating of scaffolds is a promising technique for creating oriented porous

structures by controlling thermal gradients (Pawelec et al., 2013). While pore geometry control is limited, macroscopic control of architectures can be achieved by changing the freeze-drying experimental set up (Moon et al., 2003; Munch et al., 2009), using additives (Munch et al., 2009) and changing thermal profiles (freezing protocols) (Pawelec et al., 2014). Radial pore geometries have been produced by freeze-casting using metallic cylinders with a Teflon rod in the center (Moon et al., 2003).

Chu et al. (2002) have used 3D-printed sacrificial molds to compare orthogonal versus radial channel designs, showing that regenerated bone tissue morphology can be tuned by varying channel design/orientation. However, no studies to the authors' knowledge have systematically showed the advantages of anisotropic pore structures over isotropic pore structures, controlling factors, such as overall porosity and mechanical properties. Pore anisotropy is also likely to affect the preferred direction of cell invasion and the force transmission to cells *in vivo*. A thorough evaluation of pore structure anisotropy under mechanical loading could allow a better understanding of the benefits of anisotropic scaffolds. Further, Lu et al. (1999) have introduced the concept of "interconnection density" as a factor affecting cell penetration and bone formation. Pore anisotropy would result in differing interconnection densities depending on the cross section, suggesting that oriented porosity could be used to promote directional tissue growth using pore orientation.

Spatially grading porosity is an effective way of locally varying properties, such as mechanical strength and permeability. Simske et al. (1997) describe four length scales of porosity performing different useful functions ranging from enhancing bone ingrowth to fixation during surgery. Different tissues and cell types favor different pore sizes depending on the scaffold material (Oh et al., 2007), which motivates tuning porosity both to allow to tailor for different cell types that might exist in a tissue and to allow for different tissue interfaces, such as between cartilage and bone or blood vessels and bone. Further, graded biomaterials have been shown to allow for the formation of cell density gradients and extra-cellular matrix gradients within the material, allowing for localized control of tissue formation and properties (Woodfield et al., 2005). A review by Miao and Sun (2010) on graded/gradient biomaterials is recommended for a

detailed description of fabrication techniques that have been used to achieve pore gradients.

Possibly, the most common approach to spatially graded porous ceramic materials has been the biomimetic design of scaffolds with a denser outer shell mimicking cortical bone and a porous core-simulating trabecular bone. Tampieri et al. (2001) achieved this through multi-step dipping of cellulosic sponges in slurries with different hydroxyapatite crystallinity. Werner et al. (2002) have used tape casting of hydroxyapatite slurries with differently sized porogens. Fierz et al. (2008) used 3D printing of nanoporous hydroxyapatite to create biomimetic structures with large central channels to enhance bone ingrowth in the center of the scaffold. While the biomimetic argument has largely motivated scaffold designs, again, a systematic approach to judge the improved performance of biomimetic structures and graded porous structures has not been performed to the authors' knowledge.

Last, spatial patterning of scaffold architecture could give rise to localized tuning of scaffold properties. Silva et al. (2006) produced hydroxyapatite scaffolds with open random porosity with and without anisotropic channels. The purpose of the anisotropic macro-architecture was to avoid necrotic core formation by preventing newly formed tissue blocking nutrient exchange with the core of the scaffold (Ishaug et al., 1997). Patterning the scaffold with channels was found to both enhance cell infiltration of the scaffold as well as direct tissue growth.

Scaffolds can be patterned in a variety of ways to spatially control structure and function. Architecture could be used to tune mechanical properties of the scaffold and also the mechanical environment of the cell. The cutting cone resorption process of bone carried out by groups of cells referred to as basic multicellular units (BMUs) is mechanically guided (Van Oers et al., 2008). This results in the direction of osteons having been found to match the major stress axis (Lanyon and Bourn, 1979; Burr and Martin, 1989; Petrtyl et al., 1996). One can imagine a scaffold architecture where tubular pores are spatially graded to have an orientation dependent on the local major stress axis such that newly formed bone has a morphology suited to the mechanical environment.

Roughness has been found to have profound effects on cell behavior, as previously mentioned, with high roughness resulting in strong cell attachments but low proliferation rates (Rouahi et al., 2006). Spatially grading roughness, for example, by use of additives (Malmström et al., 2007), could potentially enhance

scaffold performance. One could imagine a structure with varying roughness to encourage proliferation and migration or attachment at different parts of the scaffold. An example of this would be using high roughness outside the scaffold to encourage integration but lower roughness at pore inlets to encourage cell migration toward the core of the scaffold.

Last, spatial control of architecture could allow controlling degradation rate and tissue formation. For example, SAV could be varied by controlling pore size and surface roughness while maintaining a mechanically appropriate local porosity. This would allow controlling degradation rates throughout the scaffold. Pore size and shape could also be tuned spatially to control locally cell type infiltration, whereas macroscopic structures and pore orientation could be used to direct the diffusion of nutrients within the structure.

Conclusion

The advent and continual development of technologies, such as additive manufacturing that allow for a high degree of control over scaffold geometry, serve the basis for the exploration of precise geometries on cell and tissue behavior. A theoretical framework for systematic design of scaffold architecture at four different levels has been proposed. This framework will hopefully encourage the development of a suite of parameters to describe architecture that will allow a systematic design and evaluation of architectures quantitatively. Novel fabrication methods have also allowed for the development of architecturally heterogeneous materials. Evaluating the performance of architectures on these four levels in terms of outputs, such as mechanical performance, permeability, degradation behavior, cell response, and tissue microarchitecture, will assist in developing a structure–function relationship toolkit that could help develop biomaterials with locally optimized architecture in a way that is patient and defect-site specific. Further, the uncovering of these relationships will allow tuning fabrication techniques to architectural necessities rather than adapting technologies developed with insufficient consideration of biological implications.

Acknowledgments

The authors gratefully acknowledge the financial support of the Gates Cambridge Trust and Geistlich Pharma AG.

References

- Ambrosi, D., and Guana, F. (2005). Stress-modulated growth. *Math. Mech. Solids* 12, 319–342. doi:10.1177/1081286505059739
- Ambrosi, D., and Guillou, A. (2007). Growth and dissipation in biological tissues. *Contin. Mech. Thermodyn.* 19, 245–251. doi:10.1007/s00161-007-0052-y
- Annaz, B., Hing, K. A., Kayser, M., Buckland, T., and Di Silvio, L. (2004). Porosity variation in hydroxyapatite and osteoblast morphology. *J. Microsc.* 215, 100–110. doi:10.1111/j.0022-2720.2004.01354.x
- Anselme, K., Bigerelle, M., and Noel, B. (2002). Effect of grooved titanium substratum on human osteoblastic cell growth. *J. Biomed. Mater. Res.* 60, 529–540. doi:10.1002/jbm.10101
- Ashworth, J. C., Best, S. M., and Cameron, R. E. (2014). Quantitative architectural description of tissue engineering scaffolds. *Mater. Technol.* 29, 281–295. doi:10.1179/1753555714Y.0000000159
- Ashworth, J. C., Mehr, M., Buxton, P. G., Best, S. M., and Cameron, R. E. (2015). Cell invasion in collagen scaffold architectures characterized by percolation theory. *Adv. Healthc. Mater.* 4, 1317–1321. doi:10.1002/adhm.201500197
- Atwood, R. C., Jones, J. R., Lee, P. D., and Hench, L. L. (2004). Analysis of pore interconnectivity in bioactive glass foams using X-ray microtomography. *Scr. Mater.* 51, 1029–1033. doi:10.1016/j.scriptamat.2004.08.014
- Bernstein, A., Niemeyer, P., Salzmann, G., Südkamp, N. P., Hube, R., Klehm, J., et al. (2013). Microporous calcium phosphate ceramics as tissue engineering scaffolds for the repair of osteochondral defects: histological results. *Acta Biomater.* 9, 7490–7505. doi:10.1016/j.actbio.2013.03.021
- Bidan, C. M., Kommareddy, K. P., Rumpler, M., Kollmannsberger, P., Bréchet, Y. J. M., Fratzl, P., et al. (2012). How linear tension converts to curvature: geometric control of bone tissue growth. *PLoS ONE* 7:e36336. doi:10.1371/journal.pone.0036336

- Bidan, C. M., Kommareddy, K. P., Rimpler, M., Kollmannsberger, P., Fratzl, P., and Dunlop, J. W. C. (2013a). Geometry as a factor for tissue growth: towards shape optimization of tissue engineering scaffolds. *Adv. Healthc. Mater.* 2, 186–194. doi:10.1002/adhm.201200159
- Bidan, C. M., Wang, F. M., and Dunlop, J. W. (2013b). A three-dimensional model for tissue deposition on complex surfaces. *Comput. Methods Biomech. Biomed. Engin.* 16, 1056–1070. doi:10.1080/10255842.2013.774384
- Bignon, A., Chouteau, J., Chevalier, J., Fantozzi, G., Carret, J., Laennec, ÂR., et al. (2003). Effect of micro- and macroporosity of bone substitutes on their mechanical properties and cellular response. *J. Mater. Sci. Mater. Med.* 14, 1089–1097. doi:10.1023/B:JMSM.0000004006.90399.b4
- Bohner, M., and Baumgart, F. (2004). Theoretical model to determine the effects of geometrical factors on the resorption of calcium phosphate bone substitutes. *Biomaterials* 25, 3569–3582. doi:10.1016/j.biomaterials.2003.10.032
- Bohner, M., Loosli, Y., Baroud, G., and Lacroix, D. (2011). Commentary: deciphering the link between architecture and biological response of a bone graft substitute. *Acta Biomater.* 7, 478–484. doi:10.1016/j.actbio.2010.08.008
- Botchwey, E. A., Dupree, M. A., Pollack, S. R., Levine, E. M., and Laurencin, C. T. (2003). Tissue engineered bone: measurement of nutrient transport in three-dimensional matrices. *J. Biomed. Mater. Res. A* 67, 357–367. doi:10.1002/jbm.a.10111
- Brunette, D. M. (1986). Spreading and orientation of epithelial cells on grooved substrata. *Exp. Cell Res.* 167, 203–217. doi:10.1016/0014-4827(86)90217-X
- Burr, D. B., and Martin, R. B. (1989). Errors in bone remodeling: toward a unified theory of metabolic bone disease. *Am. J. Anat.* 186, 186–216. doi:10.1002/aja.1001860208
- Carrel, J.-P., Wiskott, A., Moussa, M., Rieder, P., Scherrer, S., and Durual, S. (2014). A 3D printed TCP/HA structure as a new osteoconductive scaffold for vertical bone augmentation. *Clin. Oral Implants Res.* 00, 1–8. doi:10.1111/clr.12503
- Chang, H., and Wang, Y. (2011). *Cell Responses to Surface and Architecture of Tissue Engineering Scaffolds*. Shanghai: InTech, 569–588.
- Chen, J., Ulerich, J. P., Abelev, E., Fasasi, A., Arnold, C. B., and Soboyejo, W. O. (2009). An investigation of the initial attachment and orientation of osteoblast-like cells on laser grooved Ti-6Al-4V surfaces. *Mater. Sci. Eng. C* 29, 1442–1452. doi:10.1016/j.msec.2008.11.014
- Chia, H. N., and Wu, B. M. (2015). Recent advances in 3D printing of biomaterials. *J. Biol. Eng.* 9, 4. doi:10.1186/s13036-015-0001-4
- Chu, T. M. G., Orton, D. G., Hollister, S. J., Feinberg, S. E., and Halloran, J. W. (2002). Mechanical and in vivo performance of hydroxyapatite implants with controlled architectures. *Biomaterials* 23, 1283–1293. doi:10.1016/S0142-9612(01)00243-5
- De Groot, K. (1988). Effect of porosity and physicochemical properties on the stability, resorption, and strength of calcium phosphate ceramics. *Ann. N. Y. Acad. Sci.* 523, 227–233. doi:10.1111/j.1749-6632.1988.tb38515.x
- De Mulder, E. L. W., Buma, P., and Hannink, G. (2009). Anisotropic porous biodegradable scaffolds for musculoskeletal tissue engineering. *Materials (Basel)* 2, 1674–1696. doi:10.3390/ma2041674
- Deligianni, D. D., Katsala, N. D., Koutsoukos, P. G., and Missirlis, Y. F. (2001). Effect of surface roughness of hydroxyapatite on human bone marrow cell adhesion, proliferation, differentiation and detachment strength. *Biomaterials* 22, 87–96. doi:10.1016/S0142-9612(00)00174-5
- Descamps, M., Richart, O., Hardouin, P., Hornez, J. C., and Leriche, A. (2008). Synthesis of macroporous β -tricalcium phosphate with controlled porous architectural. *Ceram. Int.* 34, 1131–1137. doi:10.1016/j.ceramint.2007.01.004
- Despang, F., Bernhardt, A., Lode, A., Ditttrich, R., Hanke, T., and Shenoy, S. J., et al. (2013). Synthesis and physicochemical, in vitro and in vivo evaluation of an anisotropic, nanocrystalline hydroxyapatite bisque scaffold with parallel-aligned pores mimicking. *J. Tissue Eng. Regen. Med.* doi:10.1002/term.1729
- Discher, D. E., Janmey, P., and Wang, Y. (2005). Tissue cells feel and respond to the stiffness of their substrate. *Science* 310, 1139–1143. doi:10.1126/science.1116995
- Doblaré, M., Garcia, J. M., and Gomez-Benito, M. J. (2004). Modelling bone tissue fracture and healing: a review. *Eng. Fract. Mech.* 71, 1809–1840. doi:10.1016/j.engfractmech.2003.08.003
- Dunlop, J. W. C., Fischer, F. D., Gamsjäger, E., and Fratzl, P. (2010). A theoretical model for tissue growth in confined geometries. *J. Mech. Phys. Solids* 58, 1073–1087. doi:10.1016/j.jmps.2010.04.008
- Engelmayr, G. C., Cheng, M., Bettinger, C. J., Borenstein, J. T., Langer, R., and Freed, L. E. (2008). Accordion-like honeycombs for tissue engineering of cardiac anisotropy. *Nat. Mater.* 7, 1003–1010. doi:10.1038/nmat2316
- Engelmayr, G. C., Papworth, G. D., Watkins, S. C., Mayer, J. E., and Sacks, M. S. (2006). Guidance of engineered tissue collagen orientation by large-scale scaffold microstructures. *J. Biomech.* 39, 1819–1831. doi:10.1016/j.jbiomech.2005.05.020
- Engler, A. J., Sen, S., Sweeney, H. L., and Discher, D. E. (2006). Matrix elasticity directs stem cell lineage specification. *Cell* 126, 677–689. doi:10.1016/j.cell.2006.06.044
- Fenchel, W. (1929). Über Krümmung und Windung geschlossener Raumkurven. *Math. Ann.* 101, 238–252.
- Fierz, F. C., Beckmann, F., Huser, M., Irsen, S. H., Leukers, B., Witte, F., et al. (2008). The morphology of anisotropic 3D-printed hydroxyapatite scaffolds. *Biomaterials* 29, 3799–3806. doi:10.1016/j.biomaterials.2008.06.012
- Fu, Q., Rahaman, M. N., Bal, B. S., and Brown, R. F. (2009). In vitro cellular response to hydroxyapatite scaffolds with oriented pore architectures. *Mater. Sci. Eng. C* 29, 2147–2153. doi:10.1007/s10856-008-3668-y
- Gamsjäger, E., Bidan, C. M., Fischer, F. D., Fratzl, P., and Dunlop, J. W. C. (2013). Modelling the role of surface stress on the kinetics of tissue growth in confined geometries. *Acta Biomater.* 9, 5531–5543. doi:10.1016/j.actbio.2012.10.020
- Guyot, Y., Papantoniou, I., Chai, Y. C., Van Bael, S., Schrooten, J., and Geris, L. (2014). A computational model for cell/ECM growth on 3D surfaces using the level set method: a bone tissue engineering case study. *Biomech. Model. Mechanobiol.* 13, 1361–1371. doi:10.1007/s10237-014-0577-5
- Habibovic, P., Yuan, H., van der Valk, C. M., Meijer, G., van Blitterswijk, C. A., and de Groot, K. (2005). 3D microenvironment as essential element for osteoinduction by biomaterials. *Biomaterials* 26, 3565–3575. doi:10.1016/j.biomaterials.2004.09.056
- Hing, K., Annaz, B., and Saeed, S. (2005). Microporosity enhances bioactivity of synthetic bone graft substitutes. *J. Mater. Sci. Mater. Med.* 16, 467–475. doi:10.1007/s10856-005-6988-1
- Hofmann, S., Hagenmüller, H., Koch, A. M., Müller, R., Vunjak-Novakovic, G., Kaplan, D. L., et al. (2007). Control of in vitro tissue-engineered bone-like structures using human mesenchymal stem cells and porous silk scaffolds. *Biomaterials* 28, 1152–1162. doi:10.1016/j.biomaterials.2006.10.019
- Hollister, S. J., Maddox, R. D., and Taboas, J. M. (2002). Optimal design and fabrication of scaffolds to mimic tissue properties and satisfy biological constraints. *Biomaterials* 23, 4095–4103. doi:10.1016/S0142-9612(02)00148-5
- Hrabe, J., Hrabetová, S., and Segeth, K. (2004). A model of effective diffusion and tortuosity in the extracellular space of the brain. *Biophys. J.* 87, 1606–1617. doi:10.1529/biophysj.103.039495
- Hulbert, S. F., Young, F. A., Mathews, R. S., Klawitter, J. J., Talbert, C. D., and Stelling, F. H. (1970). Potential of ceramic materials as permanently implantable skeletal prostheses. *J. Biomed. Mater. Res.* 4, 433–456. doi:10.1002/jbm.820040309
- Hutmacher, D. W. (2001). Scaffold design and fabrication technologies for engineering tissues – state of the art and future perspectives. *J. Biomater. Sci. Polym. Ed.* 12, 107–124. doi:10.1163/156856201744489
- Ishaug, S. L., Crane, G. M., Miller, M. J., Yasko, A. W., Yaszemski, M. J., and Mikos, A. G. (1997). Bone formation by three-dimensional stromal osteoblast culture in biodegradable polymer scaffolds. *J. Biomed. Mater. Res.* 36, 17–28. doi:10.1002/(SICI)1097-4636(199707)36:1<17::AID-JBM3>3.3.CO;2-D
- Jinnai, H., Watashiba, H., Kajihara, T., Nishikawa, Y., Takahashi, M., and Ito, M. (2002). Surface curvatures of trabecular bone microarchitecture. *Bone* 30, 191–194. doi:10.1016/S8756-3282(01)00672-X
- Jones, J. R., Poologasundarampillai, G., Atwood, R. C., Bernard, D., and Lee, P. D. (2007). Non-destructive quantitative 3D analysis for the optimisation of tissue scaffolds. *Biomaterials* 28, 1404–1413. doi:10.1016/j.biomaterials.2006.11.014
- Karageorgiou, V., and Kaplan, D. (2005). Porosity of 3D biomaterial scaffolds and osteogenesis. *Biomaterials* 26, 5474–5491. doi:10.1016/j.biomaterials.2005.02.002
- Knychala, J., Bouropoulos, N., Catt, C. J., Katsamenis, O. L., Please, C. P., and Sengers, B. G. (2013). Pore geometry regulates early stage human bone marrow cell tissue formation and organisation. *Ann. Biomed. Eng.* 41, 917–930. doi:10.1007/s10439-013-0748-z
- Kuboki, Y., Jin, Q., and Takita, H. (2001). Geometry of carriers controlling phenotypic expression in BMP-induced osteogenesis and chondrogenesis. *J. Bone Joint Surg.* 83(1 suppl 2), S105–S115.

- Lan Levensgood, S. K., Polak, S. J., Wheeler, M. B., Maki, A. J., Clark, S. G., Jamison, R. D., et al. (2010). Multiscale osteointegration as a new paradigm for the design of calcium phosphate scaffolds for bone regeneration. *Biomaterials* 31, 3552–3563. doi:10.1016/j.biomaterials.2010.01.052
- Lanyon, L. E., and Bourn, S. (1979). The influence of mechanical function on the development and remodeling of the tibia. An experimental study in sheep. *J Bone Joint Surg. Am.* 61, 263–273.
- Leber, C., Choi, H., Bose, S., and Bandyopadhyay, A. (2010). Micromachined Si channel width and tortuosity on human osteoblast cell attachment and proliferation. *Mater. Sci. Eng. C* 30, 71–77. doi:10.1016/j.msec.2009.08.010
- Leong, K. F., Cheah, C. M., and Chua, C. K. (2003). Solid freeform fabrication of three-dimensional scaffolds for engineering replacement tissues and organs. *Biomaterials* 24, 2363–2378. doi:10.1016/S0142-9612(03)00030-9
- Leukers, B., Gulkan, H., Irsen, S. H., Milz, S., Tille, C., Schieker, M., et al. (2005). Hydroxyapatite scaffolds for bone tissue engineering made by 3D printing. *J. Mater. Sci. Mater. Med.* 6, 1121–1124. doi:10.1007/s10856-005-4716-5
- Lu, J., Flautre, B., and Anselme, K. (1999). Role of interconnections in porous bioceramics on bone recolonization in vitro and in vivo. *J. Mater. Sci. Mater. Med.* 10, 111–120. doi:10.1023/A:1008973120918
- Majumdar, S., Kothari, M., Augat, P., Newitt, D. C., Link, T. M., Lin, J. C., et al. (1998). High-resolution magnetic resonance imaging: three-dimensional trabecular bone architecture and biomechanical properties. *Bone* 22, 445–454. doi:10.1016/S8756-3282(98)00030-1
- Malda, J., Woodfield, T. B. F., van der Vloodt, F., Kooy, F. K., Martens, D. E., Tramper, J., et al. (2004). The effect of PEGT/PBT scaffold architecture on oxygen gradients in tissue engineered cartilaginous constructs. *Biomaterials* 25, 5773–5780. doi:10.1016/j.biomaterials.2004.01.028
- Malmström, J., Adolfsson, E., Arvidsson, A., and Thomsen, P. (2007). Bone response inside free-form fabricated macroporous hydroxyapatite scaffolds with and without an open microporosity. *Clin. Implant Dent. Relat. Res.* 9, 79–88. doi:10.1111/j.1708-8208.2007.00031.x
- Miao, X., and Sun, D. (2010). Graded/gradient porous biomaterials. *Materials* 3, 26–47. doi:10.3390/ma3010026
- Michna, S., Wu, W., and Lewis, J. A. (2005). Concentrated hydroxyapatite inks for direct-write assembly of 3-D periodic scaffolds. *Biomaterials* 26, 5632–5639. doi:10.1016/j.biomaterials.2005.02.040
- Moon, J.-W., Hwang, H.-J., Awano, M., and Maeda, K. (2003). Preparation of NiO-YSZ tubular support with radially aligned pore channels. *Mater. Lett.* 57, 1428–1434. doi:10.1016/S0167-577X(02)01002-9
- Münch, B., and Holzer, L. (2008). Contradicting geometrical concepts in pore size analysis attained with electron microscopy and mercury intrusion. *J. Am. Ceram. Soc.* 91, 4059–4067. doi:10.1111/j.1551-2916.2008.02736.x
- Munch, E., Saiz, E., Tomsia, A. P., and Deville, S. (2009). Architectural control of freeze-cast ceramics through additives and templating. *J. Am. Ceram. Soc.* 92, 1534–1539. doi:10.1111/j.1551-2916.2009.03087.x
- Nelson, C. M., Jean, R. P., Tan, J. L., Liu, W. F., Sniadecki, N. J., Spector, A. A., et al. (2005). Emergent patterns of growth controlled by multicellular form and mechanics. *Proc. Natl. Acad. Sci. U.S.A.* 102, 11594–11599. doi:10.1073/pnas.0502575102
- Oakley, C., and Brunette, D. (1993). The sequence of alignment of microtubules, focal contacts and actin filaments in fibroblasts spreading on smooth and grooved titanium substrata. *J. Cell Sci.* 354, 343–354.
- Oh, S. H., Park, I. K., Kim, J. M., and Lee, J. H. (2007). In vitro and in vivo characteristics of PCL scaffolds with pore size gradient fabricated by a centrifugation method. *Biomaterials* 28, 1664–1671. doi:10.1016/j.biomaterials.2006.11.024
- Otsuki, B., Takemoto, M., Fujibayashi, S., Neo, M., Kokubo, T., and Nakamura, T. (2006). Pore throat size and connectivity determine bone and tissue ingrowth into porous implants: three-dimensional micro-CT based structural analyses of porous bioactive titanium implants. *Biomaterials* 27, 5892–5900. doi:10.1016/j.biomaterials.2006.08.013
- Pawelec, K. M., Husmann, A., Best, S. M., and Cameron, R. E. (2013). Understanding anisotropy and architecture in ice templated biopolymer scaffolds. *Mater. Sci. Eng. C Mater. Biol. Appl.* 37, 141–147. doi:10.1016/j.msec.2014.01.009
- Pawelec, K. M., Husmann, A., Best, S. M., and Cameron, R. E. (2014). A design protocol for tailoring ice-templated scaffold structure a design protocol for tailoring ice-templated scaffold structure. *Interface* 11, 20130958. doi:10.1098/rsif.2013.0958
- Petrtyl, M., Hert, J., and Fiala, P. (1996). Spatial organization of the haversian bone in man. *J. Biomech.* 29, 161–169. doi:10.1016/0021-9290(94)00035-2
- Polak, S. J., Rustom, L. E., Genin, G. M., Talcott, M., and Wagoner Johnson, A. J. (2013). A mechanism for effective cell-seeding in rigid, microporous substrates. *Acta Biomater.* 9, 7977–7986. doi:10.1016/j.actbio.2013.04.040
- Ramage, L., Nuki, G., and Salter, D. M. (2009). Signalling cascades in mechano-transduction: cell-matrix interactions and mechanical loading. *Scand. J. Med. Sci. Sports* 19, 457–469. doi:10.1111/j.1600-0838.2009.00912.x
- Ripamonti, U., Roden, L. C., and Renton, L. F. (2012). Osteoinductive hydroxyapatite-coated titanium implants. *Biomaterials* 33, 3813–3823. doi:10.1016/j.biomaterials.2012.01.050
- Rodríguez-Lorenzo, L. M., Vallet-Regí, M., Ferreira, J. M. F., Ginebra, M. P., Aparicio, C., and Planell, J. A. (2002). Hydroxyapatite ceramic bodies with tailored mechanical properties for different applications. *J. Biomed. Mater. Res.* 60, 159–166. doi:10.1002/jbm.1286
- Rosa, A. L., Beloti, M. M., and van Noort, R. (2003). Osteoblastic differentiation of cultured rat bone marrow cells on hydroxyapatite with different surface topography. *Dent. Mater.* 19, 768–772. doi:10.1016/S0109-5641(03)00024-1
- Rouahi, M., Gallet, O., Champion, E., Dentzer, J., Hardouin, P., and Anselme, K. (2006). Influence of hydroxyapatite microstructure on human bone cell response. *J. Biomed. Mater. Res. A* 78, 222–235. doi:10.1002/jbm.a.30682
- Rumpler, M., Woesz, A., Dunlop, J. W. C., van Dongen, J. T., and Fratzl, P. (2008). The effect of geometry on three-dimensional tissue growth. *J. R. Soc. Interface* 5, 1173–1180. doi:10.1098/rsif.2008.0064
- Saxton, M. J. (2010). Two-dimensional continuum percolation threshold for diffusing particles of nonzero radius. *Biophys. J.* 99, 1490–1499. doi:10.1016/j.bpj.2010.06.033
- Scarano, A., Degidi, M., Perrotti, V., Degidi, D., Piattelli, A., and Iezzi, G. (2014). Experimental evaluation in rabbits of the effects of thread concavities in bone formation with different titanium implant surfaces. *Clin. Implant Dent. Relat. Res.* 16, 572–581. doi:10.1111/cid.12033
- Seitz, H., Rieder, W., Irsen, S., Leukers, B., and Tille, C. (2005). Three-dimensional printing of porous ceramic scaffolds for bone tissue engineering. *J. Biomed. Mater. Res. B Appl. Biomater.* 74B, 782–788. doi:10.1002/jbm.b.30291
- Shih, Y.-R. V., Tseng, K.-F., Lai, H.-Y., Lin, C.-H., and Lee, O. K. (2011). Matrix stiffness regulation of integrin-mediated mechanotransduction during osteogenic differentiation of human mesenchymal stem cells. *J. Bone Miner. Res.* 26, 730–738. doi:10.1002/jbmr.278
- Silva, M. M. C. G., Cyster, L. A., Barry, J. J. A., Yang, X. B., Oreffo, R. O. C., Grant, D. M., et al. (2006). The effect of anisotropic architecture on cell and tissue infiltration into tissue engineering scaffolds. *Biomaterials* 27, 5909–5917. doi:10.1016/j.biomaterials.2006.08.010
- Simske, S. J., Ayers, R. A., and Bateman, T. A. (1997). Porous materials for bone engineering. *Mater. Sci. Forum* 250, 151–182. doi:10.4028/www.scientific.net/MSF.250.151
- Sotta, P., and Long, D. (2003). The crossover from 2D to 3D percolation: theory and numerical simulations. *Eur. Phys. J. E Soft Matter* 11, 375–387. doi:10.1140/epje/i2002-10161-6
- Starly, B., Yildirim, E., and Sun, W. (2007). A tracer metric numerical model for predicting tortuosity factors in three-dimensional porous tissue scaffolds. *Comput. Methods Programs Biomed.* 87, 21–27. doi:10.1016/j.cmpb.2007.04.003
- Takano, Y., Turner, C. H., Owan, I., Lau, T., Forwood, M. R., and Burr, D. B. (1999). Elastic anisotropy and collagen orientation. *J. Orthop. Res.* 17, 59–66. doi:10.1002/jor.1100170110
- Tambe, D. T., Hardin, C. C., Angelini, T. E., Rajendran, K., Park, C. Y., Serrapicamal, X., et al. (2011). Collective cell guidance by cooperative intercellular forces. *Nat. Mater.* 10, 469–475. doi:10.1038/nmat3025
- Tampieri, A., Celotti, G., and Sprio, S. (2001). Porosity-graded hydroxyapatite ceramics to replace natural bone. *Biomaterials* 22, 1365–1370. doi:10.1016/S0142-9612(00)00290-8
- Tsuruga, E., Takita, H., Itoh, H., Wakisaka, Y., and Kuboki, Y. (1997). Pore size of porous hydroxyapatite as the cell-substratum controls BMP-induced osteogenesis. *J. Biochem.* 121, 317–324. doi:10.1093/oxfordjournals.jbchem.a021589
- Van Oers, R. F. M., Ruimerman, R., Tanck, E., Hilbers, P. A. J., and Huiskes, R. (2008). A unified theory for osteonal and hemi-osteonal remodeling. *Bone* 42, 250–259. doi:10.1016/j.bone.2007.10.009
- Vielreicher, M., Schu, S., Detsch, R., Schmidt, M. A., Buttgerit, A., Boccaccini, A., et al. (2013). Taking a deep look: modern microscopy technologies to optimize the design and functionality of biocompatible scaffolds for tissue engineering in regenerative medicine. *J. R. Soc. Interface* 10, 20130263. doi:10.1098/rsif.2013.0263

- Wang, J. H.-C., Jia, F., Gilbert, T. W., and Woo, S. L.-Y. (2003). Cell orientation determines the alignment of cell-produced collagenous matrix. *J. Biomech.* 36, 97–102. doi:10.1016/S0021-9290(02)00233-6
- Werner, J., Linner-Krcmar, B., Friess, W., and Greil, P. (2002). Mechanical properties and in vitro cell compatibility of hydroxyapatite ceramics with graded pore structure. *Biomaterials* 23, 4285–4294. doi:10.1016/S0142-9612(02)00191-6
- Woesz, A., Rumpfer, M., Stampfl, J., Varga, F., Fratzl-Zelman, N., Roschger, P., et al. (2005). Towards bone replacement materials from calcium phosphates via rapid prototyping and ceramic gelcasting. *Mater. Sci. Eng. C* 25, 181–186. doi:10.1016/j.msec.2005.01.014
- Wolf, K., Te Lindert, M., Krause, M., Alexander, S., Te Riet, J., Willis, A. L., et al. (2013). Physical limits of cell migration: control by ECM space and nuclear deformation and tuning by proteolysis and traction force. *J. Cell Biol.* 201, 1069–1084. doi:10.1083/jcb.201210152
- Woodfield, T. B. F., Van Blitterswijk, C. A., De Wijn, J., Sims, T. J., Hollander, A. P., and Riesle, J. (2005). Polymer scaffolds fabricated with pore-size gradients as a model for studying the zonal organization within tissue-engineered cartilage constructs. *Tissue Eng.* 11, 1297–1311. doi:10.1089/ten.2005.11.1297
- Zadpoor, A. A. (2014). Bone tissue regeneration: the role of scaffold geometry. *Biomater. Sci.* 3, 231–245. doi:10.1039/c4bm00291a
- Zalc, J. M., Reyes, S. C., and Iglesia, E. (2004). The effects of diffusion mechanism and void structure on transport rates and tortuosity factors in complex porous structures. *Chem. Eng. Sci.* 59, 2947–2960. doi:10.1016/j.ces.2004.04.028
- Zhang, H., Landmann, F., Zahreddine, H., Rodriguez, D., Koch, M., and Labouesse, M. (2011). A tension-induced mechanotransduction pathway promotes epithelial morphogenesis. *Nature* 471, 99–103. doi:10.1038/nature09765

Conflict of Interest Statement: The authors declare that the research was conducted in the absence of any commercial or financial relationships that could be construed as a potential conflict of interest.

Copyright © 2015 Gariboldi and Best. This is an open-access article distributed under the terms of the Creative Commons Attribution License (CC BY). The use, distribution or reproduction in other forums is permitted, provided the original author(s) or licensor are credited and that the original publication in this journal is cited, in accordance with accepted academic practice. No use, distribution or reproduction is permitted which does not comply with these terms.



Therapeutic ion-releasing bioactive glass ionomer cements with improved mechanical strength and radiopacity

Maximilian Fuchs¹, Eileen Gentleman², Saroash Shahid³, Robert G. Hill³ and Delia S. Brauer^{1*}

¹ Otto Schott Institute of Materials Research, Friedrich Schiller University Jena, Jena, Germany, ² Craniofacial Development and Stem Cell Biology, King's College London, London, UK, ³ Unit of Dental Physical Sciences, Oral Growth and Development, Barts and The London School of Medicine and Dentistry, Queen Mary University of London, London, UK

OPEN ACCESS

Edited by:

Wolfram Höland,
Ivoclar Vivadent AG, Liechtenstein

Reviewed by:

Ahmed El-Fiqi,
Dankook University, South Korea
Jin Nakamura,
National Institute for Materials
Science, Japan

*Correspondence:

Delia S. Brauer,
Otto Schott Institute of Materials
Research, Friedrich Schiller
University Jena, Fraunhoferstr. 6,
Jena 07743, Germany
delia.brauer@uni-jena.de

Specialty section:

This article was submitted to
Biomaterials, a section of the
journal *Frontiers in Materials*

Received: 27 July 2015

Accepted: 18 September 2015

Published: 14 October 2015

Citation:

Fuchs M, Gentleman E, Shahid S,
Hill RG and Brauer DS (2015)
Therapeutic ion-releasing bioactive
glass ionomer cements with
improved mechanical strength and
radiopacity.
Front. Mater. 2:63.
doi: 10.3389/fmats.2015.00063

Bioactive glasses (BG) are used to regenerate bone, as they degrade and release therapeutic ions. Glass ionomer cements (GIC) are used in dentistry, can be delivered by injection, and set *in situ* by a reaction between an acid-degradable glass and a polymeric acid. Our aim was to combine the advantages of BG and GIC, and we investigated the use of alkali-free BG ($\text{SiO}_2\text{--CaO--CaF}_2\text{--MgO}$) with 0–50% of calcium replaced by strontium, as the beneficial effects of strontium on bone formation are well documented. When mixing BG and poly(vinyl phosphonic-co-acrylic acid), ions were released fast (up to 90% within 15 min at pH 1), which resulted in GIC setting, as followed by infrared spectroscopy. GIC mixed well and set to hard cements (compressive strength up to 35 MPa), staying hard when in contact with aqueous solution. This is in contrast to GIC prepared with poly(acrylic acid), which were shown previously to become soft in contact with water. Strontium release from GIC increased linearly with strontium for calcium substitution, allowing for tailoring of strontium release depending on clinical requirements. Furthermore, strontium substitution increased GIC radiopacity. GIC passed ISO10993 cytotoxicity test, making them promising candidates for use as injectable bone cements.

Keywords: bone cement, strontium, compressive strength, bioactive glass, bone filler

Introduction

In 2010, about 5.5% of the EU population were diagnosed with osteoporosis, with 22% of women aged 50 and above (Hernlund et al., 2013). In osteoporosis, bone mass and density are reduced, owing to osteoclasts resorbing too much bone and osteoblasts not forming enough new bone, resulting in an increased risk of fractures. Incidences of clinical vertebral fractures in the EU have been reported to range from 170 to 470 per 100,000 (Hernlund et al., 2013), and about a third of these fractures can be persistently painful after non-operative care (Agency for Healthcare Research and Quality, 2010). Vertebroplasty and kyphoplasty are common procedures which restore fractured vertebrae by injecting a bone cement such as poly(methyl methacrylate) (PMMA) (Lewis, 2006), and the aim is to relieve pain while restoring dimensions and strength of the vertebrae. Glass ionomer cements (GIC) have the potential to overcome some of the limitations of acrylic cements, such as shrinkage during polymerization and a highly exothermic setting reaction, as they set by an acid–base reaction

between a polymeric acid [such as poly(acrylic acid), PAA] and a degradable glass (Wilson, 1996). Furthermore, GIC form a chemical bond to bone (Wilson et al., 1983), which is in contrast to acrylic cements, where mechanical stability is achieved by mechanical interlocking only.

Several commercial dental GIC contain strontium in the glass component (Stamboulis et al., 2004), and the release of strontium ions has been shown to enhance tooth remineralization (Thuy et al., 2008) and promote antibacterial properties (Guida et al., 2003; Brauer et al., 2013), particularly in synergy with fluoride ions (Dabsie et al., 2009). Furthermore, strontium ions are known to enhance osteoblastic bone formation and reduce osteoclastic bone resorption (Marie et al., 2001), and they are used for the treatment of osteoporosis (Marie, 2005). Strontium-containing bioactive glasses (BG) have been shown to release strontium ions when in contact with aqueous solutions (Fredholm et al., 2012), and they have been suggested to combine the benefits of strontium ions with those of BG (bioactivity, apatite formation, controlled release of therapeutic ions, and delivery versatility) (Gentleman et al., 2010; Autefage et al., 2015).

Dental GIC contain aluminum ions, which play an important role in both glass degradation (hydrolysis of Si–O–Al bonds) and in stability of the cements (cross-linking of PAA chains by Al^{3+}); however, as they are neurotoxic (Joshi, 1990) and negatively affect bone mineralization (Cournot-Witmer et al., 1981; Boyce et al., 1982; Blades et al., 1998), dental GIC are not ideal for orthopedic applications. Efforts have been made to replace aluminum with iron (Hurrell-Gillingham et al., 2006) or zinc (Darling and Hill, 1994); however, these also have drawbacks and particularly too high a zinc release has been shown to result in cytotoxic reactions (Brauer et al., 2011a). Materials based on magnesium-containing BG can therefore provide a promising alternative.

In previous studies, GIC based on magnesium-containing BG and PAA have been shown to be promising candidates for use as bone cements (Brauer et al., 2011a, 2013) and to show antibacterial properties (Brauer et al., 2013). However, their mechanical properties and hydrolytic stability were poor compared to GIC using aluminum- or zinc-containing glasses (Brauer et al., 2011a). Our hypothesis was that a polyelectrolyte with a larger concentration of functional groups would allow for formation of more hydrolytically and mechanically stable GIC, and here we therefore prepare GIC with poly(vinylphosphonic-co-acrylic acid) (PVPA–PAA) rather than PAA.

Our aim was to characterize the setting behavior, mechanical properties, ion release, and *in vitro* cell compatibility of GIC based on PVPA–PAA and BG (SiO_2 –CaO–CaF₂–MgO) with 0, 2.5, 10, or 50% of Ca replaced by Sr on a molar base.

Materials and Methods

Glass Synthesis and Characterization

Bioactive glasses (SiO_2 –CaO–CaF₂–MgO) where either no calcium (Sr0) or 2.5, 10, or 50% of calcium (Sr2.5, Sr10, Sr50) were replaced by strontium on a molar base (Table 1) were prepared using a standard melt-quench route as described previously (Brauer et al., 2013). Glasses were mixed with isopropanol and ground for 50 min in an agate planetary mill (Pulverisette,

Fritsch GmbH, Idar-Oberstein, Germany) and then sieved using a 40 μm analytical sieve. The amorphous state of the glasses was investigated using powder X-ray diffraction (XRD; D5000, Siemens) using $Cu_{K\alpha}$ radiation and then measured with a step time of 31 s and step width of 0.02° in the range of 10°–60° 2 θ . Thermal properties of the glasses were analyzed using differential thermal analysis (DTA; DTA-50, Shimadzu; heating rate, 10 K min^{−1}). Glass composition was analyzed using scanning electron microscopy with energy-dispersive X-ray spectroscopy (EDX) with fluoride (Field Emission JEOL 7001 F, EDAX Trident EDX; K α ; 25 keV).

Glass Dissolution

Glass solubility was analyzed in a hydrochloric acid/potassium chloride (HCl/KCl) buffer, which was obtained by mixing 134 mL of 0.2 mol L^{−1} hydrochloric acid solution (Titrisol, Merck, p.a.) with 50 mL of 0.2 mol L^{−1} potassium chloride (VEB Jenapharm Laborchemie Apolda, p.a.) solution, filling to a total volume of 200 mL and storing at 37°C. Seventy-five milligrams of glass powder was immersed in 50 mL buffer solution and stored at 37°C for 5, 15, 60, 360, or 1440 min. Afterward, solution and remaining powder were separated by filtering using medium porosity filter paper (5 μm particle retention, VWR). The remaining powder was analyzed using attenuated total reflectance Fourier transform infrared spectroscopy (ATR-FTIR; Alpha, Bruker Daltonics GmbH, Bremen, Germany) and the solutions were analyzed using inductively coupled plasma optical emission spectroscopy (ICP-OES; Varian Liberty 150, Agilent Technologies, Böblingen, Germany). Data represent mean \pm standard deviation (SD).

Cement Formation

Before mixing cements, glass powders were annealed by heating to and holding for 10 min at 50 K below glass transition before being allowed to cool to room temperature. Cements were prepared using poly(vinyl phosphonic-co-acrylic acid) (PVPA–PAA; 40 wt% solution; weight average chain length between 40 and 70 kD according to manufacturer), which was provided by First Scientific Dental GmbH (Elmshorn, Germany). Cements were obtained by mixing glass powder and polymer solution in a weight ratio of 2:1, giving the cement into PTFE molds (4 mm in diameter; 7 mm in height) and allowing to set inside the mold for 60 min at 37°C.

Cement Setting Behavior and Mechanical Properties

Cement setting was followed by ATR-FTIR, by placing the freshly mixed cement onto the diamond window of the spectrometer and obtaining a spectrum every 5 min for up to 60 min. FTIR spectra of the untreated glasses and PVPA–PAA solution were measured for comparison.

Mechanical properties of the cements were measured on specimens which (after setting at 37°C for 60 min) were removed from the mold and kept for 23 h either in deionized water or at 100% relative humidity (100% RH) at 37°C. For storing at 100% RH, specimens together with some damp tissue were placed inside a closed container; physical contact between specimen and tissue was avoided. Specimens without treatment in deionized

TABLE 1 | Nominal glass composition (mol%) and strontium for calcium substitution (%).

Glass	SiO ₂	CaO	CaF ₂	SrO	SrF ₂	MgO	Substitution
Sr0	47.32	10.41	11.04	–	–	31.23	0
Sr2.5	47.32	10.15	10.76	0.26	0.28	31.23	2.5
Sr10	47.32	9.37	9.93	1.04	1.10	31.23	10
Sr50	47.32	5.21	5.52	5.21	5.52	31.23	50

water or at 100% RH (thus set for 60 min at 37°C inside the mold only) were analyzed as controls. Compressive strength and Young's modulus were measured using a hydraulic testing machine (Zwick 1445, Zwick GmbH, Ulm, Germany) with a 10 kN load cell at a test velocity of 1 mm min⁻¹. Per composition, 10 separate specimens were tested. Results were analyzed using one-way analysis of variance (ANOVA; Origin 8.5.0, OriginLab Corp., Northampton, MA, USA) followed by Bonferroni *post hoc* test; $p \leq 0.05$ was considered significant. Results are presented as mean \pm confidence interval.

Radiopacity

Glass ionomer cement radiopacity was measured according to the specifications laid out in BS EN ISO 9917-1:2007 standard for water-based dental cements. One-millimeter-thick GIC disks 10 mm in diameter were prepared by packing the cement mixture into Teflon molds of the same dimensions. GICs were allowed to set in the molds for 1 h while clamped between two acetate sheets. Thereafter, the disks were stored at 37°C and 100% RH. After 24 h, the samples were removed from the molds and radiographed, along with a six-step aluminum step wedge (0.5 to 5.0 mm), using a digital X-ray unit. The samples and the step wedge were irradiated at 65 kV from a distance of 10 cm. Exposure time was 0.4 s. Exact height of the cement disks was measured using a micrometer, and measured radiopacity was normalized to a specimen height of 1.0 mm. Measurements were performed in triplicates and results are presented as mean \pm SD.

Cell Culture, Cement Cytotoxicity (ISO 10993), and Ion Release

MC3T3-E1 mouse osteoblasts were obtained from the European Collection of Cell Cultures (Salisbury, UK) and cultured under standard conditions (37°C, 5% CO₂/95% air, 100% RH) in Alpha Minimum Essential Medium (α MEM) supplemented with 10% (v/v) fetal bovine serum (FBS) and 2 mM L-glutamine (all from Invitrogen, Paisley, UK).

To create conditioned media for cytotoxicity testing (ISO 10993:5), 10 mm diameter, 1 mm thick cement disks, organo-tin stabilized poly(vinyl chloride) (PVC) sheet (positive control), and non-toxic PVC (noDOP®) tubing (negative control) were prepared. Positive and negative control samples were provided by Raumedic (Münchberg, Germany) and sterilized in 70% ethanol for 1 h. Cement samples were sterilized under UV light for 2 h on each side.

Conditioned media were created by soaking cement samples or positive and negative control samples in α MEM for 7 days at 37°C. A material surface area to culture medium volume ratio of 3 cm² mL⁻¹ was maintained as directed in ISO10993:5.

Cells were seeded at 20,000 cells/cm² in 96-well plates in basal medium and allowed to attach for 24 h. Culture medium was then exchanged with conditioned medium supplemented with 10% FBS and 2 mM L-glutamine. Conditioned medium was added to cells either neat or diluted by factors of 2, 4, 8, or 16 with basal medium and allowed to incubate for 24 h. Cell metabolic activity was determined by MTT (3-(4,5-Dimethylthiazol-2-yl)-2,5-diphenyltetrazolium bromide; Sigma-Aldrich, Dorset, UK) assay, as previously described (Gentleman et al., 2010). Briefly, 20 μ L of a 5 mg/mL solution of MTT in phosphate buffered saline was added to each well and plates were returned to the incubator for 4 h. Culture medium was then removed, the formazan product dissolved in dimethyl sulfoxide, and the solution's absorbance was read on a colorimetric plate reader at 592 nm. Data represent mean (\pm SD) of three separate samples for each composition or control and are normalized to negative controls. Statistical analysis of MTT activity was carried out by ANOVA followed by *post hoc* Tukey test and was limited to comparisons carried out with the non-diluted conditioned medium. Differences were considered significant if $p < 0.05$. Ions released into the cell culture medium were analyzed using ICP-OES (calcium, strontium, magnesium, and silicon) and fluoride-selective electrode (fluoride). For ICP-OES analysis, solutions were diluted by a factor 1:20 and acidified using 69% nitric acid before analysis. Fluoride concentrations were measured using a fluoride ion selective electrode (Elit 8221, Nico2000 Ltd.) with a AgCl reference electrode.

Results

Glass Characterization

All glasses were amorphous according to powder XRD results, with XRD patterns displaying the typical amorphous halos (Figure 1A). Significant amounts of fluoride were lost during melting (Brauer et al., 2011b), resulting in overall changes in the glass compositions as presented in Table 2. DTA curves (Figure 1B) and summarized thermal properties (Table 3) show comparable thermal behavior for glasses Sr0, Sr2.5, and Sr10 but lower glass transition and higher crystallization temperatures for Sr50.

Glass Dissolution

Experiments were performed in a buffer solution set to pH 1, as this was the pH of the PVPA–PAA solution. Upon immersion of glass powders, a fast pH rise was observed (Figure 2A). A pH of 1.15 was reached within the first few minutes and pH 1.2 at 6 h, where it remained for the duration of the experiment (24 h). This was accompanied by a release of ions (Figure 2B), where a very fast release was observed within the first minutes of the experiments,

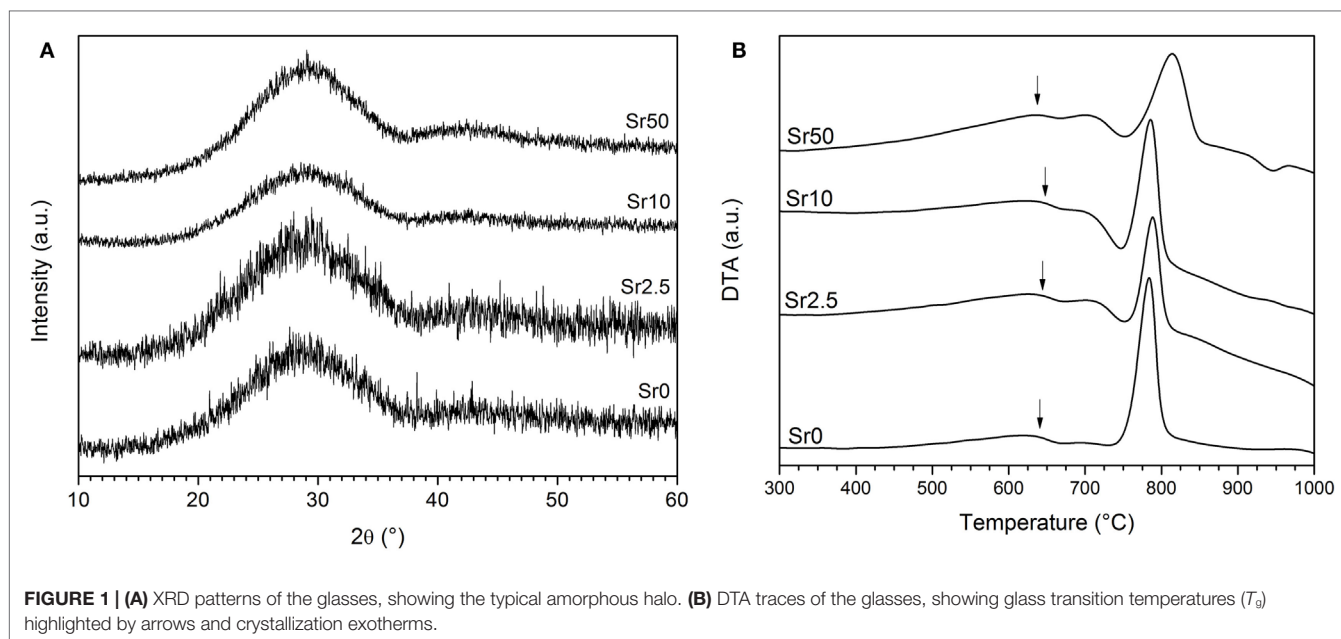


TABLE 2 | EDX results compared to nominal glass composition (mol%; fluoride content presented as F; Ca and Sr presented as oxides only).

Glass	SiO ₂	CaO	SrO	MgO	F
Sr0	42.62	9.38		28.13	19.88
	45.2 ± 0.3	20.56 ± 0.07	–	28.8 ± 0.1	5.4 ± 0.1
Sr2.5	42.62	9.14	0.23	28.13	19.88
	41.9 ± 0.5	23.31 ± 0.05	1.03 ± 0.01	22.8 ± 0.2	10.9 ± 0.2
Sr10	42.62	8.44	0.94	28.13	19.88
	40.3 ± 0.5	20.12 ± 0.04	2.38 ± 0.01	21.6 ± 0.2	15.6 ± 0.2
Sr50	42.62	4.69	4.69	28.13	19.88
	37.8 ± 0.4	11.84 ± 0.01	11.30 ± 0.07	22.8 ± 0.2	16.3 ± 0.2

TABLE 3 | DTA results: glass transition (T_g), crystallization onset ($T_{c,o}$), and crystallization peak ($T_{c,p}$) temperatures (°C), error is ±5 K.

Glass	T_g	$T_{c,o}$	$T_{c,p}$
Sr0	644	751	785
Sr2.5	637	753	789
Sr10	649	754	786
Sr50	635	760	813

and concentrations increased more slowly afterward. Absolute concentrations shown in **Figure 2B** correspond to a release of about 90% of calcium and 75% of strontium and magnesium ions within the first hour, reaching 100 and 90%, respectively, at 24 h. Release of silicon ions ranged from about 10% at 5 min to 20% at 24 h. This ion release caused structural changes observed by FTIR, where the non-bridging oxygen band at 930 cm⁻¹ had already disappeared at an immersion time of 5 min, and no pronounced changes in FTIR spectra were observed afterwards (**Figure 2C**). Release of Mg²⁺ and silicon ions did not vary much with strontium for calcium substitution in the glass. By contrast, concentrations of Ca²⁺ ions decreased with strontium for calcium

substitution in the glass (owing to lower amounts of Ca²⁺ ions present in the glass) and concentrations of Sr²⁺ ions increased linearly ($R^2 = 0.999$; **Figure 2D**).

Cement Formation and Properties

Cements from PVPA-PAA and glasses Sr0 and Sr2.5 showed very good mixing properties; however, with increasing strontium for calcium substitution, the glasses became more reactive and working times shorter, with glass Sr50 setting very quickly. All glasses, when mixed with PVPA-PAA solution, set to hard and brittle cements within 1 h at 37°C. Cements stayed hard when stored in water or at 100% RH.

Poly(vinylphosphonic-*co*-acrylic acid) solution showed pronounced bands at about 1715, 1640, 1170, 995, and 930 cm⁻¹, with additional low-intensity bands at 1455 and 1415 cm⁻¹ (**Figure 3**). Upon mixing with the glass powder, the band at 1715 cm⁻¹ disappeared, new bands appeared at 1560, 1050, and 977 cm⁻¹, and the two bands at 1455 and 1415 cm⁻¹ increased in intensity. The band at 1715 cm⁻¹ can be assigned to the symmetric stretch of the carboxylic –C=O band (Socrates, 2004). Upon reaction with the glass and formation of the polysalt matrix, i.e., a change from mostly carboxyl (–COOH) to carboxylate groups (–COO⁻), the –C=O band disappeared, owing to the π electrons in the carboxylate group being delocalized. A similar effect is observed with the –P=O stretch vibration band at 1170 cm⁻¹ (Socrates, 2004), which also disappeared once the salt matrix of the GIC has formed. The band at 1642 cm⁻¹ may be related to –C=O or possibly –P=O bonds, connected by hydrogen bonds (Socrates, 2004), and the intensity also decreased upon salt formation. The band at 1050 cm⁻¹ is most likely related to P–O vibrations in the salt matrix, while the high intensity band formed at 1560 cm⁻¹ and the double band at 1455 and 1415 cm⁻¹ are related to asymmetric and symmetric –COO⁻ stretch bands, respectively (Socrates, 2004).

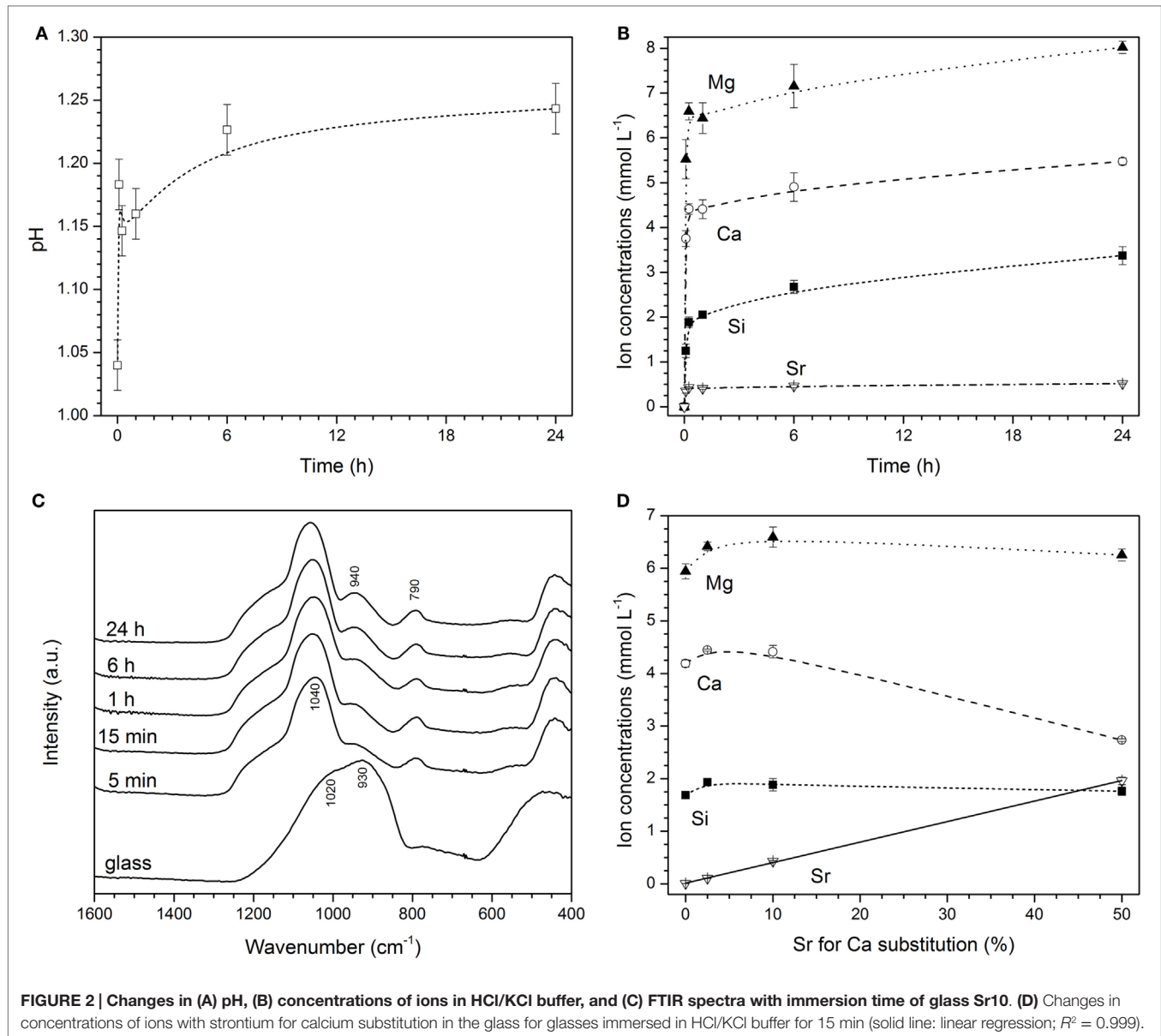


FIGURE 2 | Changes in (A) pH, (B) concentrations of ions in HCl/KCl buffer, and (C) FTIR spectra with immersion time of glass Sr10. (D) Changes in concentrations of ions with strontium for calcium substitution in the glass for glasses immersed in HCl/KCl buffer for 15 min (solid line: linear regression; $R^2 = 0.999$).

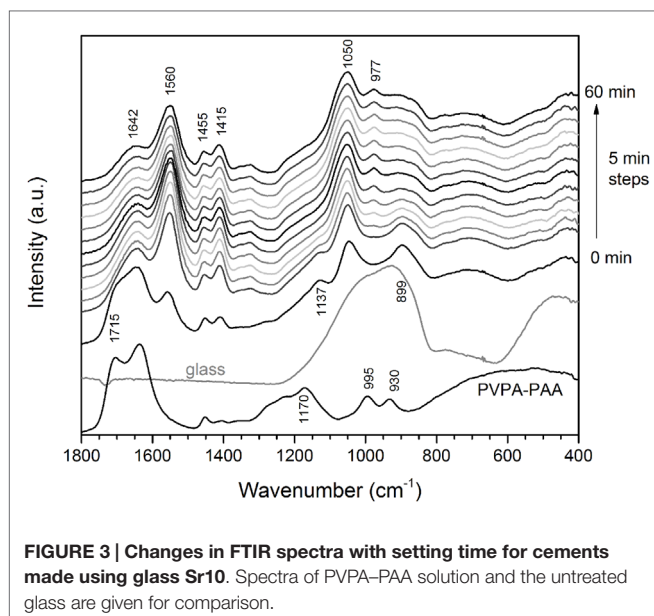
Cements gave average compressive strength of at least 20 MPa and Young's moduli of 4 GPa and above (Figures 4A,B, respectively). There seemed to be no clear trend in mechanical properties (average compressive strength or Young's modulus) with glass composition; but both compressive strength and Young's modulus seemed to increase with storage time in water and particularly at 100% RH. Maximum compressive strength was between 38 and 39 MPa for cements made from Sr0 and Sr2.5 at 24 h at 100% RH, while maximum compressive strength obtained for cements from glasses Sr10 and Sr50 were between 30 and 35 MPa (Figure 4C). Maximum Young's moduli showed no clear trend but seemed to decrease with increasing strontium for calcium substitution in the glass (Figure 4D).

Radiopacity increased with increasing strontium for calcium substitution in the glass (Figure 5A), showing a linear increase

for substitutions from 2.5 to 50% ($R^2 = 0.999$; Figure 5B). Cements from glass Sr10 showed radiopacity comparable to that of aluminum, while radiopacity of cements from glasses Sr0 and Sr2.5 was lower and that of Sr50 well above it (225% of that of aluminum). The radiopacity of cement from glass Sr0 was off scale, i.e., lower than the first step of the step wedge (0.5 mm Al), and it is therefore not included in Figure 5B.

Cytotoxicity and Ion Release into Cell Culture Medium

MC3T3-E1 cells exposed to conditioned medium soaked with the negative control had normal morphologies, whereas those cultured with conditioned medium soaked with the positive control had abnormal rounded morphologies and often detached from the culture surface (Figures 6A,B, respectively). Quantification



of cell metabolic activity by MTT assay demonstrated that cells exposed to conditioned medium soaked with the positive control had significantly lower metabolic activity than those exposed to conditioned medium soaked with the negative control (non-diluted, $p < 0.001$) (**Figure 7A**). MC3T3-E1 exposed to medium soaked with cements made from glasses Sr0 to Sr10 had normal morphologies (**Figures 6C–E**) and their metabolic activities were never significantly lower than that of the negative control. Cells exposed to medium soaked with cement from glass Sr50 contained cells with normal morphologies but also some rounded cells (**Figure 6F**); however, their metabolic activity was not significantly different from that of the negative control ($p > 0.05$).

Concentrations of Mg^{2+} , Ca^{2+} , F^{-} , and silicon ions in cell culture medium soaked with cements from glasses Sr0 to Sr50 did not vary greatly with glass composition. The only exception were the concentrations of Sr^{2+} ions, which increased linearly ($R^2 = 0.999$) with strontium for calcium substitution in the glass (**Figure 7B**).

Discussion

Bioactive glasses are successfully used to regenerate bone; they degrade in physiological solutions and release ions to stimulate bone formation. When in contact with aqueous solutions, particularly at low pH (Bingel et al., 2015), BGs show a fast release of modifier ions (Hoppe et al., 2011; Brauer, 2015), including sodium, calcium, strontium, or magnesium ions (Fredholm et al., 2012; Bingel et al., 2015; Blochberger et al., 2015). This ability of BG to release ions can also be exploited for preparing GIC. The glasses in the present study were shown to release ions fast when in contact with a solution of a pH comparable to that of the PVPA–PAA solution used (**Figure 2B**), with the majority of ions being released during the first 5 min of immersion. Over the remaining time of the experiment (up to 24 h) ionic concentrations kept increasing, but much more slowly. When following changes in

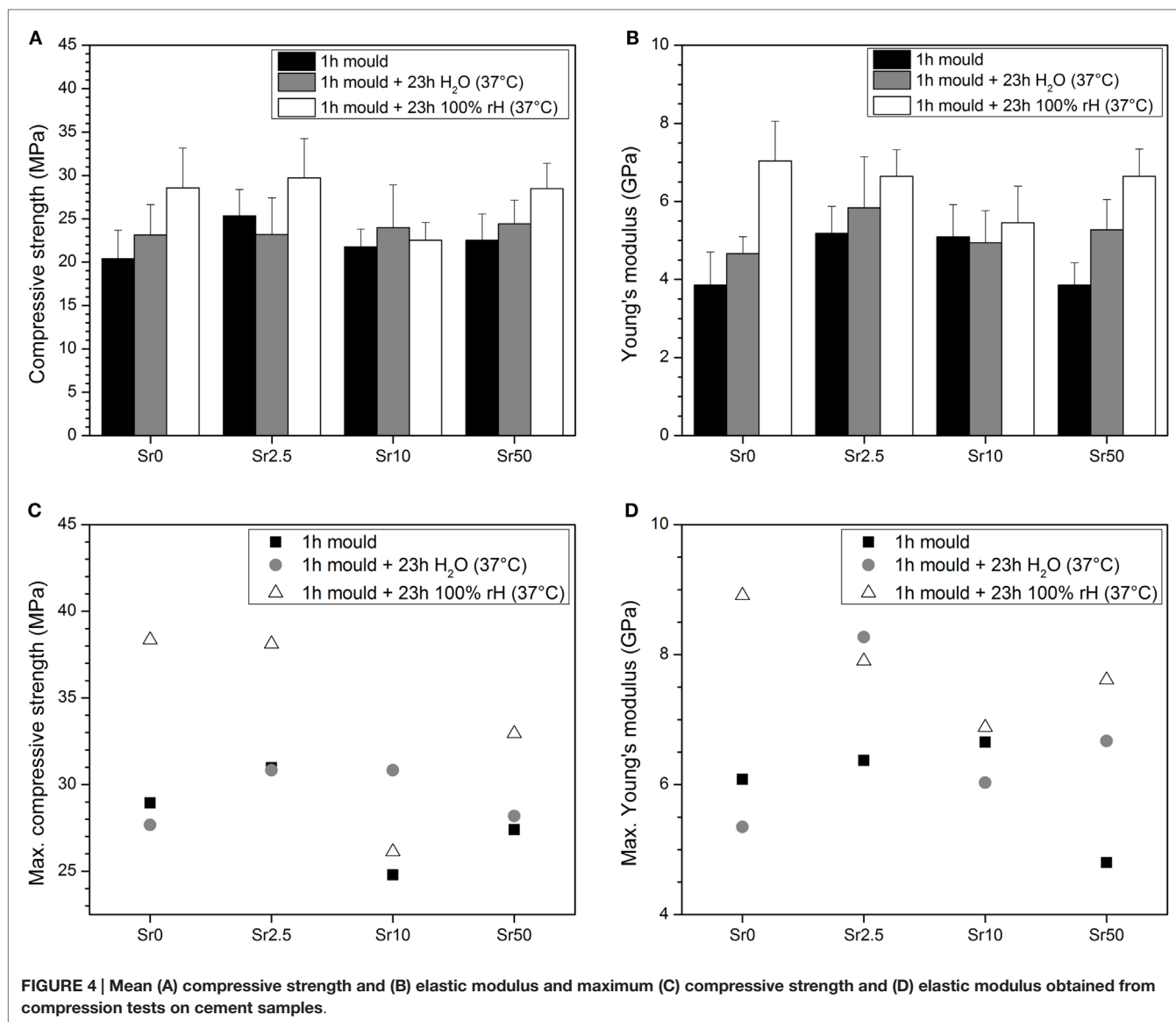
glass structure during immersion by FTIR (**Figure 2C**), it became obvious that indeed after the initial dramatic changes over the first 5 min (where the non-bridging oxygen band disappeared nearly completely) no pronounced structural changes seemed to occur.

Dental GICs set by a neutralization reaction between a polymeric acid and an acid-degradable (fluoro–) aluminosilicate glass (Wilson, 1996). In aluminosilicate glasses, aluminum, an intermediate element according to Dietzel's rules (Dietzel, 1941), has been shown to be present in fourfold coordination mostly, forming Si–O–Al bonds and AlO_4^{-} groups, which are charge-balanced by modifier cations (Neuville et al., 2006). These Si–O–Al bonds are readily hydrolyzed at low pH (Griffin and Hill, 1999), allowing for rapid glass degradation and ion release, which enables the GIC to set by formation of ionic bridges between carboxylate groups by metal cations such as Al^{3+} . As aluminum ions are known to be neurotoxic (Joshi, 1990) and negatively affect bone mineralization (Cournot-Witmer et al., 1981; Boyce et al., 1982; Blades et al., 1998), magnesium ions have been studied as a possible alternative.

This makes the use of magnesium-containing BG of particular interest here, as it has been suggested that MgO acts as an intermediate oxide in BG, partially entering the silicate network (Watts et al., 2010). This would mean that some magnesium is present as Si–O–Mg bonds, which may be acid hydrolyzable in analogy to Si–O–Al bonds in dental GIC (Griffin and Hill, 1999). And although recent results showed that there is no pronounced difference in the release patterns of Ca^{2+} and Mg^{2+} ions from BGs (Blochberger et al., 2015), Mg^{2+} ions with their smaller ionic radius compared to calcium ions [Mg^{2+} 0.072 nm; Ca^{2+} 0.100 nm; both sixfold coordination (Shannon, 1976)] and thus higher field strength may be of interest for effective cross-linking of the carboxylate groups in the GIC matrix.

Cement setting and subsequent mechanical properties are influenced by a range of (to some extent interconnected) factors. Ion release from the glass has a strong influence on cement setting, and working and setting time are likely to depend on how fast ions are actually released from the glass. Ion field strength is likely to affect both cement setting and mechanical properties, with small cations of high charge, e.g., Al^{3+} , resulting in better setting and improved mechanical properties compared to, e.g., alkaline earth metal cations. The polymeric acid component has also been shown to affect setting and mechanical properties, with molecular weight being one factor here and other factors including the type and number of functional groups per monomer unit (Hill et al., 1989; Griffin and Hill, 1998). These functional groups were observed in FTIR spectra (**Figure 3**), and the spectra allowed for following the reaction between PVPA–PAA and the glass, particularly by the decrease in intensity of carboxyl and phosphonic acid groups, and the increase in intensity of the corresponding salt bands.

In the present study, we did not see a pronounced influence of glass composition on GIC mechanical properties (**Figure 4**), but maximum Young's moduli seemed to decrease with increasing strontium for calcium substitution in the glass (**Figure 4D**). This may be explained by the larger ionic radius of Sr^{2+} compared to Ca^{2+} , which can be expected to result in it being a slightly less



effective ion for cross-linking of the polycarboxylate chains. It was also noticeable that the glass with the highest strontium for calcium substitution showed a shorter working time and poorer mixing properties than glasses with lower substitutions. Indeed, it was very difficult to obtain a homogeneously mixed cement of glass Sr50 unless the glass powder was annealed first to reduce its reactivity. For all other glass compositions, it was possible to obtain cements from both annealed and non-annealed glass powders, although annealing resulted in increased working times and easier mixing. This influence of strontium for calcium substitution is likely to be related to the ion release from the glass. Relative ion release, i.e., the percentage of ions released from a glass, has been shown to increase with strontium for calcium substitution in BG (Fredholm et al., 2012) owing to a lower oxygen density, i.e., an expanded silicate network, in the glass (Fredholm et al., 2010; Du and Xiang, 2012), caused by the larger ionic radius of Sr^{2+} ions compared to Ca^{2+} ions (Martin

et al., 2012). The same effect is likely to have influenced not only ion release and subsequent cement setting in the present study but also the lower T_g and crystallization temperature (Lotfikhshairesh et al., 2010) observed for glass Sr50 (Table 1). The effect of annealing on working times may possibly be explained by the removal of surface stresses introduced during the grinding process.

In our previous study, we showed that GIC prepared from the same glass compositions but using PAA (rather than PVPA-PAA) as the polymeric acid exhibited poor hydrolytic stability (Brauer et al., 2011a, 2013), with the cements becoming soft when in contact with water. In the present study, all cements stayed hard during storage in either water or at 100% relative humidity. This difference was probably caused by differences in the functional groups of the polymers, as PAA only has one carboxyl group per repeating unit, while PVPA-PAA has a phosphonic acid group, i.e., a diprotic acid group, in addition to the carboxyl group

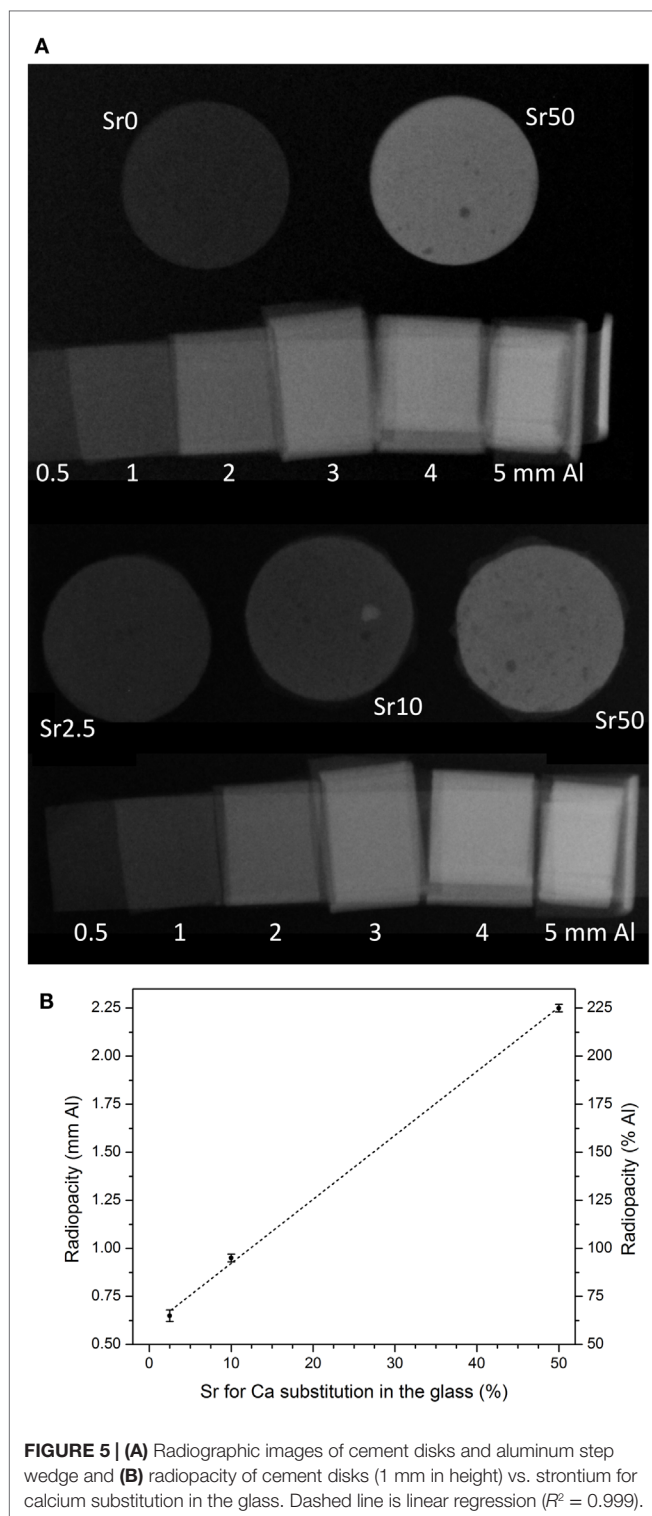


FIGURE 5 | (A) Radiographic images of cement disks and aluminum step wedge and **(B)** radiopacity of cement disks (1 mm in height) vs. strontium for calcium substitution in the glass. Dashed line is linear regression ($R^2 = 0.999$).

(Figure 8). This provides for more protons to attack the glass but also, once deprotonated, for more ionic cross-links to form between metal cations and the polymeric acid.

The radiopacity of implants is often increased in order to enable or facilitate visualization of the material during medical imaging such as radiography or fluoroscopy, and radiopacifiers such as

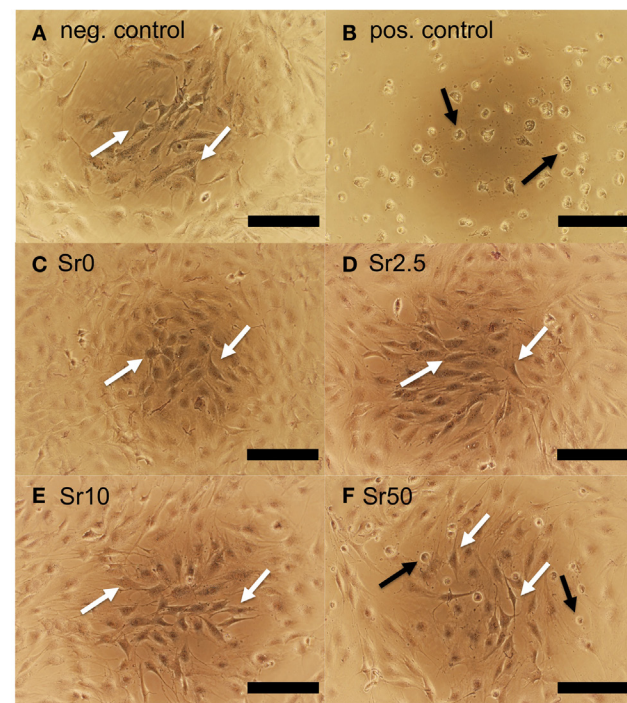
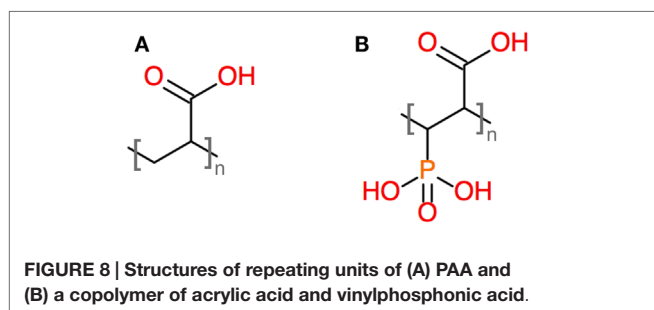
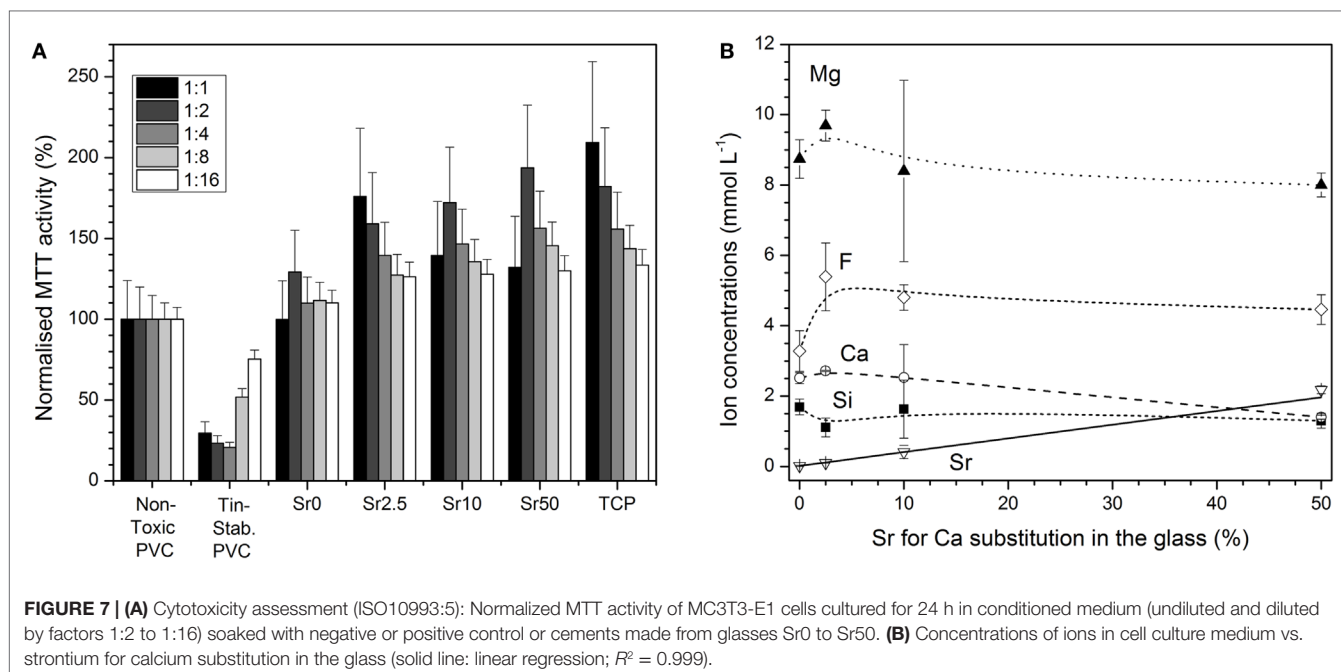


FIGURE 6 | MC3T3-E1 cells cultured for 24 h in conditioned medium soaked with (A) negative and (B) positive control and (C–F) cements prepared with glasses Sr0 to Sr50. Examples of cells with normal morphologies are indicated with white arrows; cells with poorly spread morphologies are indicated with black arrows (scale bar is 200 μm).

barium sulfate are commonly added to cement systems including acrylic cements (Jasper et al., 2002). Density and atomic number are two main factors influencing the radiopacity of a material, and if high atomic number elements are present in a material, it can be expected to possess an inherent radiopacity. Incorporation of strontium into calcium phosphate cements has been shown to increase their radiopacity (Schumacher and Gelinsky, 2015), and in a similar effect, increasing strontium for calcium substitution in the glass, and thus the presence of increasing amounts of strontium ions in the GIC, made the GIC in the present study increasingly radiopaque (Figure 5).

Comparing the radiopacity of these GICs to that of bone slices of the same thickness is complicated owing to the lack of available literature. Radiographic images of alveolar sockets and surrounding bone, however, showed radiographic densities of about 1.6 mm Al (Fernandes Gomes et al., 2006). While no exact thickness of the bone was given, the thickness was more than 1 mm (i.e., more than the thickness of our GIC specimens here), as the radiographs showed the entire jawbone. This suggests that the radiopacity of the GIC prepared with Sr50 is well above that of bone and that even a lower strontium for calcium substitution (e.g., 30–40%) might be sufficient to obtain radiopaque cements, which would show in a radiograph.

If implant materials are used to fill bone defects, their role as void filler can be combined with a role as a release device for therapeutic agents. For inorganic implant materials, such as BG



or GIC, an easy way of achieving this is by incorporating ions which can be released into the body and perform their therapeutic action there (Hoppe et al., 2011). Key is here to keep ionic concentrations in the range where therapeutic benefits are obtained but no toxic effects are observed. Therefore, caution should be exercised when substituting reportedly therapeutic ions into BG or GIC. Although zinc, for example, plays a number of essential biological roles in the body, particularly in bone formation, toxicity can result if the concentrations released are too high (Brauer et al., 2011a).

Glass ionomer cement studied here released various ions originating from the BG, but did not show any cytotoxic effects according to ISO 10993:5 (Figure 7). Instead, they performed at least as well as the non-toxic PVC control. GICs released about 1.5–2 mM of silicon ions (Figure 7B), originating from degradation of the BG silicate matrix. Ionic dissolution products from BG have been shown to increase osteoblast proliferation via gene upregulation (Xynos et al., 2000), and silicon ions are thought to play a key role here (Hoppe et al., 2011). The great benefit is that supplementation with growth factors is not necessary when using BG, owing to the stimulatory effects of silicon

and also calcium ions (Jones, 2013). If BGs are incorporated into GIC, comparable benefits through ion release may possibly be observed.

Apart from adding radiopacity to the cements, the presence of strontium in the glass allowed for the release of strontium ions (Figure 7B), which, when released from BG, showed anabolic and anticatabolic effects *in vitro* (Gentleman et al., 2010). And, indeed, strontium ions are the active component in a drug for the treatment of osteoporosis (Marie, 2005; Bonnellye et al., 2008). In the present study, strontium concentrations in cell culture medium were between 0.1 (Sr2.5) and 2.2 mM (Sr50), which corresponds to a concentration range from 9 to 192 ppm. Concentrations in a similar range were recently shown to stimulate osteoblasts (25 ppm) and inhibit osteoclasts (80 ppm) (Gentleman et al., 2010). Strontium ions released from GIC have also previously been shown to have antibacterial properties and reduce cell counts of *Streptococcus faecalis* or *Staphylococcus aureus* when present in concentrations between 0.16 and 2.5 mM (Brauer et al., 2013).

The benefits of fluoride ions in preventing dental caries are well documented (Featherstone, 2000), and, indeed, the release of fluoride ions is one of the advantages of using dental GIC (Ewoldsen and Demke, 2001). However, fluoride ions also affect bone health. As high concentrations of fluoride, traditionally administered orally as sodium fluoride, are not effective in preventing fractures (Aaseth et al., 2004), its use for treating osteoporosis was dismissed for several years. Recently, however, the use of low fluoride concentrations, in combination with other therapeutic agents, is being reexamined (Reid et al., 2007). In addition, synergistic effects of fluoride and strontium ions in promoting antibacterial activity have been suggested (Dabsie et al., 2009). Cell culture studies on fluoride-releasing BGs showed that low concentrations of fluoride released from the

glass (between 1.5 and 1.8 ppm) enhanced cell attachment and proliferation, while initial high release of fluoride ions (between 10 and 35 ppm) followed by much reduced release (0.3 to 2 ppm) through formation of a protective fluorapatite surface layer on the BGs showed significantly increased alkaline phosphatase (ALP) activity, a marker for mineralization, indicating that fluoride-containing BGs can direct cell differentiation (Gentleman et al., 2013). In the present study, fluoride concentrations in the culture medium were between 3 and 6 mM (corresponding to 60–100 ppm), indicating that lower fluoride concentrations in the glass component (and subsequently in the GIC) may be advantageous.

The GICs studied here also released magnesium ions, and concentrations in undiluted cell culture medium ranged from about 8 to 10 mM. Magnesium ions present in and released from BGs have been shown to reduce apatite precipitation (Diba et al., 2012; Blochberger et al., 2015), but some beneficial effects on osteoblast proliferation, differentiation, and ALP activity have been suggested (Hoppe et al., 2011).

References

- Aaseth, J., Shimshi, M., Gabrilove, J. L., and Birketvedt, G. S. (2004). Fluoride: a toxic or therapeutic agent in the treatment of osteoporosis? *J. Trace Elem. Exp. Med.* 17, 83–92. doi:10.1002/jtra.10051
- Agency for Healthcare Research and Quality. (2010). *Department of Research & Scientific Affairs, American Academy of Orthopaedic Surgeons*. Rosemont, IL: Based on data from the HCUP Nationwide Inpatient Sample.
- Autefage, H., Gentleman, E., Littmann, E., Hedegaard, M. A. B., von Erlich, T., O'Donnell, M., et al. (2015). Sparse feature selection methods identify unexpected global cellular response to strontium-containing materials. *Proc. Natl. Acad. Sci. U.S.A.* 112, 4280–4285. doi:10.1073/pnas.1419799112
- Bingel, L., Groh, D., Karpukhina, N., and Brauer, D. S. (2015). Influence of dissolution medium pH on ion release and apatite formation of Bioglass® 45S5. *Mater. Lett.* 143, 279–282. doi:10.1016/j.matlet.2014.12.124
- Blades, M. C., Moore, D. P., Revell, P. A., and Hill, R. (1998). In vivo skeletal response and biomechanical assessment of two novel polyalkenoate cements following femoral implantation in the female New Zealand white rabbit. *J. Mater. Sci. Mater. Med.* 9, 701–706.
- Blochberger, M., Hupa, L., and Brauer, D. S. (2015). Influence of zinc and magnesium substitution on ion release from Bioglass® 45S5 at physiological and acidic pH. *Biomed. Glasses* 1, 93–107. doi:10.1515/bglass-2015-0009
- Bonnelye, E., Chabadel, A., Saltel, F., and Jurdic, P. (2008). Dual effect of strontium ranelate: stimulation of osteoblast differentiation and inhibition of osteoclast formation and resorption *in vitro*. *Bone* 42, 129–138. doi:10.1016/j.bone.2007.08.043
- Boyce, B. F., Elder, H. Y., Elliot, H. L., Fogelman, I., Fell, G. S., Junor, B. J., et al. (1982). Hypercalcemic osteomalacia due to aluminum toxicity. *Lancet* 2, 1009–1013. doi:10.1016/S0140-6736(82)90049-6
- Brauer, D. S. (2015). Bioactive glasses – structure and properties. *Angew. Chem. Int. Ed. Engl.* 54, 4160–4181. doi:10.1002/anie.201405310
- Brauer, D. S., Gentleman, E., Farrar, D. F., Stevens, M. M., and Hill, R. G. (2011a). Benefits and drawbacks of zinc in glass ionomer bone cements. *Biomed. Mater.* 6, 045007. doi:10.1088/1748-6041/6/4/045007
- Brauer, D. S., Mneimne, M., and Hill, R. G. (2011b). Fluoride-containing bioactive glasses: fluoride loss during melting and ion release in tris buffer solution. *J. Non Cryst. Solids* 357, 3328–3333. doi:10.1016/j.jnoncrysol.2011.05.031
- Brauer, D. S., Karpukhina, N., Kedia, G., Bhat, A., Law, R. V., Radecka, I., et al. (2013). Bactericidal strontium-releasing injectable bone cements based on bioactive glasses. *J. R. Soc. Interface* 10, 20120647. doi:10.1098/rsif.2012.0647
- Cournot-Witmer, G., Zingraff, J., Plachot, J. J., Escaig, F., Lefèvre, R., Boumati, P., et al. (1981). Aluminum localization in bone from hemodialyzed patients – relationship to matrix mineralization. *Kidney Int.* 20, 375–385. doi:10.1038/ki.1981.149
- Dabsie, F., Gregoire, G., Sixou, M., and Sharrock, P. (2009). Does strontium play a role in the cariostatic activity of glass ionomer? Strontium diffusion and antibacterial activity. *J. Dent.* 37, 554–559. doi:10.1016/j.jdent.2009.03.013
- Darling, M., and Hill, R. (1994). Novel polyalkenoate (glass-ionomer) dental cements based on zinc silicate-glasses. *Biomaterials* 15, 299–306. doi:10.1016/0142-9612(94)90055-8
- Diba, M., Tapia, F., Boccaccini, A. R., and Strobel, L. A. (2012). Magnesium-containing bioactive glasses for biomedical applications. *Int. J. Appl. Glass Sci.* 3, 221–253. doi:10.1111/j.2041-1294.2012.00095.x
- Dietzel, A. (1941). Structural chemistry of glass. *Naturwissenschaften* 29, 537–547. doi:10.1007/BF01513796
- Du, J. C., and Xiang, Y. (2012). Effect of strontium substitution on the structure, ionic diffusion and dynamic properties of 45S5 bioactive glasses. *J. Non Cryst. Solids* 358, 1059–1071. doi:10.1016/j.jnoncrysol.2011.12.114
- Ewoldsen, N., and Demke, R. S. (2001). A review of orthodontic cements and adhesives. *Am. J. Orthod. Dentofacial Orthop.* 120, 45–48. doi:10.1067/mod.2001.117207
- Featherstone, J. D. B. (2000). The science and practice of caries prevention. *J. Am. Dent. Assoc.* 131, 887–899. doi:10.14219/jada.archive.2000.0307
- Fernandes Gomes, M., Pinheiro de Abreu, P., Cantarelli Morosoli, A. R., Marotta Araujo, M., and das Gracas Vilela Goulart, M. (2006). Densitometric analysis of the autogenous demineralized dentin matrix on the dental socket wound healing process in humans. *Braz. Oral Res.* 20, 324–330.
- Fredholm, Y. C., Karpukhina, N., Brauer, D. S., Jones, J. R., Law, R. V., and Hill, R. G. (2012). Influence of strontium for calcium substitution in bioactive glasses on degradation, ion release and apatite formation. *J. R. Soc. Interface* 9, 880–889. doi:10.1098/rsif.2011.0387
- Fredholm, Y. C., Karpukhina, N., Law, R. V., and Hill, R. G. (2010). Strontium containing bioactive glasses: glass structure and physical properties. *J. Non Cryst. Solids* 356, 2546–2551. doi:10.1016/j.jnoncrysol.2010.06.078
- Gentleman, E., Fredholm, Y. C., Hill, R. G., Lotfibakhshaei, N., O'Donnell, M. D., Hill, R. G., et al. (2010). The effects of strontium-substituted bioactive glasses on osteoblasts and osteoclasts *in vitro*. *Biomaterials* 31, 3244–3252. doi:10.1016/j.biomaterials.2010.01.121
- Gentleman, E., Stevens, M. M., Hill, R. G., and Brauer, D. S. (2013). Surface properties and ion release from fluoride-containing bioactive glasses promote osteoblast differentiation and mineralization *in vitro*. *Acta Biomater.* 9, 5771–5779. doi:10.1016/j.actbio.2012.10.043
- Griffin, S., and Hill, R. (1998). Influence of poly(acrylic acid) molar mass on the fracture properties of glass polyalkenoate cements. *J. Sci. Mater.* 33, 5383–5396. doi:10.1023/A:1004498217028
- Griffin, S. G., and Hill, R. G. (1999). Influence of glass composition on the properties of glass polyalkenoate cements. Part I: influence of aluminium to silicon ratio. *Biomaterials* 20, 1579–1586. doi:10.1016/S0142-9612(99)00058-7

Acknowledgments

The authors wish to thank Mrs. Brunhilde Drefler, Institute of Geography, University Jena, for her help and support with ICP-OES measurements and Dr. Christian Bocker, Otto Schott Institute, for EDX analyses. PVPAA-PAA solution was kindly provided by Ade Akinmade, First Scientific Dental Materials, Elmshorn, Germany. DB gratefully acknowledges funding from the Carl Zeiss Foundation, Germany. EG acknowledges funding from the Wellcome Trust, UK, for a Research Career Development Fellowship.

- Guida, A., Towler, M. R., Wall, J. G., Hill, R. G., and Eramo, S. (2003). Preliminary work on the antibacterial effect of strontium in glass ionomer cements. *J. Mater. Sci. Lett.* 22, 1401–1403. doi:10.1023/A:1025794927195
- Hernlund, E., Svedbom, A., Ivergård, M., Compston, J., Cooper, C., Stenmark, J., et al. (2013). Osteoporosis in the European Union: medical management, epidemiology and economic burden. A report prepared in collaboration with the international osteoporosis foundation (IOF) and the European federation of pharmaceutical industry associations (EFPIA). *Arch. Osteoporos.* 8, 136. doi:10.1007/s11657-013-0136-1
- Hill, R. G., Wilson, A. D., and Warrens, C. P. (1989). The influence of poly(acrylic acid) molecular weight on the fracture toughness of glass-ionomer cements. *J. Sci. Mater.* 24, 363–371. doi:10.1007/BF00660982
- Hoppe, A., Güldal, N. S., and Boccaccini, A. R. (2011). A review of the biological response to ionic dissolution products from bioactive glasses and glass-ceramics. *Biomaterials* 32, 2757–2774. doi:10.1016/j.biomaterials.2011.01.004
- Hurrell-Gillingham, K., Reaney, I. M., Brook, I., and Hatton, P. V. (2006). *In vitro* biocompatibility of a novel Fe₂O₃ based glass ionomer cement. *J. Dent.* 34, 533–538. doi:10.1016/j.jdent.2005.07.011
- Jasper, L. E., Deramond, H., Mathis, J. M., and Belkoff, S. M. (2002). Material properties of various cements for use with vertebroplasty. *J. Mater. Sci. Mater. Med.* 13, 1–5. doi:10.1023/A:1013170610826
- Jones, J. R. (2013). Review of bioactive glass: from Hench to hybrids. *Acta Biomater.* 9, 4457–4486. doi:10.1016/j.actbio.2012.08.023
- Joshi, J. G. (1990). Aluminum, a neurotoxin which affects diverse metabolic reactions. *Biofactors* 2, 163–169.
- Lewis, G. (2006). Injectable bone cements for use in vertebroplasty and kyphoplasty: state-of-the-art review. *J. Biomed. Mater. Res. Part B Appl. Biomater.* 76B, 456–468. doi:10.1002/jbm.b.30398
- Lotfikhshai, N., Brauer, D. S., and Hill, R. G. (2010). Bioactive glass engineered coatings for Ti6Al4V alloys: influence of strontium substitution for calcium on sintering behaviour. *J. Non Cryst. Solids* 356, 2583–2590. doi:10.1016/j.jnoncrsol.2010.05.017
- Marie, P. J. (2005). Strontium as therapy for osteoporosis. *Curr. Opin. Pharmacol.* 5, 633–636. doi:10.1016/j.coph.2005.05.005
- Marie, P. J., Ammann, P., Boivin, G., and Rey, C. (2001). Mechanisms of action and therapeutic potential of strontium in bone. *Calcif. Tissue Int.* 69, 121–129. doi:10.1007/s002230010055
- Martin, R. A., Twyman, H. L., Rees, G. J., Barney, E. R., Moss, R. M., Smith, J. M., et al. (2012). An examination of the calcium and strontium site distribution in bioactive glasses through isomorphic neutron diffraction, X-ray diffraction, EXAFS and multinuclear solid state NMR. *J. Mater. Chem.* 22, 22212–22223. doi:10.1039/c2jm33058j
- Neuville, D. R., Cormier, L., and Massiot, D. (2006). Al coordination and speciation in calcium aluminosilicate glasses: effects of composition determined by Al-27 MQ-MAS NMR and Raman spectroscopy. *Chem. Geol.* 229, 173–185. doi:10.1016/j.chemgeo.2006.01.019
- Reid, I. R., Cundy, T., Grey, A. B., Horne, A., Clearwater, J., Ames, R., et al. (2007). Addition of monofluorophosphate to estrogen therapy in postmenopausal osteoporosis: a randomized controlled trial. *J. Clin. Endocrinol. Metab.* 92, 2446–2452. doi:10.1210/jc.2006-2264
- Schumacher, M., and Gelinsky, M. (2015). Strontium modified calcium phosphate cements – approaches towards targeted stimulation of bone turnover. *J. Mater. Chem. B* 3, 4626–4640. doi:10.1039/C5TB00654F
- Shannon, R. D. (1976). Revised effective ionic radii and systematic studies of interatomic distances in halides and chalcogenides. *Acta Crystallogr. Sect. A* 32, 751–767. doi:10.1107/S0567739476001551
- Socrates, G. (2004). *Infrared and Raman Characteristic Group Frequencies. Tables and Charts*. Chichester, NY: John Wiley & Sons.
- Stamboulis, A., Law, R. V., and Hill, R. G. (2004). Characterisation of commercial ionomer glasses using magic angle nuclear magnetic resonance (MAS-NMR). *Biomaterials* 25, 3907–3913. doi:10.1016/j.biomaterials.2003.10.074
- Thuy, T. T., Nakagaki, H., Kato, K., Phan, A. H., Inukai, J., Tsuboi, S., et al. (2008). Effect of strontium in combination with fluoride on enamel remineralization in vitro. *Arch. Oral Biol.* 53, 1017–1022. doi:10.1016/j.archoralbio.2008.06.005
- Watts, S. J., O'Donnell, M. D., Law, R. V., and Hill, R. G. (2010). Influence of magnesia on the structure and properties of bioactive glasses. *J. Non Cryst. Solids* 356, 517–524. doi:10.1016/j.jnoncrsol.2009.04.074
- Wilson, A. D. (1996). A hard decade's work: steps in the invention of the glass-ionomer cement. *J. Dent. Res.* 75, 1723–1727. doi:10.1177/00220345960750100301
- Wilson, A. D., Prosser, H. J., and Powis, D. M. (1983). Mechanism of adhesion of poly-electrolyte cements to hydroxyapatite. *J. Dent. Res.* 62, 590–592. doi:10.1177/00220345830620051801
- Xynos, I. D., Edgar, A. J., Buttery, L. D. K., Hench, L. L., and Polak, J. M. (2000). Ionic products of bioactive glass dissolution increase proliferation of human osteoblasts and induce insulin-like growth factor II mRNA expression and protein synthesis. *Biochem. Biophys. Res. Commun.* 276, 461–465. doi:10.1006/bbrc.2000.3503

Conflict of Interest Statement: The authors declare that the research was conducted in the absence of any commercial or financial relationships that could be construed as a potential conflict of interest.

Copyright © 2015 Fuchs, Gentleman, Shahid, Hill and Brauer. This is an open-access article distributed under the terms of the Creative Commons Attribution License (CC BY). The use, distribution or reproduction in other forums is permitted, provided the original author(s) or licensor are credited and that the original publication in this journal is cited, in accordance with accepted academic practice. No use, distribution or reproduction is permitted which does not comply with these terms.



Development of Magnesium and Siloxane-Containing Vaterite and Its Composite Materials for Bone Regeneration

Shinya Yamada¹, Akiko Obata^{1*}, Hirotaka Maeda¹, Yoshio Ota² and Toshihiro Kasuga^{1*}

¹ Department of Frontier Materials, Graduate School of Engineering, Nagoya Institute of Technology, Nagoya, Japan,

² Yabashi Industries Co., Ltd., Ogaki, Japan

OPEN ACCESS

Edited by:

Aldo R. Boccaccini,
University of Erlangen-Nuremberg,
Germany

Reviewed by:

Steve Meikle,
University of Brighton, UK
Alexander Hoppea,
Johnson Matthey, Netherlands

*Correspondence:

Akiko Obata
obata.akiko@nitech.ac.jp;
Toshihiro Kasuga
kasuga.toshihiro@nitech.ac.jp

Specialty section:

This article was submitted to
Biomaterials,
a section of the journal
Frontiers in Bioengineering and
Biotechnology

Received: 30 June 2015

Accepted: 17 November 2015

Published: 02 December 2015

Citation:

Yamada S, Obata A, Maeda H, Ota Y
and Kasuga T (2015) Development of
Magnesium and Siloxane-Containing
Vaterite and Its Composite Materials
for Bone Regeneration.
Front. Bioeng. Biotechnol. 3:195.
doi: 10.3389/fbioe.2015.00195

Development of novel biomaterials with Mg²⁺, Ca²⁺, and silicate ions releasability for bone regeneration is now in progress. Several inorganic ions have been reported to stimulate bone-forming cells. We featured Ca²⁺, silicate, and especially, Mg²⁺ ions as growth factors for osteoblasts. Various biomaterials, such as ceramic powders and organic-inorganic composites, that release the ions, have been developed and investigated for their cytocompatibilities in our previous work. Through the investigation, providing the three ions was found to be effective to activate osteogenic cells. Magnesium and siloxane-containing vaterite was prepared by a carbonation process as an inorganic particle that can has the ability to simultaneously release Ca²⁺, silicate, and Mg²⁺ ions to biodegradable polymers. Poly (L-lactic acid) (PLLA)- and bioactive PLLA-based composites containing vaterite coatings were discussed regarding their degradability and cytocompatibility using a metallic Mg substrate as Mg²⁺ ion source. PLLA/SiV composite film, which has a releasability of silicate ions besides Ca²⁺ ion, was coated on a pure Mg substrate to be compared with the PLLA/V coating. The degradability and releasability of inorganic ions were morphologically and quantitatively monitored in a cell culture medium. The bonding strength between the coatings and Mg substrates was one of the key factors to control Mg²⁺ ion release from the substrates. The cell culture tests were conducted using mouse osteoblast-like cells (MC3T3-E1 cells); cellular morphology, proliferation, and differentiation on the materials were evaluated. The PLLA/V and PLLA/SiV coatings on Mg substrates were found to enhance the proliferation, especially the PLLA/SiV coating possessed a higher ability to induce the osteogenic differentiation of the cells.

Keywords: bioceramics, magnesium, calcium, silicate, bone regeneration

INTRODUCTION

Various types of bioactive ceramics and glasses have been investigated for application in bone regeneration (Jarcho, 1981; Winter et al., 1981; LeGeros, 2002). Calcium phosphate and calcium silicate glasses, such as Bioglass® 45S5, are well known to have excellent bioactivity and promote new bone formation *in vivo*. Recently, several ions released from these materials have been found to influence cell functions and some of the ions can accelerate osteogenesis, angiogenesis, and

antibacterial activity (Hoppe et al., 2011). Calcium (Ca^{2+}) ions released from composite materials, consisting of a type II collagen gel and hydroxyapatite (HA), have been demonstrated to have a stimulatory effect on the activation of mouse primary osteoblasts (Maeno et al., 2005). Ca^{2+} ion concentrations of 2–4 mM are reported to be suitable for enhancing the proliferation and survival of osteoblasts, whereas concentrations of 6–8 mM favor their differentiation and biomineralization of extracellular matrix (ECM). Ca^{2+} ion concentrations >10 mM were found to be cytotoxic for cells.

Stimulatory effects for the enhancement of bone formation were found for the soluble silica species and Ca^{2+} ions that were released from Bioglass® 45S5 (Xynos et al., 2000a). The cellular numbers of human osteoblasts (HOBs) cultured in the ionic products of Bioglass® 45S5, obtained by its dissolution in Dulbecco's modified eagle medium (DMEM), increased by $155.1 \pm 6.5\%$ compared with normal DMEM after 4 days of culture. HOBs cultured on the Bioglass® 45S5 disk exhibited higher alkaline phosphatase (ALP) activity, which is known to be associated with osteoblastic differentiation of HOBs, compared with those grown on a bioinert (plastic) substrate, after 6 days of culture (Xynos et al., 2000b). Trace amounts of Ca^{2+} and silicate ions are believed to be beneficial for the promotion of bone formation.

Additionally, magnesium (Mg^{2+}) ions have been reported to enhance cell adhesion to materials, along with the differentiation and biomineralization of osteoblasts. The expression of various integrin family members, which are a class of adhesion proteins, was increased on Mg^{2+} -modified alumina compared with Mg^{2+} -free controls (Zreiqat et al., 2002). The stimulatory effects of Mg^{2+} ions on early bone cell differentiation have also been reported, whereby osteoblasts cultured on bioactive $\text{SiO}_2\text{--CaO--P}_2\text{O}_5\text{--MgO}$ glass exhibited a high ALP activity (Saboori et al., 2009). Moreover, the effects of Mg^{2+} ions on angiogenic function have been clarified by Maier et al. (2004). Mg^{2+} ions stimulate the proliferation of human umbilical vein endothelial cells (HUVECs) and enhance the mitogenic response to angiogenic factors. These stimulatory effects of the released inorganic ions on cellular activities should be beneficial to the design of new biomaterials for bone regeneration.

Magnesium- and siloxane-containing vaterite (MgSiV) has been developed as a material that provides Mg^{2+} , Ca^{2+} , and silicate ions upon degradation in our previous work (Yamada et al., 2014a). Of the calcium carbonates, vaterite, calcite, and aragonite, vaterite is the most thermodynamically unstable polymorph. The chemical structure and their degradation behavior in physical condition were examined. From cell culture tests, mouse osteoblast-like cells had an improved proliferation, differentiation, and mineralization in the extract of the MgSiV and the dependence on the ion-type contained in the extract; these cell functions were significantly enhanced when all of the ions, Mg^{2+} , Ca^{2+} , and silicate ions, were simultaneously provided to the cells.

The improved functions of the cells were also observed in the results of the cell culture tests for metallic magnesium (Mg) substrates coated with a siloxane-containing vaterite (SiV) and poly(L-lactic acid) (PLLA) composite layer (Yamada et al., 2013, 2014b). The metallic Mg substrate coated with the composite layer releases the three kinds of ions at the same time; Ca^{2+} and

silicate ions are supplied by SiV, and Mg^{2+} ions are from the metallic Mg substrates. The cell proliferation and differentiation were accelerated on the metallic Mg substrate coated with the composite layer in comparison with those on the sample releasing only Ca^{2+} and Mg^{2+} ions or no ions.

The up-regulation effects by the three kinds of ions on the cells were found to be similar even though the providing process was different between the MgSiV and the Mg substrate coated with the composite layer. These findings imply that biomaterials providing the three kinds of ions would be good for achievement of the rapid mineralization of osteogenic cells. In addition, such inorganic ions supplied by bioceramics can be regarded to be one of the important factors for promoting bone formation *in vivo*.

In this review, we provide an overview of materials providing Mg^{2+} , Ca^{2+} , and silicate ions, i.e., the MgSiV and the Mg substrates coated with PLLA/SiV composite layer, and osteoblast-like cell reactions to the materials. In addition, new composite materials that possess an excellent 3D structure (cotton wool-like structure), flexibility, and a providing ability of Ca^{2+} and silicate ions are introduced as well. They have been expected to be good candidates for bone fillers.

MAGNESIUM- AND SILOXANE-CONTAINING VATERITE

The development of SiV (Nakamura et al., 2013) and its composites with biodegradable polymer, such as PLLA or poly(lactic-co-glycolic acid) (PLGA), as materials providing Ca^{2+} and silicate ions has been published in our previous work (Obata et al., 2009, 2010; Wakita et al., 2010; Fujikura et al., 2013). Electrospun fibremats consisting of the PLLA/SiV composites possessed excellent cell compatibility *in vitro* and a formation of mineralized tissue *in vivo*. Especially, in the results of cell culture tests, the PLLA/SiV composites accelerated the proliferation and the differentiation of mouse osteoblast-like cells in comparison with a composite consisting of vaterite and PLLA (Obata et al., 2009). This implies that the ions released from the PLLA/SiV composites, particularly silicate ions, must contribute to the enhanced cell functions. Many reports demonstrated that such ions are able to enhance osteogenic cell functions, proliferation, differentiation, and mineralization, and regarded to be one of the important factors for bone formation in the body (Hoppe et al., 2011). Thus, the SiV-containing composites are expected to be some of the good candidates for new biomaterials promoting bone formation.

In contrast, the ions released from the SiV and its composites are believed to have no up-regulation effect on cell adhesion. Cell adhesion is a significant process of progressing proliferation for adherent cells, such as osteoblasts and fibroblasts. To improve cell adhesion should be useful to improve proliferation and following biological reactions of these cells. Mg^{2+} ions have been found to improve cell adhesion to substrate surfaces (Zreiqat et al., 2002). Thus, to incorporate magnesium to the SiV was expected to achieve new biomaterials having higher cell compatibility, along with enhanced cell adhesion, proliferation, differentiation, and mineralization. In addition, MgSiV is expected to possess buffering action in aqueous solution since it releases carbonate ions as well, while most of silica-based bioactive glasses, such

as 45S5-type bioactive glass, increase its surrounding pH. This might be good for cells cultured on the material surfaces. The preparation of MgSiV powders has been reported in our previous work (Yamada et al., 2014a). In the present short review, some of their significant results are introduced briefly.

Preparation

Magnesium and siloxane-containing vaterite powders were synthesized by a carbonation process in methanol using calcium hydroxide, 3-aminopropyltriethoxysilane (APTES), and magnesium hydroxide as calcium, silicate, and magnesium sources, respectively (Yamada et al., 2014a). All the chemicals were mixed into the slurry under carbon dioxide gas flow, resulting in the formation of a precursor gel. The obtained gel was aged for 12 h at room temperature, dried at 110°C for 24 h, and then grounded to form particles. The obtained MgSiV contained 2.0 wt% of magnesium and 2.8 wt% of silicon. SiV powders were also prepared by the same method without adding magnesium source.

Structure

The prepared MgSiV samples exhibit flat-spherical morphology, around 1.3 μm in diameter and 0.6 μm in thickness (Figure 1). They consist of primary particles with several being 10 nm in size. On the other hand, the SiV have a spherical morphology, $\sim 1.4 \mu\text{m}$ in diameter. The reason why the morphologies are different between the two samples is that it is expected that the orientation of the vaterite phase in MgSiV might be varied by Mg^{2+} ions. Vaterite is known to have a characteristic symmetry and orientation of carbonate ions in its crystalline structure. The orientation is parallel to the *c*-axis (Wang and Becker, 2009). The siloxane derived from APTES is believed to contribute to the stabilization of the *c*-face (Nakamura et al., 2013). The Mg^{2+} ions in the MgSiV might influence the orientation, resulting in the formation of the flat-spherical particles. The surface areas of the two samples are also different; they were 103 and 34 m^2/g for the MgSiV and SiV, respectively, from the results of BET-nitrogen adsorption.

The crystalline phase of MgSiV consists predominantly of vaterite one and contains small amounts of calcite and calcium magnesium carbonate. X-ray diffraction (XRD) pattern of the MgSiV demonstrates that the peaks corresponding to the *c*-axis-dependent plane of vaterite shifted to a higher angle (Figure 2). By

contrast, the *ab* plane shows no shift. Mg might be incorporated into the vaterite crystalline structure and substitute for some of the Ca-sites in vaterite, since the lattice spacing for the vaterite (004) plane changed from 0.426 to 0.421 nm by adding Mg to SiV. The MgSiV and SiV were found to also contain the amorphous calcium carbonate (ACC) phase in their structures from the results of Fourier transform infrared spectroscopy (FTIR) analysis (data not shown here).

Ion Release

The MgSiV powders release Mg^{2+} , Ca^{2+} , and silicate ions through their crystalline transformation from vaterite to aragonite phase in aqueous solution. They were immersed in the Tris-HCl buffer solution (pH 7.4) for 7 days, and the amount of the released ions was measured by inductively coupled plasma atomic emission spectroscopy (ICP-AES) (Figure 3). Their crystalline phases at each time point during the immersion were characterized by XRD (Figure 4). The crystalline phase of the MgSiV transformed from vaterite into aragonite in 12 h after the immersion and simultaneously released 60% of the total Mg and 80% of the total Si. The release of the two ions continued until day 7, while the release rate decreased after 12 h. A total amount of 83% of the total Mg and almost all Si in the MgSiV were released in the 7 days. On the other hand, the Ca-release behavior was different from those of Mg and Si. The amount of the released Ca was maximum after 12 h and then continued to decline until day 7. The increase in the Ca amount in 12 h after the immersion is believed to originate from the dissolution of ACC. On the other hand, the decline in the amount is due to the formation of precipitates at the bottom of the containers used.

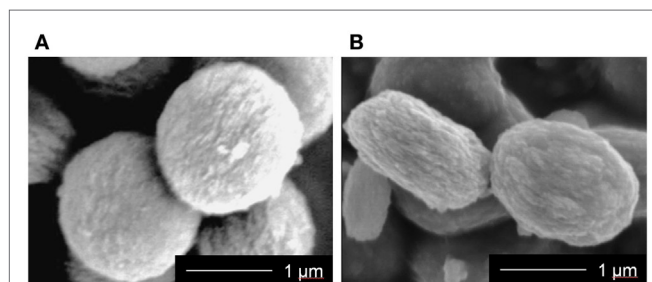


FIGURE 1 | SEM images of (A) SiV and (B) MgSiV. Reprinted with permission from Yamada et al. (2014a).

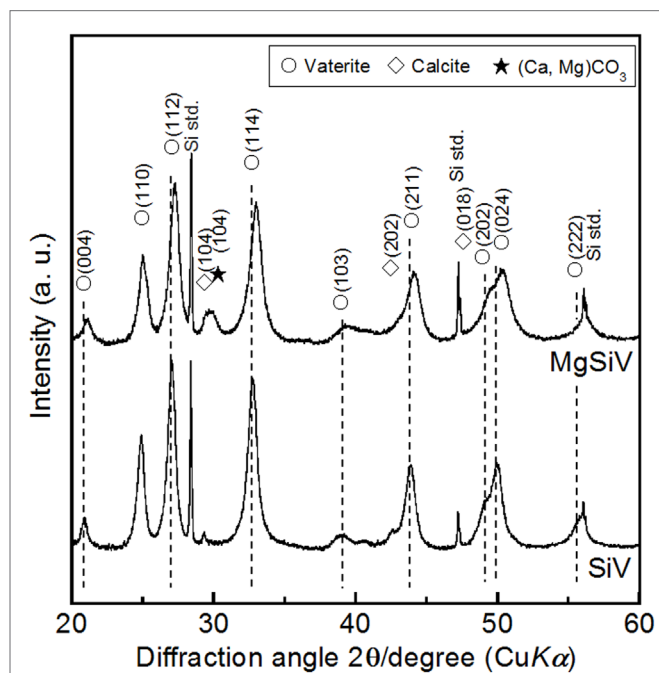


FIGURE 2 | XRD patterns of SiV and MgSiV. Reprinted with permission from Yamada et al. (2014a).

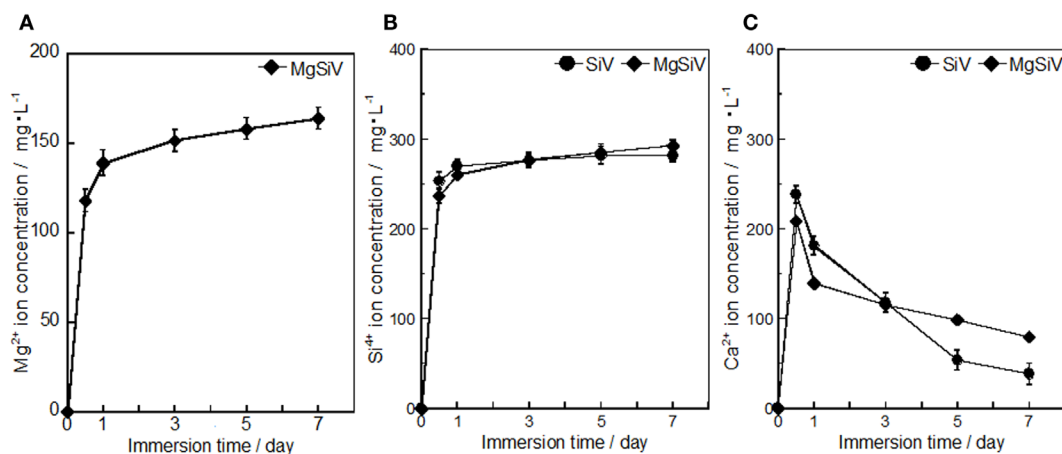


FIGURE 3 | Amounts of (A) Mg, (B) Si, and (C) Ca elements dissolved from SiV and MgSiV. Reprinted with permission from Yamada et al. (2014a).

The SiV powders possess ion-release behavior similar to the MgSiV. The transformation of the crystal phase of the SiV is, however, different from the MgSiV; its phase changed from vaterite to calcite in 12 h after the immersion. This is because aragonite phase precipitates more easily in an aqueous solution containing a large amount of Mg²⁺ ions (Kitano, 1962; Bischoff, 1968; Sawada et al., 1990; Böttcher et al., 1997; Morse et al., 1997; Kitamura, 2001; Zhang et al., 2012). No Mg²⁺ ion is incorporated in the lattice of aragonite because it has a tightly bound hydration shell (Falini et al., 1996, 2009). After 12 h, small peaks corresponding to vaterite phase are still seen for the MgSiV, while the crystal phase of SiV completely transformed to calcite. Mg must be incorporated into the vaterite crystalline structure in the MgSiV, since the peaks corresponding to vaterite in the MgSiV shifted compared with those of the SiV. The Mg incorporated into the vaterite dissolved from the MgSiV in 12 h, because the peaks revert to the original positions of the SiV. Vaterite disappeared and the predominant crystalline phase was aragonite after 7 days. The particle shape of the MgSiV varied after the immersion; no original MgSiV particles were found, but needle-like ones, which is a typical shape of aragonite, were newly observed in the samples after 7 days of immersion.

PLLA/SiV COMPOSITE COATING ON A METALLIC MAGNESIUM SUBSTRATE

Metallic Mg and its alloys possess biodegradability and proper mechanical properties and are regarded to be good candidates for metallic biomaterials (Staiger et al., 2006; Witte et al., 2008; Witte, 2010). They have the suitable properties for being used as vascular stents or orthopedic implants; they possess high reactivity with water and dissolve in body fluid through corrosion, which would contribute to the avoidance of secondary surgery after healing and achieve a complete replacement of bone tissue. In addition, they have the similar Yong's modulus (41–45 GPa) to that of human cortical bone, which might contribute to the decrease of bone resorption around the implants. The modulus is lower

than that of any other metallic biomaterials, such as titanium alloys (Staiger et al., 2006).

On the other hand, there are concerns that metallic Mg rapidly degrades and produces corrosion, hydroxyl ions, and bubbles of hydrogen gas around the surrounding tissues (Witte et al., 2005). This induces an extremely high local alkali concentration (pH > 9.0) on the metallic Mg surface, which is harmful for cells (Shen et al., 2012). The bubbles of hydrogen gas formed in 1 week after implantation, which induced vacant spaces around the metallic Mg. This is attributed to poor integration of the metallic Mg implanted into body tissue (Witte et al., 2005). To solve these problems, the metallic Mg surfaces were coated with biodegradable polymer, such as poly(ϵ -caprolactone) (PCL) and PLLA (Wong et al., 2010; Xu and Yamamoto, 2012). The cytocompatibility of the metallic Mg was improved by the polymer coatings.

Bioactive coatings consisting of PLLA-based composites containing SiV or vaterite (V) powders have been developed in our previous work, since Mg²⁺, Ca²⁺, and silicate ions must be provided from the metallic Mg, vaterite phase, and siloxane in the SiV, respectively, which were expected to enhance osteogenic cell activities. The adhesion, proliferation, and differentiation of MC3T3-E1 cells cultured on the prepared samples were estimated to clarify the effects of the each ion released from the samples on the cell functions (Yamada et al., 2013, 2014b).

Preparation

The SiV and V powders were prepared by a carbonation method aforementioned. The composites of PLLA and SiV or V were prepared by a melt-blending method, dissolved in chloroform, and then coated on surfaces of a commercially available pure metallic Mg with a spin coater. The amount of SiV or V in the composites was set to be 60 wt% (~47 vol%).

Morphology, Bonding Strength, and Degradation

The surface morphology of the coatings on the metallic Mg was different among the PLLA/SiV, PLLA/V, and pure PLLA

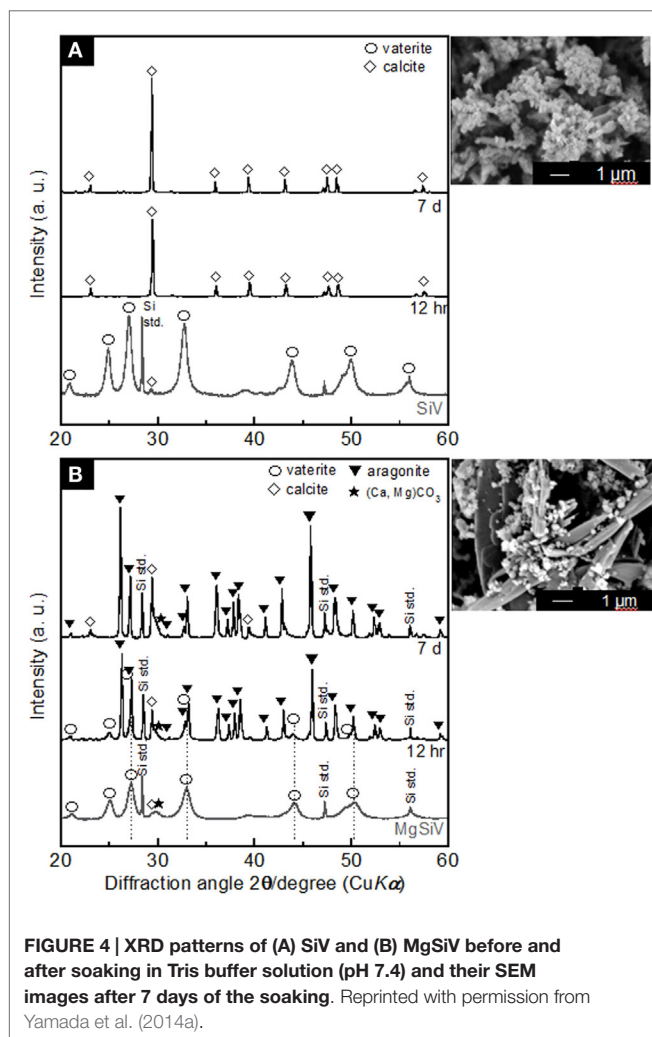


FIGURE 4 | XRD patterns of (A) SiV and (B) MgSiV before and after soaking in Tris buffer solution (pH 7.4) and their SEM images after 7 days of the soaking. Reprinted with permission from Yamada et al. (2014a).

(Figures 5A–C), since the diameters of the powders are different; it is $\sim 1.5 \mu\text{m}$ for SiV and $0.5 \mu\text{m}$ for V. The thickness also varied among them; it was 5.3 ± 0.4 , 3.0 ± 0.1 , and $1.8 \pm 0.2 \mu\text{m}$ for PLLA/SiV, PLLA/V, and pure PLLA. Roughnesses of the coatings were 0.40 ± 0.00 , 0.19 ± 0.01 , and $0.08 \pm 0.01 \mu\text{m}$ for the PLLA/SiV, PLLA/V, and pure PLLA, respectively. This might be due to the difference in the viscosity of the composite or pure PLLA solution. The layer prepared using a spin-coating method depends on the concentration and viscosity of polymer solutions (Schubert and Dunkel, 2003).

Tensile bonding strength tests for the three types of coating demonstrated that the PLLA/SiV coating possesses the highest strength; the rank order of the strength was the PLLA/SiV > PLLA/V > pure PLLA. The difference in the bonding strength would be due to the changes in the molecular weight of PLLA in the coatings by adding the powders. The bonding mechanism was reported to be influenced by molecular weight of polymer in coatings (Xu and Yamamoto, 2012). More free ends of the polymer chains are in the polymers with a lower molecular weight in comparison with those with a higher molecular weight. In the case of the PLLA composite coatings, a larger number of

free carboxyl groups for electrostatic intermolecular interaction between polymer chain and the metallic Mg surface is supposed to be contained in PLLA/SiV, based on the results of the tensile bonding tests. The molecular weights are, however, 82 kDa for PLLA/SiV, 46 kDa for PLLA/V, and 90 kDa for pure PLLA. The varied coating thicknesses of the coatings between them might contribute to the differences in the bonding strength.

All the coated samples release a trace amount of Mg^{2+} ions in α -MEM, while no detachment of the coating layer from the metallic Mg substrates was happened for them. The amount of the ions significantly decreases by the coatings compared with the uncoated (pure) metallic Mg, except the PLLA/V coating (Figure 6). Up to $30 \mu\text{g/mL}$ of the ions were released from the uncoated Mg for 7 days of culturing. On the other hand, the PLLA/SiV and PLLA-coated samples released only 11 and $5 \mu\text{g/mL}$ of the ions, respectively. The PLLA/V-coated sample possessed a completely different releasing behavior from those of the other two samples; the value of the released ions was the same level of the uncoated Mg at day 3 ($16 \mu\text{g/mL}$) and then reached about 1.4 times as large as that at day 7 ($43 \mu\text{g/mL}$). This might be because a large amount of pores formed on the surface of the PLLA/V coating, while no pore or tiny one were done on the surfaces of the other two samples (Figures 5D–F). The pores on the PLLA/V coating were generated through the detachment of V powders and the degradation of the PLLA matrix. The Ca^{2+} ions released from the PLLA/V coating might accelerate the corrosion of the metallic Mg, resulting in the enhanced release of Mg^{2+} ion. Thus, the chemical component of the filler in coatings is important for achievement of suppressing the corrosion of the metallic Mg and the rapid release of Mg^{2+} ions from the substrates.

Cytocompatibility

The proliferation of MC3T3-E1 cells on the three types of coated samples and the uncoated one was evaluated by counting live cells after 1, 3, and 7 days of culturing (Figure 7A). Results represent the mean values of the experiments in triplicate. Statistical analysis was performed using Student's *t*-test and single-factor ANOVA (SPSS 21 software; IBM, USA) followed by Tukey's multiple comparison test. Values of $p < 0.05$ were considered to be significant. Although almost no proliferation ability was found for the cells cultured on the metallic Mg, the cells proliferated on the coated samples, especially the proliferation on the PLLA/SiV- and PLLA/V-coated samples was excellent. The uncoated sample should degrade rapidly and generate extremely high alkali condition surrounding its surface after seeding the cells, resulting in the poor cell activity. The polymer coatings suppress such harmful influence on the seeded cells by the metallic Mg, which improves the cell activity. The surface morphology and roughness of the coatings might relate to the cell proliferation ability. However, although the PLLA/SiV coating possess much rougher surface than the PLLA/V one, the proliferation ability of the cells was the similar between the two samples. The crystallinity of polymer was also reported to influence cell proliferation (Park and Cima, 1996; Iafisco et al., 2012). The crystallinities of PLLAs in the PLLA/SiV, PLLA/V, and pure PLLA coatings were 12, 9, and 14%, respectively. Thus, the cells on the samples can be regarded to proliferate independently of the crystallinity of the coatings. The Ca^{2+} and Mg^{2+} ions released

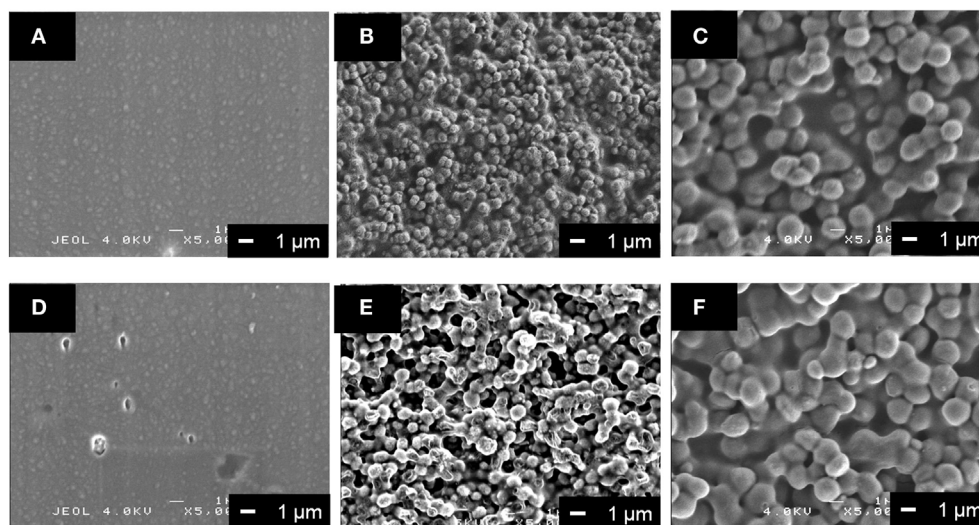


FIGURE 5 | SEM images of (A,D) PLLA coating, (B,E) PLLA/V coating, and (C,F) PLLA/SiV coating (A–C) before and (D–F) after soaking in α -MEM at 37°C for 7 days. Reprinted with permission from Yamada et al. (2013).

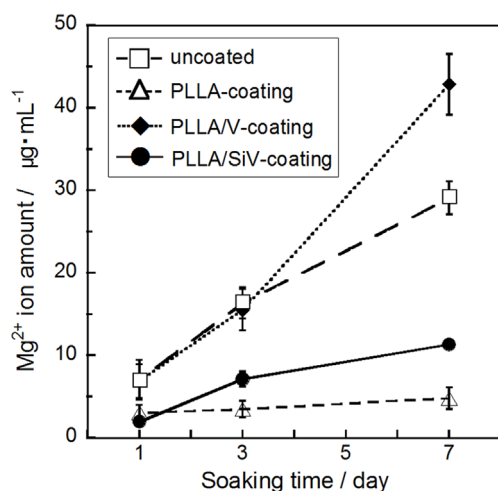


FIGURE 6 | Mg^{2+} ion concentrations dissolved from uncoated, PLLA coating, PLLA/V coating, and PLLA/SiV coating. Reprinted with permission from Yamada et al. (2013).

from the PLLA/SiV- and PLLA/V-coated samples may influence the cell proliferation, since the two ions have been reported to influence osteoblast functions (Diba et al., 2012).

Although there was no significant difference in the proliferation between the PLLA/SiV and PLLA/V coatings, adhering and spreading of the cells varied between the two. The morphology of the cells cultured on the two samples was observed after staining with a Giemsa's solution (Figure 7C). The cells exhibit spindle-like shape on the PLLA/SiV coating, while they did circular and a less-spread shape on the PLLA/V one. The aspect ratios of the cells varied between the two samples; the ratio of PLLA/SiV samples

was higher than that of the PLLA/V ones. The proliferation is comparable between the two samples; nevertheless, the instability of the PLLA/V coatings as shown in Figure 5E might inhibit the cell spreading.

The osteogenic differentiation of the cells varied on the three types of coated samples. The rank order of the ALP activity was the PLLA/SiV > PLLA/V > pure PLLA \approx the uncoated Mg substrate after 21 days of culturing (Figure 7B). There are two possible reasons why the differentiation varied among the samples, the shape of adhesive cells, and the ions released from the samples. Cell morphologies influence gene expression (Lavenus et al., 2011). As aforementioned, the cells showed a good spreading on the PLLA/SiV coating in comparison with those on the PLLA/V ones. The good spreading should be good for exhibiting their high performances. On the other hand, the ions, especially silicate ions, are known to accelerate osteogenic cell differentiation (Xynos et al., 2001). In addition, MgSiV is expected to possess buffering action in aqueous solution since it releases carbonate ions as well, while most of silica-based bioactive glasses, such as 45S5-type bioactive glass, increase its surrounding pH. This might be good for cells cultured on the material surfaces. Thus, the PLLA/SiV coating is useful for improving the cytocompatibility of the metallic Mg because of its strong bonding with the Mg surface, the stability in an aqueous solution, and the ability of providing three kinds of ions, Mg^{2+} , Ca^{2+} , and silicate ions, which enhance osteogenic cell functions.

BONE-VOID FILLERS WITH COTTON WOOL-LIKE STRUCTURE AND ION-PROVIDING ABILITY

Bone-void filler is one of the most common biomaterials for bone reconstruction. Materials for the bone-void fillers are required to

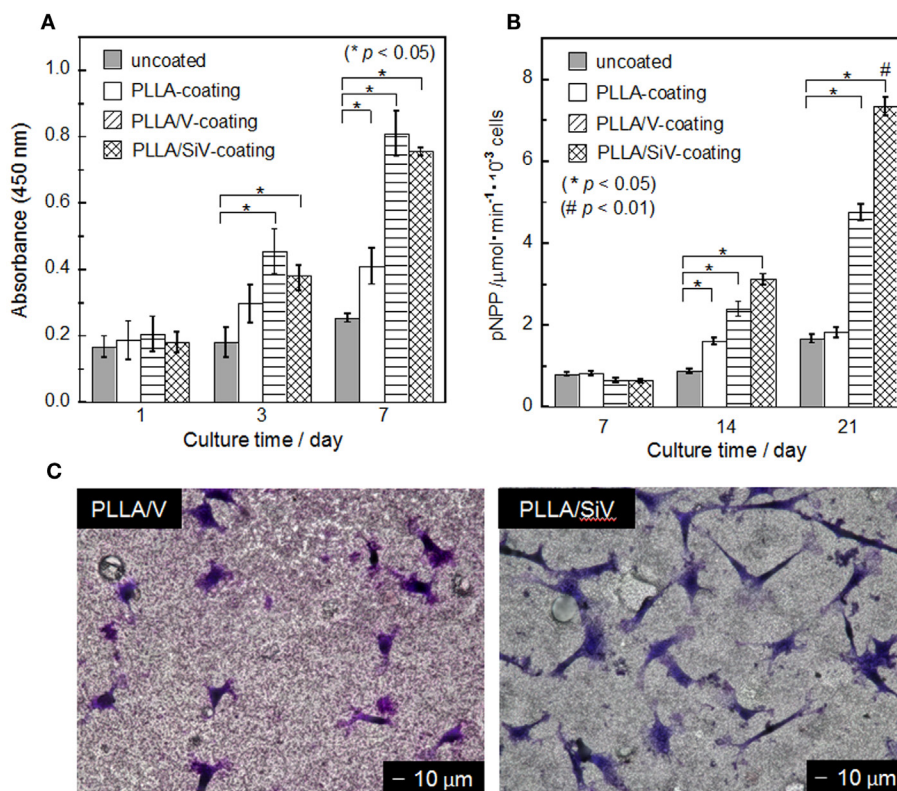


FIGURE 7 | (A) Cell number (mean ± SEM; * $p < 0.05$ as compared to uncoated by *t*-test), **(B)** ALP activity (mean ± SEM; * $p < 0.05$ as compared to uncoated by *t*-test, * $p < 0.05$ as compared to other three samples by Tukey's multiple comparison test), and **(C)** morphology of MC3T3-E1 cells cultured on samples. **(C)** After 3 days of culturing. Reprinted with permission from Yamada et al. (2013).

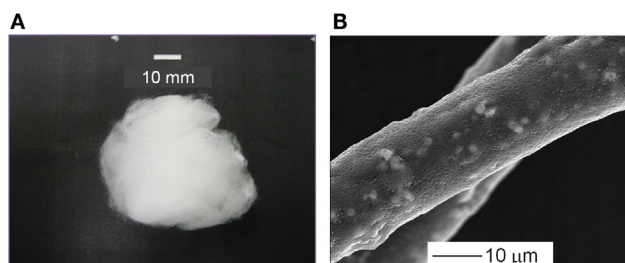


FIGURE 8 | (A) Appearance and **(B)** SEM images of cotton wool-like structured PLLA/SiV composites. Reprinted with permission from Obata et al. (2013).

have bioactivity and porous structure for achieving excellent cell integration and rapid bone regeneration in body. Electrospun fibremats have been widely investigated for the use in bone tissue engineering because of their flexibility and high interconnected porosity (Li et al., 2002; Sill and von Recum, 2008). A conventional electrospinning system consists of a syringe pump, a power supply, and a metallic plate (collector). A polymer-based solution is put in a syringe set in the syringe pump and then electrically charged with the power supply. The electrically charged solution is sprayed onto the earthed collector. Electrospun fibers

tightly overlap one another on the collector, resulting in the fabrication of fibremats. However, fabricating thick fibremats, e.g., several millimeter in thickness, had been regarded to be difficult with the conventional electrospinning system, because electrospun fibers hardly sprayed onto a collector when thickness of fibremats formed reaches several hundred micrometer (Pham et al., 2006). Pore sizes of electrospun fibremats are not enough big to induce tissue ingrowth. PLLA/SiV composites having a cotton wool-like structure have been developed with two-types of our original electrospinning systems (Kasuga et al., 2012; Obata et al., 2013). The obtained samples were evaluated in their mechanical properties, ion-releasing ability, and cell compatibility.

Preparation

Two different systems for electrospinning were used to fabricate a cotton wool-like structure. One is the system having a vessel (100 mm in diameter) filled with ethanol as a collector (Kasuga et al., 2012). Electrospun fibers are collected in the ethanol, which avoids adhesion between the fibers. In addition, electrical charges on electrospun fibers are expected to be neutralized instantly after entering the ethanol. The electrospun fibers contain large gaps between them, resulting in the formation of 3D structure. Another one is the system having a metallic plate collector (like a conventional system) and a fan which blows air against

electrospun fibers (Obata et al., 2013). The air can immediately evaporate the solvent in the electrospun fibers (chloroform) in between a tip of syringe and the collector and prevent the fiber sticking to each other.

Structure, Ions-Releasing Ability, and Mechanical Properties

The PLLA composite containing 10, 20, or 30 wt% of SiV with a cotton wool-like structure has been successfully fabricated. The fibers are 10–20 μm in diameter and have pores with $\sim 1 \mu\text{m}$ in diameter on their surfaces. The SiV powders disperse inside of the fibers and some of them are observed on the fiber surfaces (Figure 8). The pores might be formed due to the evaporation of chloroform in the fibers during the electrospinning (Huang et al., 2003; Kim et al., 2005). The pores are expected to play a role in the achievement of ion releasing from the fibers in an aqueous solution. An aqueous solution must penetrate inside the fibers through the pores, and the SiV powders can be exposed to the solution even at central parts of the fibers. In fact, Ca^{2+} and silicate ions gradually release from the fibers and their amounts depend on the contents of SiV in the composite fibers. Thus, the amounts of the ions released are controllable by changing the content of SiV. When the samples are used as bone-void fillers, they would be tightly packed into irregularly shaped bone defects. Mechanical elasticities of the prepared samples are almost the same as that of the pure PLLA sample. That is, they are able to be packed into such defects without collapse. In addition, handling of the samples during operation must be improved.

REFERENCES

- Bischoff, J. L. (1968). Kinetics of calcite nucleation: magnesium ion inhibition and ionic strength catalysis. *J. Geophys. Res.* 73, 3315–3322. doi:10.1029/JB073i010p03315
- Böttcher, M. E., Gehlken, P.-L., and Steele, D. F. (1997). Characterization of inorganic and biogenic magnesium calcites by Fourier transform infrared spectroscopy. *Solid State Ionics*. 101–103, 1379–1385. doi:10.1016/S0167-2738(97)00235-X
- Diba, M., Tapia, F., Boccaccini, A. R., and Strobel, L. A. (2012). Magnesium-containing bioactive glasses for biomedical applications. *Int. J. Appl. Glass Sci.* 3, 221–253. doi:10.1111/j.2041-1294.2012.00095.x
- Falini, G., Fermani, S., Tosi, G., and Dinelli, E. (2009). Calcium carbonate morphology and structure in the presence of seawater ions and humic acids. *Cryst. Growth Des.* 9, 2065–2072. doi:10.1021/cg8002959
- Falini, G., Gazzano, M., and Ripamonti, A. (1996). Magnesium calcite crystallization from water-alcohol mixtures. *Chem. Commun.* 9, 1037–1038. doi:10.1039/c9960001037
- Fujikura, K., Lin, S., Nakamura, J., Obata, A., and Kasuga, T. (2013). Preparation of electrospun fiber mats using siloxane-containing vaterite and biodegradable polymer hybrids for bone regeneration. *J. Biomed. Mater. Res. B Appl. Biomater.* 101, 1350–1358. doi:10.1002/jbm.b.32952
- Hoppe, A., Güldal, N. S., and Boccaccini, A. R. (2011). A review of the biological response to ionic dissolution products from bioactive glasses and glass-ceramics. *Biomaterials* 32, 2757–2774. doi:10.1016/j.biomaterials.2011.01.004
- Huang, Z.-M., Zhang, Y.-Z., Kotaki, M., and Ramakrishna, S. (2003). A review on polymer nanofibers by electrospinning and their applications in nanocomposites. *Compos. Sci. Technol.* 63, 2223–2253. doi:10.1016/S0266-3538(03)00178-7
- Iafisco, M., Palazzo, B., Ito, T., Otsuka, M., Senna, M., Delgado-Lopez, J. M., et al. (2012). Preparation of core-shell poly(L-lactic) acid-nanocrystalline apatite hollow microspheres for bone repairing applications. *J. Mater. Sci. Mater. Med.* 23, 2659–2669. doi:10.1007/s10856-012-4732-1

Cell Compatibility

The cotton wool-like structured samples are required to have the ability of cell penetration to achieve rapid bone regeneration inside of them in body. Although the pore size of the samples can be easily varied by mechanically pressing, when their porosity is set to 90 and 96%, the pore sizes in the samples are enough to induce the cell penetration. Results of culture tests using MC3T3-E1 cells for the samples with 90 and 96% in porosity demonstrated that cells successfully migrate into the cotton wool-like structures and proliferate inside of them. In addition, the live cell numbers in the cotton wool-like structures were significantly higher than those on the fibremats. This implies that the cotton wool-like structure can provide a large space allowing the cells to adhere and proliferate.

SUMMARY

Since inorganic ions were found to stimulate osteogenic cells to proliferate, differentiate, and mineralize, several types of biomaterials releasing such ions have been developed. In this review, we focused on materials releasing three types of ions, Ca^{2+} , Mg^{2+} , and silicate ions, and their cytocompatibility with osteoblast-like cells. The materials possessed the controlled release of the ions in the culture media. Providing several types of the ions simultaneously was important for achieving enhanced cell functions. Especially, the materials releasing all the three types of ions exhibited higher properties than the others in the results of cell culture tests. Combinatorial effects of inorganic ions provided on cells might exist and are expected to be minutely clarified in the future.

- Jarcho, M. (1981). Calcium phosphate ceramics as hard tissue prosthetics. *Clin. Orthop. Relat. Res.* 157, 259–278.
- Kasuga, T., Obata, A., Maeda, H., Ota, Y., Yao, X., and Oribe, K. (2012). Siloxane-poly(lactic acid)-vaterite composites with 3D cotton-like structure. *J. Mater. Sci. Mater. Med.* 23, 2349–2357. doi:10.1007/s10856-012-4607-5
- Kim, G.-T., Lee, J.-S., Shin, J.-H., Ahn, Y.-C., Hwang, Y.-J., Shin, H.-S., et al. (2005). Investigation of pore formation for polystyrene electrospun fiber: effect of relative humidity. *Korean J. Chem. Eng.* 22, 783–788. doi:10.1007/BF02705799
- Kitamura, M. (2001). Crystallization and transformation mechanism of calcium carbonate polymorphs and the effect of magnesium ion. *J. Colloid Interface Sci.* 236, 318–327. doi:10.1006/jcis.2000.7398
- Kitano, Y. (1962). The behavior of various inorganic ions in the separation of calcium carbonate from a bicarbonate solution. *Bull. Chem. Soc. Jpn.* 35, 1973–1980. doi:10.1246/bcsj.35.1973
- Lavenus, S., Berreur, M., Trichet, V., Pilet, P., Louarn, G., and Layrolle, P. (2011). Adhesion and osteogenic differentiation of human mesenchymal stem cells on titanium nanopores. *Eur. Cell. Mater.* 22, 84–96.
- LeGeros, R. Z. (2002). Properties of osteoconductive biomaterials: calcium phosphates. *Clin. Orthop. Relat. Res.* 395, 81–98. doi:10.1097/00003086-200202000-00009
- Li, W. J., Laurencin, C. T., Caterson, E. J., Tuan, R. S., and Ko, F. K. (2002). Electrospun nanofibrous structure: a novel scaffold for tissue engineering. *J. Biomed. Mater. Res.* 60, 613–621. doi:10.1002/jbm.10167
- Maeno, S., Niki, Y., Matsumoto, H., Morioka, H., Yatabe, T., Funayama, A., et al. (2005). The effect of calcium ion concentration on osteoblast viability, proliferation and differentiation in monolayer and 3D culture. *Biomaterials* 26, 4847–4855. doi:10.1016/j.biomaterials.2005.01.006
- Maier, J. A., Bernardini, D., Rayssiguier, Y., and Mazur, A. (2004). High concentrations of magnesium modulate vascular endothelial cell behaviour in vitro. *Biochim. Biophys. Acta* 1689, 6–12. doi:10.1016/j.bbdis.2004.02.004

- Morse, J. W., Wang, Q., and Tsio, M. Y. (1997). Influences of temperature and Mg:Ca ratio on CaCO₃ precipitates from seawater. *Geology* 25, 85–87. doi:10.1130/0091-7613(1997)025<0085:IOTAMC>2.3.CO;2
- Nakamura, J., Poologasundarampillai, G., Jones, J. R., and Kasuga, T. (2013). Tracking the formation of vaterite particles containing aminopropyl-functionalized silsesquioxane and their structure for bone regenerative medicine. *J. Mater. Chem. B* 1, 4446–4454. doi:10.1039/c3tb20589d
- Obata, A., Hotta, T., Wakita, T., Ota, Y., and Kasuga, T. (2010). Electrospun microfiber meshes of silicon-doped vaterite/poly(lactic acid) hybrid for guided bone regeneration. *Acta Biomater.* 6, 1248–1257. doi:10.1016/j.actbio.2009.11.013
- Obata, A., Ozasa, H., Kasuga, T., and Jones, J. R. (2013). Cotton wool-like poly(lactic acid)/vaterite composite scaffolds releasing soluble silica for bone tissue engineering. *J. Mater. Sci. Mater. Med.* 24, 1649–1658. doi:10.1007/s10856-013-4930-5
- Obata, A., Tokuda, S., and Kasuga, T. (2009). Enhanced in vitro cell activity on silicon-doped vaterite/poly(lactic acid) composites. *Acta Biomater.* 5, 57–62. doi:10.1016/j.actbio.2008.08.004
- Park, A., and Cima, L. G. (1996). In vitro cell response to differences in poly-L-lactide crystallinity. *J. Biomed. Mater. Res.* 31, 117–130. doi:10.1002/jbm.1996.820310102
- Pham, Q. P., Sharma, U., and Mikos, A. G. (2006). Electrospun poly(ϵ -caprolactone) microfiber and multilayer nanofiber/microfiber scaffolds: characterization of scaffolds and measurement of cellular infiltration. *Biomacromolecules* 7, 2796–2805. doi:10.1021/bm060680j
- Saboori, A., Rabiee, M., Moztaaradeh, F., Sheikhi, M., Tahriri, M., and Karimi, M. (2009). Synthesis, characterization and in vitro bioactivity of sol-gel-derived SiO₂-CaO-P₂O₅-MgO bioglass. *Mater. Sci. Eng. C* 29, 335–340. doi:10.1016/j.msec.2008.07.004
- Sawada, K., Ogino, T., and Suzuki, T. (1990). The distribution coefficients of Mg²⁺ ion between CaCO₃ polymorphs and solution and the effects on the formation and transformation of CaCO₃ in water. *J. Cryst. Growth* 106, 393–399. doi:10.1016/0022-0248(90)90084-X
- Schubert, D., and Dunkel, T. (2003). Spin coating from a molecular point of view: its concentration regimes, influence of molar mass and distribution. *Mater. Res. Innovat.* 7, 314–321. doi:10.1007/s10019-003-0270-2
- Shen, Y., Liu, W., Wen, C., Pan, H., Wang, T., Darvell, B. W., et al. (2012). Bone regeneration: importance of local pH-strontium-doped borosilicate scaffold. *J. Mater. Chem.* 22, 8662–8670. doi:10.1039/c2jm16141a
- Sill, T. J., and von Recum, H. A. (2008). Electrospinning: applications in drug delivery and tissue engineering. *Biomaterials* 29, 1989–2006. doi:10.1016/j.biomaterials.2008.01.011
- Staiger, M. P., Pietak, A. M., Huadmai, J., and Dias, G. (2006). Magnesium and its alloys as orthopedic biomaterials: a review. *Biomaterials* 27, 1728–1734. doi:10.1016/j.biomaterials.2005.10.003
- Wakita, T., Obata, A., Poologasundarampillai, G., Jones, J. R., and Kasuga, T. (2010). Preparation of electrospun siloxane-poly(lactic acid)-vaterite hybrid fibrous membranes for guided bone regeneration. *Compos. Sci. Technol.* 70, 1889–1893. doi:10.1016/j.compscitech.2010.05.014
- Wang, J., and Becker, U. (2009). Structure and carbonate orientation of vaterite (CaCO₃). *Am. Mineral.* 94, 380–386. doi:10.2138/am.2009.2939
- Winter, M., Griss, P., de Groot, K., Tagai, H., Heimke, G., von Dijk, H. J., et al. (1981). Comparative histocompatibility testing of seven calcium phosphate ceramics. *Biomaterials* 2, 159–IN151. doi:10.1016/0142-9612(81)90043-0
- Witte, F. (2010). The history of biodegradable magnesium implants: a review. *Acta Biomater.* 6, 1680–1692. doi:10.1016/j.actbio.2010.02.028
- Witte, F., Hort, N., Vogt, C., Cohen, S., Ulrich Kainer, K., Willumeit, R., et al. (2008). Degradable biomaterials based on magnesium corrosion. *Curr. Opin. Solid State Mater. Sci.* 12, 63–72. doi:10.1016/j.cossms.2009.04.001
- Witte, F., Kaese, V., Haferkamp, H., Switzer, E., Meyer-Lindenberg, A., Wirth, C. J., et al. (2005). In vivo corrosion of four magnesium alloys and the associated bone response. *Biomaterials* 26, 3557–3563. doi:10.1016/j.biomaterials.2004.09.049
- Wong, H. M., Yeung, K. W., Lam, K. O., Tam, V., Chu, P. K., Luk, K. D., et al. (2010). A biodegradable polymer-based coating to control the performance of magnesium alloy orthopaedic implants. *Biomaterials* 31, 2084–2096. doi:10.1016/j.biomaterials.2009.11.111
- Xu, L., and Yamamoto, A. (2012). Characteristics and cytocompatibility of biodegradable polymer film on magnesium by spin coating. *Colloids Surf. B Biointerfaces* 93, 67–74. doi:10.1016/j.colsurfb.2011.12.009
- Xynos, I. D., Edgar, A. J., Buttery, L. D., Hench, L. L., and Polak, J. M. (2000a). Ionic products of bioactive glass dissolution increase proliferation of human osteoblasts and induce insulin-like growth factor II mRNA expression and protein synthesis. *Biochem. Biophys. Res. Commun.* 276, 461–465. doi:10.1006/bbrc.2000.3503
- Xynos, I. D., Hukkanen, M. V., Batten, J. J., Buttery, L. D., Hench, L. L., and Polak, J. M. (2000b). Bioglass® 45S5 stimulates osteoblast turnover and enhances bone formation in vitro: implications and applications for bone tissue engineering. *Calcif. Tissue Int.* 67, 321–329. doi:10.1007/s002230001134
- Xynos, I. D., Edgar, A. J., Buttery, L. D., Hench, L. L., and Polak, J. M. (2001). Gene-expression profiling of human osteoblasts following treatment with the ionic products of Bioglass® 45S5 dissolution. *J. Biomed. Mater. Res.* 55, 151–157. doi:10.1002/1097-4636(200105)55:2<151::AID-JBM1001>3.0.CO;2-D
- Yamada, S., Maeda, H., Obata, A., Lohbauer, U., Yamamoto, A., and Kasuga, T. (2013). Cytocompatibility of siloxane-containing vaterite/poly(L-lactic acid) composite coatings on metallic magnesium. *Materials* 6, 5857. doi:10.3390/ma6125857
- Yamada, S., Ota, Y., Nakamura, J., Sakka, Y., and Kasuga, T. (2014a). Preparation of siloxane-containing vaterite doped with magnesium. *J. Ceram. Soc. Jpn.* 122, 1010–1015. doi:10.2109/jcersj2.122.1010
- Yamada, S., Yamamoto, A., and Kasuga, T. (2014b). Poly(L-lactic acid)/vaterite composite coatings on metallic magnesium. *J. Mater. Sci. Mater. Med.* 25, 2639–2647. doi:10.1007/s10856-014-5302-5
- Zhang, Z., Xie, Y., Xu, X., Pan, H., and Tang, R. (2012). Transformation of amorphous calcium carbonate into aragonite. *J. Cryst. Growth* 343, 62–67. doi:10.1016/j.jcrysgro.2012.01.025
- Zreiqat, H., Howlett, C. R., Zannettino, A., Evans, P., Schulze-Tanzil, G., Knabe, C., et al. (2002). Mechanisms of magnesium-stimulated adhesion of osteoblastic cells to commonly used orthopaedic implants. *J. Biomed. Mater. Res.* 62, 175–184. doi:10.1002/jbm.10270

Conflict of Interest Statement: The authors declare that the research was conducted in the absence of any commercial or financial relationships that could be construed as a potential conflict of interest.

Copyright © 2015 Yamada, Obata, Maeda, Ota and Kasuga. This is an open-access article distributed under the terms of the Creative Commons Attribution License (CC BY). The use, distribution or reproduction in other forums is permitted, provided the original author(s) or licensor are credited and that the original publication in this journal is cited, in accordance with accepted academic practice. No use, distribution or reproduction is permitted which does not comply with these terms.



Effect of porosity of alumina and zirconia ceramics toward pre-osteoblast response

Chrystalleni Hadjicharalambous^{1,2}, Oleg Prymak³, Kateryna Loza³, Ales Buyakov⁴, Sergei Kulkov⁴ and Maria Chatzinikolaïdou^{1,2*}

¹ Department of Materials Science and Technology, University of Crete, Heraklion, Greece, ² IESL-FORTH, Heraklion, Greece,

³ Inorganic Chemistry, Center for Nanointegration Duisburg-Essen (CeNIDE), University of Duisburg-Essen, Essen, Germany,

⁴ Tomsk State University and ISPMS RAS, Tomsk, Russia

It is acknowledged that cellular responses are highly affected by biomaterial porosity. The investigation of this effect is important for the development of implanted biomaterials that integrate with bone tissue. Zirconia and alumina ceramics exhibit outstanding mechanical properties and are among the most popular implant materials used in orthopedics, but few data exist regarding the effect of porosity on cellular responses to these materials. The present study investigates the effect of porosity on the attachment and proliferation of pre-osteoblastic cells on zirconia and alumina. For each composition, ceramics of three different porosities are fabricated by sintering, and characterized using scanning electron microscopy, energy dispersive X-ray spectroscopy and X-ray powder diffraction. Cell proliferation is quantified, and microscopy is employed to qualitatively support the proliferation results and evaluate cell morphology. Cell adhesion and metabolic activity are found comparable among low porosity zirconia and alumina. In contrast, higher porosity favors better cell spreading on zirconia and improves growth, but does not significantly affect cell response on alumina. Between the highest porosity materials, cell response on zirconia is found superior to alumina. Results show that an average pore size of ~150 μm and ~50% porosity can be considered beneficial to cellular growth on zirconia ceramics.

OPEN ACCESS

Edited by:

Aldo R. Boccaccini,
University of Erlangen-Nuremberg,
Germany

Reviewed by:

Hélder A. Santos,
University of Helsinki, Finland
Banani Kundu,
Dankook University, South Korea

*Correspondence:

Maria Chatzinikolaïdou
mchatzin@materilas.uoc.gr

Specialty section:

This article was submitted to
Biomaterials, a section of the
journal *Frontiers in Bioengineering
and Biotechnology*

Received: 17 July 2015

Accepted: 13 October 2015

Published: 28 October 2015

Citation:

Hadjicharalambous C, Prymak O,
Loza K, Buyakov A, Kulkov S and
Chatzinikolaïdou M (2015)
Effect of porosity of alumina and
zirconia ceramics toward
pre-osteoblast response.
Front. Bioeng. Biotechnol. 3:175.
doi: 10.3389/fbioe.2015.00175

Keywords: zirconia, alumina, ceramic mechanical properties, cell adhesion, cell proliferation, porosity, pre-osteoblasts MC3T3-E1

INTRODUCTION

Zirconia (ZrO_2) and alumina (Al_2O_3) ceramics are among the strongest materials used in medicine. They exhibit outstanding mechanical properties, which make them suitable for load-bearing and wear-resistant applications in bone (Bauer et al., 2013). More than 20 years ago, zirconia and alumina were introduced for total hip arthroplasty (Piconi et al., 2003; Chevalier and Gremillard, 2009). Their clinical success is reflected by the implantation of more than 3.5 million alumina components and more than 600,000 zirconia femoral heads worldwide since 1990 despite some limitations (Chevalier, 2006; Roualdes et al., 2010). Besides the suitability of mechanical properties, the biological response elicited by ceramic materials is also crucial for the clinical success of an implant. Events that take place at the tissue–material interface principally determine implant integration into bone (Masters and Anseth, 2004). Specifically, it is acknowledged that a strong initial attachment of osteoblastic

cells or their precursors onto biomaterials leads to better bonding between bone and implant (Anselme, 2000; Kimura et al., 2012). In this respect, several studies have shown that zirconia and alumina ceramics have good biocompatibility (Manicone et al., 2007; Bauer et al., 2013) and show no cytotoxic effects when added to cell cultures, either in monolithic (Josset et al., 1999) or nanopowder forms (Roualdes et al., 2010). Nevertheless, they are generally considered as bioinert materials as they are not capable of creating a biologically relevant interface with bone (Dehestani et al., 2012).

Previous studies on hydroxyapatite (HA) ceramics (Hing, 2005; Lew et al., 2012; Michailidis et al., 2014) as well as on metallic scaffolds of titanium (St-Pierre et al., 2005) and tantalum (Balla et al., 2010) have shown that material bioactivity is affected by the degree of scaffold porosity. An explanation for this is that effective circulation of fluid and transportation of nutrients through a porous structure favor cell migration and proliferation, and lead to better bonding with host tissues. The formation of pores in ceramics broadens their possible applications as they can also be used to deliver biomolecules such as bone morphogenetic proteins (BMPs) with sustained release profiles in the human body (Lew et al., 2012). Within non-resorbable HA scaffolds, a porosity threshold of around 60% exists, below which sustainable bone integration cannot be expected (Hing, 2005). Additionally, a pore size of 100 μm is often considered as a minimum requirement for healthy ingrowth in porous HA, but 300 μm is the optimum size for osteoconduction (Lew et al., 2012).

Such detailed information is not available for either zirconia or alumina ceramics. However, previous *in vivo* experiments indicated that macroporous (pore size > 50 nm) alumina allowed the apposition of physiological bone tissue unlike dense alumina implants, which were surrounded by fibrous tissue (Eckert et al., 2000). Other studies have shown that porous alumina coatings improved the mechanical properties of titanium implants, while the pores could be impregnated with bioactive materials, providing a good surface for osteoblastic growth (Karlsson et al., 2003; Walpole et al., 2009). Similarly, a series of studies investigated the use of highly porous zirconia (84–87% porosity) as a substrate for HA coating, which resulted in a strong and bioactive scaffold with good bone regeneration demonstrated *in vivo* (Kim et al., 2008). It was suggested that zirconia had a positive impact on the osteoconductivity of the scaffold in addition to enhancing its mechanical properties. From these studies, it was proposed that even a bioinert ceramic could be used as a substrate material for tissue growth if it had an appropriate architecture and pore characteristics, and therefore further research in this regard was important.

In previous studies, we investigated the osteogenic potential of pre-osteoblasts on porous magnesia and yttria-stabilized zirconia ceramics (Hadjicharalambous et al., 2015b), as well as the pre-osteoblastic cell response on zirconia, alumina, and zirconia/alumina composite (Hadjicharalambous et al., 2015a). The objective of this study was to investigate the effect of zirconia and alumina ceramic substrate porosity on cellular adhesion and proliferation. Ceramics of three different porosities were produced by sintering and characterized regarding porosity, pore size, and phase composition by X-ray powder diffraction (XRD) and energy

dispersive X-ray spectroscopy (EDS). The impact of porosity was investigated using MC3T3-E1 pre-osteoblasts by analyzing the metabolic activity of the cells with the PrestoBlue® assay as well as their morphology on the different substrates by SEM.

MATERIALS AND METHODS

Ceramic Fabrication and Characterization

Alumina and zirconia ceramics with three porosities (A, B, and C from smaller to larger porosity) were fabricated for the experiments. Starting powders of Al_2O_3 or ZrO_2 stabilized with 3 mol% yttrium oxide or yttria Y_2O_3 (Siberian Enterprise Chemical Group, Russia) were used. Pure zirconia undergoes phase transformation from the tetragonal to the monoclinic phase during sintering; this process occurs with a volume change, leading to sudden failure of the material when zirconia cools. ZrO_2 stabilized with yttria can maintain its tetragonal phase at room temperature and is the principal kind of zirconia considered for current medical use (Manicone et al., 2007). Briefly, the ceramic powders were cold pressed on a hydraulic press under 100 MPa pressure in steel die molds in order to obtain cylindrical (15 mm in diameter, 5 mm in height) forms. To create porosity, organic material particles (polyethylene) were added as pore formers into the powder mixtures. The size range of the porogens was 50–150 μm with a mean size of 100 μm for 49 and 63% porosity samples, and 30–120 μm with a mean size of 75 μm for lower porosity samples.

The compacted powder samples were sintered in air at a peak temperature of 1350°C (for 49 and 63% porosity), 1400°C (for 30 and 34% porosity), and 1450°C (for 23 and 24% porosity) in LHT 02/17 High-Temperature Furnaces (Nabertherm) with an isothermal exposure time of 1 h. During thermal treatment, the organic material was extracted, generating the desired pores within the microstructure.

The porosity of each sample was calculated by dividing the scaffold density (ρ_{scaffold}) by the theoretical material density (ρ_{material}), and subtracting the result from one (Karageorgiou and Kaplan, 2005; Galmarini, 2011):

$$P_{\text{total}} = (1 - \rho_{\text{scaffold}} / \rho_{\text{material}}) \times 100$$

The scaffold density was determined by dividing the weight by the volume of the scaffold and the material density is the density of the material of which the scaffold is fabricated (specifically, for alumina samples: $\rho_{\text{material}} = 3.99 \text{ g cm}^{-3}$; and for zirconia samples: $\rho_{\text{material}}(\text{Zr-A}) = 5.84$, $\rho_{\text{material}}(\text{Zr-B}) = 5.88$, $\rho_{\text{material}}(\text{Zr-C}) = 5.90 \text{ g cm}^{-3}$ as calculated based on their monoclinic and tetragonal phase compositions shown in **Table 1**). The average pore size was measured for each of the three porosity types through analysis of scanning electron microscopy images (Philips SEM-515).

X-ray powder diffraction was performed with a Bruker D8 Advance X-ray diffractometer in Bragg–Brentano mode with $\text{Cu K}\alpha$ radiation ($\lambda = 1.5418 \text{ \AA}$; 40 kV and 40 mA). The ceramic samples were investigated in the range of 10–90° 2 θ with a step size of 0.01° 2 θ and a counting time of 0.6 s. Rietveld refinement with the TOPAS 4.2 program package from Bruker was

TABLE 1 | Pore sizes and porosities of zirconia and alumina ceramics.

Sample	Chemical composition	Porosity (%)	Small pore mean size (μm)	Large pore mean size (μm)
Zr-A	(Zr,Y)O _{1.95} , ZrO ₂	23	3.1	—
Zr-B	(Zr,Y)O _{1.95} , ZrO ₂	30	6.8	—
Zr-C	(Zr,Y)O _{1.95} , ZrO ₂	49	0.7	167 \pm 113
Al-A	Al ₂ O ₃	24	3.4	—
Al-B	Al ₂ O ₃	34	2.2	—
Al-C	Al ₂ O ₃	63	2.1	141 \pm 113

performed in order to analyze the crystallographic properties of the samples. In this way, the weight amount of crystalline phases, their lattice parameters and percentage of yttrium substitution in the yttria-stabilized zirconia, as well as the average crystallite size and the crystallographic density were determined. The patterns of rhombohedral Al₂O₃ (#043-1484, corundum), monoclinic ZrO₂ (#83-0940), and tetragonal phase Zr_{0.9}Y_{0.1}O_{1.95} (#82-1241) from the ICDD database were used as reference for the qualitative phase analysis, which was performed with a DiffraSuite EVA V1.2 from Bruker. For each Rietveld refinement, the instrumental correction, as determined with a standard powder sample LaB₆ from NIST (National Institute of Standards and Technology) as standard reference material [SRM 660b; $a(\text{LaB}_6) = 4.15689 \text{ \AA}$], was taken into account.

For the morphological characterization of the ceramic samples, scanning electron microscopy was performed on a FEI Quanta 400 ESEM instrument in high vacuum after sputtering with Au/Pd (80:20). Energy-dispersive X-ray spectroscopy (EDS) with an accelerating voltage of 15 kV was carried out with a Genesis 4000 instrument with SUTW-Si(Li) detector.

Cell Culture and Reagents

Minimum essential Eagle's medium (α -MEM), penicillin/streptomycin, fetal bovine serum (FBS), and trypsin/EDTA were purchased from Sigma (St. Louis, MO, USA). PrestoBlue® reagent for cell viability was purchased from Invitrogen Life Technologies (Carlsbad, CA, USA) and cell culture plates from Corning.

The MC3T3-E1 murine pre-osteoblastic cells (Beck et al., 1998) were cultured in α -MEM medium supplemented with 10% fetal bovine serum (FBS) and 1% penicillin/streptomycin (primary medium) and maintained at 37°C in a humidified atmosphere of 5% CO₂ in air. Cells were splitted once a week with trypsin/EDTA. Confluent cells were harvested using trypsin/EDTA, counted on a hemocytometer, and seeded onto the ceramic samples. For all experiments, cells between passage 6 and 15 were used.

Cell Culture on Porous Ceramics

Ceramic sample preparation and the cell seeding procedure were performed as previously described (Hadjicharalambous et al., 2015b). Cells (5×10^4 cells) were seeded onto the samples in a 30 μL cell suspension in primary medium. The medium was replaced with fresh medium every 2 days.

Cell Proliferation Assay

The PrestoBlue® assay (Invitrogen, CA, USA) was used to monitor proliferation of MC3T3-E1 pre-osteoblasts after 2, 4, and

8 days of culture. PrestoBlue® assay is dependent on the cellular reduction of a blue colored, cell permeant, resazurin-based compound by viable cells to a red product, which can be detected spectrophotometrically and provides a measure of cell viability. Assessment of proliferation at each time point was performed as described in Hadjicharalambous et al. (2015b). For each ceramic surface, three replicates were used ($n = 3$). Data from three independent experiments were averaged as mean values \pm SEM for each time point and sample. Statistical analysis was performed using ANOVA (GraphPad Prism 5 software) to evaluate the differences among ceramic samples. A p value of <0.05 was considered significant.

Scanning Electron Microscopy

The morphology of adherent MC3T3-E1 cells was assessed by scanning electron microscopy (SEM). Cells (5×10^4 cells/sample) were cultured on alumina and zirconia substrates for 1 or 10 days as described above, rinsed with 0.2 M sodium cacodylate buffer and fixed in 2% glutaraldehyde and 2% paraformaldehyde for 1 h, at 4°C. Cells were then post fixed in 1% osmium tetroxide for 30 min at 4°C and dehydrated through a series of increasing concentrations of ethanol (from 30 to 100%) and dried by applying critical drying with CO₂ at 33°C and 73 atm (Baltec CPD 030). Following sputtering with a 20 nm thick layer of gold (Baltec SCD 050), ceramic samples were observed under a scanning electron microscope (JEOL JSM-6390 LV) with an accelerating voltage of 15 kV.

Fluorescence Microscopy

Living cells on the ceramic samples were fluorescently labeled with carboxyfluorescein diacetate succinimidyl ester (CFSE) (Invitrogen, CA, USA). One hundred thousand cells were cultured on the ceramic substrates for 1 or 7 days. At the end of incubation, the ceramics were washed once with PBS, pH 7.4 and cells were then stained with 20 μm CFSE dye in PBS for 15 min and viewed by fluorescence microscopy (496ex/516em).

RESULTS

Ceramic Characterization

Pore size and porosity characteristics of zirconia and alumina ceramics are provided in **Table 1**. **Figure 1** shows the surface morphology of alumina and zirconia ceramics with different porosities A, B, and C, as investigated by SEM. According to the microscopic characterization, the low porosity ceramics (A and B) contain only small pores ($<6 \mu\text{m}$ on average), whereas the higher porosity Al-C and Zr-C samples contain small as well as large pores with average size of 141 and 167 μm , respectively, as shown in **Table 1**. The visible grain size of alumina ceramics was larger in comparison to zirconia samples, and in accordance with the XRD results (**Table 2**).

The ceramic samples with different porosities were characterized by XRD and two representative diffractograms for alumina (Al-A, 24% porosity) and yttria-stabilized zirconia (Zr-B, 30% porosity) are depicted in **Figure 2**. It was shown that all alumina ceramics consist only of rhombohedral Al₂O₃ phase

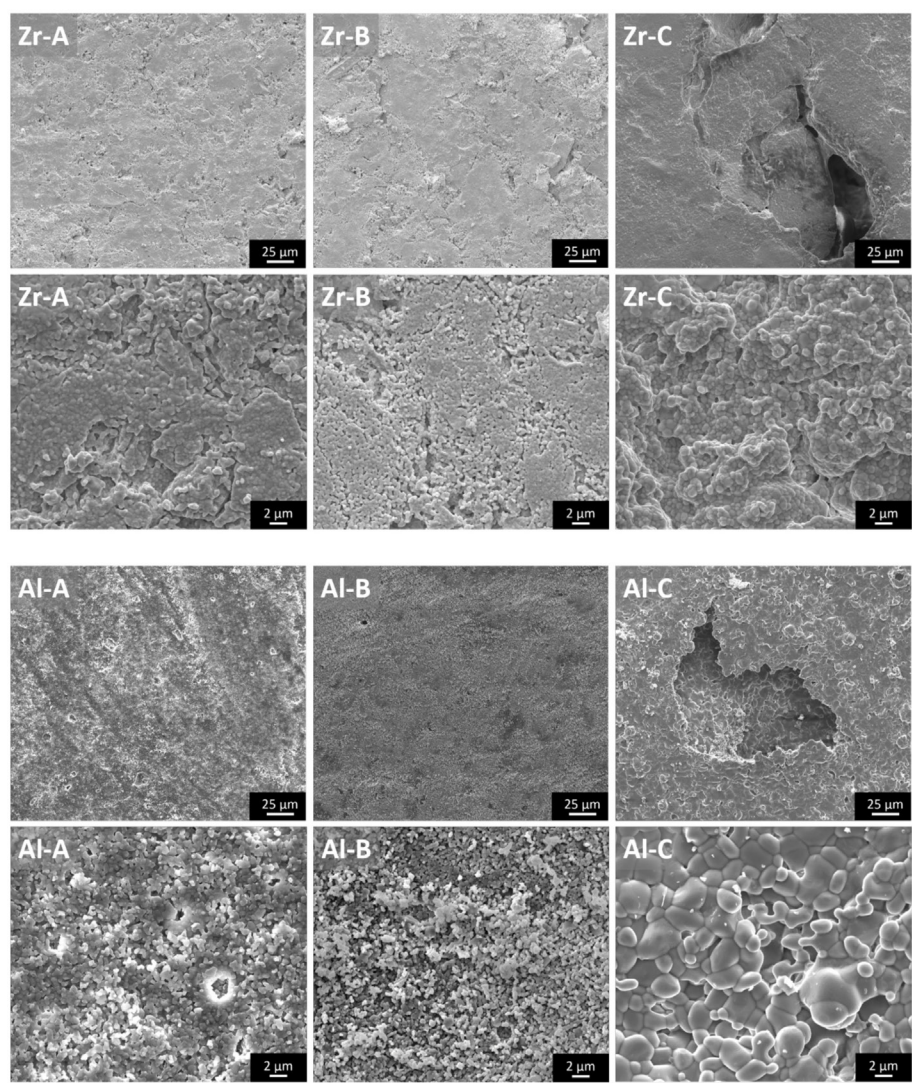


FIGURE 1 | The microstructure of zirconia and alumina ceramics as shown by scanning electron microscopy images. The large pores of nanostructural Zr-C and microstructural Al-C ceramics are visible. Original magnifications are x1000 for larger and x8000 for smaller scale bar images.

TABLE 2 | Crystallographic properties of alumina and yttria-stabilized zirconia as determined by Rietveld refinement.

Sample	Phases	Wt. %	Density (g cm ⁻³)	Lattice parameters				Volume of unit cell	Crystallite sizes (nm)
				<i>a</i> /Å	<i>b</i> /Å	<i>c</i> /Å	β/°	<i>V</i> /Å ³	
Al-A	Al ₂ O ₃	100	3.99	4.759 (1)	–	12.996 (1)	–	254.94 (1)	>500
Al-B	Al ₂ O ₃	100	3.99	4.759 (1)	–	12.995 (1)	–	254.92 (1)	>500
Al-C	Al ₂ O ₃	100	3.98	4.761 (1)	–	12.999 (1)	–	255.19 (1)	>500
Zr-A	ZrO ₂ (monoc.)	59	5.75	5.176 (1)	5.225 (1)	5.326 (1)	99.10	142.25 (3)	68
	Zr _{0.85} Y _{0.15} O _{1.95}	41	5.97	3.622 (3)	–	5.174 (1)	–	67.88 (2)	63
Zr-B	ZrO ₂ (monoc.)	47	5.76	5.176 (1)	5.222 (1)	5.325 (1)	99.11	142.12 (2)	56
	Zr _{0.87} Y _{0.13} O _{1.95}	53	5.98	3.618 (1)	–	5.178 (1)	–	67.77 (1)	105
Zr-C	ZrO ₂ (monoc.)	49	5.78	5.164 (1)	5.212 (1)	5.327 (1)	99.05	141.59 (3)	76
	Zr _{0.89} Y _{0.11} O _{1.95}	51	6.01	3.616 (1)	–	5.176 (1)	–	67.66 (2)	59
Bondars et al. (1995)	ZrO ₂ (tetrag.)		6.10	3.596 (1)	–	5.184 (1)	–	67.04 (1)	–

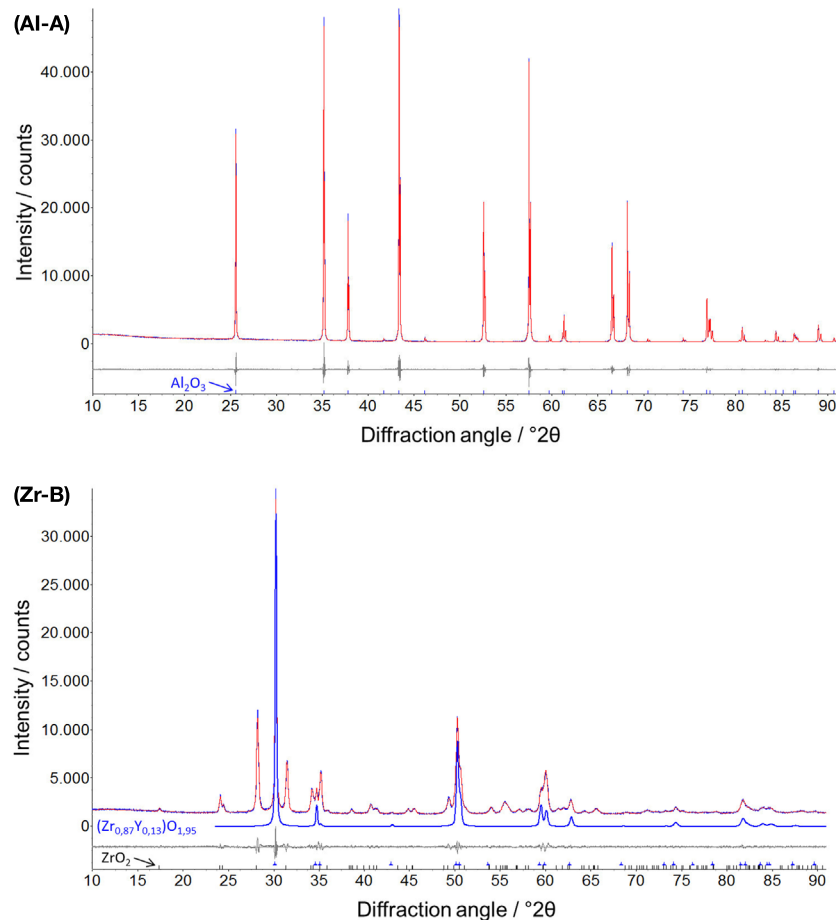


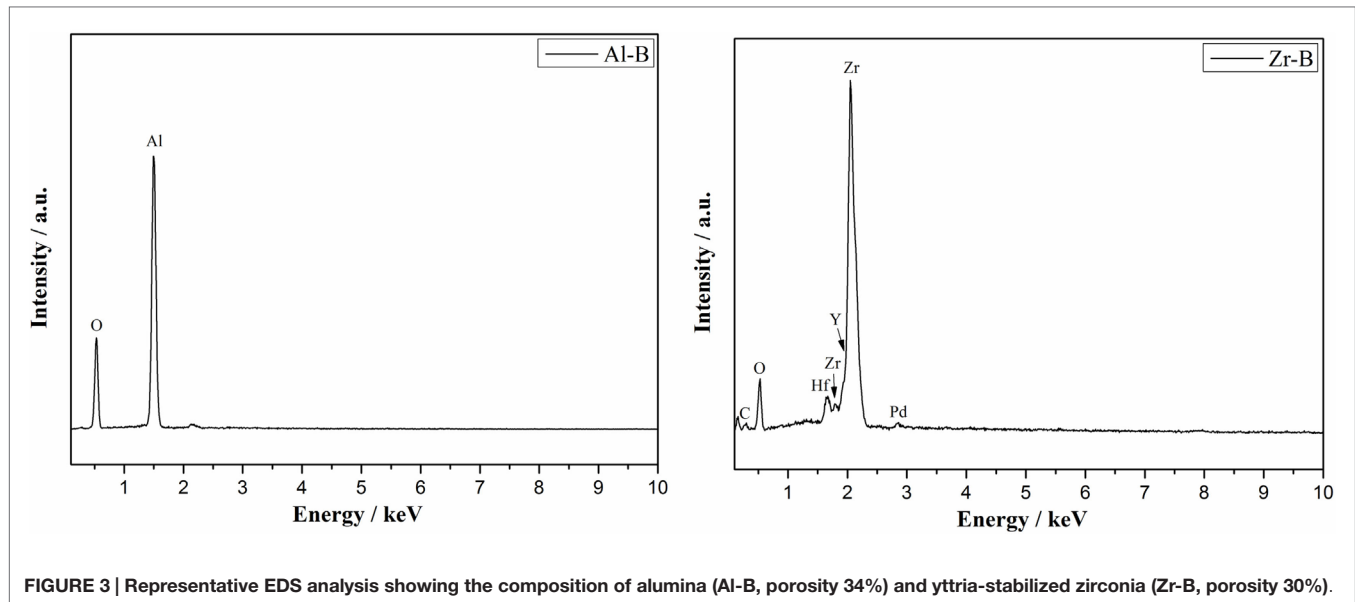
FIGURE 2 | Representative X-ray powder diffractograms of alumina (Al-A, Rwp = 5.5) and yttria-stabilized zirconia (Zr-B, Rwp = 3.5) with additionally denoted rhombohedral Al_2O_3 (corundum) and tetragonal $\text{Zr}_{0.87}\text{Y}_{0.13}\text{O}_{1.95}$ phases. Profile and difference plots from Rietveld refinement are shown.

(corundum), whereas the yttria-stabilized zirconia ceramics consist of a two phase system of both monoclinic ZrO_2 phase and tetragonal phase $\text{Zr}_{0.87}\text{Y}_{0.13}\text{O}_{1.95}$ in approximately equal amounts.

By means of Rietveld refinement, the crystallographic properties of the investigated ceramics were determined (Table 2). The calculated lattice parameters and the resulting crystallographic densities for the corundum phase were very similar among alumina ceramics, confirming the phase stability in all samples. The determined crystallite size of Al_2O_3 phases, using the Scherrer equation (Scherrer, 1918) were in the μm -region, which can also be confirmed by the corresponding sharp peaks in the diffractogram (Figure 2, Al-A). In contrast to alumina, the yttria-stabilized zirconia samples exhibited nanocrystalline phases with the calculated crystallite size being approximately 60–100 nm. The presence of smaller crystallites (a crystallite is part of one grain) within yttria-stabilized zirconia, in comparison to larger crystallites in alumina, was also confirmed by scanning electron microscopy (Figure 1). No significant dependence of the crystallite size upon the porosity of ceramic samples could be detected.

Using Rietveld refinement and comparing the calculated volumes of the unit cells for Zr-containing phases (Table 2), it was possible to estimate the percent substitution of smaller Zr atoms (159 pm) by larger Y atoms (180 pm). It was shown that with increasing porosity, the volume of the tetragonal unit cell $(\text{Zr,Y})\text{O}_{1.95}$ decreases slightly, whereas the volume of the monoclinic ZrO_2 unit cell (no significant substitution) remains almost unchanged. In this way the amount of incorporated Y-atoms into the tetragonal phase was determined as 15, 13, and 11 mol% for the 23, 30, and 49% porous zirconia, respectively (Table 2). With the calculated weight percentage of the monoclinic ZrO_2 and tetragonal $(\text{Zr,Y})\text{O}_{1.95}$ phases and defined site occupancy of Zr/Y-atoms in the corresponding unit cells, about 4.5 wt.% of Y could be determined crystallographically in the yttria-stabilized zirconia.

A good correlation between the above results and the EDS quantitative analysis of chemical elements was found (Figure 3). In alumina samples only the Al (64 wt.%) and O (35 wt.%) elements were found, confirming the composition of corundum phase. In yttria-stabilized zirconia samples, the Zr (64 wt.%), Y (8 wt.%), O (13 wt.%) elements were identified in addition to Hf



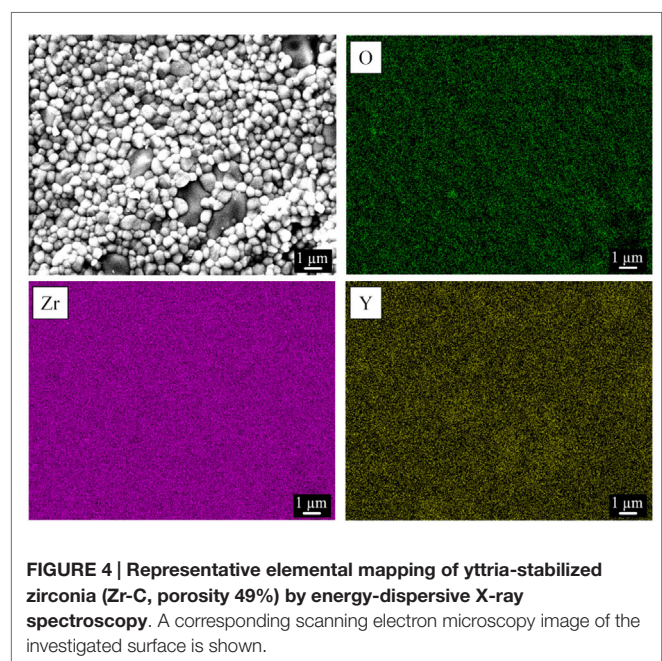
(10 wt.% or 3 at.%), which was present as a natural impurity of ZrO_2 ceramics (Wang et al., 2010). Notably, a decreasing amount of yttrium was detected with increasing sample porosity and specifically 8.3, 7.9, 7.5 wt.% of yttrium for Zr-A, Zr-B, and Zr-C, respectively. A similar effect was also observed by XRD.

Figure 4 shows the EDS maps of oxygen, zirconium, and yttrium in yttria-stabilized zirconia. The images indicate a regular distribution of the three elements in the ceramic sample, confirming in this way a homogeneous distribution of the crystalline monoclinic ZrO_2 and tetragonal $(\text{Zr}_x\text{Y}_{1-x})\text{O}_{1.95}$ phases and as a result, a good substitution of Zr by Y atoms. These results were confirmed in all three zirconia samples.

Cell Metabolic Activity

The PrestoBlue[®] assay was used to quantitatively determine the proliferation of viable MC3T3-E1 cells on porous zirconia and alumina substrates. A comparison of the cellular metabolic activity on the different samples after 2, 4, and 8 days of culture is depicted in **Figure 5**. Pre-osteoblasts displayed similar metabolic activities on Al-A, Al-B, Zr-A, and Zr-B porous ceramics, regardless of chemistry or porosity, and no significant differences between these substrates were observed. Among zirconia substrates, cell densities were found significantly higher on the highest porosity sample Zr-C for all culture time points. Among alumina, improved metabolic activity was observed on Al-C, but this was not significantly higher than on Al-A or Al-B samples.

Fluorescence microscopy was also employed to qualitatively observe live CFSE-stained cells on the ceramic samples, and assess their growth. As depicted in **Figure 6**, cell proliferation was observed on both Al-C and Zr-C after 7 days of culture, but was evidently higher on Zr-C, as shown by the formation of a uniform layer of green fluorescing cells on this material. Cells on lower porosity ceramics were also stained with CFSE in an attempt to monitor changes in living cell numbers, however, it was not possible to record clear images of cells on the samples (data



not shown), due to strong background fluorescence interference coming from the samples themselves.

Cellular Attachment and Morphology

Pre-osteoblastic cell morphology on the different porous alumina and zirconia ceramic substrates was investigated by scanning electron microscopy. **Figure 7** shows the morphologies of the cells on samples after 1 day of culture. The results showed that cellular appearance and density strongly depended on the substrate. Between zirconia and alumina, cell adhesion morphology was more flattened on zirconia. Specifically, cells adherent on Zr-A or Al-A were found to exhibit branched

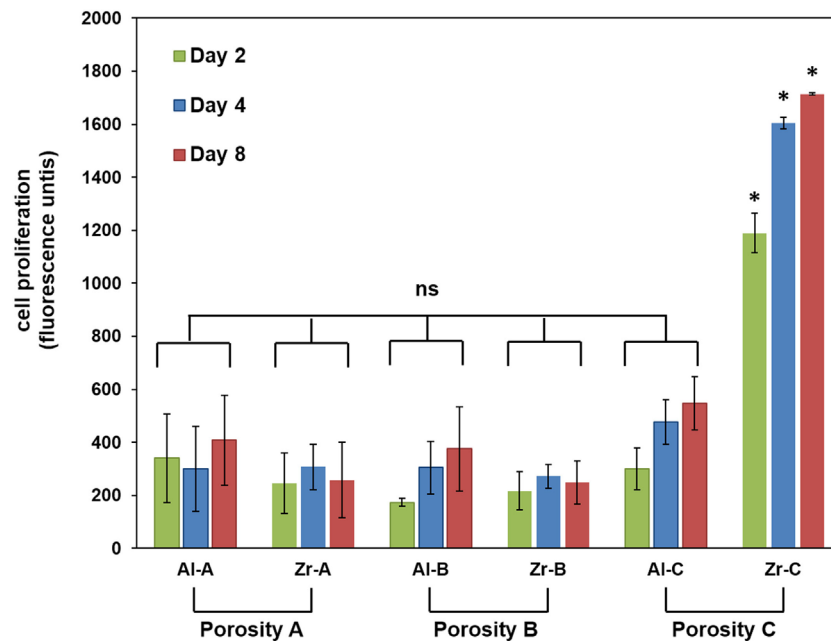


FIGURE 5 | Cell proliferation by PrestoBlue® assay for 24% (Al-A), 34% (Al-B), and 63% (Al-C) porous Al_2O_3 and 23% (Zr-A), 30% (Zr-B), and 49% (Zr-C) porous ZrO_2 substrates up to 8 days of culture. The metabolic activity of pre-osteoblasts on the highest porosity (49%) zirconia samples was significantly higher (about threefold) compared to other samples at all time points (* $p < 0.05$, $n = 9$). All other samples showed non-significant (ns) differences in cellular growth among them.

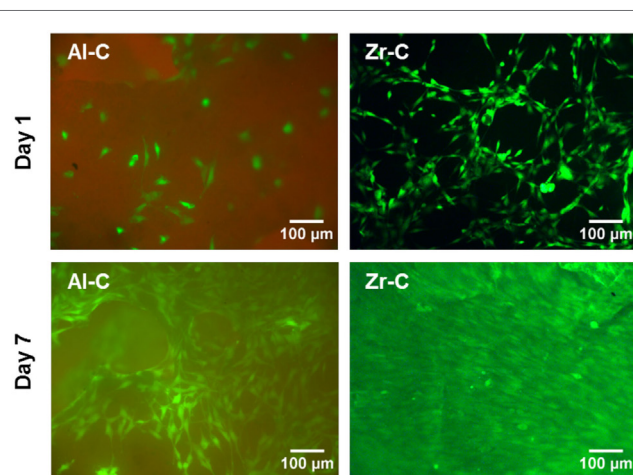


FIGURE 6 | Fluorescent live cell staining of MC3T3-E1 cells cultured for 1 day (upper panel) and 7 days (lower panel) on 63% porous alumina (Al-C, left) and 49% porous zirconia (Zr-C, right) ceramics. Original magnification is $\times 10$. After 7 days of culture, cell growth was observed and higher cell densities were evident on zirconia than alumina. Scale bar represents 100 μm .

morphology characterized by long spindle-like cellular extensions, attaching to the sub-micrometer features of the ceramics as well as nearby cells. In contrast, cells cultured on either 30% porous zirconia (Zr-B) or 34% porous alumina (Al-B) appeared small and round-shaped with under-developed filopodia,

whereas cell density appeared to be higher on Zr-B. A further increase in the porosity of zirconia ceramics resulted in a profound effect on cell adhesion, with cells exhibiting flattened morphology and very good membrane spreading on the 49% porous zirconia (Zr-C) substrate (Figure 7A). Interestingly, increasing porosity in alumina ceramics to 63% (Al-C) had no evident impact on cell morphology, as cell spreading on the substrates was limited and spindled morphology was dominant (Figure 7B).

Cellular growth on the Al-C and Zr-C ceramic samples after 10 days of culture was also assessed by SEM. As shown in Figure 8, proliferation of the MC3T3-E1 pre-osteoblastic cells occurred on both Al-C and Zr-C samples. However, cells on Zr-C formed a dense layer that could also bridge large pore openings, unlike cells cultured on Al-C. In addition, the cell matrix on Zr-C appeared more uniform as individual cells could not always be identified (SEM observations), contrary to cells on Al-C, which maintain their initial spindle-shaped morphology and were easily distinguished.

DISCUSSION

In recent years, it has been recognized that biomaterial porosity greatly influences cellular behavior not only at the proliferative but also the differentiation stage (Bignon et al., 2003; Karageorgiou and Kaplan, 2005; Lew et al., 2012). Therefore, it has been suggested that by adapting surface properties to the desired cell behavior, we may open up the possibility of controlling cell behavior, thereby improving implant performance (Ni et al., 2014).

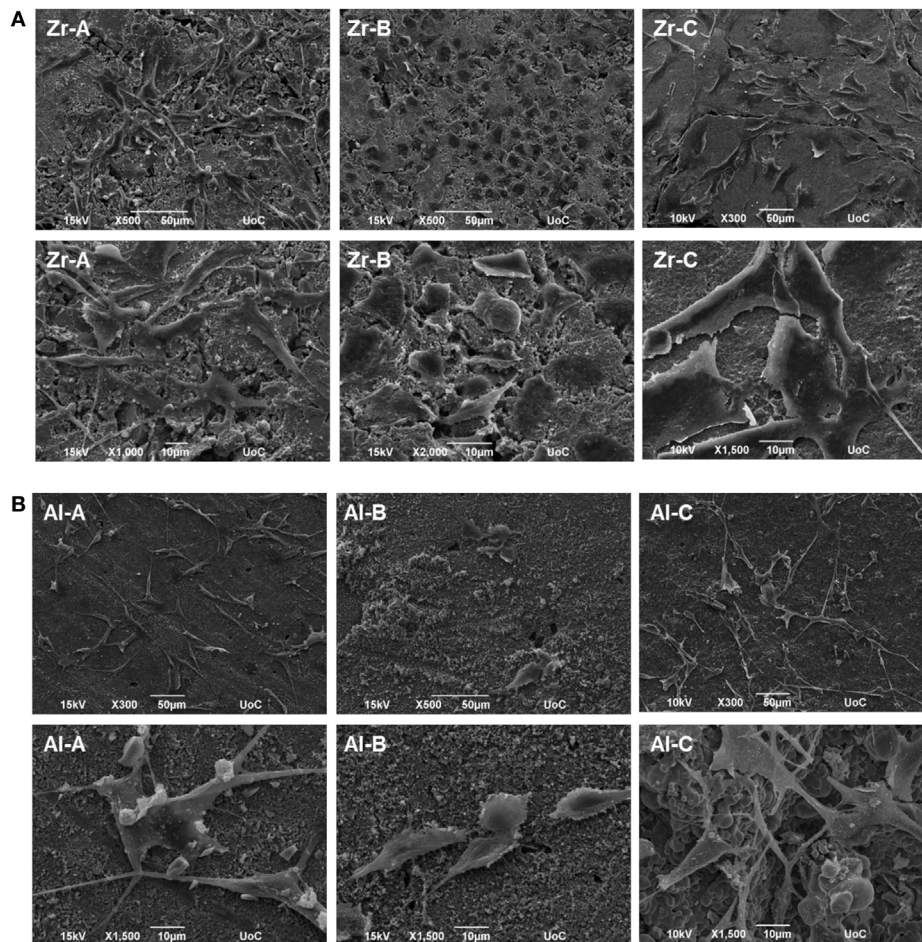


FIGURE 7 | Scanning electron microscopy (SEM) images showing morphology of MC3T3-E1 cells after day 1, on (A) zirconia of 23% (Zr-A), 30% (Zr-B), and 49% (Zr-C) porosities or (B) alumina of 24% (Al-A), 34% (Al-B), and 63% (Al-C) porosities. Increasing porosity resulted in better cell spreading on zirconia but not on alumina ceramics, where cells mostly displayed a long and spindled morphology. Original magnifications are x500 or x300 for upper, and x1000 to x2000 for lower images in (A,B).

The present *in vitro* cell–material interaction study clearly indicates that porosity is an important parameter regarding cell adhesion and growth on ceramic materials, as assessed both qualitatively and quantitatively by employing microscopy and cell viability methods, respectively. Enhanced cellular response in terms of adhesion density (qualitative observation, as shown in **Figure 7**) and proliferation of pre-osteoblasts, was observed when the porosity of zirconia increased from 23 to 49%, with the simultaneous introduction of pores of approximately 55–280 μm (average size 150 μm), which are presumed to have a positive impact on cell growth (Lew et al., 2012).

Cell adhesion and proliferation also depend on material chemistry (Hing, 2005). In this study, alumina and zirconia ceramics did not exhibit significant differences in cellular growth or adhesion, when porosity was low (samples with A and B porosities).

Though material chemistry can be a determinant factor in cell–material interactions, metal oxides such as alumina and zirconia are generally considered bioinert. Their particles (at 2 μm

size) have been reported not to be toxic to osteoblasts (Roualdes et al., 2010), whereas their ionic forms of Zr^{4+} and Al^{3+} exhibit low to medium toxicity, but such ionic forms are present only at low pH (Franks and Gan, 2007).

In a previous report (Lohmann et al., 2002), higher osteoblast proliferation was observed in the presence of zirconia than in the presence of alumina particles, an effect that the authors found to be related to the higher reactive surface of the alumina particles, which were significantly smaller than the zirconia ones. However, in our study we used sintered ceramics in which alumina particles on the material surface were larger than zirconia particles for all porosities, as shown by SEM (**Figure 1**). Considering this, the higher proliferation we observed on porous zirconia cannot be explained on the basis of crystallite size, since the crystallite size of the zirconia ceramics was smaller than the crystallite size of alumina. Hence, it appears that chemical composition or surface topography differences (due to larger crystallite size in alumina ceramics) alone are not sufficient to induce a differential pre-osteoblast adhesion and

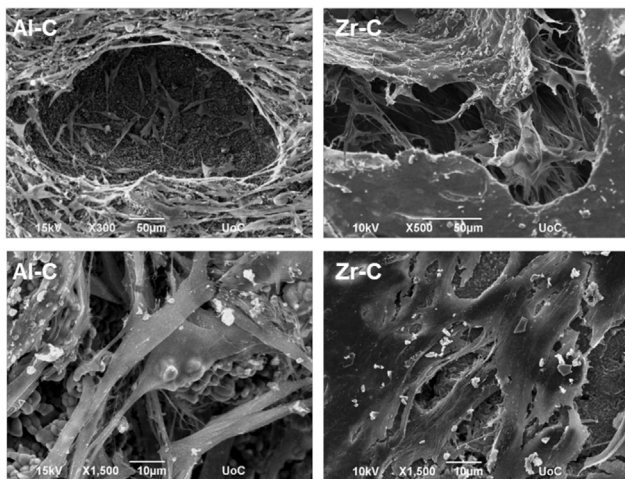


FIGURE 8 | Scanning electron microscopy (SEM) images showing cell morphology of MC3T3-E1 cells after 10 days, on 49% porous zirconia (Zr-C, right) or 63% porous alumina (Al-C, left) ceramics. A smoother, denser multilayer spreading over pore openings was observed on zirconia. Original magnifications are $\times 500$ and $\times 300$ for upper, and $\times 1500$ for lower images.

growth among alumina and zirconia ceramics of low porosities (porosities A and B).

On the other hand, we found that the introduction of larger pores is critical to significantly enhance both cell adhesion and proliferation in zirconia ceramics. This results in higher interconnection between the smaller pores inside the Zr-C sample, and as a consequence, in better circulation of nutrient medium for the cells. The increased total surface of interconnected pores (small and large) in the Zr-C ceramic provides better conditions for a significantly higher cell adhesion (Figures 5–7) and growth within Zr-C. Similarly, a recent study (Song and Cho, 2014) reported better pre-osteoblast spreading and growth on a porous zirconia scaffold (pores between 200 and 400 μm) in comparison to a non-porous zirconia disk. In addition, the authors showed that cell spreading on porous zirconia was better compared to spreading on a porous zirconia scaffold coated with HA. A limitation in their comparison was partial obstruction of the pores caused by the coating, however the importance of substrate architecture (pores) in cell behavior on zirconia ceramics was highlighted.

In this study, we observed better cell adhesion and spreading followed by greater osteoblast proliferation on zirconia

(49% porosity) than on alumina (63% porosity) porous scaffolds of similar pore size (porosity C). More flattened cell adhesion on Zr-C than on Al-C on day 1 was followed by the formation of a smoother, more uniform extracellular matrix on Zr-C, as incubation time progressed. Cell survival is dependent on the transformation from spherical to spread-out shape (Andersen et al., 2005) and initial cell adhesion is essential to subsequent proliferation (Anselme, 2000). As far as cell proliferation and differentiation are concerned, a flattened, fully spread cell morphology was reported to be better (Xia et al., 2011). The initially observed flatter cell morphology on Zr-C may serve as a possible explanation as to why Zr-C elicits higher proliferation versus Al-C.

Also, according to the SEM micrographs of the ceramic samples, a greater number of large and deep pores was observed on the surface of Zr-C scaffolds in comparison to Al-C (qualitative observation), which may have contributed to the differences in cell proliferation observed between the highest porosity alumina and zirconia scaffolds.

CONCLUSION

Enhancement of cellular response regarding the adhesion and proliferation of MC3T3-E1 pre-osteoblasts was observed by increasing substrate porosity in zirconia ceramics. Our results show that $\sim 50\%$ porosity and an average pore size of 150 μm is beneficial to cellular growth. This suggests an important advantage for porosity in zirconia ceramics, rendering an otherwise bioinert material into a cell-supporting scaffold. Unlike zirconia, cell proliferation on alumina was not significantly improved with increasing porosity. Finally, porous zirconia was found superior to porous alumina as it favored better cell spreading, pore infiltration, and higher growth.

ACKNOWLEDGMENTS

The authors acknowledge Prof. M. Epple (University of Duisburg-Essen, Germany) for experimental support, Ms. Alexandra Siakouli (University of Crete, Greece) for expert technical assistance with SEM, and Mr. Vladimir Promakhov (Tomsk State University, Russia) for technical assistance in preparing the ceramic samples. Financial support by the Greek Grant Thales-MIS 380278 from the General Secretariat for Research and Technology, and the Russian Grant No. 14.607.21.0069-RFMEFI60714X0069 is acknowledged.

REFERENCES

- Andersen, L. K., Contera, S. A., Justesen, J., Duch, M., Hansen, O., Chevallier, J., et al. (2005). Cell volume increase in murine MC3T3-E1 pre-osteoblasts attaching onto biocompatible tantalum observed by magnetic AC mode atomic force microscopy. *Eur. Cell. Mater.* 10, 61–68.
- Anselme, K. (2000). Osteoblast adhesion on biomaterials. *Biomaterials* 21, 14. doi:10.1016/S0142-9612(99)00242-2
- Balla, V. K., Bodhak, S., Bose, S., and Bandyopadhyay, A. (2010). Porous tantalum structures for bone implants: fabrication, mechanical and in vitro biological properties. *Acta Biomater.* 6, 3349–3359. doi:10.1016/j.actbio.2010.01.046
- Bauer, S., Schmuki, P., Mark, K. V. D., and Park, J. (2013). Engineering bio-compatible implant surfaces. *Prog. Mater. Sci.* 58, 261326. doi:10.1016/j.pmatsci.2012.09.001
- Beck, G. R., Sullivan, E. C., Moran, E., and Zerler, B. (1998). Relationship between alkaline phosphatase levels, osteopontin expression, and mineralization

- in differentiating MC3T3-E1 osteoblasts. *J. Cell. Biochem.* 68, 269–280. doi:10.1002/(SICI)1097-4644(19980201)68:2<269::AID-JCB13>3.0.CO;2-A
- Bignon, A., Chouteau, J., Chevalier, J., Fantozzi, G., Carret, J. P., Chavassieux, P., et al. (2003). Effect of micro- and macroporosity of bone substitutes on their mechanical properties and cellular response. *J. Mater. Sci. Mater. Med.* 14, 1089–1097. doi:10.1023/B:JMSM.000004006.90399.b4
- Bondars, B. Y., Heidemane, G., Grabis, J., Laschke, K., Boysen, H., Schneider, J., et al. (1995). Powder diffraction investigations of plasma sprayed zirconia. *J. Sci. Mater.* 30, 4. doi:10.1007/BF00375275
- Chevalier, J. (2006). What future for zirconia as a biomaterial? *Biomaterials* 27, 535–543. doi:10.1016/j.biomaterials.2005.07.034
- Chevalier, J., and Gremillard, L. (2009). Ceramics for medical applications: a picture for the next 20 years. *J. Eur. Ceram. Soc.* 29, 1245–1255. doi:10.1016/j.jeurceramsoc.2008.08.025
- Dehestani, M., Ilver, L., and Adolfsson, E. (2012). Enhancing the bioactivity of zirconia and zirconia composites by surface modification. *J. Biomed. Mater. Res. B Appl. Biomater.* 100, 832–840. doi:10.1002/jbm.b.32647
- Eckert, K. L., Mathey, M., Mayer, J., Homberger, F. R., Thomann, P. E., Groscurth, P., et al. (2000). Preparation and in vivo testing of porous alumina ceramics for cell carrier applications. *Biomaterials* 21, 63–69. doi:10.1016/S0142-9612(99)00134-9
- Franks, G. V., and Gan, Y. (2007). Charging behavior at the alumina–water interface and implications for ceramic processing. *J. Am. Ceram. Soc.* 90, 3373–3388. doi:10.1111/j.1551-2916.2007.02013.x
- Galmarini, S. (2011). *Ceramics: Sintering and Microstructure. Work practices "Ceramics Process": TP3 Sintering.* 1–15.
- Hadjicharalambous, C., Buyakov, A., Buyakova, S., Kulkov, S., and Chatzinikolaïdou, M. (2015a). Porous alumina, zirconia and alumina/zirconia for bone repair: fabrication, mechanical and in vitro biological response. *Biomed. Mater.* 10, 025012. doi:10.1088/1748-6041/10/2/025012
- Hadjicharalambous, C., Mygdali, E., Prymak, O., Buyakov, A., Kulkov, S., and Chatzinikolaïdou, M. (2015b). Proliferation and osteogenic response of MC3T3-E1 pre-osteoblastic cells on porous zirconia ceramics stabilized with magnesia or yttria. *J. Biomed. Mater. Res. A* 103, 3612–3624. doi:10.1002/jbm.a.35475
- Hing, K. A. (2005). Bioceramic bone graft substitutes: influence of porosity and chemistry. *Int. J. Appl. Ceram. Technol.* 2, 184–199. doi:10.1111/j.1744-7402.2005.02020.x
- Josset, Y., Oum'Hamed, Z., Zarrinpour, A., Lorenzato, M., Adnet, J. J., and Laurent-Maquin, D. (1999). In vitro reactions of human osteoblasts in culture with zirconia and alumina ceramics. *Biomed. Mater. Res.* 47, 13. doi:10.1002/(SICI)1097-4636(19991215)47:4<481::AID-JBM4>3.3.CO;2-P
- Karageorgiou, V., and Kaplan, D. (2005). Porosity of 3D biomaterial scaffolds and osteogenesis. *Biomaterials* 26, 5474–5491. doi:10.1016/j.biomaterials.2005.02.002
- Karlsson, M., Pålsgård, E., Wilshaw, P., and Di Silvio, L. (2003). Initial in vitro interaction of osteoblasts with nano-porous alumina. *Biomaterials* 24, 3039–3046. doi:10.1016/S0142-9612(03)00146-7
- Kim, H. W., Shin, S. Y., Kim, H. E., Lee, Y. M., Chung, C. P., Lee, H. H., et al. (2008). Bone formation on the apatite-coated zirconia porous scaffolds within a rabbit calvarial defect. *J. Biomater. Appl.* 22, 485–504. doi:10.1177/0885328207078075
- Kimura, Y., Matsuzaka, K., Yoshinari, M., and Inoue, T. (2012). Initial attachment of human oral keratinocytes cultured on zirconia or titanium. *Dent. Mater. J.* 31, 346–353. doi:10.4012/dmj.2011-189
- Lew, K. S., Othman, R., Ishikawa, K., and Yeoh, F. Y. (2012). Macroporous bio-ceramics: a remarkable material for bone regeneration. *J. Biomater. Appl.* 27, 345–358. doi:10.1177/0885328211406459
- Lohmann, C. H., Dean, D. D., Koster, G., Casasola, D., Buchhorn, G. H., Fink, U., et al. (2002). Ceramic and PMMA particles differentially affect osteoblast phenotype. *Biomaterials* 23, 1855–1863. doi:10.1016/S0142-9612(01)00312-X
- Manicone, P. F., Rossi Iommetti, P., and Raffaelli, L. (2007). An overview of zirconia ceramics: basic properties and clinical applications. *J. Dent.* 35, 819–826. doi:10.1016/j.jdent.2007.07.008
- Masters, K. S., and Anseth, K. S. (2004). Cell–material interactions. *Adv. Chem. Eng.* 29, 7–46. doi:10.1016/S0065-2377(03)29002-5
- Michailidis, N., Stergioudi, F., Viglakis, K., and Chatzinikolaïdou, M. (2014). Production of novel ceramic porous surfaces tailored for bone tissue engineering. *CIRP Ann. Manuf. Technol.* 63, 557–560. doi:10.1016/j.cirp.2014.03.044
- Ni, S., Li, C., Ni, S., Webster, T., and Chen, T. (2014). Understanding improved osteoblast behavior on select nanoporous anodic alumina. *Int. J. Nanomed.* 9, 3325–3334. doi:10.2147/IJN.S60346
- Piconi, C., Maccauro, G., Muratori, F., and Brach Del Prever, E. (2003). Alumina and zirconia ceramics in joint replacements. *J. Appl. Biomater. Biomech.* 1, 19–32.
- Roualdes, O., Duclos, M. E., Gutknecht, D., Frappart, L., Chevalier, J., and Hartmann, D. J. (2010). In vitro and in vivo evaluation of an alumina–zirconia composite for arthroplasty applications. *Biomaterials* 31, 2043–2054. doi:10.1016/j.biomaterials.2009.11.107
- Scherrer, P. (1918). Bestimmung der Grösse und der inneren Struktur von Kolloidteilchen mittels Röntgenstrahlen. *Nachr. Ges. Wiss. Göttingen* 26, 2.
- Song, Y.-G., and Cho, I.-H. (2014). Characteristics and osteogenic effect of zirconia porous scaffold coated with β -TCP/HA. *J. Adv. Prosthodont.* 6, 285. doi:10.4047/jap.2014.6.4.285
- St-Pierre, J.-P., Gauthier, M., Lefebvre, L.-P., and Tabrizian, M. (2005). Three-dimensional growth of differentiating MC3T3-E1 pre-osteoblasts on porous titanium scaffolds. *Biomaterials* 26, 73197328. doi:10.1016/j.biomaterials.2005.05.046
- Walpole, A. R., Xia, Z., Wilson, C. W., Triffitt, J. T., and Wilshaw, P. R. (2009). A novel nano-porous alumina biomaterial with potential for loading with bioactive materials. *J. Biomed. Mater. Res. A* 90, 46–54. doi:10.1002/jbm.a.32067
- Wang, X., Riffin, W. L. G., and Chen, J. (2010). Hf contents and Zr/Hf ratios in granitic zircons. *Geochem. J.* 44, 7. doi:10.2343/geochemj.1.0043
- Xia, L., Zhang, Z., Chen, L., Zhang, W., Zeng, D., Zhang, X., et al. (2011). Proliferation and osteogenic differentiation of human periodontal ligament cells on akermanite and β -TCP bioceramics. *Eur. Cell. Mater.* 22, 68–82.

Conflict of Interest Statement: The authors declare that the research was conducted in the absence of any commercial or financial relationships that could be construed as a potential conflict of interest.

Copyright © 2015 Hadjicharalambous, Prymak, Loza, Buyakov, Kulkov and Chatzinikolaïdou. This is an open-access article distributed under the terms of the Creative Commons Attribution License (CC BY). The use, distribution or reproduction in other forums is permitted, provided the original author(s) or licensor are credited and that the original publication in this journal is cited, in accordance with accepted academic practice. No use, distribution or reproduction is permitted which does not comply with these terms.



Properties and crystallization phenomena in $\text{Li}_2\text{Si}_2\text{O}_5\text{--Ca}_5(\text{PO}_4)_3\text{F}$ and $\text{Li}_2\text{Si}_2\text{O}_5\text{--Sr}_5(\text{PO}_4)_3\text{F}$ glass–ceramics via twofold internal crystallization

OPEN ACCESS

Edited by:

Malcolm Xing,
University of Manitoba, Canada

Reviewed by:

Steve Meikle,
University of Brighton, UK
Athina Bakopoulou,
Aristotle University of Thessaloniki,
Greece

*Correspondence:

Markus Rampf,
Research and Development,
Inorganic Chemistry, Technical
Fundamentals, Ivoclar Vivadent AG,
Benderstr. 2,
Schaan FL-9494, Liechtenstein
markus.rampf@ivoclarvivadent.com

Specialty section:

This article was submitted to
Biomaterials, a section of the journal
Frontiers in Bioengineering and
Biotechnology

Received: 13 May 2015

Accepted: 10 August 2015

Published: 03 September 2015

Citation:

Rampf M, Dittmer M, Ritzberger C,
Schweiger M and Höland W (2015)
Properties and crystallization
phenomena in $\text{Li}_2\text{Si}_2\text{O}_5\text{--Ca}_5(\text{PO}_4)_3\text{F}$
and $\text{Li}_2\text{Si}_2\text{O}_5\text{--Sr}_5(\text{PO}_4)_3\text{F}$ glass–
ceramics via twofold
internal crystallization.
Front. Bioeng. Biotechnol. 3:122.
doi: 10.3389/fbioe.2015.00122

Markus Rampf*, Marc Dittmer, Christian Ritzberger, Marcel Schweiger and
Wolfram Höland

Research and Development, Inorganic Chemistry, Technical Fundamentals, Ivoclar Vivadent AG, Schaan, Liechtenstein

The combination of specific mechanical, esthetic, and chemical properties is decisive for the application of materials in prosthodontics. Controlled twofold crystallization provides a powerful tool to produce special property combinations for glass–ceramic materials. The present study outlines the potential of precipitating $\text{Ca}_5(\text{PO}_4)_3\text{F}$ as well as $\text{Sr}_5(\text{PO}_4)_3\text{F}$ as minor crystal phases in $\text{Li}_2\text{Si}_2\text{O}_5$ glass–ceramics. Base glasses with different contents of CaO/SrO , P_2O_5 , and F^- were prepared within the glasses of the $\text{SiO}_2\text{--Li}_2\text{O--K}_2\text{O--CaO/SrO--Al}_2\text{O}_3\text{--P}_2\text{O}_5\text{--F}$ system. Preliminary studies of nucleation by means of XRD and scanning electron microscopy (SEM) of the nucleated base glasses revealed X-ray amorphous phase separation phenomena. Qualitative and quantitative crystal phase analyses after crystallization were conducted using XRD in combination with Rietveld refinement. As a main result, a direct proportional relationship between the content of apatite-forming components in the base glasses and the content of apatite in the glass–ceramics was established. The microstructures of the glass–ceramics were investigated using SEM. Microstructural and mechanical properties were found to be dominated by $\text{Li}_2\text{Si}_2\text{O}_5$ crystals and quite independent of the content of the apatite present in the glass–ceramics. Biaxial strengths of up to 540 MPa were detected. $\text{Ca}_5(\text{PO}_4)_3\text{F}$ and $\text{Sr}_5(\text{PO}_4)_3\text{F}$ influence the translucency of the glass–ceramics and, hence, help to precisely tailor the properties of $\text{Li}_2\text{Si}_2\text{O}_5$ glass–ceramics. The authors conclude that the twofold crystallization of $\text{Li}_2\text{Si}_2\text{O}_5\text{--Ca}_5(\text{PO}_4)_3\text{F}$ or $\text{Li}_2\text{Si}_2\text{O}_5\text{--Sr}_5(\text{PO}_4)_3\text{F}$ glass–ceramics involves independent solid-state reactions, which can be controlled via the chemical composition of the base glasses. The influence of the minor apatite phase on the optical properties helps to achieve new combinations of features of the glass–ceramics and, hence, displays new potential for dental applications.

Keywords: glass–ceramics, lithium disilicate, calcium fluoroapatite, strontium fluoroapatite, prosthodontics, twofold crystallization

Introduction

Glass–ceramics are the result of the controlled devitrification of base glasses including nucleation and crystallization and represent a distinct category of technical materials. The development of glass–ceramics targets the creation of specific material properties as well as property combinations. Wild crystallization is counterproductive and has to be avoided. The chemical composition of the base glass, nucleation techniques, and crystallization heat treatments, hence, are the most important parameters where research and development of these materials begins (Höland and Beall, 2012). In this manner, the knowledge about processes and mechanisms involved in glass–ceramic technology has been continuously advanced since in the mid 1950s Stookey (1959) discovered the first glass–ceramic material via precipitation of $\text{Li}_2\text{Si}_2\text{O}_5$ from a base glass using Ag clusters as agent for heterogeneous nucleation. $\text{Li}_2\text{Si}_2\text{O}_5$ is still subject of a multitude of glass–ceramic research. Nucleation mechanisms have been extensively studied (Headley and Loehman, 1984) and besides Stookey's heterogeneous nucleation, Vogel (1963) found evidence for the influence of glass-in-glass phase separations on nucleation of lithium silicate glass–ceramics from non-stoichiometric base glasses. Enhancing its mechanical and chemical properties, since that time product-oriented research and development on $\text{Li}_2\text{Si}_2\text{O}_5$ crystals focused on multi-component glass systems, including P_2O_5 as agent for internal heterogeneous nucleation.

Höland et al. (1994) developed translucent glass–ceramics for dental applications in the system $\text{SiO}_2\text{--Li}_2\text{O--ZrO}_2\text{--P}_2\text{O}_5$ initiating further in depth studies of the glass system extended by, e.g., Al_2O_3 and K_2O (Bischoff et al., 2011). Though, the final identification of the exact mechanisms running is difficult, basic principles of the crystallization and nucleation have been understood. Li_2SiO_3 and $\text{Li}_2\text{Si}_2\text{O}_5$ crystals precipitate in a parallel reaction at temperatures $<600^\circ\text{C}$ before the crystallization rate of $\text{Li}_2\text{Si}_2\text{O}_5$ overcomes the one of Li_2SiO_3 at temperatures $>700^\circ\text{C}$. Dissolution of Li_2SiO_3 at higher temperatures initiates an enhanced secondary crystallization of $\text{Li}_2\text{Si}_2\text{O}_5$. While amorphous lithium phosphate can be found in form of glass-in-glass phase separations in the nucleated base glass, crystalline Li_3PO_4 was only found after heat treatments $>780^\circ\text{C}$ (Höland and Beall, 2012). Amorphous or disordered nanoscale Li_3PO_4 phase separations play an uncontroversial role in the nucleation mechanism of lithium silicate. Based on the sound knowledge about nucleation and crystallization mechanisms, materials for restorative dentistry with a toughness of up to $2.9\text{ MPa}\cdot\text{m}^{0.5}$ and flexural biaxial strength up to 600 MPa with well-suited optical properties could be achieved (Cramer von Clausbruch et al., 2000; Höland et al., 2005; Apel et al., 2007, 2008; Höland and Beall, 2012). Furthermore, $\text{Li}_2\text{Si}_2\text{O}_5$ glass–ceramics are suited for various processing techniques, such as sintering, molding, and CAD/CAM machining in an intermediate Li_2SiO_3 stage of the glass–ceramic.

However, to meet the special demands for esthetics in prosthodontics, more and more advanced glass–ceramics are needed. Multi-component glass systems allowing the controlled precipitation of more than a single crystal phase in the glassy matrix display state of the art technique with high potential (Ritzberger et al., 2015). Already in 1994, an apatite-containing

leucite glass–ceramic for use in restorative dentistry was reported by Höland et al. (1994, 2000). By applying a combination of surface nucleation during which leucite formed and controlled internal nucleation of fluoroapatite, Höland et al. (1994, 2000) managed to produce leucite–apatite glass–ceramics in the $\text{SiO}_2\text{--Al}_2\text{O}_3\text{--CaO--Na}_2\text{O--K}_2\text{O--P}_2\text{O}_5\text{--F}$ base glass system, which led to the development of the commercial product IPS d.Sign®. Contrary to numerous research published on the development of bioactive glass–ceramics for biomedical materials, in the field of prosthodontics the use of fluoroapatite is limited to the control of optical or mechanical material properties. The minor apatite phase in the leucite glass–ceramics introduced a special hue originating in the bulk of the material that helped to achieve controlled translucency comparable to natural teeth.

A first report on the parallel existence of $\text{Li}_2\text{Si}_2\text{O}_5$ crystals and fluoroapatite in a devitrificated glass was made by Kuzielova et al. (2006). However, a bioactive and, hence, chemically not durable glass was subject of these studies. The present work illustrates the qualitatively and quantitatively controlled internal crystallization of fluoroapatite within different chemically durable glass–ceramics (without adding a different material, such as a glass) with $\text{Li}_2\text{Si}_2\text{O}_5$ as main crystal phase. Preliminary studies on phase separation processes occurring during the nucleation heat treatment and principles of twofold crystallization are shown. Furthermore mechanical and optical properties of the resulting glass–ceramics are discussed with respect to dental applications.

Materials and Methods

Glass Formation and Thermal Analysis

Using the raw materials quartz, lithium carbonate, potassium carbonate, calcium carbonate or strontium carbonate, aluminum oxyhydroxyhydrate, aluminum metaphosphate and calcium fluoride or lithium fluoride base glasses of different compositions were melted as shown in **Table 1**. Melting took place in a Pt–Rh10 crucible at 1500°C in an electric furnace. After a dwell time of 1 h, the glasses were quenched in water. Thermal analysis of the dried glass granules measuring less than about 1 mm in diameter was performed in nitrogen atmosphere by differential scanning calorimetry (DSC) using a Netzsch STA 409 apparatus, regulated at a heating rate of 10 K/min . An accuracy of $\pm 1^\circ\text{C}$ can be reached according to the reference measurements using the transition of low-quartz to high-quartz at 573°C as a standard gage.

In a subsequent step, the quenched glass frits were melted again at a temperature of 1500°C . After a dwell time of 2 h, the glasses were cast into a graphite mold to form blocks measuring about $13\text{ mm} \times 14\text{ mm} \times 30\text{ mm}$. The glass blocks were immediately removed from the mold and cooled to room temperature under ambient conditions.

Nucleation

Besides nucleation, the first heat treatment was required to relief stresses in the glass structure and, hence, allows further machining of the glass. The cooled glass blocks were placed in a furnace pre-heated to 500°C . After a dwell time of 30 min, the glass blocks were allowed to cool to room temperature. To study the effect of the dwell time at 500°C , one glass block of glass D (**Table 1**) was heat

TABLE 1 | Chemical compositions of the base glasses calculated from the initial weight of the raw materials, taking into account the evaporation of P₂O₅ and F⁻.

	A	B	C	D	E	F	G
mol% SiO ₂	65.0	63.9	62.8	62.4	59.7	63.5	62.8
mol% Li ₂ O	27.0	26.6	26.2	26.0	24.8	26.5	26.2
mol% K ₂ O	2.0	2.0	2.0	2.0	2.0	2.0	2.0
mol% CaO	3.0	4.0	5.0	5.4	8.0	5.0	–
mol% SrO	–	–	–	–	–	–	5.0
mol% Al ₂ O ₃	1.5	1.5	1.5	1.5	1.5	1.5	1.5
mol% P ₂ O ₅	0.9	1.2	1.5	1.6	2.4	1.5	1.5
mol% F ⁻	0.6	0.8	1.0	1.1	1.6	–	1.0

treated for 10 h prior to cooling. The cooling rate in the glass transition range was approximately 2–3 K/min. Small glass plates were cut from the glass blocks. For crystal phase analysis, the surface of the glass plates was ground using a 40-μm diamond grit grinding disk. X-ray diffraction patterns (XRD patterns) were recorded in a 2θ-range from 10° to 60° in 0.014° steps (D8 Advance, Bruker, Karlsruhe, Germany) using CuK_α radiation ($\lambda = 0.154$ nm). Micrographs of the glass plates after nucleation, polished with a 0.5-μm diamond grit grinding disk and subsequently etched by soaking into 20% H₃PO₄ for 2 min, were taken by means of scanning electron microscopy (SEM) (Supra 40VP, Zeiss, Oberkochen, Germany). Prior to the analysis, the samples were coated with an approximately 2 nm Au–Pd layer by sputtering.

Crystallization

The second heat treatments took place in an oven of the Programat® type (Ivoclar Vivadent AG, Schaan, Liechtenstein). Small glass plates of approximately 2 mm thickness, cut from the nucleated glass blocks, were used. A detailed investigation of the temperature-dependent crystal phase formation was conducted considering glass D. The nucleated glass plates were heat treated for 30 min at 520, 540, 560, 580, 600, 700, or 800°C. After the dwell time, the samples were allowed to cool to 500°C in the furnace before opening it. Prior to XRD analysis, conducted as described above, the surface of the glasses and glass–ceramics was removed using a 40-μm diamond grit grinding disk.

A quantitative study of the crystal phase formation was conducted applying Rietveld refinement. Glass–ceramics nucleated at 500°C for 30 min and subsequently crystallized via a second heat treatment for 30 min at 800°C were used. The glass–ceramic material was crushed and comminuted in a mortar grinder (Mortar Grinder RM 200, Retsch, Haan, Germany) and subsequently sieved <45 μm. Then the powder was elutriated with approximately the same mass of Al₂O₃ in acetone. The solvent was evaporated in an oven pre-heated at 80°C. Al₂O₃ was used as an internal standard in a concentration of about 50 wt.%. After recording the powder XRD patterns from 10° to 100° 2θ in 0.014° steps, the quantification of the crystal phases was done with the TOPAS software from Bruker.

Microstructure Formation

The microstructures of the glass–ceramics crystallized at 800°C for 30 min were investigated applying SEM. Small plates of the nucleated glass blocks were crystallized at 800°C for 30 min and

subsequently polished with a 0.5-μm diamond grit grinding disk. The surface of the samples was etched with vapor of 40% HF acid and coated with a 1–2 nm Au–Pd layer prior to SEM analysis. In order to utilize the contrast provided by elements with high specific weight via the detection of backscattered ions during SEM, glass–ceramic G was determined. The sample preparation was conducted as described above; however, the surface was etched by soaking into 3% HF acid for 10 s.

Mechanical and Optical Properties of the Glass–Ceramics

Small circular plates were milled from the blocks of nucleated glass using a CEREC® InLab milling machine (Sirona, Bensheim, Germany). Crystallization of the plates took place as described above via a second heat treatment for 30 min at 800°C. The samples were prepared for the testing of the biaxial fracture strength according to ISO 6872 including a surface finishing with a 15 μm diamond grit grinding disk. The measurements were conducted using a universal testing apparatus (Zwick 1456, Zwick GmbH & Co. KG, Ulm, Germany). The biaxial strengths are given as the means of data sets ±SD. Ten samples of each series were tested. Normality of the data sets was determined applying a Jarque–Bera test. Significant deviations (>95%) between the different data sets were examined using the Student's *t*-test.

Small glass plates measuring approximately 10 mm × 10 mm × 2 mm were cut from the nucleated glass blocks and crystallized at 800°C for 30 min. Afterwards the glass–ceramic plates were prepared for translucency (CR) measurements and color evaluation according to BS5612, DIN5033, and DIN6174, respectively. A spectrometer of the type CM-3700d (Konica-Minolta, Tokyo, Japan) was used for the spectroscopic analysis.

The opalescence *O* of the glass–ceramics was estimated using an equation derived by Kobashigawa et al. (2001) (Eq. 1) and repeatedly used by Lee (Lee et al., 2005, 2006; Lee, 2007), with *a* and *b* being color-related parameters detected with the CM-5 spectrometer (Konica-Minolta, Tokyo, Japan). While the *a*-value gives a measure for the intensity proportion of red and green, the *b*-value deals with yellow and blue. The Δ values *a* and *b* describe the differences of these parameters detected in either the transmission or reflection mode. Glass–ceramic plates measuring approximately 10 mm × 10 mm × 1 mm were used.

$$O = \sqrt{(\Delta a)^2 + (\Delta b)^2} \quad (1)$$

Results

Glass Formation and Thermal Analysis

The results of the thermal analysis of the base glasses after quenching in water are shown in **Figure 1**. The exact values for exothermic T_{exo} or endothermic T_{endo} peak temperatures are given in **Table 2**. The onset indicating that the glass transition temperature T_g is in the range of 450–455°C for samples A–E. A slightly increased T_g can be observed for the F^- free reference sample F at about 462°C, while the substitution of CaO by SrO in glass G yields a reduction of T_g to about 442°C. All samples show at least one exothermic peak in the DSC curve indicating crystallization. Increasing the content of the components CaO, P_2O_5 , and F^- (samples A–E) clearly decreases the temperature for the first exothermic processes detectable by DSC from about 720 to 565°C. A second exothermic signal indicating crystallization is evident at about 830°C for glass A and at approximately 800°C for glass B. However, the latter is rather weak. While glasses C and D as well as F and G do not show any further exothermic signals during thermal analysis, three more exothermic peaks are evident for glass E at about 610, 680, and 786°C.

A comparison of the endothermic signals, which indicates the dissolution of the crystal phases, reveals that no significant difference can be observed between the glasses having different CaO/SrO, P_2O_5 , and F^- contents, with the exception of glass E. All of them show two endothermic peaks between 900 and 965°C. The thermal analysis of the F^- free reference sample F reveals only one endothermic signal at about 949°C.

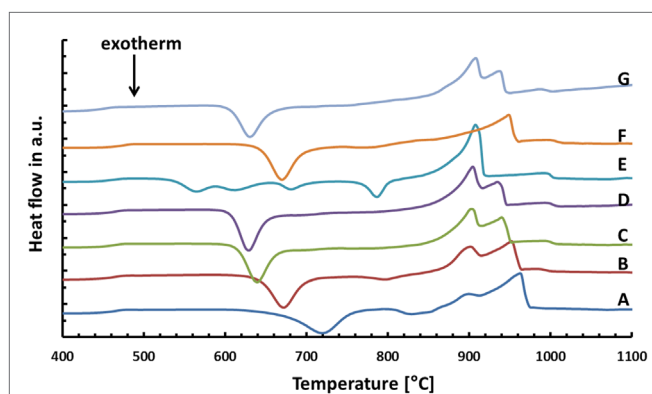


FIGURE 1 | Thermal analysis of different base glasses.

TABLE 2 | Thermal analysis of the base glasses by means of DSC.

Base glass		A	B	C	D	E	F	G
T_g	[°C]	451	454	452	457	451	462	442
$T_{\text{exo}1}$	[°C]	719	672	639	629	564	670	630
$T_{\text{exo}2}$	[°C]	829	979	—	—	611	772	—
$T_{\text{exo}3}$	[°C]	849	—	—	—	681	—	—
$T_{\text{exo}4}$	[°C]	—	—	—	—	786	—	—
$T_{\text{endo}1}$	[°C]	905	902	904	905	909	949	908
$T_{\text{endo}2}$	[°C]	963	953	941	937	—	—	936

Nucleation

Two different phase separation phenomena could be observed by means of SEM of the glasses after etching the surface with H_3PO_4 . The investigation of the microstructures revealed cloudy separation areas in the range of 1 μm in diameter as well as sharp non-spherical phase separations with dimensions <100 nm (**Figure 2**). No crystalline phase formation could be detected by means of XRD analysis of the glass samples after the first heat treatment at 500°C for 30 min or 10 h.

Crystallization

Results on the temperature-dependent crystal phase formation in the nucleated base glass D are presented in **Figure 3**. The nucleated base glass is X-ray-amorphous $\text{Li}_2\text{Si}_2\text{O}_5$ and traces of Li_2SiO_3 crystals are the only crystal phases present in the diffractogram after a second heat treatment at 540°C for 30 min. The precipitation of fluoroapatite can be detected after heat treatments at 700 as well as 800°C. While the relative intensity of the Li_2SiO_3 peaks decreases when the crystallization temperature is increased from 700 to 800°C, the contrary can be observed for peaks assigned to fluoroapatite. The presence of crystalline Li_3PO_4 was definitely detected after heat treatment at 600°C.

The qualitative and quantitative composition of the glass–ceramics after crystallization at 800°C for 30 min is shown in **Table 3**. Increasing the content of CaO, P_2O_5 , and F^- in samples A–E enhances the crystallization of fluoroapatite in the glass–ceramics. In the same manner, the amount of residual glass phase is reduced from sample A–D. Glass–ceramic A, B, C, and D contain 56.4, 57.8, 58.7, and 58.1 wt.% $\text{Li}_2\text{Si}_2\text{O}_5$. Sample E, comprising the largest amount of CaO, P_2O_5 , and F^- and the lowest fraction of Li_2O and SiO_2 has the least percentage of $\text{Li}_2\text{Si}_2\text{O}_5$ (50.3 wt.%) and the highest fraction of Li_2SiO_3 (2.9 wt.%) of all the glass–ceramics analyzed. The F^- free reference sample F shows the largest content of Li_3PO_4 crystals. Compared to the corresponding F^- containing glass C, less $\text{Li}_2\text{Si}_2\text{O}_5$ crystal content is formed. The substitution of CaO by SrO yields the crystallization of $\text{Sr}_5(\text{PO}_4)_3\text{F}$ in glass G.

Microstructure Formation

After etching of the polished surface of the glass–ceramics crystallized at 800°C for 30 min with HF vapor, only one type of crystal morphology is evident in each of the micrographs presented in **Figure 4**. It involves $\text{Li}_2\text{Si}_2\text{O}_5$ crystals. While the microstructures of glass–ceramics F and G are rather similar, quite different microstructures were found in the glass ceramics A, C, E, and F as shown in **Figure 4**. $\text{Li}_2\text{Si}_2\text{O}_5$ crystals in the range of >>10 μm are present in the material A. The size of the $\text{Li}_2\text{Si}_2\text{O}_5$ crystals clearly

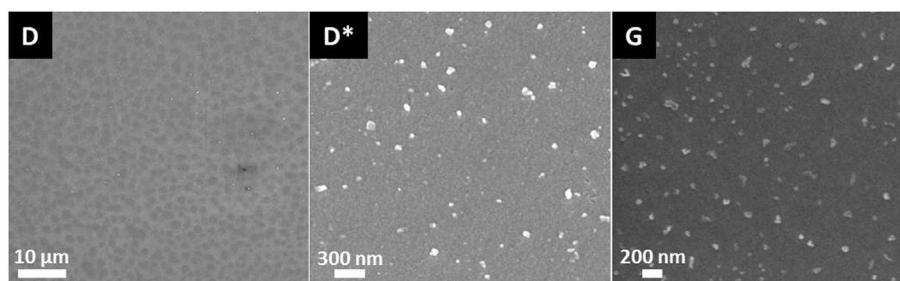


FIGURE 2 | Microstructures of glass D after nucleation for 10 h at 500°C and of glass G after nucleation at 500°C for 30 min.

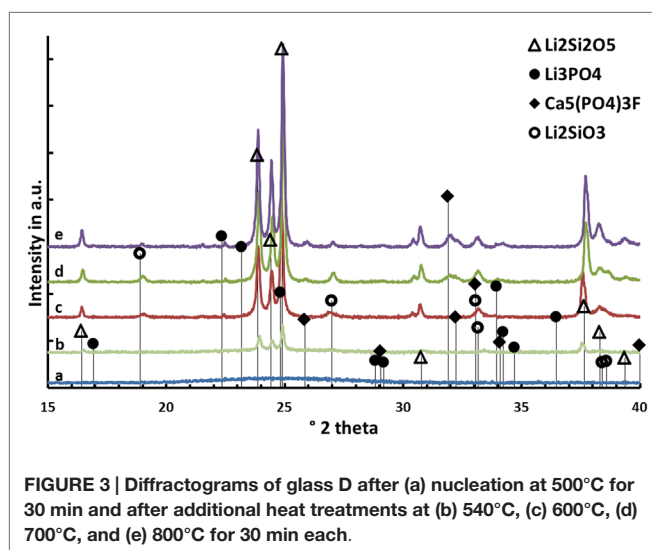


FIGURE 3 | Diffractograms of glass D after (a) nucleation at 500°C for 30 min and after additional heat treatments at (b) 540°C, (c) 600°C, (d) 700°C, and (e) 800°C for 30 min each.

decreases with an increasing fraction of CaO, P_2O_5 , and F^- , as shown in a comparison of A, C, and E. Furthermore, the presence of F^- refines the microstructure as can be seen by comparing glass ceramics C and F.

The micrographs in Figure 5 display lath or plate-like crystals in a glassy matrix. According to the micrograph taken by backscattered electrons (Figure 5 left), the glass seems to be enriched with ions of relatively high specific weight, such as Sr^{2+} , compared to the crystalline structures which obviously comprise rather light ions, such as Li^+ . Regularly distributed black spots with a diameter of approximately 200 nm are present in both micrographs in Figure 5. These black spots indicate holes in the microstructure which are the result of removing a crystalline or amorphous phase from the microstructure by etching.

Mechanical Properties

The biaxial strength of the glass ceramics is presented in Table 4. Glass–ceramic D produces the highest mean strength among all the samples reaching a strength of 538 ± 59 MPa. The strength of sample series D is statistically significantly higher compared to that of the glass–ceramics of types A, B, and E revealing a strength of 217 ± 5 , 437 ± 20 , and 351 ± 49 MPa. Series A exhibits a significantly lower fracture strength than any other glass–ceramic

investigated during this study. The difference in the strength of the materials C, D, F, and G is statistically not significant.

Optical Properties

The translucency and opalescence properties of the glass–ceramics are presented in Table 4. Increasing the content of CaO, P_2O_5 , and F^- in the compositions A–C decreases the CR value and, hence, reduces the translucency of the glass–ceramics. The relatively small change of the base glass composition from C to D yields a slight increase of the translucency. Composition E shows the highest CR value of all the series. The F^- free reference sample F shows a lower translucency compared to that of the fluoroapatite-containing glass–ceramics C and D, while the SrO-containing glass–ceramic G has a slightly decreased translucency compared to the corresponding CaO-containing sample C.

The opalescence of the glass–ceramics increases consistently with an increasing ratio of CaO, P_2O_5 , and F^- in the base glass. There is no significant difference in terms of the apatite-free reference sample F. Only a slightly increased opalescence can be observed compared to that of the corresponding apatite-forming composition C.

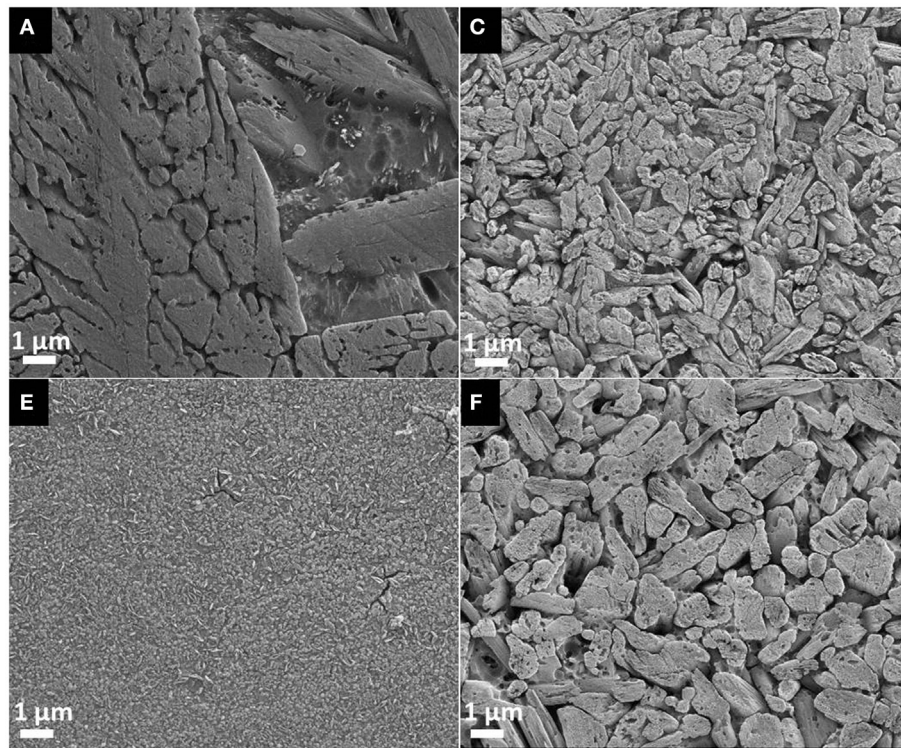
Discussion

Different base glasses, which allow the controlled volume crystallization of $Li_2Si_2O_5$ as main crystal phase and $Ca_5(PO_4)_3F$ or $Sr_5(PO_4)_3F$ as minor crystal phase, have been developed. In a systematic series of experiments, the components CaO, P_2O_5 , and F^- were simultaneously increased from base glass A to base glass E in the stoichiometric ratio of $Ca_5(PO_4)_3F$. The increase of the mentioned components was conducted at the expense of SiO_2 and Li_2O , ensuring a constant molar ratio of SiO_2/Li_2O . Besides the components, necessary for the formation of the desired crystal phases, the glass system was extended by Al_2O_3 and K_2O in order to enhance the processability and chemical stability of the glasses.

Beyond controversy, the P_2O_5 content plays an important role in the studied glass system. It is essential for the nucleation of lithium silicate as well as mandatory for the crystallization of $Ca_5(PO_4)_3F$. The preliminary study for nucleation by means of SEM (Figure 2) of the base glasses after heat treatment at 500°C for 30 min revealed the presence of phase separations. There is no crystalline phase present according to XRD analysis (Figure 3), though. The shape and size of the phase separations

TABLE 3 | Qualitative and quantitative composition of glass–ceramics after subsequent heat treatment at 500 and 800°C for a duration of 30 min each.

	A	B	C	D	E	F	G
wt.% $\text{Ca}_5/\text{Sr}_5(\text{PO}_4)_3\text{F}$	2.0	4.1	6.6	7.4	12.2	–	9.5
wt.% $\text{Li}_2\text{Si}_2\text{O}_5$	56.4	57.8	58.7	58.1	50.3	54.3	53.6
wt.% Li_3PO_4	2.7	1.8	1.9	2.0	1.3	3.5	1.6
wt.% Li_2SiO_3	1.5	–	–	–	2.9	–	1.1
wt.% amorphous phase	37.4	36.3	32.8	32.5	33.3	42.2	34.2

**FIGURE 4 | Microstructure of glass–ceramics A, C, E, and F crystallized for 30 min at 800°C, polished and subsequently etched in 40% HF vapor for 30 s.**

visible in the micrographs in **Figure 2** (D* and G) indicate a nanocrystalline phase, which is observable after etching with H_3PO_4 . The phase separations being amorphous or disordered nanocrystalline phases of the Li_3PO_4 kind seems likely according to previous observations made in non-stoichiometric $\text{Li}_2\text{Si}_2\text{O}_5$ forming glasses (Bischoff et al., 2011). On a larger scale ($> 1 \mu\text{m}$), there were rather diffuse separation areas visible (**Figure 2**, D) which give evidence for the enrichment of ions, most probably P_2O_5 , in certain areas. Due to the huge discrepancy in the size of the two different kinds of phase separation phenomena observed, they seem to be independent of each other. Assuming that both are enriched with P_2O_5 , since etching with H_3PO_4 uncovered the phases, the formation of P_2O_5 sites enriched with Li^+ , on the one hand, as well as the parallel formation of P_2O_5 sites enriched with Ca^{2+} ions should be considered. While the Li^+ -rich sites could be responsible for the formation of small amorphous or disordered nanocrystalline Li_3PO_4 phase separations, known to nucleate

lithium silicate (Höland and Beall, 2012), the large and rather cloudlike areas could accommodate Ca^{2+} rich P_2O_5 sites which later on initiate apatite formation. Depletion of these glass areas of Li^+ and Si^{4+} -Q-groups coordinated in tetrahedrons with O^{2-} , as a consequence of lithium silicate precipitation, could have an enhancing effect on the crystallization of apatite, which occurred clearly subsequently to the early formation of lithium silicate and Li_3PO_4 (**Figures 3** and **6**).

The principles of twofold crystallization of $\text{Li}_2\text{Si}_2\text{O}_5$ and $\text{Ca}_5(\text{PO}_4)_3\text{F}$ in glass D, based on the XRD patterns shown in **Figure 3**, are summarized in the schema presented in **Figure 6**. As a function of temperature, $\text{Li}_2\text{Si}_2\text{O}_5$ and Li_2SiO_3 are the first two crystalline phases that formed at temperatures above 540°C, prior to the precipitation of Li_3PO_4 at temperatures $< 600^\circ\text{C}$. The formation of crystalline Li_3PO_4 occurred surprisingly about 180°C below the temperatures reported so far in the literature for P_2O_5 containing $\text{Li}_2\text{Si}_2\text{O}_5$ glass systems (Höland and Beall, 2012). P_2O_5

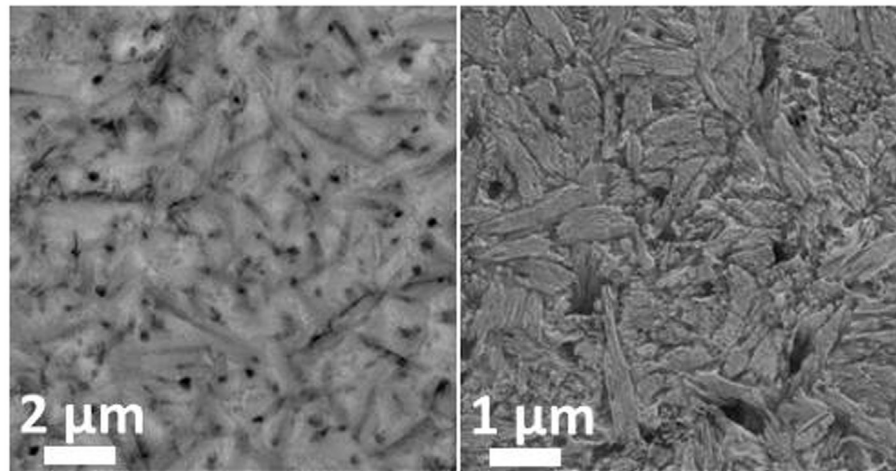


FIGURE 5 | Microstructure of glass-ceramic G. Left: backscattered electrons; right: secondary electrons.

TABLE 4 | Mechanical and optical properties of the glass–ceramics.

	A	B	C	D	E	F	G
σ_{biax} [MPa]	217 ± 5	437 ± 20	429 ± 103	538 ± 59	351 ± 49	499 ± 34	534 ± 52
CR in%	74.6	69.8	66.1	66.7	50.5	60.3	69.9
O in%	4.5	6.4	9.9	15.2	26.8	11.0	7.2

phase separation phenomena and the early parallel formation of $\text{Li}_2\text{Si}_2\text{O}_5$ and Li_2SiO_3 happen in analogy to the principles reported in the literature (Höland and Beall, 2012), which describe the nucleating effect of amorphous or disordered nanocrystalline Li_3PO_4 phases on these crystal phases. The $\text{Ca}_5(\text{PO}_4)_3\text{F}$ crystal phase formation happening at temperatures definitely above the crystallization of lithium silicates as well as Li_3PO_4 seems to be independent and subordinated, though. However, comparing the crystal phase compositions of the apatite-forming glass–ceramic C with the corresponding F^- free reference sample F (Table 3), one can see the significantly increased Li_3PO_4 content in the apatite-free material F. The structural integration of P_2O_5 in, e.g., an amorphous fluoroapatite pre-phase and, hence, hindering the crystallization of Li_3PO_4 could explain this phenomenon. Further in-depth investigation of the involved mechanism is necessary to identify the exact mechanisms running.

Although the exact crystallization and nucleation mechanisms are still a point of discussion, the qualitative and quantitative crystallization of fluoroapatite as minor phase in $\text{Li}_2\text{Si}_2\text{O}_5$ -dominated glass–ceramics could be precisely controlled via the chemical composition of the base glasses (Table 3). Lithium disilicate and fluoroapatite could be precipitated in bulk glasses by means of twofold crystallization. The content of fluoroapatite in the glass–ceramic materials could be controlled by raising the ratio of apatite-forming oxides and ions CaO , P_2O_5 , and F^- in a lithium disilicate forming glass composition (Tables 1 and 3). Assuming, for the sake of simplicity, that fluoroapatite forms prior to and independently of the formation of $\text{Li}_2\text{Si}_2\text{O}_5$ and Li_3PO_4 , the maximum theoretically possible content of fluoroapatite in the glass–ceramics can be

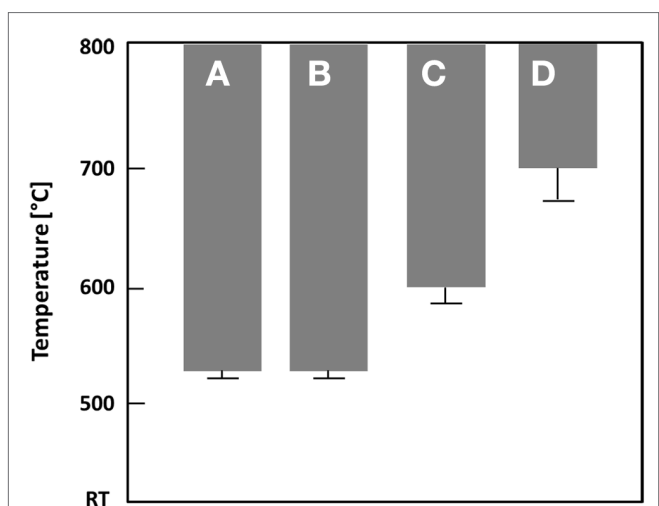
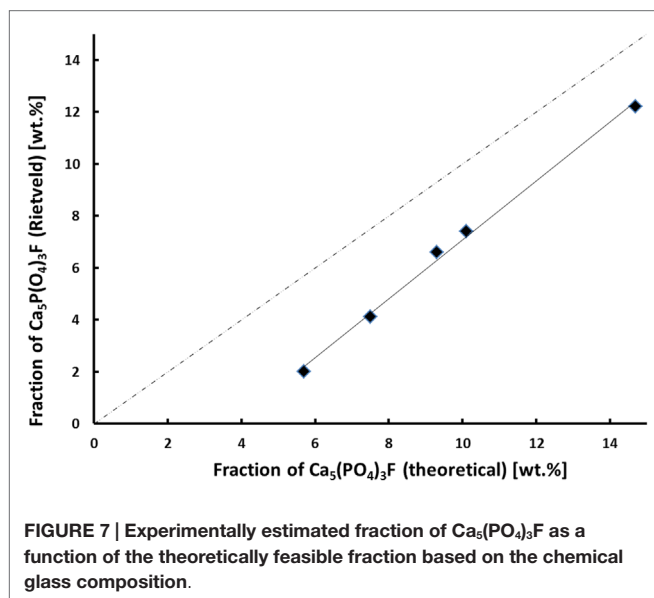


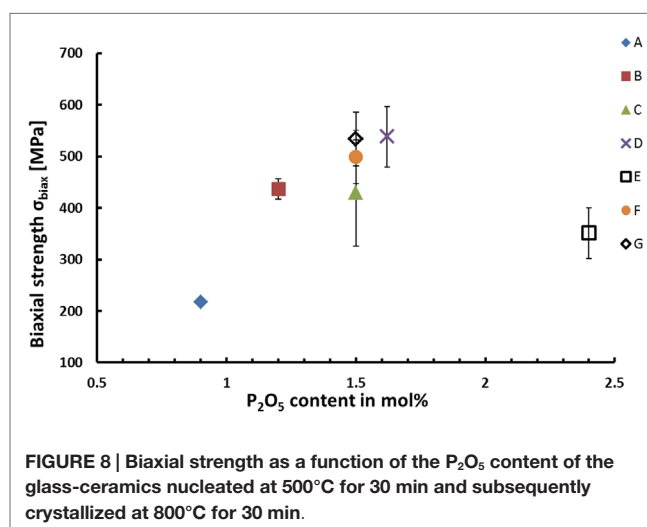
FIGURE 6 | Schematic summary of the phase formation sequence of $\text{Li}_2\text{Si}_2\text{O}_5$ (A), Li_2SiO_3 (B), Li_3PO_4 (C), and $\text{Ca}_5(\text{PO}_4)_3\text{F}$ (D) as a function of crystallization temperature for glass D after nucleation at 500°C for 30 min.

calculated. Figure 7 shows the actual percentage of $\text{Ca}_5(\text{PO}_4)_3\text{F}$ detected and estimated by means of powder XRD in combination with Rietveld refinement as a function of the theoretically possible fraction based on the chemical composition of the glasses. The content of fluoroapatite increases linearly with the increasing ratio of apatite-forming components. However, according to the slope



of the linear regression curve in **Figure 7**, the crystallization of fluoroapatite becomes more efficient with the increasing content of those components, since the difference between the theoretically estimated and the experimentally determined values decreases from approximately 3.7 to 2.5 wt.%. Similar to the hindering effect of F^- on the crystallization of Li_3PO_4 , discussed above, the latter could be explained by the formation of amorphous $\text{CaO-P}_2\text{O}_5\text{-F}$ rich phase separation sites within the glass microstructure. This phenomenon was already reported in the literature (Höland and Beall, 2012). Furthermore, a higher content of F^- , which acts as network modifier, increases the number of disconnecting points in the glass network (Vogel, 1994) and, thus, facilitates required diffusion processes. With regard to the sample series C and F, the significant shift of the first exothermal DSC signal to a lower temperature resulting from the addition of F^- could be further evidence for the enhancing influence of F^- on crystallization. Quasi isothermal crystallization or long-term crystallization experiments could help to gain valuable information on this topic.

High biaxial strengths of >500 MPa could be achieved for glass–ceramics containing more than 5 wt.% apatite. The experimental results prove that apatite could be precipitated as minor crystal phase in glass–ceramics without affecting the mechanical properties of these materials. The micrographs shown in **Figure 5** provide an indirect proof for the existence of a most probably needle-like, nanometer-scaled apatite phase randomly distributed within the $\text{Li}_2\text{Si}_2\text{O}_5$ microstructure. However, suited sample preparation parameters for the direct observation of apatite crystals in the present glass–ceramics have not yet been found. Nevertheless, the microstructural effects of $\text{Li}_2\text{Si}_2\text{O}_5$ crystals dominate the mechanical properties. The influence of their size and morphology on the strength of glass–ceramics have been established by various authors in a multitude of investigations (Cramer von Clausbruch et al., 2000; Höland et al., 2005; Apel et al., 2007, 2008; Zheng et al., 2008; Dittmer et al., 2014). In summary, a high volume fraction of interlocking lath-like $\text{Li}_2\text{Si}_2\text{O}_5$ crystals yields high-strength materials. The most efficient way of controlling



the microstructure of lithium disilicate glass–ceramics derived from bulk glasses is by means of internal nucleation sites, in most cases via the content of P_2O_5 (Cramer von Clausbruch et al., 2000; Höland et al., 2005). Similar to the results of numerous studies presented so far in the systems $\text{SiO}_2\text{-Li}_2\text{O-Al}_2\text{O}_3\text{-K}_2\text{O-(ZrO}_2\text{)-P}_2\text{O}_5$ (Höland et al., 2006; Höland and Beall, 2012), the findings of the present work clearly suggest the nucleating effect of the P_2O_5 content on the microstructure (**Figure 4**) and the biaxial strength as demonstrated in **Figure 8**. According to the mean values, there seems to be an optimum with respect to the biaxial strength which should be at approximately 1.6 mol% P_2O_5 . As presented in **Figure 4**, C, interlocking plate-like crystals in the range of approximately 1 μm yield the best results. Obviously, the microstructures of A (**Figure 4**, A) and E (**Figure 4**, E) were too coarse or too fine, respectively, for imparting good mechanical strengths to the glass–ceramic material.

Similar to the mechanical properties described above, the optical properties were mostly influenced by the morphology and size of $\text{Li}_2\text{Si}_2\text{O}_5$ crystals in the microstructure. Major effects on the translucency and opalescence can rather be correlated to the P_2O_5 content and, hence, the morphology and size of $\text{Li}_2\text{Si}_2\text{O}_5$ crystals, than to the content of fluoroapatite in the glass–ceramic. However, a study of the translucency of the $\text{Ca}_5(\text{PO}_4)_3\text{F}$ -comprising glass–ceramic C and the corresponding apatite-free material F revealed a certain effect of the apatite crystals on this optical property. Although the $\text{Li}_2\text{Si}_2\text{O}_5$ crystals visible in the micrograph of glass–ceramic F (**Figure 4**, F) are significantly larger than the ones found in C (**Figure 4**, C), glass–ceramic F exhibits a better translucency than C. This is in contrast to the literature and the knowledge about glass–ceramics and ceramics (Höland and Beall, 2012). One would expect to obtain improved translucency with finer microstructures, since scattering effects at interfaces or grain boundaries will decrease with decreasing sizes (Nassau, 2001). This effect appears especially for crystal sizes near or even below the wavelength spectrum of visible light and, hence, provides evidence that submicron-sized apatite crystals distributed within the $\text{Li}_2\text{Si}_2\text{O}_5$ -dominated microstructure introduce a further type of interface besides the one formed by $\text{Li}_2\text{Si}_2\text{O}_5$ as well as Li_3PO_4

crystals and the glass matrix. Optical reflection and scattering due to this additional type of phase boundary could explain the relatively high opacity of glass–ceramic C compared to that of F.

In summary and with respect to crystallization phenomena, the twofold precipitation of $\text{Li}_2\text{Si}_2\text{O}_5$ and $(\text{Ca}/\text{Sr})_5(\text{PO}_4)_3\text{F}$ provides a further means of precisely controlling the optical properties of lithium disilicate glass–ceramics, which is a prerequisite for the successful application of this material in prosthodontics. Of major importance is the fact that the precipitation of the minor phase can be specifically controlled without affecting the good mechanical and chemical properties of $\text{Li}_2\text{Si}_2\text{O}_5$ glass–ceramics, which are relevant to dental applications. Investigations that have been running in parallel to the present study have proved this to be true for the fracture toughness as well as the chemical durability.

Conclusion

The controlled precipitation of $(\text{Ca}/\text{Sr})_5(\text{PO}_4)_3\text{F}$ as a minor phase in $\text{Li}_2\text{Si}_2\text{O}_5$ -based glass–ceramics from bulk glasses via a solid-state reaction can be achieved by adding CaO/SrO , P_2O_5 , and F^- in multi-component base glasses.

References

- Apel, E., Deubener, J., Bernard, A., Höland, M., Müller, R., Kappert, H., et al. (2008). Phenomena and mechanism of crack propagation in glass–ceramics. *J. Mech. Behav. Biomed. Mater.* 1, 313–325. doi:10.1016/j.jmbbm.2007.11.005
- Apel, E., van 't Hoen, C., Rheinberger, V., and Höland, W. (2007). Influence of ZrO_2 in the crystallization and properties of lithium disilicate glass–ceramics derived from a multicomponent system. *J. Eur. Ceram. Soc.* 27, 1571–1577. doi:10.1016/j.jeurceramsoc.2006.04.103
- Bischoff, C., Eckert, H., Apel, E., Rheinberger, V., and Höland, W. (2011). Phase evolution in lithium disilicate glass–ceramics based in non-stoichiometric compositions of a multi-component system: structural studies by ^{29}Si single and double resonance solid state NMR. *Phys. Chem. Chem. Phys.* 13, 4540–4551. doi:10.1039/c0cp01440k
- Cramer von Clausbruch, S., Schweiger, M., Höland, W., and Rheinberger, V. (2000). The effect of P_2O_5 on the crystallization and microstructure of glass–ceramics in the SiO_2 – Li_2O – K_2O – ZnO – P_2O_5 system. *J. Non Cryst. Sol.* 263–264, 388–394. doi:10.1016/S0022-3093(99)00647-X
- Dittmer, M., Ritzberger, C., Schweiger, M., Rheinberger, V., Wörle, M., and Höland, W. (2014). Phase and microstructure formation and their influence on the strength of two types of glass–ceramics. *J. Non Cryst. Sol.* 384, 55–60. doi:10.1016/j.jnoncrsol.2013.03.009
- Headley, T. J., and Loehman, R. E. (1984). Crystallization of a glass–ceramic by epitaxial growth. *J. Am. Ceram. Soc.* 67, 620–625. doi:10.1111/j.1151-2916.1984.tb19606.x
- Höland, W., Apel, E., van't Hoen, C., and Rheinberger, V. (2006). Studies of crystal phase formation in high-strength lithium disilicate glass–ceramics. *J. Non Cryst. Sol.* 352, 4041–4050. doi:10.1016/j.jnoncrsol.2006.06.039
- Höland, W., and Beall, G. H. (2012). *Glass-Ceramic Technology*. Hoboken, NJ: Wiley.
- Höland, W., Frank, M., Schweiger, M., and Rheinberger, V. (1994). “Development of translucent glass–ceramics for dental applications,” in Proceedings of the 5th International Otto Schott Colloquium, ed. Rüssel C. (Frankfurt: Verlag der Deutschen Glastechnischen Gesellschaft), 117–121.
- Höland, W., Rheinberger, V., van 't Hoen, C., and Apel, E. (2005). P_2O_5 As an effective nucleating agent of lithium disilicate glass–ceramics. *Phosphorus Res. Bull.* 19, 36–41. doi:10.3363/prb1992.19.0_36
- The investigation of two different phase separation phenomena in the nucleated base glasses indicates the existence of chemically different P_2O_5 sites.
- A strong nucleating activity of amorphous or disordered nanocrystalline P_2O_5 on the crystallization of lithium silicate could be approved, while there is no evidence for the need of any crystalline heterogeneous phase for the nucleation of fluoro-apatite. Lithium silicate crystal phase formation starts ca. 160°C prior to the crystallization of $\text{Ca}_5(\text{PO}_4)_3\text{F}$. The authors conclude on the existence of two different solid-state reactions without competitive character.
- The quantity of apatite precipitated in the glass–ceramics is almost directly proportional to the content of apatite-forming components provided in the base glasses. The efficiency of apatite crystallization increases with the increasing content of CaO/SrO , P_2O_5 , and F^- .
- The mechanical and optical properties of the high-strength and chemically durable glass–ceramics are for the most part influenced by the morphology and size of the $\text{Li}_2\text{Si}_2\text{O}_5$ crystals. However, the precipitation of $\text{Ca}_5(\text{PO}_4)_3\text{F}$ or $\text{Sr}_5(\text{PO}_4)_3\text{F}$ facilitates the precise control of the translucency and opalescence which is a prerequisite for the successful application of the material in restorative dentistry.
- Höland, W., Rheinberger, V., Wegner, S., and Frank, M. (2000). Needle-like apatite-leucite glass–ceramic as a base material for the veneering of metal restorations in dentistry. *J. Mater. Sci. Mater. Med.* 11, 1–7. doi:10.1023/A:1008973800554
- Kuzielova, E., Hrubá, J., Palou, M., and Smrckova, E. (2006). Influence of P_2O_5 upon the crystallization of lithium disilicate and fluoroapatite in bio-glass ceramics. *Ceram. Silik.* 50, 159–162.
- Kobashigawa A. I. Angeletakis C. (2001). *Opalescent Fillers for Dental Restorative Composites*. US patent No 6,232,367 B1. Washington, DC: U.S. Patent and Trademark Office.
- Lee, Y. (2007). Influence of scattering/absorption characteristics on the color of resin composites. *Dent. Mater.* 23, 124–131. doi:10.1016/j.dental.2006.01.007
- Lee, Y., Lu, H., and Powers, J. (2005). Measurement of opalescence of resin composites. *Dent. Mater.* 21, 1068–1074. doi:10.1016/j.dental.2005.03.015
- Lee, Y., Lu, H., and Powers, J. (2006). Changes in opalescence and fluorescence properties of resin composites after accelerated aging. *Dent. Mater.* 22, 653–660. doi:10.1016/j.dental.2005.08.004
- Nassau, K. (2001). *The Physics and Chemistry of Color*. Hoboken, NJ: Wiley.
- Ritzberger, C., Schweiger, M., and Höland, W. (2015). Principles of crystal phase formation in ivoclar vivadent glass–ceramics for dental restorations. *J. Non Cryst. Sol.* (in press). doi:10.1016/j.jnoncrsol.2015.04.034
- Stookey, S. D. (1959). Catalyzed crystallization of glass in theory and practice. *Ind. Eng. Chem.* 51, 805–808. doi:10.1021/ie50595a022
- Vogel, W. (1963). *Struktur und Kristallisation der Gläser*. Leipzig: Verlag für Grundstoffindustrie.
- Vogel, W. (1994). *Glass Chemistry*. Berlin: Springer Verlag.
- Zheng, X., Wen, G., Song, L., and Huang, X. (2008). Effects of P_2O_5 and heat treatment on crystallization and microstructure in lithium disilicate glass ceramics. *Acta Mater.* 56, 549–558. doi:10.1016/j.actamat.2007.10.024

Conflict of Interest Statement: The authors are employees of the company Ivoclar Vivadent AG. A patent was filed on the present subject.

Copyright © 2015 Rampf, Dittmer, Ritzberger, Schweiger and Höland. This is an open-access article distributed under the terms of the Creative Commons Attribution License (CC BY). The use, distribution or reproduction in other forums is permitted, provided the original author(s) or licensor are credited and that the original publication in this journal is cited, in accordance with accepted academic practice. No use, distribution or reproduction is permitted which does not comply with these terms.



Radiopaque strontium fluoroapatite glass-ceramics

Wolfram Höland*, Marcel Schweiger, Marc Dittmer and Christian Ritzberger

Research and Development, Inorganic Chemistry, Technical Fundamentals, Ivoclar Vivadent AG, Schaan, Liechtenstein

OPEN ACCESS

Edited by:

Malcolm Xing,
University of Manitoba, Canada

Reviewed by:

Ashutosh Goel,
Rutgers, The State University of
New Jersey, USA
Piergiorgio Gentile,
University of Sheffield, UK

*Correspondence:

Wolfram Höland,
Research and Development,
Inorganic Chemistry, Technical
Fundamentals, Ivoclar Vivadent AG,
Benderstr. 2, Schaan FL 9494,
Liechtenstein
wolfram.hoeland@ivoclarvivadent.
com

Dedicated to Prof. Dr. Werner Vogel,
Jena, Germany, on the occasion of
his 90th birthday.

Specialty section:

This article was submitted to
Biomaterials, a section of the
journal *Frontiers in Bioengineering
and Biotechnology*

Received: 23 June 2015

Accepted: 15 September 2015

Published: 13 October 2015

Citation:

Höland W, Schweiger M, Dittmer M
and Ritzberger C (2015) Radiopaque
strontium fluoroapatite glass-
ceramics.
Front. Bioeng. Biotechnol. 3:149.
doi: 10.3389/fbioe.2015.00149

The controlled precipitation of strontium fluoroapatite crystals was studied in four base glass compositions derived from the $\text{SiO}_2\text{--Al}_2\text{O}_3\text{--Y}_2\text{O}_3\text{--SrO--Na}_2\text{O--K}_2\text{O/Rb}_2\text{O/Cs}_2\text{O--P}_2\text{O}_5\text{--F}$ system. The crystal phase formation of these glasses and the main properties of the glass-ceramics, such as thermal and optical properties and radiopacity were compared with a fifth, a reference glass-ceramic. The reference glass-ceramic was characterized as Ca-fluoroapatite glass-ceramic. The four strontium fluoroapatite glass-ceramics showed the following crystal phases: (a) $\text{Sr}_5(\text{PO}_4)_3\text{F}$ – leucite, KAlSi_2O_6 , (b) $\text{Sr}_5(\text{PO}_4)_3\text{F}$ – leucite, KAlSi_2O_6 , and nano-sized NaSrPO_4 , (c) $\text{Sr}_5(\text{PO}_4)_3\text{F}$ – pollucite, $\text{CsAlSi}_2\text{O}_6$, and nano-sized NaSrPO_4 , and (d) $\text{Sr}_5(\text{PO}_4)_3\text{F}$ – Rb-leucite, $\text{RbAlSi}_2\text{O}_6$, and nano-sized NaSrPO_4 . The proof of crystal phase formation was possible by X-ray diffraction. The microstructures, which were studied using scanning electron microscopy, demonstrated a uniform distribution of the crystals in the glass matrix. The Sr-fluoroapatites were precipitated based on an internal crystallization process, and the crystals demonstrated a needle-like morphology. The study of the crystal growth of needle-like Sr-fluoroapatites gave a clear evidence of an Ostwald ripening mechanism. The formation of leucite, pollucite, and Rb-leucite was based on a surface crystallization mechanism. Therefore, a twofold crystallization mechanism was successfully applied to develop these types of glass-ceramics. The main focus of this study was the controlled development of glass-ceramics exhibiting high radiopacity in comparison to the reference glass-ceramic. This goal could be achieved with all four glass-ceramics with the preferred development of the Sr-fluoroapatite – pollucite-type glass-ceramic. In addition to this main development, it was possible to control the thermal properties. Especially the Rb-leucite containing glass-ceramic showed the highest coefficient of thermal expansion (CTE). These glass-ceramics allow optical properties, especially the translucency and color, to be tailored to the needs of biomaterials for dental applications. The authors conclude that it is possible to use twofold crystallization processes to develop glass-ceramic biomaterials featuring different properties, such as specific radiopacity values, CTEs, and optical characteristics.

Keywords: glass-ceramics, phosphate crystals, nucleation and crystallization, crystal growth, Ostwald ripening, radiopacity, dental restoration, biomaterial

Introduction

The precipitation of fluoroapatites, in glass-ceramics using the methods of controlled nucleation and crystallization of glasses, is well known. Fluoroapatite glass-ceramics were reported by Clifford and Hill (1996) and Moisescu et al. (1999). Furthermore, bioactive glass-ceramics, which bond to living bone, contain fluoroapatite crystals. Such a product was developed by Kokubo (1991) who applied the method of twofold nucleation to create a fluoroapatite–wollastonite glass-ceramic. Dejneka and Pinckney (1998) developed fluoroapatite glass-ceramics with special optical properties. All these different types of apatite glass-ceramics were discussed and described on the basis of their chemical nature and microstructure formation by Höland and Beall (2012). Höland et al. (2004) reported on the formation of Sr-fluoroapatite glass-ceramics with the possibility of forming a primary crystal phase of NaSrPO₄. Moreover, van't Hoen et al. (2007) also succeeded in growing different types of siliceous oxyapatites in glass-ceramics. The substitution of different ions in fluoroapatite-type glass-ceramics was studied by Chen et al. (2014) and Hill et al. (2004, 2010) with the aim of developing strontium fluoroapatite and chlorapatite-type glass-ceramics. The development of an aluminosilicate glass-ceramic of the pollucite-type (CsAlSi₂O₆) was achieved by Beall and Rittler (1982). Twofold nucleation and crystallization of both leucite (KAlSi₂O₆) and Ca-fluoroapatite (Ca₅(PO₄)₃F) was reported by Höland et al. (1994, 2000, 2004, 2008). The growth of needle-like Ca₅(PO₄)₃F crystals was discovered as an Ostwald ripening process by Müller et al. (1999) and Höland et al. (2000) and in a different chemical system by Höche et al. (2001).

Radiopaque glasses are known as glass ionomer cements in dentistry (Tsuge, 2009). Also, glass-ceramics were developed as radiopaque materials in inorganic–organic composites as dental fillers. Müller (1973) succeeded in developing such a glass-ceramic with high contents of La₂O₃. The purpose of the present study was to develop a glass-ceramic with high radiopacity and additional properties of controlled translucency and special coefficients of thermal expansion.

Fundamental research on the nucleation process of phosphosilicate glass-ceramics showed the special function of glass-in-glass phase separation. The basis for these processes of controlled immiscibility in glasses on the way to forming glass-ceramics via controlled nucleation and crystallization was established by Vogel (1963, 1985) and discussed in detail by Kreidl (1983). This phenomenon of microstructure formation provided a basis for the development of many different types of glass-ceramics. Building on these fundamentals, Vogel and Höland (1987) developed a phosphosilicate base glass consisting of three glassy phases: two droplet phases and a glass matrix. By annealing this glass in a controlled way, the precipitation of two crystal phases was possible: the mica-type and the calcium fluoroapatite crystals. This established the basis for the development of a bioactive biomaterial for bone substitution.

Nevertheless, the authors of this manuscript will neither focus on bioactive glass-ceramics nor on glass-ceramics for technical application. Their main aim is to develop glass-ceramics

as biomaterials for applications in restorative dentistry. In the development of new dental restorative biomaterials (e.g., materials for dental inlays, onlays, or crowns), new properties are explored, for example, how to make it easier for dental practitioners to detect the interface between the biomaterial and the natural tooth very precisely. In order to enable such a distinction, the radiopacity of the biomaterial could be increased, for example.

For this purpose, the authors selected four glass compositions derived from the SiO₂–Al₂O₃–Y₂O₃–SrO–Na₂O–K₂O/Rb₂O/Cs₂O–P₂O₅–F system. They studied the processes of nucleation and crystallization of strontium fluoroapatite and additional crystal phases designed the microstructure of the glass-ceramics and determined the main properties of these types of glass-ceramics with the aim of controlling the radiopacity and to develop additional properties (optical, thermal).

In addition to these four selected glass-ceramics, a fifth glass-ceramic composition was prepared, which was free of Y₂O₃, SrO, Cs₂O, and Rb₂O. However, this composition contained CaO to allow the precipitation of calcium fluoroapatite, Ca₅(PO₄)₃F crystals. This experimental, not commercial glass-ceramic was used as a reference material, primarily for the radiopacity study.

Materials and Methods

Processing and Chemical Compositions

Four compositions of base glasses were selected to develop the new glass-ceramics. As mentioned, the glasses were derived from the chemical SiO₂–Al₂O₃–Y₂O₃–SrO–Na₂O–K₂O/Rb₂O/Cs₂O–P₂O₅–F system, but with additives of small amounts of ZrO₂, TiO₂, CeO₂, B₂O₃, and Li₂O. The chemical compositions are shown in **Table 1**.

As a reference to these four compositions, a fifth base glass was used, which was derived from the chemical SiO₂–Al₂O₃–CaO–Na₂O–K₂O–P₂O₅–F system with additives of small amounts of

TABLE 1 | Chemical composition in wt.-% and (mol.-%) of the base glasses used to develop glass-ceramics.

	1	2	3	4	5 (Reference)
SiO ₂	47.0 (58.7)	48.6 (59.4)	44.6 (60.4)	49.0 (61.1)	59.3 (66.0)
Al ₂ O ₃	12.2 (9.0)	12.6 (9.1)	11.3 (9.0)	12.4 (9.1)	13.0 (8.5)
Y ₂ O ₃	9.2 (3.1)	6.2 (2.2)	0.4 (0.1)	0.4 (0.1)	
La ₂ O ₃			1.1 (0.3)		
CaO					1.5 (1.8)
SrO	7.5 (5.5)	7.8 (5.5)	10.1 (7.9)	8.1 (5.9)	
ZnO					1.6 (1.3)
Na ₂ O	8.3 (10.1)	8.6 (10.2)	6.4 (8.4)	8.3 (10.0)	8.2 (8.9)
K ₂ O	9.4 (7.5)	9.7 (7.6)	3.0 (2.6)	3.4 (2.7)	9.0 (6.4)
P ₂ O ₅	3.4 (1.8)	3.4 (1.8)	3.1 (1.8)	3.3 (1.7)	0.4 (0.2)
F	0.6 (2.4)	0.6 (2.3)	0.6 (2.6)	0.6 (2.4)	0.9 (3.2)
Cs ₂ O			17.1 (4.9)		
Rb ₂ O				12.0 (4.8)	
ZrO ₂	0.8 (0.5)	0.9 (0.5)	0.7 (0.5)	0.9 (0.6)	3.8 (2.1)
TiO ₂	0.2 (0.2)	0.2 (0.2)	0.2 (0.2)	0.2 (0.2)	1.4 (1.2)
CeO ₂	0.9 (0.4)	0.9 (0.4)	0.9 (0.4)	0.9 (0.4)	0.8 (0.3)
B ₂ O ₃	0.3 (0.3)	0.3 (0.3)	0.3 (0.4)	0.2 (0.2)	0.1 (0.1)
Li ₂ O	0.2 (0.5)	0.2 (0.5)	0.2 (0.5)	0.3 (0.8)	

ZnO, ZrO₂, TiO₂, CeO₂, and B₂O₃ (**Table 1**). The basis for the design of the chemical compositions follows the ideas:

- To study the influence of an increase of Y₂O₃ in glass-ceramics 1 and 2 over the reference sample 5.
- To investigate the influence of relatively high contents of Cs₂O (glass 3) and Rb₂O (glass 4) over glass-ceramics 5, 1 and 2.
- The additives of many other components to the glass-ceramics (especially the alkali ions) were necessary to reach the best melting conditions for the base glasses and an optimum of sintering to produce dense powder compacts.

The glasses were molten based on the raw materials of SiO₂, TiO₂, ZrO₂, CeO₂, Y₂O₃, aluminum-oxyhydroxy hydrate, carbonates of sodium, potassium, rubidium, cesium, strontium, calcium, magnesium, lithium, aluminum metaphosphate, sodium fluoride, and boron oxide hydrate. The melt was carried out in a platinum crucible and the conditions used were 1600°C with a melting time of 2 h.

The main aim of this study was to produce glass-ceramics via the powder compact route, which has been discussed in detail by Höland and Beall (2012). The reason for applying this method was the ability to take advantage of a twofold nucleation and crystallization process involving both surface and internal mechanisms. This is the same methodology which is applied to produce leucite-fluoroapatite glass-ceramics (Höland et al., 2000). After melting the glasses, the process was started by pouring the hot melt into water and drying the produced glass frits. The glass frits were investigated by X-ray diffraction (XRD). Next, the frits were ground by ball milling to a grain size of <90 µm to a mean grain size of approximately 35 µm. Subsequently, the glass granules were heat treated at 900°C, and in a separate sample preparation to 1000°C for 1 h. After these heat treatments, all the samples were ground again to a grain size of approximately 35 µm. This process was followed by the final process of powder compact preparation. This was carried out in the Programat® P700 furnace (Ivoclar Vivadent AG) under a vacuum of 20–25 mbar and at a heating rate of 40 K/min at different temperatures:

- Disks with a diameter of 20 mm and a thickness of 2 mm for scanning electron microscopy (SEM) studies and optical measurements, and 1 mm thickness for determining the radiopacity:
 - glass-ceramic 1: 960°C for 1 min
 - glass-ceramic 2: 940°C for 1 min
 - glass-ceramic 3: 1150°C for 1 min
 - glass-ceramic 4: 1030°C for 1 min
 - glass-ceramic 5: 960°C for 1 min
- Bars (27 mm × 5 mm × 4 mm) for measuring the coefficients of thermal expansion:
 - glass-ceramic 1: 940 and 960°C for 1 min
 - glass-ceramic 2: 920 and 940°C for 1 min
 - glass-ceramic 3: 1130 and 1150°C for 1 min
 - glass-ceramic 4: 1010 and 1030°C for 1 min
 - glass-ceramic 5: 940 and 960°C for 1 min.

These different temperatures were selected from a great variety of trials to reach the best condition of dense powder compact preparation. In order to study the microstructure of the base glasses by SEM and to investigate the internal crystal growth mechanism (without additional surface crystallization), however, monolithic samples were prepared. Therefore, in a separate processing step, portions of the glass melt were cast on a copper plate and cooled to room temperature, with a cooling range of 3–5 K/min from the T_g range to room temperature. The surface of the samples was removed by grinding and the volume was investigated by SEM and XRD.

These monolithic samples were also used to study the crystal growth of Sr-fluoroapatite (Sr₅(PO₄)₃F). This procedure allowed the analysis of the crystallization mechanism of the internally formed crystals without the influence of the surface crystallization mechanism. However, in order to compare these results with the growth of needle-like Ca₅(PO₄)₃F in a different chemical glass-ceramic system (Höland et al., 1994, 2000), the growth of crystals was studied at 1000°C. For this purpose, the glass-ceramic No. 2 was annealed at 1000°C for different times: 30, 60, 120, 240 and 480 min. The resulting microstructures were studied with SEM, and the crystal numbers, crystal lengths, and crystal diameters were determined and plotted as functions of time.

Methods

The chemical compositions of all the base glasses were analyzed by X-ray fluorescence (XRF) using Tiger S8, Bruker AXS, Karlsruhe, Germany with regard to the main constituents. However, Li₂O and B₂O₃ were determined according to atomic absorption spectrometry (AAS) using HT-200, Varian, Darmstadt, Germany. Fluorine was analyzed using the fluoride selective electrode method. All these compositions are shown in **Table 1**.

The determination of the T_g values of the glasses was studied by means of differential scanning calorimetry (DSC). These DSC investigations of glass grains were carried out with the apparatus STA 449 F3 (Netzsch, Germany) using a heating rate of 10 K/min and N₂ atmosphere.

The microstructures of the monolithic base glasses and the powder compact glass-ceramic samples were studied by means of scanning electron microscopic, SEM, investigations of etched samples. Mainly HF etching (aqueous 3% HF solution, for 10 s) was used in addition to etching with H₃PO₄. The SEM investigations were carried out with the apparatus Supra 40VP (Carl Zeiss, Oberkochen, Germany).

The crystal phase was successfully analyzed by XRD, with the D8 Advance device using a LYNXEYE detector and Cu–K_α radiation (Bruker, Karlsruhe, Germany).

Thermal properties as T_g values of the glasses and the coefficients of thermal expansion (CTEs) of the powder compact glass-ceramics were determined. The T_g values were established as important characteristics (fixed point) of glasses using DSC STA 449 Netzsch (Selb, Germany). The T_g points were determined as onset points of the DSC peaks. The CTE parameters were analyzed by using the apparatus TA Instruments DIL Type 803 (Hüllhorst, Germany) (formerly Bähr).

The optical properties in terms of L^* , a^* , b^* values according to DIN5033 and DIN6174 were established with a CM-3700d

Spectrometer (Konica Minolta). The optical values of CR were determined according the British Standard 5612. A value of 100 would represent a 100% opaque product and the value 0 a material that is transparent in visible light.

The radiopacity was characterized on sintered samples with a diameter of 20 mm and a thickness of 1 mm. The specific radiopacity was analyzed according to EN ISO 4049. The radiopacity values were calculated on the basis of the gray shade of the radiograph in comparison to an aluminum standard. The radiographs were taken with a Heliodent^{plus} X-ray system (Sirona, Bensheim, Germany) on a Carestream CS7600 No. 2 imaging plate (Carestream Dental, Atlanta, GA, USA). The evaluation of the specific gray shade was done with the Adobe® Photoshop software (Adobe® Systems, San José, CA, USA).

Results

Base Glasses

The monolithic base glasses No. 1 and 5 were optically transparent in visible light, while the other glasses No. 2–4 showed an opalescent effect. But XRD studies of all four monolithic glass samples, showed the formation of primary crystal phases, precipitated during cooling of the glass melts. The microstructures of these glasses No. 1–4 were characterized by nano-sized spherical crystals of different types: nano-sized $\text{Sr}_5(\text{PO}_4)_3\text{F}$ crystals in glasses No. 1 and 2 (with a very minor content of NaSrPO_4 in glass No. 2) and nano-sized NaSrPO_4 crystals in glasses No. 3 and 4. The crystals were analyzed by XRD. The general formation of NaSrPO_4 was described by Bredig (1942). **Figure 1** shows the approximately 50 nm crystals [mainly $\text{Sr}_5(\text{PO}_4)_3\text{F}$ with minor NaSrPO_4], which have precipitated in glass No. 2 in isolated form in the glass matrix. Heat treating these samples at 600 or 700 or 800°C for 1 h did not change the microstructure.

Using a H_3PO_4 etching procedure, the crystals were etched away and holes of approximately 50 nm were visible in the SEM

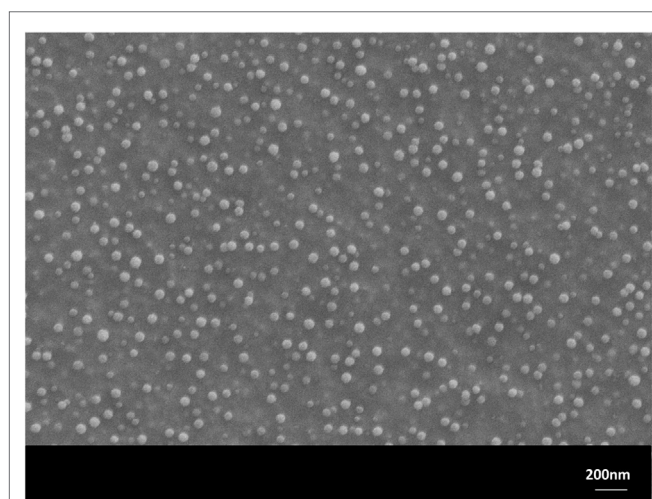


FIGURE 1 | Microstructure of glass No. 2 after 1 h heat treatment at 600°C. $\text{Sr}_5(\text{PO}_4)_3\text{F}$ (with minor NaSrPO_4) spherical crystals of nanometer size are visible. Monolithic sample, polished surface, HF etched. SEM.

micrograph. The glass frits No. 1–4, which were produced by pouring the hot melt into water (representing a fast cooling rate), were also investigated by XRD. All these glasses contained nano-sized crystals. Glasses No. 1 and 2 showed $\text{Sr}_5(\text{PO}_4)_3\text{F}$ crystals (glass two with a minor content of NaSrPO_4) and glasses No. 3 and 4 showed NaSrPO_4 crystals. But the base glass No. 5, the reference sample, was a crystal-free material, and was produced either as a monolithic sample or a frit.

The glass frits were also used to determine the T_g values of the glasses, that is the glass matrices with the nano-sized crystals. These characteristic T_g values were detected between 570 and 670°C (glass No. 1: 658°C, glass No. 2: 627°C, glass No. 3: 565 No. 4: 568°C, glass No. 5: 588°C, all with an error margin of ± 3 K) according to **Figure 2**. These values gave hints for further heat treatment cycles to control the crystallization processes in a range from 800 to 1000°C.

Microstructure Formation of Glass-Ceramics

Scanning electron microscopy studies allowed the characterization of the design of the powder compact glass-ceramics and XRD enabled the determination of the type of crystal phases. The main crystal phase formation and the design of the microstructure of the glass-ceramics are shown in **Figures 3–7**.

The microstructures shown in the SEMs in **Figures 3–7** have to be interpreted on the basis of the preparation method of HF etching and in correlation with the XRD studies. HF treatment of these types of glass-ceramics results in the etching of the SiO_2 -rich glass matrix and especially the interface of the glass surrounding the aluminosilicate or phosphate crystals. With regard to the aluminosilicates, therefore, the interface between the crystals and the glass matrix was etched away and as a consequence the crystals fell out of the surface of the glass-ceramic. As a result, holes were created in the surface of the sample, and these holes represent the size of the aluminosilicate crystals.

The phosphate-rich crystals, however, were not etched by the aqueous HF solution. Instead, the SiO_2 -rich matrix was etched. Therefore, the phosphate crystals ended up protruding from the surface. Based on these SEM and XRD findings, the microstructures of the glass-ceramics No. 1 to 5 show microstructure design according **Figures 3–7** with the specific crystal phases demonstrated in **Table 2** and **Figure 8**.

The crystal phases were determined according to the following XRD reference pattern:

- strontium fluoroapatite ($\text{Sr}_5(\text{PO}_4)_3\text{F}$): PDF 00-050-1744
- leucite (KAlSi_2O_6) phase: PDF 00-038-1423) (see also **Figure 8**)
- sodium strontium orthophosphate (NaSrPO_4): PDF 00-033-1282
- pollucite ($\text{CsAlSi}_2\text{O}_6$): PDF 00-029-0407
- rubidium leucite (RbSi_2O_6): PDF 00-029-1077
- calcium fluoroapatite ($\text{Ca}_5(\text{PO}_4)_3\text{F}$): PDF 01-074-4390

The crystal growth of needle-like $\text{Sr}_5(\text{PO}_4)_3\text{F}$ in the monolithic (no powder compact preparation) glass-ceramic No. 2, annealed at 1000°C, is demonstrated in **Figures 9A–C** in respect to the number of crystals, the crystal length, and the diameter of the crystals as

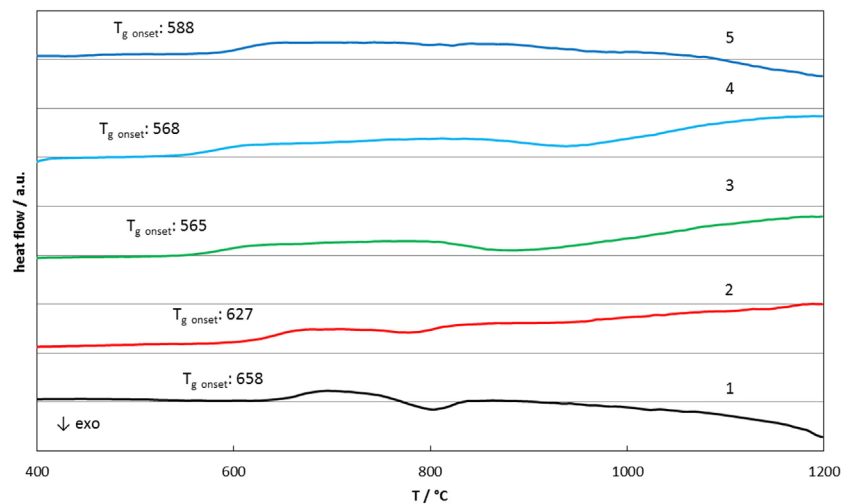


FIGURE 2 | Differential scanning calorimetry results of glasses 1–5.

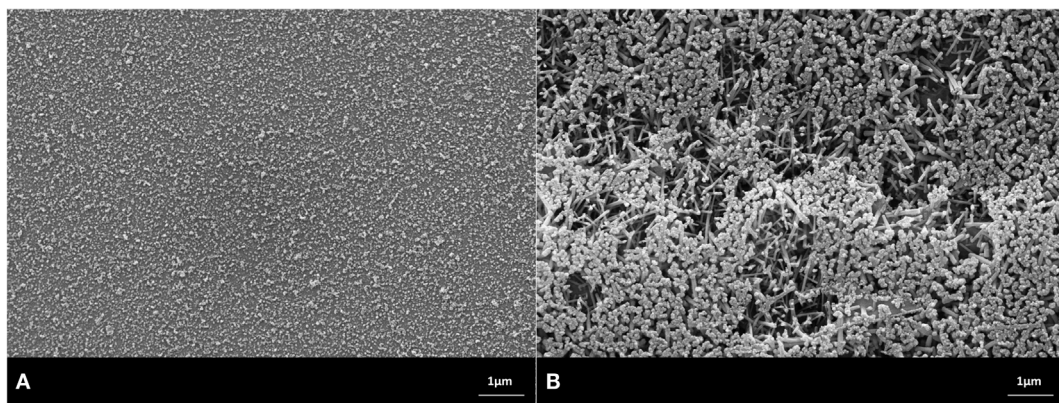


FIGURE 3 | Microstructures of heat-treated glass frits of composition No. 1, processed at (A) 900°C/h, (B) 1000°C/h. Fractured surface, HF etched sample (10 s, 3% HF). SEM. (A) Glass-ceramic with the crystal phase of $\text{Sr}_5(\text{PO}_4)_3\text{F}$. (B) Glass-ceramic containing crystals of $\text{Sr}_5(\text{PO}_4)_3\text{F}$ and KAlSi_2O_6 .

functions of time (30 min up to 480 min). The **Figures 9A–C** show characteristics of functional relationships. The first relation involves a decrease of the number of crystals with increasing annealing time (**Figure 9A**). The second function demonstrates the growth of crystals in length with increasing time (**Figure 9B**) and the third shows the increase of the crystal diameter with increasing time. The errors are shown as SDs in **Figures 9B,C**. A typical microstructure of this investigation is shown in **Figure 10**, demonstrating the microstructure of the needle-like strontium fluoroapatite glass-ceramic after annealing at 1000°C for 30 min.

Processing of the final products of powder compacts proceeded according to the procedure reported in Section “Processing and Chemical Compositions.” According to this procedure, these glass-ceramics prepared from glass frits at 900°C for 1 h, whose microstructures are shown in **Figures 3A, 4A, 5A, 6A** and 7, were ground and additionally heat treated. The temperatures of

the additional heat treatment were also mentioned in Section “Processing and Chemical Compositions.” These temperatures were selected to produce dense powder compacts. Lower temperatures than these did not allow the preparation of dense compacts. During this additional heat treatment, another surface crystallization process was discovered on the surface of the sintered glass grains of glass-ceramics No. 1 and 2: leucite crystals were formed. The proof of such a process could be demonstrated with SEM and XRD studies.

Properties of the Glass-Ceramics Thermal Properties

Table 3 shows the CTE values of glass-ceramics No. 1–5. The characteristic values cover a wide range from 10.9 to $19.4 \times 10^{-6} \text{ K}^{-1}$. The reference sample shows the lowest CTE value of $8.9 \times 10^{-6} \text{ K}^{-1}$.

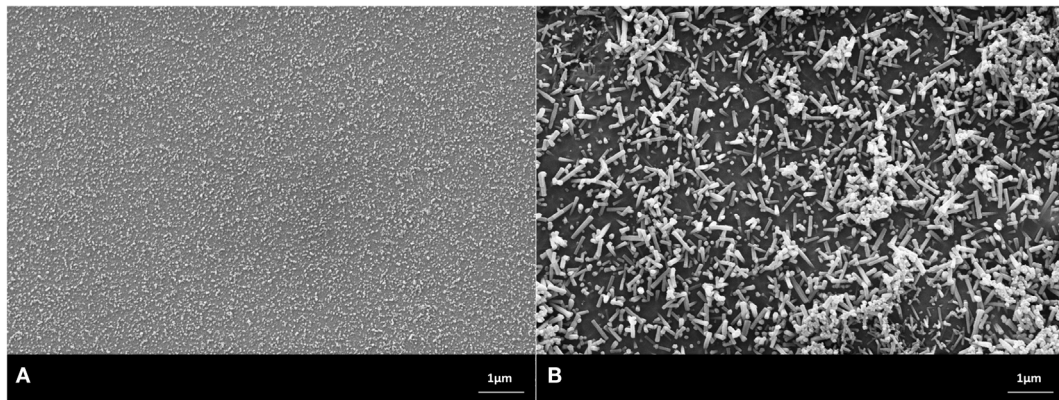


FIGURE 4 | Microstructures of heat-treated glass frits of composition No. 2, processed at (A) 900°C/h, (B) 1000°C/h. Fractured surface, HF etched sample (10 s, 3% HF). SEM. **(A)** Glass-ceramic with the crystal phase of $\text{Sr}_5(\text{PO}_4)_3\text{F}$ and a minor content of NaSrPO_4 . **(B)** Glass-ceramic containing crystals of $\text{Sr}_5(\text{PO}_4)_3\text{F}$, KAlSi_2O_6 , and a minor content of NaSrPO_4 .

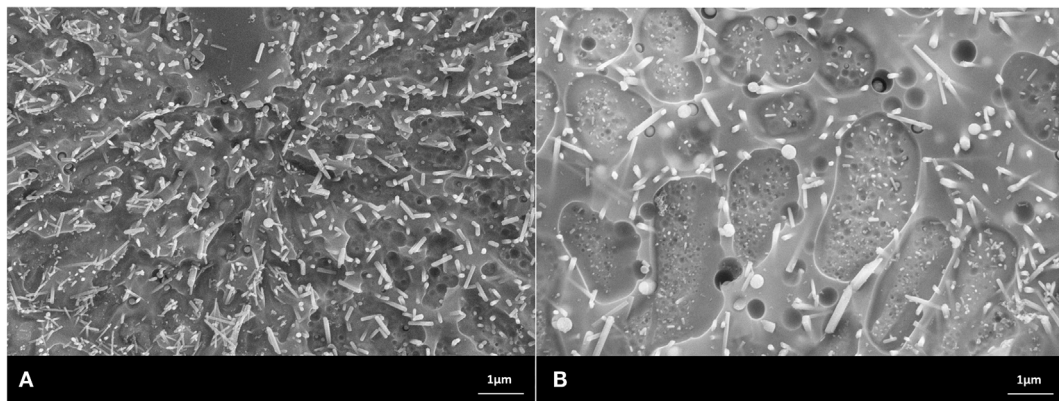


FIGURE 5 | Microstructures of heat-treated glass frits of composition No. 3, processed at (A) 900°C/h, (B) 1000°C/h. Fractured surface, HF etched sample (10 s, 3% HF). SEM. **(A,B)** Glass-ceramics with crystal phases of $\text{Sr}_5(\text{PO}_4)_3\text{F}$, $\text{CsAlSi}_2\text{O}_6$, and NaSrPO_4 .

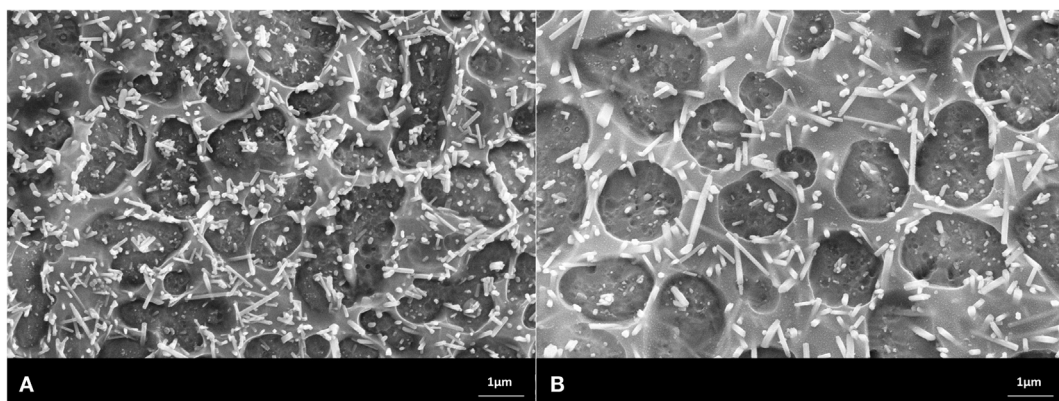
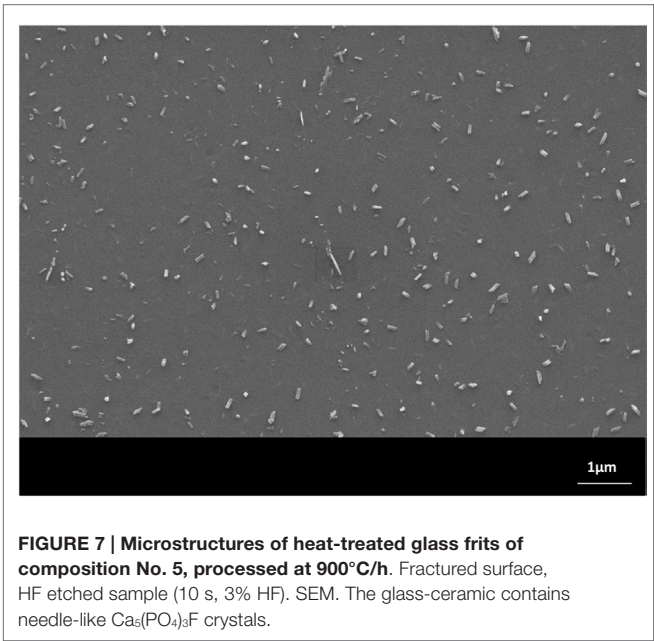


FIGURE 6 | Microstructures of heat-treated glass frits of composition No. 4, processed at (A) 900°C/h, (B) 1000°C/h. Fractured surface, HF etched sample (10 s, 3% HF). SEM. **(A,B)** Glass-ceramics with crystal phases of $\text{Sr}_5(\text{PO}_4)_3\text{F}$, $\text{RbAlSi}_2\text{O}_6$, and NaSrPO_4 .



Optical Properties

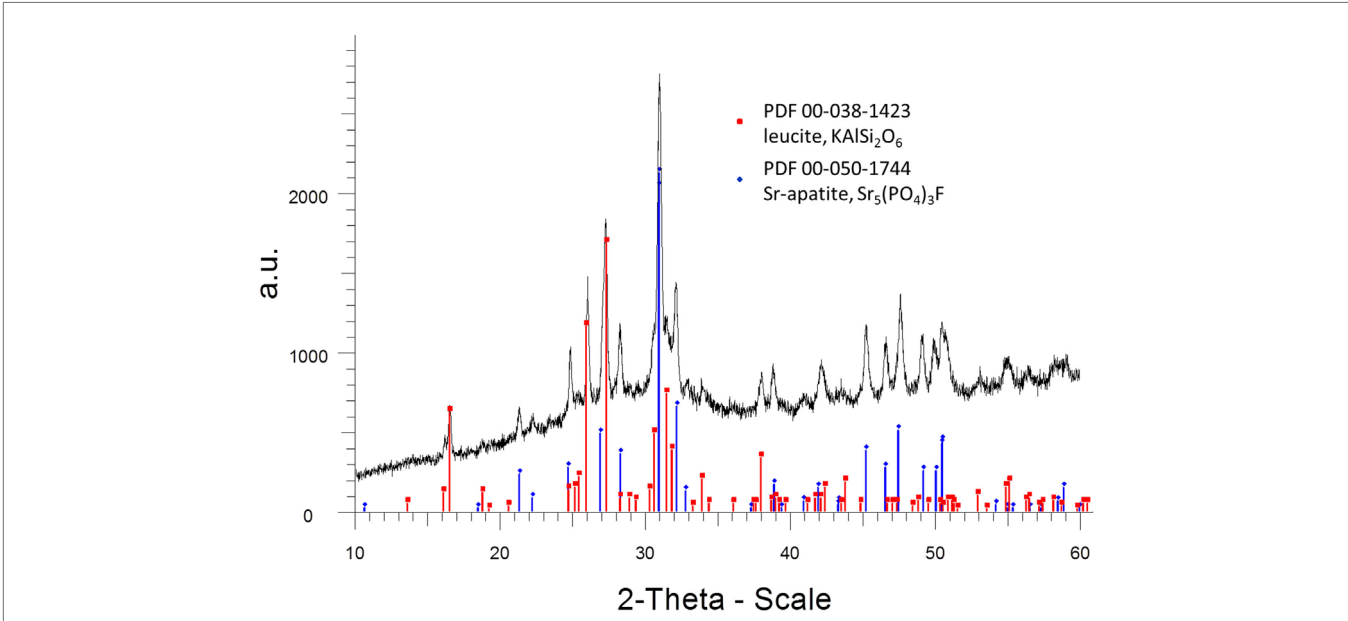
Qualitatively, the glass-ceramics could be characterized as yellowish translucent (glass-ceramic No. 1, 2, and 5) and white with low translucency (glass-ceramic No. 3 and 4). The quantitative values are shown in **Table 3**. The colors are represented by the L^* , a^* , b^* parameters and the translucency is given with the CR values. The glass-ceramics No. 1 and 2, which were processed from a glass frit at 900°C for 1 h and prepared from this glass-ceramic to form a powder compact at 960°C (glass-ceramic No. 1) and 940°C (glass-ceramic No. 2), were developed as Sr-fluoroapatite – leucite glass-ceramics. These products show the highest translucency in comparison to glass-ceramics No. 3 and 4 (Sr-fluoroapatite – pollucite, and Sr-fluoroapatite – Rb-leucite glass-ceramics).

Radiopacity

The radiopacity of the glass-ceramics No. 1 and 2 (Sr-fluoroapatite – leucite glass-ceramics) could be increase by a factor of three in comparison to the reference sample glass-ceramic No. 5 of the Ca-fluoroapatite-type. But a much higher increase of radiopacity could be reached by the development of

TABLE 2 | Main crystal formation in glass-ceramics at 900 and 1000°C/h.

Glass-ceramic	Crystal phases after heat treatment of 900°C/h	Crystal phases after heat treatment of 1000°C/h
1	$\text{Sr}_5(\text{PO}_4)_3\text{F}$, 100 nm in length (Figure 3A)	$\text{Sr}_5(\text{PO}_4)_3\text{F}$, 800 nm in length and KAlSi_2O_6 , size 1 μm (holes in Figure 3B)
2	$\text{Sr}_5(\text{PO}_4)_3\text{F}$, >100 nm in length, minor NaSrPO_4 (Figure 4A)	$\text{Sr}(\text{PO}_4)_3\text{F}$, KAlSi_2O_6 (Figures 4B and 8)
3	$\text{Sr}_5(\text{PO}_4)_3\text{F}$, $\text{CsAlSi}_2\text{O}_6$, minor NaSrPO_4 (Figure 5A)	$\text{Sr}_5(\text{PO}_4)_3\text{F}$, $\text{CsAlSi}_2\text{O}_6$, minor NaSrPO_4 (Figure 5B)
4	$\text{Sr}_5(\text{PO}_4)_3\text{F}$, RbSi_2O_6 , minor NaSrPO_4 (Figure 6A)	$\text{Sr}_5(\text{PO}_4)_3\text{F}$, RbSi_2O_6 , minor NaSrPO_4 (Figure 6B)
5	$\text{Ca}_5(\text{PO}_4)_3\text{F}$ (400–600 nm in length) (Figure 7)	



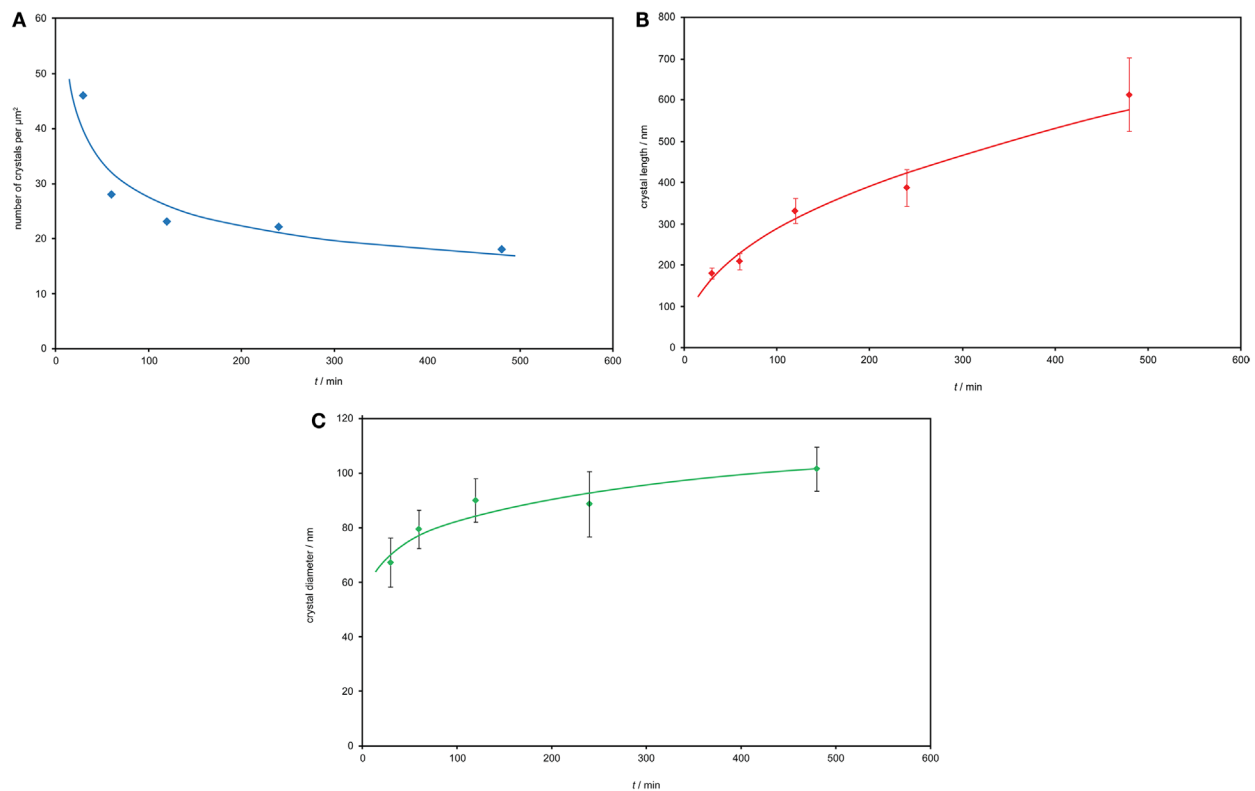


FIGURE 9 | Crystal growth of needle-like $\text{Sr}_5(\text{PO}_4)_3\text{F}$ at 1000°C in the monolithic glass-ceramic No. 2. **(A)** Crystal number – time function. **(B)** Crystal length – time relationship. **(C)** Crystal diameter – time function.

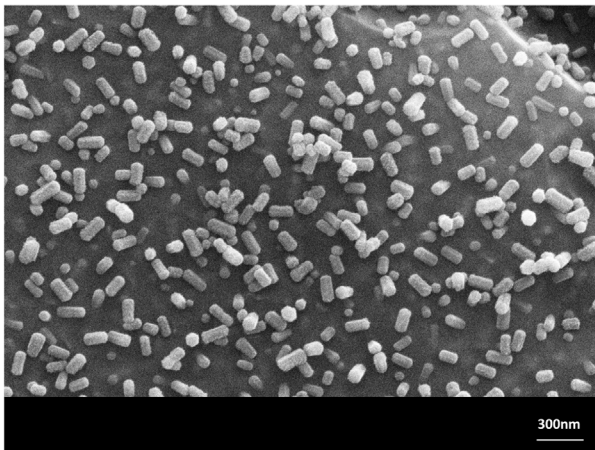


FIGURE 10 | Microstructure of the monolithic glass-ceramic No. 2 annealed at 1000°C for 30 min. Needle-like $\text{Sr}_5(\text{PO}_4)_3\text{F}$ crystals were growing. SEM, HF etched surface.

Sr-fluoroapatite-pollucite type glass-ceramics (glass-ceramic No. 3). The increase of radiopacity in comparison to the reference glass-ceramics represents a factor of five (Table 3).

Discussion

Vogel (1963, 1985) established the fundamentals of controlled nucleation via glass-in-glass phase separation and used this knowledge to develop glass-ceramics combining a number of different properties. In his studies, he showed the possibilities of glass-in-glass phase separation of different glass-forming systems. His main and unexpected discovery was finding a way to control these processes in glass systems with different glass network formers. His expertise focused on controlling the micro-immiscibility in phosphosilicate glasses. The authors of this paper applied these fundamentals established by Vogel to control the nucleation in a nano-scaled microstructure. That is, the authors of this paper used the nano-glass-in-glass phase separation as a primary stage of the internal nucleation process, which was followed by the internal crystal phase formation and crystal growth of uniform phases in the volume of the glass-ceramics.

In the selected base glasses, the glass-in-glass phase separation proceeded in different ways, according to their chemical nature, which is different to that reported by Hill et al. (2010). In glasses No. 1–4, the process of amorphous glass-in-glass phase separation took place very rapidly during the cooling of the glass melt to room temperature. This led to the precipitation of nano-scaled $\text{Sr}_5(\text{PO}_4)_3\text{F}$ in glasses No. 1 and 2. These nano-sized crystals show

TABLE 3 | Main properties of the final glass-ceramics prepared as powder compacts.

Glass-ceramic	CTE _(100–400°C) 10 ^{−6} ·K ^{−1}	Optical properties				Radiopacity % Ratio related to Al
		L*	a*	b*	CR	
1	13.4	85.2	−1.0	20.10	62.9	350
2	12.6	88.4	−1.3	15.4	59.8	316
3	10.9	94.4	−1.7	6.0	82.5	500–550
4	19.4	94.4	−1.6	5.3	85.1	395
5	8.9	84.2	1.6	11.5	56.9	104

a spherical shape, which indicates that crystal formation takes place within an amorphous glass droplet during the cooling of the melt. These crystals grow in needle-like morphology at high temperatures of 1000°C.

The crystal growth process of the needle-like Sr₅(PO₄)₃F follows an Ostwald ripening mechanism as demonstrated in **Figures 9A–C** for glass-ceramic No. 2 in a monolithic sample. That is, the number of crystals per volume [but determined per area, which can be transformed to volume terms according to DeHoff and Aigeltinger (1970) and Toshev and Gutzow (1967)] decreases as a function of time, while the diameter and length of the crystals grow. Therefore, fundamentals of the theory of Ostwald ripening [reported by Slezov (2009) and Gutzow and Schmelzer (2013)] are fulfilled: The thermodynamically driving force of the process is the reduction of the surface of the crystals by reducing the number of crystals and growing of larger ones. During this process, the total amount of the new phase remains constant but the Gibbs free energy decreases. In more detail, it could be shown that the number of crystals is inversely proportional to the time of annealing (**Figure 9A**) to some power (−p). In a first approximation, the authors could determine a relationship of the number of crystals per surface area of the sections through the sample, N_s , to the time, t , of annealing, according to Eq. 1.

$$N_s \sim t^{-p} \quad (1)$$

Calculating the curvature of **Figure 9A**, the best approximation was reached with p of −0.306.

But also a calculation of this function with p of −3/2 (Eq. 2) showed good results.

$$N \sim t^{-3/2} \quad (2)$$

Equation 2 is known to describe the number of cluster per volume, N , for the coarsening kinetics of ensembles of spherical clusters in the process of kinetic limited growth (Schmelzer, 2015: personal communication), when processes of incorporation at the interface determine the growth rate. This situation might be possible also for the growth of needle-like Sr₅(PO₄)₃F crystals, but a final answer requires more detailed studies, in particular, in performing the determination of the bulk particle number, N , from N_s and appropriately accounting for the shape of the crystallites.

As another point of discussion, a comparison to the findings concerning the growth process of Sr₅(PO₄)₃F crystals should be done with the growth of needle-like Ca₅(PO₄)₃F in a different glass-ceramic system seems as shown by Müller et al. (1999)

and Höland et al. (2000). Most importantly, both crystal growth processes appear to follow an Ostwald ripening mechanism. A comparison of the results clearly shows that the number of Sr₅(PO₄)₃F crystals per volume (determined per area) is much higher than that of Ca₅(PO₄)₃F. However, the crystal length of Sr₅(PO₄)₃F with a maximum of approximately 500 nm is much smaller than that of Ca₅(PO₄)₃F, which grew up to 6 μm.

The primary crystal formation in glasses No. 2, 3, and 4 is different to that of glasses No. 1 and 2. The NaSrPO₄ nano-sized crystals were precipitated during the cooling of the melts of glasses 2, 3, and 4. However, this minor content of NaSrPO₄ does not influence the formation of Sr₅(PO₄)₃F. The NaSrPO₄ crystals remain stable in a very low volume fraction, even after annealing at temperatures of up to 1000°C. This phenomenon is similar to that discovered in glass-ceramics precipitation Ca₅(PO₄)₃F and NaCaPO₄ in a different glass-ceramic system (Höland and Beall, 2012).

The reference glass-ceramic No. 5 contained Ca₅(PO₄)₃F crystals in needle-like morphology. These crystals also grew according to the Ostwald ripening process (Höland and Beall, 2012). However, this glass-ceramic did not contain other crystal phases.

In addition to using the powder compact method for the internal nucleation and crystallization of Sr- or Ca-fluoroapatites, the authors applied this process in order to control surface nucleation and crystallization. This powder compact method involves a glass grain activation process according to the principles of tribochemistry. In this case, the tribochemical reaction was based on the ball milling grinding technology. Activated glass grains initiated the surface nucleation and crystallization of the framework silicates leucite (KAlSi₂O₆) or Rb-leucite (RbAlSi₂O₆) or pollucite (CsAlSi₂O₆). These crystals started to grow on the surface of the glass grains at 1000°C for leucite (glass-ceramic No. 1 and 2) and at 900°C for pollucite (glass-ceramic 3) and Rb-leucite (glass-ceramic No. 4). In a parallel reaction to this twofold nucleation and crystallization of fluoroapatites (via internal mechanisms) and leucite, Rb-leucite, and pollucite crystals (via surface mechanisms), a third reaction was found to take place. This third reaction is the solid-state-liquid-state sintering of the crystallized glass grains to form a glass-ceramic powder compact. This sintering involves a diffusion process in which the glass matrix is the main component. To produce a densely sintered glass-ceramic compact, these processes of powder compact formation took place at temperatures that were higher than those used for the formation of the glass-ceramic, that is, above 900°C. The reaction time was very short but led to the additional formation of leucite

crystals. Therefore, because of their crystal phases, the four glass-ceramics have to be characterized as follows:

Glass-ceramic No. 1: $\text{Sr}_5(\text{PO}_4)_3\text{F}$ –leucite, KAlSi_2O_6 ,

Glass-ceramic No. 2: $\text{Sr}_5(\text{PO}_4)_3\text{F}$ –leucite, KAlSi_2O_6 – NaSrPO_4 ,

Glass-ceramic No. 3: $\text{Sr}_5(\text{PO}_4)_3\text{F}$ –pollucite, $\text{CsAlSi}_2\text{O}_6$ – NaSrPO_4 ,

Glass-ceramic No. 4: $\text{Sr}_5(\text{PO}_4)_3\text{F}$ –Rb-leucite, $\text{RbAlSi}_2\text{O}_6$ – NaSrPO_4 .

The final powder compact glass-ceramics show different properties according to their chemical nature, crystal phase formation, and the very special design of their microstructure.

The main aim of this study was the development of glass-ceramics with a high level of radiopacity. The radiopacity was controlled by precipitating Sr-fluoroapatite crystals instead of Ca-fluoroapatites, and by incorporating Y^{3+} ions into the glass structure. Therefore, glass-ceramics No. 1 and 2 show much higher radiopacities than the reference glass-ceramic No. 5. An additional effect of increasing the radiopacity could be realized by adding Rb^+ and Cs^+ ions to the glass-ceramic. This incorporation of Rb^+ and Cs^+ ions in the glass-ceramics led to the crystallization of Rb-leucite and pollucite, respectively. Based on these findings, the pollucite-type glass-ceramic No. 3 containing Sr-fluoroapatite crystals showed the highest radiopacity.

In addition, it was established that the CTE values could be controlled. Glass-ceramic No. 4, characterized as Sr-fluoroapatite–Rb-leucite glass-ceramic, with nano-sized phases of NaSrPO_4 , showed the highest CTE of all the studied glass-ceramics. The optical properties (translucency and color) of all the glass-ceramics discussed provide a basis on which further biomaterials for dental applications can be developed.

Conclusion

The authors conclude that glass-ceramics derived from the chemical SiO_2 – Al_2O_3 – Y_2O_3 – SrO – Na_2O – K_2O /Rb₂O/Cs₂O– P_2O_5 –F

system can be developed as powder compact products. The processes of nucleation and crystallization were utilized by applying twofold mechanisms of internal and surface reactions. Based on these fundamentals, leucite-type, Rb-leucite-type, and pollucite-type glass-ceramics containing needle-like $\text{Sr}_5(\text{PO}_4)_3\text{F}$ crystals were developed.

In respect to the primary nano-sized crystal formation, the findings allow the conclusion that the formation of these spherical crystals of disordered $\text{Sr}_5(\text{PO}_4)_3\text{F}$ or NaSrPO_4 is based on glass-in-glass phase separation. Nano-sized $\text{Sr}_5(\text{PO}_4)_3\text{F}$ turns into needle-like $\text{Sr}_5(\text{PO}_4)_3\text{F}$. The growth of crystals follows an Ostwald ripening mechanism. The authors conclude that this process give a basis of tailor-made processing of glass-ceramics exhibiting controlled optical properties, especially controlled translucency and brightness.

Nevertheless, the NaSrPO_4 nano-phase was shown to have no epitaxial effect on $\text{Sr}_5(\text{PO}_4)_3\text{F}$ formation. This is similar to the phenomenon discovered in KAlSi_2O_6 – $\text{Ca}_5(\text{PO}_4)_3\text{F}$ – NaCaPO_4 glass-ceramics.

In summary, the authors conclude that twofold crystallization processes can be successfully applied to develop glass-ceramic biomaterials which combine different properties, such as specific radiopacity values, CTEs, and other optical characteristics. The main conclusion in respect of developing glass-ceramics showing high radiopacity is the influence of the large atoms/ions and their atomic/ionic mass of Cs^+ and Rb^+ over other alkali ions. Also, the increase of radiopacity of all the Sr-apatite glass-ceramics in comparison to Ca-fluoroapatite glass-ceramics should be based on the larger ion and greater atomic/ionic mass of Sr^{2+} over Ca^{2+} within the apatite crystal structure.

Acknowledgments

The authors like to thank J. P. Schmelzer (University Rostock, Germany) for his contribution to the discussion on Ostwald ripening of crystals.

References

- Beall, G. H., and Rittler, H. L. (1982). "Glass-ceramics based on pollucite," in *Nucleation and Crystallization in Glasses*, Vol. 4, eds Simmons J. H., Uhlmann D. R., and Beall G. H. (Columbus, OH: Adv. Ceram., The Am. Ceram. Soc., Inc), 301–312.
- Bredig, M. A. (1942). Isomorphism and allotropy in compounds of the type A_2XO_4 . *J. Phys. Chem.* 46, 747–764. doi:10.1021/j150421a009
- Chen, X., Hill, R., and Karpukhina, N. (2014). Chlorapatite glass-ceramics. *Int. J. Appl. Glass Sci.* 5, 1–10. doi:10.1111/ijag.12082
- Clifford, A., and Hill, R. (1996). Fluoroapatite-mullite glass-ceramic. *J. Non Cryst. Sol.* 196, 346–351. doi:10.1016/0022-3093(95)00611-7
- DeHoff, R. T., and Aigeltinger, E. H. (1970). Experimental quantitative microscopy with special application of sintering. *Perspect. Powder Metal.* 66, 81–137.
- Dejneka, M. J., and Pinckney, L. R. (1998). *Transparent Fluoroapatite Glass-Ceramics*. Patent Application PCT/US/1998/006245.
- Gutzow, I. S., and Schmelzer, J. W. P. (2013). *The Vitreous State: Thermodynamics, Structure, Rheology, and Crystallization*, 2nd Edn. Heidelberg: Springer.
- Hill, R. G., O'Donnell, M. D., Law, R. V., Karpukhina, N., Cochrane, B., and Tulyaganov, D. U. (2010). The early stages of nucleation and crystallization of an fluoroapatite glass-ceramic: evidence for nano-scaled crystallization. *J. Non-Cryst. Sol.* 356, 2935–2941. doi:10.1016/j.jnoncrysol.2010.05.102
- Hill, R. G., Stamboulis, A., Law, R. V., Clifford, A., Towler, M. R., and Crowley, C. (2004). The influence of strontium substitution in fluoroapatite glass and glass-ceramics. *J. Non-Cryst. Sol.* 336, 223–229. doi:10.1016/j.jnoncrysol.2004.02.005
- Höche, T., Moisesescu, C., Avramov, I., and Rüsel, C. (2001). Microstructure of SiO_2 – Al_2O_3 – CaO – P_2O_5 – K_2O –F glass-ceramics. 2. Time dependence of fluoroapatite crystal growth. *Chem. Mater.* 13, 1320–1325. doi:10.1021/cm001204h
- Höland, W., and Beall, G. H. (2012). *Glass-Ceramic Technology*, 2nd Edn. Hoboken, NJ: Wiley.
- Höland, W., Frank, M., Schweiger, M., and Rheinberger, V. (1994). Development of translucent glass-ceramics for dental application. *Glastech. Ber. Glass Sci. Technol.* 67, 117–122.
- Höland, W., Rheinberger, V., Apel, E., van't Hoen, C., Höland, M., and Dommann, A. (2004). "Glass-ceramics for medical application and dental restoration," in *Conference on Bioengineered Glass-Ceramics (The Hulbert Conference)* (Buffalo, NY).
- Höland, W., Rheinberger, V., Wegner, S., and Frank, M. (2000). Needle-like fluoroapatite-leucite glass-ceramic as a base material for the veneering of metal restorations in dentistry. *J. Mater. Sci. Mater. Med.* 11, 1–7. doi:10.1023/A:1008973800554
- Höland, W., Ritzberger, C., Apel, E., Rheinberger, V., Nesper, R., Krumeich, F., et al. (2008). Formation and crystal growth of needle-like fluoroapatite in functional glass-ceramics. *J. Mater. Chem.* 18, 1318–1332. doi:10.1039/b714913a

- Kokubo, T. (1991). Bioactive glass-ceramics properties and application. *Biomaterials* 12, 155–163. doi:10.1016/0142-9612(91)90194-F
- Kreidl, N. J. (1983). “Inorganic glass-forming systems,” in *Glass Sci. and Tech., Vol 1 Glass-Forming Systems*, eds Uhlmann D. R. and Kreidl N. J. (Orlando, FL: Academic Press, Inc), 107–299.
- Moiescu, C., Carl, G., and Rüssel, C. (1999). Glass-ceramics with different morphology of fluorfluorapatite crystals. *Phosphorus Res. Bul.* 10, 515–520. doi:10.3363/prb1992.10.0_515
- Müller, G. (1973). *Glass-Ceramics as Filler in Polymerizable Dental Filling Composites*. US-Patent 4017454.
- Müller, R., Abu-Hilal, L. A., Reinsch, S., and Höland, W. (1999). Coarsening of needle-like shaped fluorapatite crystals in $\text{SiO}_2\text{-Al}_2\text{O}_3\text{-Na}_2\text{O-K}_2\text{O-CaO-P}_2\text{O}_5\text{-F}$ glass. *J. Mater. Sci* 34, 65–69. doi:10.1023/A:1004457305970
- Slezov, V. (2009). *Kinetics of First-Order Phase Transition*. Berlin: Wiley-VCH.
- Toshev, S., and Gutzow, I. (1967). Derivation on nucleation kinetics in solids by examination of plane sections through the samples. *Phys. Stat. Sol.* 24, 349–359. doi:10.1002/pssb.19670240135
- Tsuge, T. (2009). Radiopacity of conventional, resin-modified glass ionomer, and resin-based luting materials. *J. Oral Sci.* 51, 223–230. doi:10.2334/josnusd.51.223
- van't Hoen, C., Rheinberger, V., Höland, W., and Apel, E. (2007). Crystallization of oxyapatite in glass-ceramics. *J. Eur. Ceram. Soc.* 27, 1579–1584. doi:10.1016/j.jeurceramsoc.2006.04.095
- Vogel, W. (1963). *Struktur und Kristallisation der Gläser*. Leipzig: Dt. Verlag für Grundstoffindustrie.
- Vogel, W. (1985). Chemistry of glass. *Am. Ceram. Soc.* 2, 92–120 and 330–361.
- Vogel, W., and Höland, W. (1987). The development of bioglass ceramics for medical application. *Angew. Chem. Int. Engl.* 26, 527–544. doi:10.1002/anie.198705271

Conflict of Interest Statement: The research was done for a company: Ivoclar Vivadent AG.

Copyright © 2015 Höland, Schweiger, Dittmer and Ritzberger. This is an open-access article distributed under the terms of the Creative Commons Attribution License (CC BY). The use, distribution or reproduction in other forums is permitted, provided the original author(s) or licensor are credited and that the original publication in this journal is cited, in accordance with accepted academic practice. No use, distribution or reproduction is permitted which does not comply with these terms.

ADVANTAGES OF PUBLISHING IN FRONTIERS



FAST PUBLICATION

Average 90 days
from submission
to publication



COLLABORATIVE PEER-REVIEW

Designed to be rigorous –
yet also collaborative, fair and
constructive



RESEARCH NETWORK

Our network
increases readership
for your article



OPEN ACCESS

Articles are free to read,
for greatest visibility



TRANSPARENT

Editors and reviewers
acknowledged by name
on published articles



GLOBAL SPREAD

Six million monthly
page views worldwide



COPYRIGHT TO AUTHORS

No limit to
article distribution
and re-use



IMPACT METRICS

Advanced metrics
track your
article's impact



SUPPORT

By our Swiss-based
editorial team